Glacial Isostatic Adjustment: Physical Models and Observational Constraints

By

W. Richard Peltier[1]

Patrick Pak-Cheuk Wu[2]

Donald F. Argus[3]

Tanghua Li[4]

Jesse Velay-Vitow[1]

1. Department of Physics, University of Toronto
2. Department of Earth Science, University of Calgary
3. Jet Propulsion Laboratory, Caltech
4. Earth Observatory of Singapore, Nanyang Technological University

Table of Contents

ABSTRACT

By far the most prescient insights into the interior structure of the planet have been provided on the basis of elastic wave seismology. Analysis of the travel times of shear or compression wave phases excited by individual Earthquakes, or through analysis of the elastic gravitational free oscillations that individual Earthquakes of sufficiently large magnitude may excite, has been the central focus of Earth physics research for more than a century. Unfortunately, data provide no information that is directly relevant to understanding the solid state "flow" of the polycrystalline outer "mantle" shell of the planet that is involved in the thermally driven convective circulation that is responsible for powering the "drift" of the continents and which controls the rate of planetary cooling on long timescales. For this reason, there has been an increasing focus on the understanding of physical phenomenology that is unambiguously associated with mantle flow processes that are distinct from those directly associated with the convective circulation itself. This paper reviews the past many decades of work that has been invested in understanding the most important of such processes, namely that which has come to be referred to as "glacial isostatic adjustment" (GIA). This process concerns the response of the planet to the loading and unloading of the high latitude continents by the massive accumulations of glacial ice that have occurred with almost metronomic regularity over the most recent million years of Earth history. Forced by the impact of gravitational n-body effects on the geometry of Earth's orbit around the Sun through the impact upon the terrestrial regime of received solar insolation, these surface mass loads on the continents have left indelible records of their occurrence in the "Earth System" consisting of the oceans, continents, and the great polar ice sheets on Greenland and Antarctica themselves. Although this ice-age phenomenology has been clearly recognized since early in the

last century, it was for over 50 years considered to be no more than an interesting curiosity, the understanding of which remained on the periphery of the theoretical physics of the Earth. This was the case in part because no globally applicable theory was available that could be applied to rigorously interpret the observations. Equally important to understanding the scientific lethargy that held back the understanding of this phenomenon involving mantle flow processes was the lack of appreciation of the wide range of observations that were in fact related to GIA physics. This paper is devoted to a review of the global theories of the GIA process that have since been developed as a means of interpreting the extensive variety of observations that are now recognized as being involved in the response of the planet to the loading and unloading of its surface by glacial ice. The paper will also provide examples of the further analyses of Earth physics and climate related processes that applications of the modern theoretical structures have enabled.

1. Introduction 1: Orbital forcing of continental glaciation and the astronomical theory of "ice-ages": origins of the ice loads to which glacial isostatic adjustment is the response

Prior to focusing upon the physical and mathematical structures of modern theories of the GIA process and on the observations they have been designed to explain, it will be important to understand the climate dynamical processes that have been responsible for the episodic appearance and disappearance of extensive regions of thick ice cover on the continents. It had long been recognized that so-called "ice-ages" had been a recurrent phenomenon during the past many hundreds of thousands of years of Earth history (e.g. see the contributions of Agassiz, Ademard, and others as summarized in the popular recounting of their "discovery" in Imbrie and Imbrie (1979)). However, the reason for their occurrence had remained a much debated mystery until the mid-1970's. The mystery was finally resolved dramatically with publication of the important paper by Hays, Imbrie and Shackleton (1976) in the journal Science. The analysis discussed in this paper was based upon oxygen isotope stratigraphies measured in a series of deep sea sedimentary cores drilled into and then raised from the floors of the major ocean basins. The information extracted from these sedimentary cores was of the depth dependence of the measured ratio of the concentration of the heavy isotope of oxygen ^{18}O to that of the lighter and more abundant isotope ^{16}O compared to the ratio characteristic of a standard sample of ocean water, referred to as Standard Mean Ocean Water (SMOW) according to the following definition:

$$\delta^{18}O = \left(\frac{\left[{}^{18}O/{}^{16}O \right]_{sample}}{\left[{}^{18}O/{}^{16}O \right]_{standard}} - 1 \right) \quad (1)$$

These ratios were measured mass-spectrometrically on the shells (calcium carbonate "tests") of tiny foraminifera that had lived in the water column but which upon their death these shells had

fallen to the ocean floor, accumulating in the sediment cover over time to be raised in the cores later drilled into the sediment that were employed in the analyses of Hays et al. (1976). Their work was a part of the International Ocean Drilling Programme (IODP), much of the work of which involved the collection of such sedimentary cores from a drilling ship named the "Joides Resolution" whose exploration of the ocean floors was orchestrated by what is now the Lamont Doherty Earth Observatory of Columbia University. Such ocean floor data had also played a critical role in the plate tectonic revolution of the 1960's.

The important connection between the oxygen isotopic ratio measured in a deep sea sedimentary core and ice cover on the continents is associated with the fact that both the evaporation of water from the oceans to create atmospheric water vapor, and the later precipitation of some of this water vapor as rain or snow, are mass dependent fractionation processes involving what is referred to as Rayleigh Distillation. These processes are such that during evaporation of water from the surface of the oceans, which leaves the salt behind, the vapor so produced is enriched in $H_2{}^{16}O$ relative to $H_2{}^{18}O$. Similarly, as this water vapor is transported from more tropical latitudes toward the poles by the atmospheric circulation and as some of the vapor precipitates as rain during transport, this further fractionates mass. At relatively high latitude (or high elevations in mountainous regions) the remaining vapor is finally precipitated as snow. As this snow accumulates, eventually compacting under its own weight to form ice on the continents, the oceans left behind are permanently enriched in the heavier isotope of oxygen until the continental ice sheets deglaciate, reintroducing the sequestered lighter isotope of oxygen to the ocean. The degree of this enrichment is therefore a direct measure of the mass of fresh water that has been removed from the oceans to build the continental ice sheets. By measuring $\delta^{18}O$ in the shells of foraminifera that lived in the oceans at the time determined by the

depth in a deep sea sedimentary core, we are able to infer the volume of ice that had been sequestered on the continents at that time. In Shackleton (1967) it had been shown that this variability, which had earlier been interpreted by Emiliani (1955) primarily as a proxy for ocean temperature, following the suggestion by Urey (1947), was not primarily a temperature proxy but was in fact and more accurately a continental ice volume proxy. Shackleton argued this to be especially the case during the Late Quaternary ice ages (most recent 2 million years). Shackleton demonstrated this by comparing isotopic measurements to measurements of relative sea level. Although primarily an ice volume proxy over the Late Quaternary ice ages, a correction for temperature influence is still required to improve the accuracy of the ice volume estimate (e.g. see Waelbroeck et al., 2002).

Since depth in such sedimentary cores is strongly correlated with the time in the past that the foraminiferal calcite shells at a given depth had become closed systems, each depth dependent record from each core could be turned into a time series if only one could produce an accurate relationship between depth and time. Because the sedimentation rate at different locations in different ocean basins are different, this relationship is unique for each sedimentary core. However, in each of the cores analyzed by Hays et al. (1976) it was possible to determine time as a function of depth by directly dating the foraminifera shells using the ^{14}C chronometer based upon the rate of radioactive decay of ^{14}C and measuring the ^{14}C concentration using accelerator mass spectrometry. Because the ^{14}C age differs appreciably from sidereal age, calibration of the carbon clock is required for which accurate methods are now available as they were then (e.g., see Stuiver and Reimer (1993) for an up to date discussion of the CALIB software). However, this direct method of determining time as a function of depth was applicable only to the shallowest part of such records since radiocarbon dating is accurately calibrated to

calendar years only as far back as ~30,000 years, enough to determine a sedimentation rate only in the shallowest part of each core. To complete the map from depth to time the authors made use of the then widely accepted age of the most recent reversal in polarity of Earth's magnetic field, the so-called Brunhes-Matuyama transition, which was assumed fixed to 730,000 years, on the basis of an age determined by Potassium Argon (K/Ar) chronometry applied to volcanic rocks from the island of Hawaii. Since the depth of this transition in the deep sea sedimentary cores of Hays et al. (1976) could be directly determined because these cores contained sufficient magnetic material to enable the depth of this transition to be identified using the methods of paleo-magnetism, it was possible to translate depth to time in each core given this critical additional tie point. Recognizing that the noise level in each core would be different due to the influence of differential bioturbation and other processes between cores, the authors produced a single "stacked" record by averaging over the time series produced independently for each core. By computing a power spectrum of this time series a major discovery was made, probably the most important discovery in geophysical science since the plate tectonic revolution of the 1960's.

Fig. 1.1 illustrates the $\delta^{18}O$ data and spectral analyses of it for what has become one of the most influential of such individual modern records, namely that from the sedimentary core raised from the floor of the ocean at IODP site 677 located in the Panama Basin which is off the northwest coast of South America in a region in which the rate of sediment accumulation on the ocean floor is one of the highest recorded. This circumstance ensures that the temporal resolution of the record will be optimally high. This record, from Shackleton et al. (1990), is shown on a special timescale to be discussed further below. In the left column of this figure the time series of the oxygen isotopic ratio is shown in 2 segments, respectively from 2 million years before present to 1 million years before present, and from 1 million years before present to the present

day. At the bottom of the left column are shown power spectra of these two segments of the ODP 677 record. Clearly, the first million years of the record is dominated by power at a period of approximately 41,000 years. In the most recent million years of the record, however, the spectrum is dominated by power at a period of ~100,000 years. Also evident in both segments of the record, but more prominently in the later half, is a weaker but statistically significant concentration of power over a range of periods from 19,000 to 23,000 years. The original stacked record of Hays et al. (1976) was found to be characterized by the same three periods in which power was concentrated. This was recognized by the authors as a "eureka moment" as it established that the theory for ice age occurrence suggested by the Serbian scientist Milutin Milankovic (e.g. 1941) was essentially correct although it had been considered somewhat disreputable ever since it was first advanced.

Milankovic's idea was that ice ages were caused by the small variations of the latitudinal dependence of received solar radiation during the summer season caused by variations in the geometry of Earth's orbit around the Sun due to the action of gravitational n-body effects in the solar system. Reconstructions of the geometry of Earth's orbit were being produced in the same period by Bretangnon (1974) and his results for the evolution of orbital geometry were being employed by Berger (e.g. 1976a,b) to compute time series for the summertime seasonal insolation signal that could be compared with the oxygen isotopic record of continental ice volume change. Bretangnon's results for the variations in orbital geometry were later improved by Laskar (e.g. 1985) and his reconstruction of the long timescale evolution of Earth's orbit around the Sun was much later checked by Quinn, Tremaine and Duncan (1991) by brute force integration of the gravitational n-body problem for the entire solar system, backwards in time from a modern ephemeris, and shown to be accurate back to 3 million years before present.

The data on the right hand side of Fig. 1.1, show the reconstructed summertime solar insolation anomaly at 65° north Latitude, also in two segments, the first for the period from 2 million years before present to 1 million years before present and the second from 1 million years before present to the present day. Below these time series are the power spectra for the same two segments so that direct comparisons may be made between the oxygen isotope ratio (ice volume) time series in the left column. Based upon this comparison it will be clear that although the spectral line at a period of 41,000 years and the cluster of power over the range of periods from 19,000 to 23,000 years are in common between the solar insolation forcing and climate response represented by the oxygen isotopic time series, at the dominant ~100,000 year period during the most recent million years of the proxy ice volume record, there is essentially no power in the time series for the solar insolation forcing. In the Milankovic theory it was imagined that the orbital insolation stimulus responsible for the growth of ice cover on the continents was the summertime seasonal insolation anomaly. His argument was that ice could accumulate on the high latitude continents only in periods during which the strength of summer insolation was insufficient to melt all of the snow that had fallen in the previous winter. In his opinion this would allow high latitude snow cover to build up so as to form continental ice sheets as the snow compacts under its own weight over millennia.

Fig. 1.2, graphically illustrates the nature of the variations in the orbital elements that are contributing to the variations of solar insolation responsible for the continental ice volume record of the climate response. In the Milankovic theory the dependence of the summertime seasonal insolation anomaly δQ(t) has the following dependence upon orbital obliquity, ε(t), orbital eccentricity e(t), and orbital precession with an angular frequency ω_p :

$$\delta Q(t) = A\varepsilon(t) + Be(t)\cos(\omega_p t) \qquad (2)$$

In Eq. (2) A and B are constants and ε is orbital obliquity (the angle which the spin axis makes with the plane of the ecliptic) which varies periodically on the time scale of 41,000 years and *e* which varies on dominant timescales of 100,000 and ~405,000 years. The most important characteristic of the summertime seasonal insolation signal is that the temporal variation of orbital eccentricity appears only as a modulation of the radiative forcing associated with orbital precession of frequency ω_p corresponding to a period near 21,000 years. It is therefore clear that the second term in Eq. (2) will not include significant power at the period of 100,000 years even though the eccentricity of the orbit varies on this characteristic timescale. Since, for approximately the last million years of Earth history, ice-age climate variability has occurred on precisely this timescale, it is also clear that the climate system must have been behaving in a highly nonlinear fashion whereas in the first million years of the Pleistocene its behavior was essentially linear. It is generally understood that this so-called mid-Pleistocene climate transition (e.g. see Deblonde and Peltier, 1990), was due to a significant increase in the volume of continental ice sheets that occurred over this mid-Pleistocene range of time. This is a facet of the theory of ice age occurrence that Milankovic had not envisioned as he envisioned that the response should be a linear function of the orbital insolation forcing. Individual 100,000 year pulses of ice-age ice cover have a characteristically "sawtooth" form with the glaciation phase of each cycle lasting approximately 90,000 years and the deglaciation phase approximately 10,000 years. Broecker and van Donk (1970) established this form as characteristic of the most recent Late Pleistocene ice age cycle by direct comparison with certain characteristics of the important Barbados record of relative sea level history, a record that will assume a position of considerable importance in our discussion of the glacial isostatic adjustment process. A reproduction of Fig. 7 from Broecker and van Donk (1970) is provided here as Fig. 1.3. The figure compares the

oxygen isotopic record of the most recent glacial cycle to the variability characteristic of the coral-based record of relative sea level history which is captured in the tectonically uplifted sequence of corals which record successive relative sea level high stands which very accurately follow the orbital insolation forced variability of the oxygen isotope ratio. The "sawtooth" form of the record is clearly apparent. To Broecker and van Donk it remained an enigma as to why the deglaciation process should occur on a timescale much shorter than that of glaciation. This issue has remained outstanding in the literature but is one that we will also address in Part I of this paper. It also concerns the nonlinear nature of the connection between orbital stimulus and climate response.

Although the frequency domain comparison of the spectral characteristics of the orbital insolation forcing to the spectral characteristics of the ice volume response provides convincing evidence of the importance of the Milankovic effect, an even more powerful demonstration has been provided by time domain analyses by quantitatively extending the qualitative time domain analysis of Broecker and Van Donk provided in Fig. 1.3. This time domain analysis was reported in the paper of Shackleton, Berger and Peltier (1990). In this paper, the authors investigated the general validity of the original analysis of the oxygen isotopic record from the IODP 677 core eventually published in Peltier (2007, 2015). These results were based upon the development of an orbital tuning strategy to determine the optimal map in this core from depth to time. This strategy was based upon the design of a pair of band-pass digital filters in which the pass bands were centered respectively on the obliquity period and the eccentricity-precession band covering a range of periods centered on approximately 21,000 years, both frequency bands in which the climate system was apparently responding linearly to radiative forcing. The precise forms of these filters are illustrated in Fig. 31 of Peltier (2007) and Fig. 30 of Peltier (2015). By

beginning with the time-depth relation determined by calibrated ^{14}C dating in the shallowest portion of the core, this relationship was extended to increasing depth by iteratively optimizing the correlation between the isotopic signal and the orbital insolation signal in the obliquity band and then that in the eccentricity precession band. The method was applied progressively to greater and greater depth in the core. The result of this analysis led to the conclusion that the best map from depth to time in this core was a map characterized by constant sedimentation rate at the Panama Basin IODP 677 site. This map deviated significantly from the original map that Shackleton had produced for this core based upon the conventionally assumed age of 730,000 years for the Brunhes-Matuyama magnetic reversal. If valid, this new depth-to-time map would require that the age of the Brunhes-Matuyama magnetic reversal would have to be in error by about 7% with the actual age being 780,000 years rather than the 730,000 years that had been assumed based upon conventional K/Ar dating. The age of this reversal was immediately re-determined using the $^{39}Ar/^{40}Ar$ step heating methodology that had been developed in Toronto by Professor Derek York and was reported in Baksi (1993) who found, using this much more accurate methodology for the dating of relatively young volcanic rocks, that the age of this transition was in fact 780,000 years! This is probably the clearest demonstration of the primacy of the Milankovic mechanism as control on the continental glaciation process. In Shackleton et al. (1990) the Toronto result for the IODP 677 core was shown to be correct for all deep-sea sedimentary cores analyzed. By assuming the validity of the astronomical theory of ice-ages, a prediction was made that enabled a serious error in the chronologies of all deep-sea sedimentary cores to be corrected. This result had an immediate impact upon the plate tectonic description of Earth's surface kinematics as it required that the spreading rates of all tectonic plates away from

mid-ocean ridges had to be revised as these had all been determined on the basis of the assumed 730,000 year age of the Brunhes-Matuyama magnetic reversal (e.g. see DeMets et al., 1994).

These results demonstrating the orbital control on continental glaciation processes on long time scales will prove to be very important for the understanding of all that is to follow in this paper. In particular, the fact that the oxygen isotopic time series from deep sea sedimentary cores provide proxy records of continental ice volume change is critical. These records demonstrate that the dominant timescale of continental ice volume variability for the most recent million years of Earth history is approximately 100,000 years and that the shape of individual pulses of this ice-age cycle have a distinctly "sawtooth" form. As we begin to discuss the glacial isostatic adjustment process that occurs in response to these surface mass loading events, the additional knowledge that these records provide on the magnitude of the mass exchanges between the oceans and the continents that characterize each glacial cycle will also prove to be of first order importance. To further emphasize the nature of the orbital forcing that is responsible for stimulating the development of such massive accumulations of land ice, we show in Fig. 1.4 the changes in received insolation as a function of latitude and time of year at a series of critical times within the most recent 100,000 year cycle of ice age occurrence. Especially important to note in this figure is the latitudinal variation of solar insolation at 116,000 years ago, the time of the beginning of the most recent ice age cycle. Note that at this time, high latitude insolation was reduced during summer by more than $50 W/m^2$ thereby allowing winter snow cover to begin to accumulate and so to initiate the process that is now referred to as "glacial inception", (e.g. see Vettoretti and Peltier, 2013).

2. Introduction 2: The Viscoelastic Earth. Models of Mantle Rheology, Linear and Nonlinear

The most important issue that must be resolved as we begin to discuss the construction of detailed theories of the glacial isostatic adjustment process concerns the microphysical mechanism that enables the flow of the solid-state outer shell of the planet that extends from Earth's surface to the depth of the core mantle boundary (CMB) approximately 2950 km below the surface of the almost perfectly spherical planet. This outermost solid shell consists of two primary rheological divisions, respectively an upper and relatively thin (100 km thick) "lithosphere" in which temperatures are so low that brittle failure is a regular occurrence evidenced in "Earthquakes", and a much thicker underlying, "mantle" which extends from the base of the lithosphere to the CMB. Below the CMB lies the liquid outer core of thickness 2200 km, and below this the solid inner core of radius 1221 km. A graphical depiction of this structure is shown in Fig. 2.1, based upon more than a century of seismological observations and related theory, as represented by the Preliminary Reference Earth Model (PREM) of Dziewonski and Anderson (1981). To a first order of approximation, this structure is spherically symmetric with physical properties of the spherical shell model varying only as a function of radius. These primary physical properties of an elastic model of the Earth consist of density, and the speeds of both compressional and shear waves of velocities Vp and Vs respectively. Inspection of this graphic will demonstrate that at particular depths of 420 km and 660 km, these properties of the elastic Earth exhibit near discontinuities in their values, features that are now unambiguously known on the basis of high pressure experimental physics measurements to be caused by pressure induced equilibrium thermodynamic phase transitions in Earth's mineralogical composition. The shallower of these phase transitions is due to the transformation of the mineral Olivine to the mineral Spinel (e.g. Bina and Wood, 1987). This transition is exothermic. The deeper transition is due to the transition from the Spinel phase through a dis-proportionation

reaction to a mixture of the minerals Perovskite and Magnesiowustite (e.g. Ito and Takahashi, 1989; Ishii et al., 2018). This deeper transition is endothermic. When the solid state mantle of the planet flows, these phase transitions exert significant influence on the nature of the circulation of the mantle (e.g. see Busse and Schubert, 1971; Peltier, 1972; Richter, 1973; Christensen and Yuen, 1985; Solheim and Peltier, 1994a,b; Christensen, 1995; Tackley and Schubert, 1994; Shahnas and Peltier, 2015). In particular, the shallower exothermic transition acts in such a way as to intensify the circulation through it. The deeper transition, on the other hand, acts in such a way as to impede the circulation through it. A much deeper transformation of mineral phase also exists at the base of the mantle, the Post Perovskite phase (Murakami et al., 2004) which appears to define the so-called D'' layer adjacent to the core-mantle boundary. All of these pressure induced phase transformations play an important role in controlling the nature of the thermal convection induced solid-state flow of mantle material that is responsible for continental drift and seafloor spreading. The kinematic description of this flow process provided by the plate tectonic "cartoon" in which horizontal motions at the surface of the Earth are described in terms of a finite number of quasi-rigid-body "plates" that are constrained to move by rotations about individually fixed poles provides a "shorthand" description of the impact upon the surface of the planet caused by the underlying thermally driven convective circulation.

Superimposed upon the primarily horizontal motions of the plates at Earth's surface are the motions associated with the process of glacial isostatic adjustment that are manifest most clearly in the vertical motions at Earth's surface induced by surface mass loading of the continents by temporally varying accumulations of glacial ice. As such this dynamical process is "Beyond Plate Tectonics" but as we will proceed to discuss, the two dynamical regimes are intimately connected by the fact that each relies upon the ability of the outer solid shell of the planet to flow

like a liquid on sufficiently long time scales. It is a consequence of the fact that these processes are characterized by widely separate timescales that we are able to analyze them separately. When a material flows, a fundamental characterization of this behavior is by a "viscosity", the physical property of the material that measures the rate of strain (or velocity of fluid flow) produced by an applied shear stress. In the field of continuum mechanics the relationship between stress and strain for various materials is embodied in a "constitutive relationship". The simplest such relationship for a material that cannot flow is that for a three dimensional isotropic "Hookean" elastic solid on which most of elastic wave seismology has been based, the field that has led to PREM, the properties of which were illustrated in Fig. 2.1. The three dimensional constitutive relation for this material is the following:

$$\tilde{\tau}_{kl} = \lambda \tilde{e}_{kk} \delta_{kl} + 2\mu \tilde{e}_{kl}, \qquad (3)$$

in which λ and μ are the so called elastic Lamé parameters, $\tilde{e}_{kl}$ is the strain tensor and $\tilde{\tau}_{kl}$ is the stress tensor. In terms of the elastic Lamé parameters the elastic wave speeds Vp and Vs shown on Fig. 2.1, are simply the following:

$$Vs = \sqrt{\frac{\mu}{\rho}}, \qquad (4a)$$

$$Vp = \sqrt{\frac{(\lambda + 2\mu)}{\rho}}. \qquad (4b)$$

In reality when polycrystalline aggregate Earth materials (rocks) are subjected to high levels of stress on sufficiently long timescales they may begin to flow like a viscous liquid and therefore are termed "viscoelastic". A simple extension of the elastic constitutive relation (Eq. (3)) that embodies a transition from elastic mechanical behavior on short timescales to viscous flow on

appropriately long timescales is that for a so-called "Maxwell" solid as discussed, for example, in Eringen (1966) for which the constitutive relation is the following:

$$\dot{\tau}_{kl} + \left(\tau_{kl} - 1/3\,\tau_{kk}\,\delta_{kl}\right) = 2\mu\,\dot{e}_{kl} + \lambda\,\dot{e}_{kk}\,\delta_{kl,} \tag{5}$$

in which the "dot" over a quantity denotes time differentiation and the additional Greek symbol ν represents the "viscosity" of a material that is now a viscoelastic solid, one that is capable of flow on appropriately long timescales. Eq. (5), is derived by assuming that the Maxwell solid results from the combination of an elastic solid with a viscous fluid and attaching them in series, so that the strain/displacements of the elastic solid and the viscous fluid add, but the "elastic" and "viscous" stresses are equal. Since the paper of Peltier (1974), it is this model of the mechanical behavior of the outer solid shell of the planet, consisting of lithosphere and mantle, that has come to be most widely employed in the description of the glacial isostatic adjustment process. However, it is clearly a linear model and it remains a significant issue as to whether this most fundamental assumption is appropriate to the flow of the lithosphere-mantle system. Perhaps the most compelling characteristic of this model is that the mechanical processes it is able to describe may be analyzed by employing the so-called Correspondence Principle of Biot (1954, 1955a,b). Because the constitutive equation is linear, when it is written in the Laplace transform domain it assumes the following form:

$$\left(s + \frac{\mu}{\nu}\right)\tilde{\tau}_{kl} - \frac{1}{3}\frac{\mu}{\nu}\tilde{\tau}_{kk}\,\delta_{kl} = 2\mu s + \lambda s\, e_{kk}\,\delta_{kl}. \tag{6}$$

Where the tilde denotes the Laplace transform and "s" is the Laplace transform variable. Contracting the Cartesian tensor relation (Eq. (6)) gives

$$\tilde{\tau}_{kk} = \left(3\lambda + 2\mu\right)\tilde{e}_{kk}, \tag{7}$$

and substituting this result back into Eq. (6) then results in :

$$\tilde{\tau}_{kl}=\left(\lambda+\frac{2}{3}\frac{\mu(\mu/\nu)}{(s+\mu/\nu)}\right)\tilde{e}_{kk}\delta_{kl}+\frac{2\mu s}{(s+\mu/\nu)}\tilde{e}_{kl}. \quad (8)$$

Thus

$$\tilde{\tau}_{kl}=\lambda(s)\tilde{e}_{kk}\delta_{kl}+2\mu(s)\tilde{e}_{kl} \quad (9)$$

where

$$\lambda(s)=\frac{\lambda s+\mu K/\nu}{s+\mu/\nu}, K=\lambda+\frac{2}{3}\mu \quad (10a)$$

$$\mu(s)=\mu s/(s+\mu/\nu). \quad (10b)$$

Eq. (9) has exactly the same form as the constitutive relation (Eq. (3)) for a Hookean elastic solid, where the Lamé parameters (viscoelastic "compliances") $\lambda(s)$ and $\mu(s)$ are now functions of the Laplace transform variable s. The Correspondence Principle assures us that if we are willing to solve an equivalent elastic problem to the viscoelastic problem in which we are actually interested, many times for different values of the Laplace transform variable "s", then we will have constructed the Laplace transform of the time dependent viscoelastic solutions that we are seeking. This model is especially attractive as the elastic parameters of the Maxwell model, consisting of the two elastic Lamé parameters and density, for a spherically symmetric elastic model are available, for the PREM, say, on the basis of more than a century of seismological research.

The fundamental question that needs to be answered before setting out to test the appropriateness of the Maxwell model as a means of understanding the glacial isostatic adjustment process is whether there is any *a priori* basis on which to expect that it may be an appropriate model for the description of this phenomenon. The issue is whether the flow of a solid at the pressure and temperature conditions of Earth's mantle, in which temperatures vary

from O(10^3) K at the base of the lithosphere to O(4×10^3) K at the CMB, and pressure reaches a level of 135 GPa at this deepest mantle level, may be well approximated by a simple model of this kind. Although much progress has been made in understanding the physics of mantle flow on the basis of high pressure physics experiments on appropriate assemblages of mantle minerals (e.g. see Karato, 2008 for an extensive discussion), the availability of direct measurements under such extreme conditions of what the effective viscosity should be has remained elusive. Nevertheless, considerable progress has been achieved on the basis of direct experimental measurements on the flow of mantle analogues, based upon recognition of the fact that the mantle is a polycrystalline solid.

It is extremely useful to consider what controls flow in polycrystalline solids in general for a material, a mantle analogue, whose rheological behavior may be investigated under controlled laboratory conditions. In this regard a perhaps surprisingly useful laboratory analogue of Earth's polycrystalline mantle is fine grained polycrystalline ice. For this analogous polycrystalline material, Goldsby and Kohlstedt (1997, 2001) have described the measurements on polycrystalline ice of a fixed grain size, and temperature relative to the melting temperature in exquisite detail. Examples of their results for two different temperatures at a fixed grain size of 1 mm are shown in Fig. 2.2 in which strain rate as a function of differential stress is plotted on a log-log scale. Their data demonstrate that, at the highest levels of differential stress, the relationship between strain rate and differential stress is strongly nonlinear and of power law form in which the stress exponent is approximately equal to 4. As differential stress decreases, the data exhibit two transitions in the power law relationship between these two quantities. In the first transition the stress exponent drops to a value near 2 and in the final transition the stress exponent drops to unity, demonstrating that, in this final regime of lowest differential stress, the

polycrystalline solid ice is flowing like a Newtonian viscous fluid for which the relationship between differential stress and strain rate is linear. The mechanisms supporting flow in these three regimes are fundamentally different. At the highest stress level the flow of the solid is accommodated by the propagation of dislocations of the crystal structure through the interiors of individual crystal grains, whereas at the intermediate level of differential stress these dislocations propagate along the grain boundaries. At the lowest levels of stress, the flow of the material is accommodated by the diffusion of impurities. The high stress level mechanism is referred to as dislocation climb whereas at intermediate stress levels the mechanism is referred to as grain boundary sliding. As the constitutive relation for ice plays a critical role in the field of glaciology, a particular point on these strain rate vs. differential stress diagrams is denoted as the Glen Flow Law which is clearly on the transition in differential stress between the dislocation climb regime and the grain boundary sliding regime. The Glen Flow Law is characterized by a stress exponent of 3, the average of the values of the stress exponents of 4 and 2 characteristic of the bounding regimes.

Of greatest importance for our purposes is the fact that the constitutive relationship between stress and strain may vary from highly nonlinear to entirely linear depending primarily on the grain size of the medium and the level of differential stress which is causing the flow, although the temperature relative to the melting temperature is also very important. It is the linear regime that is in accord with the Maxwell viscoelastic model discussed previously. The dependence of the Newtonian viscosity ν in this regime on the properties of the environment in which polycrystalline flow of the solid is occurring is as follows (e.g. see Herring, 1950):

$$\nu = \left(kT\, a^2 / \alpha\, D_0 \Omega \right) \exp\left[\left(E + p\, V_a \right) / kT \right], \qquad (11)$$

where k is Boltzmann's constant, T the absolute temperature, V_a the activation volume, "a" the mean grain radius, E the activation energy for self-diffusion, p the pressure, Ω the atomic volume, and α a constant. In this case the equations of motion are easily derived and are the equations of viscous hydrodynamics with the temperature and pressure dependent viscosity (Eq. (11)). The most significant unknowns in this expression for the viscosity of the polycrystalline solid are the grain size "a", the homologous temperature "T", relative to the melting temperature and the stress level.

It is clearly important for the *a priori* plausibility of the Maxwell model that a polycrystalline solid may flow as a Newtonian viscous fluid but the Maxwell model is not a hydrodynamic model. Rather, it is a viscoelastic model in which, on a timescale that depends upon the Newtonian viscosity, with the elastic constants fixed by seismological observations, the medium will transition from perfectly elastic to Newtonian viscous behavior. By inspection of the Laplace transform domain form of the constitutive relation between stress and strain in Eq. (9), for times short compared to the timescale $\frac{\nu}{\mu}$ for values of the Laplace transform variable "s" sufficiently large, based upon the Tauberian theorems, the medium will behave simply as a Hookean elastic solid. This timescale is referred to as the "Maxwell time". For times in excess of the Maxwell time the medium will begin to behave progressively more strongly as a Newtonian viscous fluid.

The Maxwell viscoelastic model is therefore a very powerful model on the basis of which one might hope to capture both the immediate elastic reaction to surface mass load removal or imposition but also the eventual, and as we will see, dominant, contribution to the glacial isostatic adjustment process due to viscous flow. However, when this model is applied, it is clearly based upon the "assumption" that the level of differential stress involved in the associated

deformations induced by surface mass loading are low enough and/or the grain size of the polycrystalline medium is small enough that diffusion creep will be the dominant flow mechanism. When we explore the implications of this assumption in Part I of this paper, we will be obliged to make an additional assumption in order to reduce the mathematical complexity of the analysis required, which is that the viscosity of the deep Earth is a function of depth only. Since, as noted previously, the outer solid shell of the planet is filled with a thermally driven convective circulation that is responsible for driving the surface plate tectonic process, this could be misconstrued to be an assumption that should be ruled out on a priori grounds. However, it is generally understood that the circulation operates at a Rayleigh number Ra of $O(10^7)$ where Ra $= \frac{g\alpha\delta T\, d^3}{\kappa\nu}$, in the heated from below limit, in which the physical properties in this non-dimensional parameter are the mean gravitational acceleration in the mantle shell g, the coefficient of thermal expansion α, the temperature difference δT between Earth's surface and the CMB, the thickness of the shell "d" within which convection is occurring, the mean thermal conductivity of the mantle κ and finally the effective molecular viscosity ν. In the circulation regime characterized by such a high Rayleigh number, although the Prandtl number $\mathrm{Pr}=\frac{\nu}{\kappa}$ is extremely large so that the inertial force is irrelevant to the detailed characteristics of the flow, as velocity shear diffuses very rapidly, the circulation is nevertheless highly nonlinear. This is because the advection of temperature is so strong that the flow is dominated by intense thermal boundary layers that bound essentially adiabatic cores of the cellular convective motions, e.g. see Jarvis and Peltier (1982) for simple steady state examples of such circulation and Solheim and Peltier (1994a,b), Shahnas and Peltier (2015) for more realistic examples which include the impacts upon the circulation due to the influence of the pressure induced mantle phase transitions

discussed in connection with Fig. 2.1. Fig. 2.3, from the authors of the latter paper illustrates a series of thermally turbulent but statistically steady flows as a function of the Rayleigh number in the absence of phase transition effects. As the Rayleigh number increases the mixing in the interior of the shell becomes extremely efficient such that the depth dependence of temperature in the shell is rendered adiabatic with pronounced thermal boundary layers existing only adjacent to the surface (the lithosphere) and the CMB.

When the influence of phase transitions is introduced, however, a marked change occurs which is illustrated in Fig. 2.4. This depicts a statistically steady flow in which the interior temperature field at a very vertical level in the spherical shell is shown in Mollweide projection. In this projection the longitude and latitude dependent map of temperature at each radial level is projected onto an ellipse. The interior level of the endothermic phase transition appears in the figure as the roof of the lower mantle, a level from which an “avalanche” of anomalously cold material is descending into the deep mantle, leading to a time-dependent cooling of an area on the CMB. The time dependency action of the endothermic phase transition that supports this avalanche effect leads to the development of an internal thermal boundary layer at 660 km depth, within which the local radial temperature gradient is significantly super-adiabatic. Given this effect due to the impact upon mixing of the endothermic phase transition, it is clearly an issue as to what the impact might be upon the depth dependence of mantle viscosity across the 660 km depth horizon. It is not therefore surprising that one of the main focuses of research on the GIA process has been to answer this important question. As we will discuss in what follows, an important recent contribution of GIA analyses has been to resolve this issue for the class of linear Maxwell models.

All of this is of course only a plausibility argument as to why the spherically symmetric viscoelastic Maxwell model to be analyzed in detail in Part I of this paper cannot be ruled out on *a priori* grounds. However, if on the basis of the very detailed analyses of this model we will describe, it is found to satisfy all of the observational constraints, this still cannot be construed as proof that the flow of the polycrystalline mantle is governed by diffusion creep or, even if it is, that the influence of lateral heterogeneity of viscosity exerts no significant influence upon the glacial isostatic adjustment process.

It is for these reasons that, in Part II of this paper, we will address the extent to which an alternative to the spherically symmetric linear Maxwell model has been developed that is enabling investigation of the influences not captured in this simplest possible model. This alternative viscoelastic model has been based on the finite element methodology that underlies the ABAQUS platform (Hibbitt et al., 2011). This has required highly significant modifications to this software platform to enable it to address the geophysical problem of glacial isostatic adjustment. As in Eq. (6), the rheology of the nonlinear Maxwell solid is derived on the basis of the assumption that the strain of the elastic solid and the viscous fluid add, but the "elastic" and "viscous" stresses are equal. The viscous component of this alternative Maxwell constitutive relation for steady state creep can be written as (e.g. Ranalli, 1995):

$$\dot{\varepsilon}_{ij} = \mathrm{A}\, \sigma_E^{'n-1} \sigma_{ij}^{'}. \qquad (12)$$

In which $\dot{\varepsilon}_{ij}$ is the deviatoric strain rate and $\sigma_{ij}^{'}$ is the deviatoric stress and

$$\sigma_E^{'n-1} = \sqrt{\left(\sigma_{ij}^{'}\sigma_{ij}^{'}\right)/2}$$

is the effective shear stress. In the above equations, "*n*" is the same stress exponent that was discussed in connection with the ice analogue above, A is the "creep parameter" determined from laboratory shear experiments (if possible) and is a function of pressure, temperature, grain

size, water content and melt fraction (e.g. Karato and Wu, 1993; Karato, 2008). Note that in the discussion of this alternative model we are using σ to denote stress in the finite element model whereas we employed the Greek letter τ to denote this quantity in the linear Maxwell model and similarly we will be employing ε to denote strain in the finite element model for which we employed "e" in the discussion of the linear Maxwell model. We will continue to make this distinction between the two models in order to emphasize the fact that our analysis of flow in terms of the linear Maxwell model is employing a Lagrangian description of the small amplitude motions involved whereas when we employ the above constitutive relationship to describe the viscous component of the flow associated with the GIA process we will be employing a fundamentally Eulerian description of this viscous component of the dynamics. By separating the elastic and viscous reaction to surface ice loading in this way in the nonlinear model we will be making the same assumption as that made by Cathles (1975) in his early work on the GIA process.

For a model of this kind described by the constitutive relation (Eq. (12)) for the viscous component of the flow, it is useful to define an effective viscosity as:

$$\nu_{eff} = \frac{1}{\sqrt{3^{2n+1}}} \frac{1}{A^*} \frac{1}{\sigma_E'^{n-1}}. \qquad (13)$$

In which A^* is the creep parameter determined if possible from uniaxial experiments and is related to the parameter A according to Ranalli (1995) by $A^* = \left(\frac{2}{3^{\lfloor n+1 \rfloor/2}}\right) A$. When the finite element methodology is employed to analyze the glacial isostatic adjustment process in the linear rheology limit in Part II of this paper, the rheological inputs are n=1 and $A^* = \frac{1}{3\nu_{eff}}$. And, for a three dimensional Earth model with linear rheology that is not spherically symmetric and so has

viscosity $\nu(r,\theta,\phi)$ in which r is radial position in the volume of the solid outer shell of the planet and θ and ϕ are latitude and longitude respectively, the former input is $A^*(r,\theta,\phi)=\frac{1}{3\nu(r,\theta,\phi)}$. Laboratory studies of polycrystalline Olivine, the dominant mantle mineral above the 420 km exothermic phase transformation, have demonstrated for this actual mantle material that diffusion creep that gives rise to linear rheology can indeed become the dominant creep mechanism if the stress level is relatively low, or the grain size is small or both (Karato and Wu, 1993; Karato, 2008). On the other hand, when the stress level is high enough or the grain size is large, dislocation climb will be the dominant mechanism as it is in the ice analogue system discussed previously (e.g. Goetze and Kohlstedt, 1973; Li et al., 2003, Cordier et al., 2004; Mainprice et al., 2005).

There are geophysical observations that require that the creep mechanism at very shallow lithosphere-asthenosphere depths be in fact nonlinear. In this region where the effective viscosity is strongly depth dependent, the operative rheology often appears to be significantly non-Newtonian. This follows from the existence of significant seismic anisotropy, a characteristic evident in the geophysical observation that the velocity of seismic surface wave propagation is a strong function of the direction of propagation relative to the direction of surface plate motion. An example of the inference of the existence of such anisotropy on the basis of shear wave splitting data has recently been provided by Reiss et al. (2016). The development of such anisotropy requires nonlinearity of the stress-strain relationship in order that individual crystal grains of the polycrystalline material may be aligned by the ambient shear. The polycrystalline ice analogue discussed previously provides an excellent example of this process as the flow of a large ice sheet such as that on Greenland, in which flow is driven gravitationally from the region where the ice is thickest towards where it is thinnest at the coast, causes the

development of a fabric in which the c-axes of individual grains are aligned normal to the flow direction, thereby creating significant anisotropy. Although direct laboratory measurements on the creep of Earth materials at lithospheric depths where the pressures and temperatures are low provide useful confirmation of the seismic observations, they are much less illuminating for the Earth's deep mantle because of the extreme conditions under which measurements must be made.

Based upon creep experiments on polycrystalline Olivine the stress exponent for dislocation creep is found to have a value near 3 (Karato and Wu, 1993; Karato, 2008). Wu (2002b) reported, based upon his use of the finite element model to describe the GIA process, with stress exponents in the range 2-4, that the effect was not large enough to be easily discriminated against on the basis of relative sea level and uplift rate data. In addition, at higher stress levels such as might obtain beneath the centers of glacial loading at the maximum of glaciation, lower effective viscosity is implied by the nonlinear constitutive relationship, suggesting that initial relaxation of the load induced surface depression should proceed quickly. For the same reason, as the stress level drops during the relaxation process, the viscosity beneath the centers of loading would be expected to increase, leading to an increase with time of the relaxation time governing the glacial isostatic adjustment process (e.g. as discussed in Barnhoorn et al., 2011). It is interesting to note that such transient rheological behavior can also be mimicked by a more complex but still linear viscoelastic model namely that referred to as a standard linear viscoelastic solid as discussed in detail in Peltier (1985), Peltier et al. (1986) as well as Lau and Holtzman (2019) and Lau et al. (2021). The conclusion of these analyses was that there was no indication in the available constraints on the GIA process of evident transient behavior such as would be expected if the rheology were significantly nonlinear.(but see also Ivins et al, 2020).,

For power law rheology, however, it is very important to note that the effective viscosity (Eq. (13)) is dependent upon both space and time because the stress level is a function of both independent variables. The spatial dependence of stress means that use of a nonlinear creep law results necessarily in lateral heterogeneity of effective viscosity, not due to lateral heterogeneity of temperature but due to the lateral heterogeneity of effective viscosity. Similarly, the Maxwell time, which is simply $\frac{\nu_{eff}}{\mu}$, is also a function of both space and time.

A primary novelty of this paper is that it is our intention to explore the extent to which the observables of the glacial isostatic adjustment process may be able to discriminate between three distinct flavors of theory that have been developed to describe the GIA phenomenon. Beginning with the simplest theory from a physical perspective, that based upon the linear spherically symmetric Maxwell model in Part I to follow, we will shift in Part II to discuss two more complex theoretical structures. The first of these will be a second model based upon the assumption of a linear rheology but one in which the viscosity of the solid outer shell of the planet is fully three dimensional. The second alternative to the spherically symmetric linear Maxwell model will be models for which the constitutive relation between stress and strain rate is fully nonlinear. We will also consider models in which rheology is a composite of linear and nonlinear mechanisms. Our goal will be to attempt to distinguish between them, if possible, on the basis of the observational constraints.

PART I. The Spherically Symmetric Maxwell Rheological Model of the Glacial Isostatic Adjustment Process

3. The response of the linearly visco-elastic model to surface mass and tidal potential loading: the Impulse Response of a Maxwell Earth Revisited

In Peltier (1974) the linear Maxwell model was first invoked as a vehicle with which to attempt to construct a global theory of the glacial isostatic adjustment process. The model was based upon application of the Correspondence Principle of linear viscoelasticity and so required the results of an equivalent elastic problem which could be employed to construct solutions in the Laplace transform domain. The appropriate equivalent elastic problem had only recently been thoroughly discussed by Farrell (1972) whose focus was upon the surface mass loading of an elastic model of the Earth in connection with his work on the surface mass loading associated with the ocean tides. His analysis was in terms of the so-called Love numbers, following Longman (1962, 1963), Love numbers that had first been introduced by A.E.H. Love (1929) in the context of a much simplified version of the same problem in his important book entitled "Some Problems in Geodynamics".

3.1. Linear Viscoelastic field equations and surface boundary conditions

The methodology employed by Farrell was based upon the mathematical formalism and related software that had been developed at the Scripps Institution of Oceanography by Gilbert and Backus (1966, 1968a, 1968b) and Gilbert (1970) for application to understanding the elastic gravitational free oscillations of the Earth that are excited by Earthquakes of sufficiently large magnitude. The field equations satisfied by such small amplitude (linear) oscillations consisted of the (linearized) equation for the conservation of momentum and Poisson's equation for the coupled variations in the gravitational field, namely:

$$\rho \nabla \cdot \tilde{\tau} - \nabla \left(\rho g \tilde{u} \cdot e_r \right) - \rho \nabla \tilde{\phi} + g \nabla \cdot \left(\rho \tilde{u} \right) e_r = \rho \frac{\partial^2 u}{\partial t^2} \approx 0 \qquad (14a)$$

$$\nabla^2 \tilde{\phi} = -4 \pi G \nabla \cdot \left(\rho \tilde{u} \right). \qquad (14b)$$

In Eq. (14a), we have included the term on the right hand side representing the inertial force that is extremely important in the free oscillations problem. In Farrell's analysis of the surface loading problem for an elastic model of the Earth this term was set to zero on the basis of the recognition that, on the timescales of the ocean tides that are extremely long compared to the periods of elastic body waves or global free oscillations, this term would contribute nothing to the dynamical process of interest as these physical processes would not be excited by the slow process of surface mass redistribution by the ocean tides. The field equations analyzed by Farrell were therefore the "quasi-static" system from which the inertial force has been eliminated. With this term eliminated the above system still differs fundamentally from that employed by Farrell in that all of the dependent variables have the tilde symbol attached which indicates that these variables are all Laplace transforms of the time dependent physical fields. This is the Laplace transform domain form of the equivalent elastic problem of Farrell (1972). They may be solved using the same methods as those employed by Longman (1962, 1963) implemented using the normal mode software of Gilbert and Backus but in the quasi-static limit and for a spherically symmetric model of the Earth.

Prior to discussing the methodology employed to construct Laplace transform domain solutions it will be important to first discuss the meaning of the individual terms in these equations. The first term on the left hand side of (14a) represents the force per unit volume acting on the material caused by the divergence of the viscoelastic stress. The third term is the buoyancy force caused by the interaction between the depth dependent background density field and the perturbation to the gravitational acceleration caused by the perturbation to the

gravitational potential, whereas the 4th term on the left hand side is the buoyancy force caused by the interaction between the density perturbation caused by the load induced deformation since this density perturbation is just $\rho' = \nabla \cdot (\rho \tilde{u})$. Although each of these terms is obviously required in a theoretical structure designed to be accurate to first order in perturbation theory, the second term on the left hand side is not so simply explicable but as we shall see it plays an extremely important role in the use of the Correspondence Principle of linear viscoelasticity to describe the GIA process. Because the theory of elasticity is an essentially Lagrangian theory and because the medium being deformed is "pre-stressed" hydrostatically by the balance between the vertical pressure gradient and the buoyancy force, as the load induced deformation proceeds individual material elements must be understood to transport their pre-stress with them as they are displaced. The second term on the left hand side of (14a), therefore describes the additional force to which pre-stress advection gives rise as first noted in the previously mentioned book of A.E.H. Love (1949). In this term the hydrostatic pre-stress is represented by the pressure gradient $\frac{\partial p}{\partial z} = -\rho g$ which is transported only radially, thus the inner product with the unit vector in the radial direction.

As in the elastic problem of Farrell (1972), we seek solutions for displacements and the perturbation to the gravitational potential in the form of expansions in spherical harmonics as:

$$u = \sum_{n=0}^{\infty} \left(U_n(r,s) P_n(\cos\theta) e_r + V_n(r,s) \frac{\partial P_n(\cos\theta)}{\partial \theta} e_\theta \right) \qquad (15a)$$

$$\varphi = \sum_{n=0}^{\infty} \varphi_n(r,s) P_n(\cos\theta) \qquad (15b)$$

in which the $P_n(\cos\theta)$ are the usual Legendre polynomials of degree "n" that are functions of the angular coordinate θ. Since the time dependent response to any variation of surface mass load (or

tidal potential load) may be calculated by space-time convolution of an appropriate Green function with the actual surface mass load, it is clearly sufficient to construct the solution for this Green function. Because we are assuming that the Earth is spherically symmetric this Green function must depend only upon radial position in the sphere and upon the angular displacement θ from the point on the surface at which the delta function surface mass (or gravitational potential) "impulse" is applied. In (15a,b), the spherical harmonic expansions involves expansion coefficients that are functions only of radius "r" and Laplace transform variable "s" for radial displacement $U_n(r,s)$, tangential displacement $V_n(r,s)$ and perturbation to the gravitational potential $\varphi_n(r,s)$ in which we have dropped the tilde from the dependent variables in (14a,b), which was employed to explicitly denote the fact that the field variables were in the Laplace transform domain. Following the original work of Longman, the gravitational potential φ must be understood to consist of the sum of two parts φ_1 and φ_2, which are, respectively, the perturbation potential of the ambient gravitational field and the potential of the externally applied gravitational force field (the load).

In order to complete the set of dependent variables required to represent the coupled system (14a), and (14b), additional variables must be introduced to represent this sixth order system in the simplest form rotationally. We take these additional variables to be the radial and tangential components of the stress tensor τ_{rr} and $\tau_{r\theta}$ respectively and a third additional variable we take, following Farrell (1972) to be related to the vertical derivative of the perturbation to the gravitational potential as:

$$q = \frac{\partial \varphi}{\partial r} + \frac{(n+1)}{r}\varphi + 4\pi G\rho u_r. \qquad (16)$$

These additional variables are also written in terms of their Legendre transforms with coefficients, $T_{r,n}, T_{\theta,n}, \wedge Q_n$. Equations (14a and 14b), then reduce to the coupled set of ordinary differential equations:

$$dY/dr = AY. \tag{17a}$$

Where $\mathbf{Y} = (U_n, V_n, T_{rn}, T_{r\theta}, \Phi_n, Q_n)$) is a vector with 6 components and A is the s dependent 6x6 matrix of coupling coefficients, the rows of which are as follows:

$$A_{1i} = \left[-2\lambda/\beta r, n(n+1)\lambda/\beta_r, 1/\beta, 0, 0, 0\right]$$

$$A_{2i} = \left[-1/r, 1/r, 0, 1/\mu, 0, 0\right]$$

$$A_{3i} = \left[\left(\frac{4}{r}\right)\left(\frac{\gamma}{r} - \rho_0 g_0\right), \frac{n(n+1)}{\sigma}\left\{\frac{2\gamma}{r} - \rho_0 g_0\right\}, -\frac{4\mu}{r\beta}, \frac{n(n+1)}{r}, -\frac{\rho_0(n+1)}{r}, \rho_0\right] \tag{17b}$$

$$A_{4i} = \left[(1/r)(\rho_0 g_0 - 2\gamma/r), (-1/r^2)\cdot\{-n(n+1)(\gamma+\mu)+2\mu\}, -\lambda/\beta r, -3/r, \rho_0/r, 0\right]$$

$$A_{5i} = \left[-r\pi G\rho_0, 0, 0, 0, -\frac{(n+1)}{r}, 1\right]$$

$$A_{6i} = \left[-(n+1)4\pi G\rho_0/r, n(n+1)4\pi G\rho_0/r, 0, 0, 0, \frac{(n+1)}{r}\right].$$

In the individual rows of this matrix two combinations of the elastic Lamé parameters have been defined in order to simplify the expressions for the matrix elements, namely:

$$\beta = \lambda + 2\mu \tag{17c}$$

and

$$\gamma = \mu\left\{\frac{(3\lambda+2\mu)}{(\lambda+2\mu)}\right\}. \tag{17d}$$

When we apply the set of coupled ordinary differential equations (17a,b), to solve the viscoelastic problem of interest, by employing the Correspondence Principle, all of the elastic parameters are to be interpreted as having the specific Laplace transform variable dependent

forms shown explicitly in equations (10a,b). The individual terms in the set of coupled ordinary differential equations (17a,b) follow by direct substitution of the poloidal expansions (15a,b), into the spherical polar coordinate forms of equations (14a,b), and use of the definition (14c). Insofar as the connection to the literature that preceded Farrell (1972) is concerned, it is worth noting that the solution 6-vector being employed here differs from those in Longman (1963) and Alterman et al. (1959). The specific choices being made here have been based upon the fact that they lead to simplified expressions for the boundary conditions.

These boundary conditions subject to which this system of equations is to be solved depend upon the forcing to which the surface of the planet is subject and we will be interested in two cases, both of which were discussed by Farrell (1972) for the elastic problem. Because the set of ordinary differential equations in Eq. (17a), is of sixth order, six boundary conditions are required, three of which are simply conditions of regularity at the origin of the spherical domain The remaining three boundary condition are those on the radial and tangential components of the stress tensor and on the gradient of the gravitational potential, namely the components $T_{r,n}, T_{\theta,n}$ and Q_n. These are respectively the normal and tangential components of the stress tensor and the variable related to the vertical derivative of the gravitational potential. It is at this point that it is important to recall that in computing the impulse response Green functions for the viscoelastic Maxwell model we will be interested in the response to a point mass load, or alternatively a geopotential load, that is brought to the surface at t=0 and instantaneously removed. That is, a load that has a delta function time dependence. Since we are constructing this solution in the Laplace transform domain and since the Laplace transform of a delta function in the time domain is a Heaviside step function in the Laplace transform domain, these boundary conditions will be

identical to the boundary conditions employed by Longman (1962, 1963) and Farrell (1972) which for surface mass loading are simply the following:

$$T_{r,n}(a) = -g(2n+1)/4\pi a^2$$
$$T_{\theta,n}(a) = 0 \qquad (18)$$
$$Q_n = -G(2n+1)/a^2$$

in which "a" is the radius of Earth's surface and these conditions are independent of s. They determine $U_n(r,s)$, $V_n(r,s)$,and $\Phi_n(r,s)$. The complete depth and s-dependent solutions to the problem in the Laplace transform domain are determined by applying a "shooting method" in which one integrates the system from a starting depth to the surface for three linearly independent starting solutions. The correct solution is then the particular linear combination of these linearly independent solutions that satisfies the boundary conditions (Eq. (18)). As commented in much greater detail in Peltier (1974), as in the analogous problem in global seismology involving the elastic gravitational free oscillations, the starting depth for each triplet of linearly independent integrations of the system from starting depth to the Earth's surface is migrated to shallower and shallower depth as the spherical harmonic degree of the surface load forcing increases. At very low spherical harmonic degree when the starting depth is in Earth's core, the system of Eqs. (14) degenerates to 4^{th} order from 6^{th} as also discussed in Peltier (1974). This and other details of the calculation are also discussed there, including the issue as to how the calculation is regularized for degree 1.

3.2. Love Numbers

In analogy with the problem of determining the static deformation of an elastic sphere, dimensionless Love numbers h_n, l_n, and k_n are introduced into the viscoelastic problem. These numbers are functions of three variables, r, n, and s. If U_n, V_n, and $\Phi_{1,n}$ arise from a force field

with potential φ_2 described through its coefficients $\varphi_{2,n}$, these Love numbers are defined by the following:

$$\left[U_n(r,s),V_n(r,s),\Phi_{1,n}(r,s)\right] = \Phi_{2,n}(r)\left[h_n(r,s)/g, l_n(r,s)/g, k_n(r,s)\right], \quad (19)$$

where $\Phi_{2,n}$ is independent of s, since the applied load is assumed to have a delta function dependence in the time domain. When attention is focused upon the solutions at r = a, then $\Phi_{2,n}(a) = ag/m_e$ (Longman, 1963), where g is the gravitational acceleration at the surface and m_e is the Earth's mass. The time dependence of the displacements U_n ,V_n, and the potential perturbation φ_1 is contained in the time dependence of the Love numbers. In the limit of large n and small θ the solutions of the spherical problem tend to the solutions for the half space (Boussinesq's problem, discussed in Peltier, 1974). This equivalence leads to the asymptotic relations

$$\left[h_n, n l_n, n k_n\right] = \frac{g m_e}{4\pi a^2 \eta}\left[\frac{-\sigma}{\mu}, 1, \frac{-3\rho\eta}{2<\rho>\mu}\right] \quad (20)$$

which are correct to order l / n. In Eq. (20), the parameters η, σ, and μ have values equal to those for the top layer of the spherical Earth models, and <ρ> is the Earth's mean density. These asymptotic results were discussed in detail by Farrell (1972).

There are in fact two distinct species of these Love numbers that will play important roles in the analyses we will describe in this paper, namely those that are obtained by applying the surface boundary conditions (Eq. (18)), and those that are obtained by applying the alternative boundary conditions:

$$\begin{aligned} T_{r,n}(a) &= 0 \\ T_{\theta,n}(a) &= 0 \\ Q_n &= -G(2n+1)/a^2 \end{aligned} \quad (21)$$

The Love numbers determined on the basis of boundary conditions (Eq. (21)), will be referred to as "Tidal" Love numbers whereas those determined on the basis of boundary conditions (Eq.

(18)), will be referred to as "Surface Load" Love numbers. The need for this second set of Love numbers will become clear below when we will discuss the response of the rotational state of the planet to the ice age cycle and the manner in which the changes in Earth's rotational state feedback on sea level history. When the context requires, we will distinguish these Love numbers by superscripts "L" or "T".

Here we will provide examples of the surface load Love numbers for a simple viscoelastic Earth model, one with the Gutenberg-Bullen model A structure as discussed for example in Alterman et al. (1961). The first visco-elastic model discussed in Peltier (1974) was one in which this elastic structure was coupled to a simple viscosity model in which it was assumed that the viscosity of the solid Earth from the surface to the core-mantle boundary was equal to 10^{21} Pa s at all depths. Although this model lacks a surface lithosphere in which the viscosity is effectively infinite and any radial structure associated with mantle phase transitions and with the depth dependent separation of the mantle solidus and the adiabat on which the mantle temperature field sits throughout the majority of its volume, it turns out that the structure of the Love numbers in the Laplace transform domain have general properties that even this simplest of models is able to capture perfectly. To illustrate this we show in Figures 3.1a and 3.1b, respectively the $h_n(a,s)$ and $nk_n(a,s)$ surface load Love numbers for this first viscoelastic model. Notable is the fact that each spectrum, which consists of distinct s-dependent forms for each value of spherical harmonic degree, is characterized by distinct asymptotic values for both large s and small s. The large s asymptotes of each of the Love numbers for each spherical harmonic degree are exactly equal to the elastic surface load Love numbers of Kaula (1963), Kuo (1969) and Farrell (1972). The meaning of the small s asymptotes may be understood in terms of the final value theorem of Laplace transforms which simply asserts that:

$$\lim_{t \to \infty} F(t) = \lim_{s \to 0} s \cdot L\left[F(t)\right] \tag{22}$$

for arbitrary F(t), indicate that as t → ∞, both $h_n(t)$ and $k_n(t)$ tend to zero. This is simply mathematical confirmation that the time domain solutions for each of the Love numbers must vanish in the limit of long time, once the point mass has been removed from the surface at t=0 after having been instantaneously emplaced. In Peltier (1974), it was then recognized that each of these Love numbers for each spherical harmonic degree could be written as the sum of an instantaneous elastic component and a viscous time dependent component as:

$$h_n(s) = h_n^V(s) + h_n^E,$$
$$k_n(s) = k_n^V(s) + k_n^E. \tag{23}$$

Where h_n^E and k_n^E are the constant large s asymptotes of each spherical harmonic degree dependent component of the spectrum. In the time domain each of these Love numbers may then be written formally as:

$$h_n(t) = L^{-1}\left[h_n^V(s)\right] + h_n^E \delta(t),$$
$$k_n(t) = L^{-1}\left[k_n^V(s)\right] + k_n^E \delta(t). \tag{24}$$

The equations in Eq. (24) emphasize that the large s asymptotes of the spectra in Figures 3.1a and 3.1b determine the immediate elastic response of the system. The weights h_n^E and k_n^E are precisely the surface mass load Love numbers that have been calculated for the elastic problem by previous authors. In Peltier (1974), a simple method was introduced with which to approximate the time dependence of the viscous component, namely a collocation method in which the $h_n^V(s)$ and $k_n^V(s)$ are sampled through the range of over which the spectra transition between the two asymptotes. This collocation technique is essentially that proposed by Schapery (1962) in which one hypothesizes a time domain solution for the viscous parts of the Love number spectra in the form of a Dirichlet series of the form

$$\theta(t)=\sum_{i=1}^{m} a_i \exp(-t/\tau_i). \quad (25)$$

Although some motivation was provided in Peltier (1974) as to why this form may be appropriate, at that point in the development of what became the "normal mode theory of glacial isostasy" this was without a firm theoretical foundation. With the τ_i determined by the set of values of s selected by sampling the Laplace transform domain spectra approximately twice per decade through the range of transition between the asymptotes determined by $1/s_i$, the a_i are then determined by minimizing the error between the exact and approximate Laplace transform domain forms of the spectra. We take the approximate solution to be $\theta^*(t)$, where

$$\theta^*(t)=\sum_{i=l}^{m} b_i \exp(-t/\alpha_i). \quad (26)$$

The mean square error between θ(t) and θ* (t) is

$$E^2=\int_0^\infty \left[\theta(t)-\theta^*(t)\right]^2 dt. \quad (27)$$

We assume that the α_i are fixed such that $1/\alpha_i = s_i$, where the s_i are the values of s at which we have computed the spectral amplitude. The b_i of the approximate solution Eq. (26) may then be determined by minimizing E^2 in Eq. (27), with respect to the b_i as

$$\frac{\partial E^2}{\partial b_i}=\int_0^\infty 2\left[\theta(t)-\theta^*(t)\right]\exp\left(\frac{-t}{\alpha_i}\right)dt=0. \quad (28)$$

Which requires

$$\int_0^\infty \theta(t)\exp\left(\frac{-t}{\alpha_i}\right)dt=\int_0^\infty \theta^*(t)\exp\left(\frac{-1}{\alpha_i}\right)dt \quad (29)$$

in order for the mean square error of the approximation to be a minimum, and thus the Laplace transform of the approximation must equal the Laplace transform of the exact solution at least at the m points s = $1/\alpha_i$, i = 1, m, or

$$\theta(s)\big|_{s=1/\alpha_i} = \theta^*(s)\big|_{s=1/\alpha_i}. \tag{30}$$

Implying that

$$\theta(s)\big|_{s=1/\alpha_i} = \sum_{i=1}^{m} \frac{b_i}{[s+1/\alpha_i]}\bigg|_{s=1/\alpha_i} = \sum_{i=1}^{m} \frac{b_i}{[1/\alpha_i+1/\alpha_i]}, \tag{31}$$

a result that follows from the fact that $L(e^{-at}) = 1/(s + a)$. Eq. (31) may be written in matrix form as:

$$\theta_i = m_{ij} b_j. \tag{32}$$

Where $m_{ij} = \alpha_i\alpha_j/(\alpha_i + \alpha_j)$. Given the b_j obtained by solving the set of simultaneous equations (Eq. (32)), these may be employed in the Dirichlet series (Eq. (25)), to approximate the time history θ(t). The sequence b_j may be thought of as a discrete approximation to the distribution function of relaxation times as mentioned above. As we will show immediately, however, the exact inverse of the viscous components of the individual Love number spectra do in fact consist of a discrete set of relaxation times. This recognition led to the final form of the "Normal Mode Theory for Glacial Isostatic Adjustment". As we will discuss, however, this collocation technique has continued to form an important element of this theory.We note that subsequent to its introduction in Peltier (1974)m there appeard many papers suggesting different empirical methods for the inversion of the Love number spectra (eg.Hanyk et al (1995), Spada et al, (2006), Tanaka et al (2009), Tang and Wenke (2019).

3.3. Transformation of the Laplace transform domain solutions into the time domain: the normal mode theory of glacial isostatic adjustment

We need next to consider the application of formal mathematical methods to invert the Laplace transform domain solution into the time domain in order to replace, if possible, the empirical collocation method discussed in the last section. If we call the three linearly independent solutions delivered by the shooting method $\mathbf{T}_1$, $\mathbf{T}_2$, $\mathbf{T}_3$, which must be combined to satisfy the boundary conditions, then in general we will have determined

$$Y(r,s)=c_1(s)T_1(r,s)+c_2(s)T_2(r,s)+c_3(s)T_3(r,s). \quad (33)$$

If we denote the boundary conditions (Eq. (18)), by **B**(a, s), then the coefficients $c_i(s)$ of the linear combination of the three solutions that must satisfy the boundary condition are determined by

$$B(s)=Y(a,s)=c_1(s)T_1(a,s)+c_2(s)T_2(a,s)+c_3(s)T_3(a,s). \quad (34a)$$

For the impulse boundary conditions as commented above the elements b_i of **B** are in fact s-independent. If we define a vector **C** as

$$C=\left[c_1(s),c_2(s),c_3(s)\right] \quad (34b)$$

and denote by **M** the matrix whose column vectors are $\mathbf{T}_1(a, s)$, $\mathbf{T}_2(a, s)$, and $\mathbf{T}_3(a, s)$, then

$$B=MC, \quad (34c)$$

so that

$$C=M^{-1}B. \quad (34d)$$

Now since $\mathbf{M}^{-1} = \mathbf{M}^*/\det \mathbf{M}$ where $\mathbf{M}^*$ is the transpose matrix of the cofactors M_{ij}^*, therefore

$$c_i=\sum_{j=1}^{3}\frac{M_{ij}^*(s)\,b_j}{detM} \quad (35)$$

and the solution satisfying the boundary conditions is

$$Y(r,s)=\sum_{ij}\frac{M_{ij}^{*}b_j}{detM}T_i(r,s)=\frac{Q(r,s)}{detM}, \qquad (36)$$

where $\mathbf{Q} = \Sigma_{ij} M_{ij}^{*} b_j T_i$. Eq. (36) now gives the general solution in a form which is useful for inversion. Suppose we define, following the discussion in Peltier (1974)

$$Y^{V}(r,s)=Y(r,s)-Y^{E}(r,s)=\frac{Q^{V}(r,s)}{detM}, \qquad (37)$$

where

$$Y^{E}=\lim_{s\to\infty}Y(r,s).$$

The time domain form of the solution (Eq. (37)), may now be written

$$Y(r,t)=\frac{1}{2\pi i}\int_{L}\frac{Q^{V}(r,s)}{detM}e^{st}ds+Y^{E}\delta(t), \qquad (38)$$

where L is the Bromwich path. If s_j (j = 1, N) are the zeros of the secular determinant det M, then Eq. (38), may be simply evaluated as (Wu 1978):

$$Y(r,t)=\sum_{k=1}^{N}Res\left[\frac{Q^{V}(r,s)e^{st}}{detM(r,s)};s_j\right]+Y^{E}(r)\delta(t). \qquad (39)$$

Since in general $d(detM)/ds\neq 0$ at s = s_j, as the zeros of the secular function det **M** are simple poles it follows that the residues at the (simple) poles s_j are

$$Res\left[\frac{Q^{V}(r,s)e^{st}}{detM(r,s)};s_j\right]=\frac{Q^{V}(r,s_j)e^{s_j t}}{(d/ds)(detM)|_{s=s_j}} \qquad (40)$$

and therefore that

$$Y(r,t)=\sum_{k=1}^{N}\frac{Q^{V}(r,s_j)e^{s_j t}}{(d/ds)(detM)}+Y^{E}\delta(t). \qquad (41)$$

If we define the vector of residues $\mathbf{R}_k$ as (Wu 1978):

$$R_k = \frac{Q^V(r, s_j)}{(d/ds)(det\, M)|_{s=s_j}} \tag{42}$$

then

$$Y(r,t) = Y^E \delta(t) + \sum_{j=1}^{N} R_j e^{-s_j t}. \tag{43}$$

Where we have written $s_j = - \overline{-s_j}$, since the N zeros of det **M** are all (usually) located on the negative real axis in the complex s plane. In this normal mode solution for the residues (Eq. (42)), the r_j are inversely proportional to the slope of the secular function det **M** as it passes through zero at the location of the mode with inverse relaxation time s_j. It will be noted that this solution based upon the application of the calculus of residues is identical to the empirical solution assumed by application of the colocation methodology in the last section. The only difference is that whereas in the collocation method the points on the real s-axis at which the Laplace transform domain form of the solution is sampled are not arbitrary but rather constitute a unique set of inverse decay times for each viscoelastic model determined by the zeros of the secular function det M.

The fact that this unique spectrum for each Love number at each spherical harmonic degree for each viscoelastic model of the Earth could be employed to determine a set of "Normal Modes of Viscous Gravitational Relaxation" was established in Peltier (1976), who plotted for simple models what came to be referred to as "relaxation diagrams" in which for each spherical harmonic degree are plotted the set of relaxation times required to represent the viscous gravitational adjustment of the surface of the Earth to the application of a mass load onto its surface. These modes were employed in the location technique to determine the amplitudes of the modes of viscous gravitational relaxation required to describe the isostatic adjustment process. Although the formal calculus of residues solution for these modal amplitudes was recorded in Wu (1978), it

was not employed. Rather as is Peltier (1976), the relaxation times in terms of which the time dependence of a given Love number was to be expressed were simply employed in the collocation technique. The calculus of residues solution was eventually published in Peltier (1985), in which it was employed in an analysis of the impact of the GIA process upon the orbit of LAGEOS (the LAser GEOdynamics Satellite) to show that the precession of the node of its orbit could be interpreted as a response to the GIA process. In this paper a comparison was presented of the modal amplitudes determined by application of the colocation technique given the known set of relaxation times provided by the zeros of det M and these determined by the residues at poles. These were shown to be in reasonably close but not perfect agreement (see Tables 3a and 3b in Peltier, 1985). The numerical problem found previously was shown to be a simple consequence of the fact that to obtain an accurate value for the residue at a given pole required that the secular function had to be sampled finely in the vicinity of the pole in order that its derivative (see Eq. (32), above) could be computed with sufficient accuracy. In the current version of the Toronto software once a first estimate is found of a zero of det M for a given Love number a method of continuous bisection is employed to determine a converged value of the residue. This method is an improvement over the collocation method in that the individual modal amplitudes are determined independently.

Although the result (Eq. (33)), normally provides highly accurate results for the residues at the poles and therefore of the modal amplitudes for each Love number it has nevertheless turned out that the collocation method has remained important as it provides a method on the basis of which to perform an extremely useful check on the results of the pure normal mode method, This is because the total strength of the viscous relaxation for each Love number at each spherical harmonic degree is known on the basis of the difference between the large s and small s

asymptotes of the individual Love number spectra. If a given normal mode decomposition is not accurately representing the total viscous relaxation then the collocation method can be employed as a check on the calculation.

3.4. Examples of the Viscoelastic Relaxation Spectra for the Normal modes of Viscous Gravitational Relaxation

Fig. 3.2, illustrates a series of models of the depth dependence of viscosity that have played important roles in the modern literature on the glacial isostatic adjustment process. They are labeled VM1, VM2 and VM3 for Viscosity Models 1, 2 and 3 respectively. These viscosity models have each been coupled to the PREM to produce a sequence of viscoelastic models of the rheological structure of the planet as basis for GIA analysis. Inspection of this sequence of models will demonstrate that they are all characterized by a sharp jump in viscosity across the 660 km depth seismic discontinuity associated with the pressure induced phase transformation of the mineral Spinel through a disproportionation reaction to a mixture of Perovskite and Magnesiowustite (MgO). Until very recently, it has remained an issue in the literature as to how large this viscosity jump (if any) might be. The viscosity of the upper mantle and transition zone above this level has been a source of much less debate for reasons we will discuss in what follows.

In Figures 3.3a,b,c, we show the relaxation diagrams for viscosity models VM1, VM2 and VM3 respectively when coupled to the PREM elastic structure. Evident is the fact that there is a discrete set of inverse decay times determined by the zeros of the secular function det M discussed in the last section. It will be observed that for each model there exists a series of modal branches which are labeled as in Peltier (1976). On the basis of the depth dependence of the deviatoric strain tensor to be discussed below. The mode labeled “L” exists as a consequence of

the existence of a surface lithosphere in which the viscosity has been assumed to be infinite and of approximate thickness 100 km. Along the Mo mantle and lithosphere L0 branch of modes the relaxation times initially increase with spherical harmonic degree, but beyond a critical degree which depends upon lithospheric thickness, th,begin to decrease. This critical spherical harmonic degree is determined by lithospheric thickness. The thicker the lithosphere the lower the spherical harmonic degree beyond which the relaxation times on the "L" branch begin to decrease. In all three of the models under discussion here, it will be observed that this critical degree is ~150, this is because all three models have the same lithospheric thickness of 100 km.

Notable also on these relaxation diagrams are the additional branches labeled M0, M1, M2 and C0. The latter modes exist only at very long wavelength (low spherical harmonic degree) but vanish once the starting depth for the triplet of integrations of the governing equations rises out of the inner core into the mantle so that the integration no longer "feels" the presence of the density jump at the CMB. M0 is the fundamental mode of the system which exists because of the density jump at Earth's surface where the boundary conditions are applied to a system that includes the prestress advection term discussed at the beginning of this section. The M1 and M2 modes exist respectively because of the density jump across the 660 km discontinuity and because of the general increase of density with depth in the lower mantle.It is important to note that there may also exist iunstable modes n the relaxation spectrum of some mudels with PREM spherically symmetric elastic structure (eg, Cambioti and Sabadini, 2010)). However such modes have extremely small real (positive) part of the eigenvalue and so grow on extremely long timescale. They are to be considered aphysical artifacts and are to be rejcted.

Given these relaxation diagrams and recognizing that an ice sheet of modest horizontal scale will be controlled entirely by the relaxation associated with only the M0 and L modes we may

immediately apply the short relaxation time modes to the interpretation of the very important Fennoscandian relaxation spectrum of McConnell (1968) who, in his doctoral thesis at Toronto, analyzed the strandline data recording the post glacial rebound of Fennoscandia using the varve chronology of Lindén (1938) to infer a horizontal wavenumber dependent relaxation time describing the time dependent shape of the surface rebound process. Induced by the elimination of the Fennoscandian ice sheet that was centered on the Gulf of Bothnia at Last Glacial Maximum. This spectrum is shown on Fig. 3.4, on which is superimposed the predictions of this spectrum by all three-viscosity models VM1, VM2 and VM3. Notable in the McConnell spectrum is the fact that beyond a critical wavenumber in his half space model there is a shift in relaxation time to lower values, i.e. higher values of the inverse relaxation time "s". As mentioned previously this is the expected signature of the presence of a perfectly elastic surface lithosphere. The fits to this spectrum of the three spherical viscoelastic models are based upon the so-called tangent plane approximation in which the effective horizontal wavenumber of a half space model such as that employed by McConnell is simply k~n/a where a is the radius of the spherical model, Inspection of the fits in Fig. 3.4, demonstrates that VM1 misfits the (inverse) relaxation times of the McConnell spectrum such that inverse relaxation time is too short, implying that the relaxation time itself is too long. On the other hand, model VM2 fits the McConnell observations very well. Inspection of the viscosity model VM1 in Fig. 3.2, compared to VM2 shows that the viscosity of the upper mantle and transition zone in model VM1 is a factor of approximately 2 higher than in VM2. That it is in fact the viscosity in this region that the Fennoscandian relaxation spectrum is measuring may be demonstrated by invoking the analytical expression for the so-called "Fréchet derivative" for relaxation time as a function of horizontal wavenumber (spherical harmonic degree) which describes the depth dependent

sensitivity of relaxation time to deep Earth viscosity. The analytical expression for this sensitivity of the viscous response in a region in which relaxation is governed by a single mode, as is the case for the rebound in response to removal of the Fennoscandian ice sheet, is given in the Appendix to Peltier (1976) and in Eq. (44), below. This "Fréchet kernel" is plotted for several spherical harmonic degrees in Fig. 3.5a. The fact that each of these kernels peaks in the region above the 660 km endothermic phase transition demonstrates that it is precisely the viscosity through the upper mantle and transition zone that the McConnell spectrum is measuring. Also evident on Fig. 3.3, is the fact that there is no significant difference between the spectra predicted for model VM3 and that for model VM2. This is clearly because the horizontal scale of the Fennoscandian ice sheet is so small that it does not significantly probe the viscosity structure below the 660 km seismic discontinuity. To establish this quantitatively we require a more formal means of establishing the range of depth over which the relaxation spectrum is sensitive to viscosity.

3.5. A kernel for the viscosity inverse problem-The case of Fennoscandian rebound

For spherically symmetric models of the internal viscoelastic structure there exists a variational principle that was discussed at length in the appendix of Peltier (1976), with which it is possible to explicitly demonstrate that the good fit of models VM2 and VM3 to the Fennoscandian relaxation spectrum is due solely to the fact that both models employ an accurate (enough) value for the viscosity of the upper mantle and transition zone. This variational principle, which is analogous to Rayleigh's variational principle of elasticity asserts the following:

$$\int_V dv\left[2\Delta_{ij}\Delta_{ij}\delta\mu(s)\right]=0. \qquad (44)$$

Where Δ_{ij} is the Laplace transformed strain deviator defined in Eq. (45), and where μ(s) is the compliance defined in Eq. (10b). The volume V is the Earth's volume. From Eq. (44), we can immediately deduce the expression for the differential kernel relating a shift in a free decay pole of the relaxation spectrum to a (small) change in the radial viscosity structure $\delta\nu(r)$. We note from Eq. (10b) that μ(s) is a function not only of the position of the pole s but also of the viscosity ν. It is a function only of these parameters since the elastic Lamé parameter μ is assumed to be a function of depth. Thus for the variation of μ(s), δμ(s), we may write

$$\delta\mu(s)=\left(\frac{\partial\mu}{\partial\nu}\right)_s\delta\nu+\left(\frac{\partial\mu}{\delta s}\right)_\nu\delta s. \tag{45}$$

But from Eq. (10b)

$$\left(\frac{\partial\mu(s)}{\partial\nu}\right)s=\frac{\mu^2\frac{s}{\nu^2}}{\left(s+(\mu/\nu)\right)^2} \tag{46}$$

$$\left(\frac{\partial\mu(s)}{\delta s}\right)\nu=\frac{\mu(\mu/\nu)}{\left(s+(\mu/\nu)\right)^2} \tag{47}$$

Both of the derivatives, Eqs. (46) and (47), are positive definite, a fact which is important to the structure of the differential kernel which we shall obtain. Substituting Eq. (45), into Eq. (44), gives

$$\int_V d\nu\left[\Delta_{ij}\Delta_{ij}\left(\left(\frac{\partial\mu(s)}{\partial\nu}\right)_s\delta\nu+\left(\frac{\partial\mu(s)}{\partial s}\right)_\nu\delta s\right)\right]=0. \tag{48}$$

Since neither s nor δs are functions of position we may extract them both from under the integral sign and write

$$\frac{\delta s}{s}=\frac{-\int_V\delta\nu\left[\Delta_{ij}\Delta_{ij}\left(\frac{\partial\mu(s)}{\delta\nu}\right)_s\frac{\delta\nu}{s}\right]}{\int_V\delta\nu\left[\Delta_{ij}\Delta_{ij}\left(\frac{\partial\mu(s)}{\delta\nu}\right)_\nu\right]}. \tag{49}$$

This is a general expression for the shift in a free decay pole which we have been seeking. Given $\delta\nu$ we can compute δs. Nowhere in the derivation of Eq. (49), have we made any explicit restriction to the consideration of radial variations of viscosity only. Eq. (49), applies equally well to variations of viscosity which are arbitrary functions of position within the spherical body so long as these variations are small. The viscosity of the background state for which Δ_{ij} is computed must of course be radially stratified. The only previous attempt to derive a variational relation like Eq. (49), appears to be that of Parsons (1972) which dealt with the non-gravitating viscous half-space problem. The kernel which we have derived has exactly the same principal part as the one obtained by Parsons (namely $\Delta_{ij}\Delta_{ij}$), but it determines the shift in an arbitrary pole of the relaxation spectrum rather than the change in the unique relaxation time for some particular wavenumber of the deformation. In the spherical problem, as we have seen, any fixed harmonic has associated with it a discrete set of relaxation times and Eq. (49), can be employed to determine the shift of any one of these which is produced by a particular viscosity variation.

If we restrict our attention to variations of viscosity $\delta\nu(r)$ which are functions of radius only then the problem of computing the kernels in Eq. (49), is reduced considerably. We employ Backus' (1967) result to the effect that for any vector field ũ defined in $0 \le r \le \alpha$ there are unique scalar fields $\widetilde{U}$, $\widetilde{V}$, $\widetilde{W}$ such that V and W average to zero on every spherical surface concentric with the origin. These fields are defined as

$$\tilde{u} = \widetilde{U}\,\hat{r} + \nabla_1 \widetilde{V} - \hat{r} \wedge \nabla_1 \widetilde{W}, \qquad (50)$$

with $\hat{r}, \hat{\theta}$ and $\hat{\phi}$ unit vectors in the directions of increasing radius $\hat{r}$, co-latitude θ and longitude φ and

$$\nabla_1 = \hat{\theta}\frac{\partial}{\partial\theta} + cosec\theta\,\hat{\phi}\frac{\partial}{\partial\phi}. \qquad (51)$$

Solutions of the spheroidal equations are such that $\widetilde{W} \equiv 0$ and the functions $\widetilde{U}$ and $\widetilde{V}$ are just the radial and tangential displacements which we calculate as solutions to the field equations. These functions, together with $\widetilde{\phi}$ are all products of the form $\widetilde{U}_l(r)\mathrm{Y}_{lm}(\theta,\phi)$, $\widetilde{V}_l(r)\mathrm{Y}_{lm}(\theta,\phi)$ and $\widetilde{\phi}_l\mathrm{Y}_{lm}(\theta,\phi$ where $\mathrm{Y}_{lm}(\theta,\phi$ is a normalized surface spherical harmonic. Backus and Gilbert (1968) describe in detail the reduction of the kernels for the elastic gravitational free oscillations problem which are similar to that in Eq. (49). Their arguments follow through exactly in the present case and we find that with $\delta v = \delta v(r)$ Eq. (49) reduces to the following form

$$\frac{\delta s}{s} = \frac{-\int_b^a dr\, r^2 K_1 \left(\frac{\partial \mu(s)}{\partial s}\right)_s \frac{\delta v}{s}}{\int_b^a dr\, r^2 K_1 \left(\frac{\partial \mu(s)}{\partial s}\right)_v}. \qquad (52)$$

The function $\mathrm{K_l}$ is given by

$$K_1 = \frac{1}{3}\left(2\partial_r U_l - F\right)^2 + \left(l/r^2\right) l(l+1)\left(r\,\partial_r V_l - V_l - U_l\right)^2$$

$$+\left(l/r^2\right)(l-1)\,l(l+1)(l+2)\,V_l^2, \qquad (53)$$

where

$$F = (1/r)\,2U_l - l(l+1)V_l. \qquad (54)$$

In Eq. (52), the integration extends from the core-mantle boundary r = b to the Earth's surface r = a. The integral over the core vanishes because μ(s) ≡ 0 there. It should be recalled that the functions U_l and V_l appearing in Eqs. (53) and (54) are eigenfunctions of the homogeneous problem and that Eq. (52), is thus valid only in the vicinity of an eigenvalue s = $\tilde{s}_j^l$. Explicit substitution of the partial derivatives (Eqs. (46), and (47)), into Eq. (52), then gives

$$\frac{\delta \tilde{s}_j^l}{\tilde{s}_j^l} = \frac{-\int_b^a dr\, r^2 \left[K_l \frac{\mu^2 / \nu}{\left(\tilde{s}_j^l + (\mu/\nu) \right)^2} \right] \frac{\delta \nu}{\nu}}{\int_b^a dr\, r^2 \left[K_l \frac{\mu^2 / \nu}{\left(\tilde{s}_j^l + (\mu/\nu) \right)^2} \right]} \quad . \tag{55}$$

If we define x and y such that

$$\tilde{s}_j^l = 10^x, \nu = 10^y, \tag{56}$$

then

$$\delta x = \frac{\delta \tilde{s}_j^l}{\tilde{s}_j^l}, \delta y = \delta \nu / \nu \tag{57}$$

and we see clearly revealed the intrinsic logarithmic scaling of the relaxation problem. Eq. (55), thus determines the relationship between the shift in the radially dependent exponent of the viscosity model and the associated shift in the exponent of a free decay pole in the relaxation spectrum. Because of the minus sign in Eq. (55), we see that as the viscosity is perturbed to larger values then the decay time $\tilde{\tau}_j^l = l / \tilde{s}_j^l$ increases. The exponential relation is such that if δy = +1 then δx = -l, a very simple result in spite of the considerable complexity of the model.

Given these fundamental results we are now in a position to understand to what depth in the Earth the Fennoscandian relaxation spectrum of McConnell (1968), is providing information on mantle viscosity. This is determined by the averaging kernel, also referred to as a derivative, namely the integrand of the numerator in Eq. (55), normalized by the integral in the denominator. Fig. 3.5a, initially discussed above, illustrates a series of degree-dependent resolving kernels that extend to a maximum value of spherical harmonic degree of *l*=15. Because the Fennoscandian ice sheet has a horizontal scale such that power is concentrated at spherical harmonic degrees that are primarily below 15 and because the kernel for this lowest degree is centered on a depth of approximately 600 km it is clear that the Fennoscandian relaxation spectrum is providing a

measurement of the average viscosity of the upper mantle and transition zone with ever decreasing sensitivity below the 660 km seismic discontinuity. In Mitrovica and Peltier (1993), the formal methodology of nonlinear Bayesian inverse theory as formulated in Tarantola and Vallette (1981, 1982) was applied to the McConnell (1968) spectrum using the analytic kernels of Peltier (1976). Using this methodology a detailed exploration was provided of the features of the depth dependence of viscosity that could be robustly inferred on the basis of McConnell's data set. Because the issue of the contrast in viscosity between that characteristic of the mean value of the upper mantle and transition zone and that of the lower mantle has been a much disputed issue in the literature we will simply quote the main result from this paper which explicitly addresses the constraint that McConnell's spectrum places upon models based upon such a restricted parameterization of the depth dependence of viscosity. This is captured in the statement in the abstract of the paper as follows. Namely "such inversions yield models with upper and lower mantle viscosities of $3.7 \times 10^{20} - 4.5 \times 10^{20}$ Pa s and $2.2 \times 10^{21} - 1.9 \times 10^{21}$ Pa s respectively" for the shallower and deeper layers. In this quotation the phrase "upper mantle" has been employed to mean the entire mantle between the base of the lithosphere and the seismic discontinuity at 660 km depth. It is further noted that "The ranges are obtained from a suite of inversions using lithospheric thicknesses from 70 km to 145 km".

Because the McConnell spectrum describes the free decay of the deformed surface of the Fennoscandian region following surface deglaciation it provides results for the depth dependence of viscosity that are independent of the space dependent thickness of the ice sheet load that was responsible for inducing the surface deformation. Furthermore, the power of the viscosity inversion it provides is amenable to detailed analysis using the analytical formulae for the derivatives only because the horizontal scale of the ice sheet was sufficiently small that the

surface relaxation is entirely described by the M0 /L0 mode of fundamental mantle relaxation. To proceed further in our understanding of the GIA process, we will be obliged to explicitly address two inextricably connected issues of relative sea level history and glaciation history. Of course, the data on the basis of which the McConnell spectrum was inferred, namely the strandline data of Sauramo (1958), on the time scale determined by the varve chronology of Lindén, (1938), are explicitly data that derive from relative sea level variations. As rebound proceeded in this region successive "strandlines" were cut into the landscape as it rose out of the sea. Knowing the ages of this succession of strandlines determined by the varve chronology one has the complete space-time history of the rebound process that McConnell transformed to obtain his relaxation spectrum. To understand the much larger scale adjustment of the surface that occurred in response to emplacement and removal of the vast Laurentide Ice Sheet (LIS) that covered all of the Canadian landmass at Last Glacial Maximum, we will have to rely upon an ability to interpret individual relative sea level histories that have been constructed on the basis of the application of radio-carbon chronometry to determine the age of the individual Sea Level Index Points (SLIPS) that define individual relative sea level (RSL) curves at different geographical locations.

4. The Sea Level Equation and the Models of Glaciation History Required to Implement it

The derivation of what is now widely referred to as the Sea Level Equation (SLE), which is shown in its modern form in Eq. (59), below followed from results in the papers of Peltier (1974) and Peltier and Andrews (1976).. These results, obtained using the methods described in previous sections of the present paper, provided examples of the construction of viscoelastic surface mass load Green functions for radial displacement and for the perturbation to the

gravitational potential induced by the loading of the surface of the planet by a point mass. The original forms of the viscous parts of the time and space dependent Green functions for these two characterizations of the response with spherical harmonic coefficients determined by the appropriate time dependent Love numbers, are shown in Figures 4.1a, and 4.1b, for the gravitation potential perturbation and the radial displacement respectively. The viscous contributions shown in these figures are actually for Heaviside forms of these Green functions as the impulse response forms of the Love numbers have been convolved with a Heaviside step function. These Green functions therefore describe the response to a point load that is brought up to the surface at t=0 and then left on the surface for all time. In Farrell and Clark (1976) it was noted that the difference between these Green functions, gravitational potential perturbation minus radial displacement, would be a Green function for relative sea level history. This paper, together with those of Peltier (1974) and Peltier and Andrews (1976), all appeared in the same issue of what was then the Geophysical Journal of the Royal Astronomical Society and which is now the Geophysical Journal International. Considering the modern form of the SLE in Eq. (59), this initial form of the SLE, included only the first of the two triple convolution integrals that appear in the modern form of this equation. That the gravitational potential perturbation should represent the surface of the sea is a simple consequence of the fact that the surface of the sea is constrained to be a surface of constant gravitational potential in the absence of tides and currents (the geoid of classical geodesy). Because the geological system records variations of sea level only *relative to* the surface of the solid Earth, it should be clear that the first of the convolution integrals in Eq. (59), is designed to predict precisely what is observed by the geological recording system. Even at this stage in the development of a theory of ice age cycle related sea level variability there was an obvious issue with this early form of the theory. This had to do

with the issue of mass conservation. Because there is no guarantee that the volume between the globally evolving shape of the surface of the solid Earth and that of the globally evolving shape of the gravitational potential field that defines the surface of the sea will at all times be equal to that required to accommodate the water equivalent mass of the loss or gain of grounded ice mass from the continents, the result produced by the first of the convolution integrals in Eq. (59), must be adjusted at every time step in the inversion of the integral equationby the addition of the term $\frac{\Delta\phi(t)}{g}$ which must be computed as the time dependent solution of Eq. (59) is being constructed. The need for this mass balance correction was also rcogmied in Farrel and Clark (1976).

Further explanatory comments are in order concerning the initial form of the Sea Level Equation, that consists of the first of the three dimensional convolution integrals in Eq. (59), together with the time dependent but space independent mass conservation term $\frac{\Delta\phi(t)}{g}$. First, it will be clear that this is an integral equation as the surface mass load per unit area "L" which is being convolved with the relative sea level Green function, defined in Eq. (58), below also contains the relative sea level history solution "S(θ,λ,t)" that the theory is intended to predict. From a formal mathematical perspective, it is worthwhile noting that the SLE, which is a construct of first order perturbation theory, is one of a class of integral equations referred to as "Fredholm" equations (e.g. see the second volume in the book(s "Methods of Mathematical Physics by Courant and Hilbert, 1953). In this class of such integral equations the SLE is a Fredholm integral equation of the "second kind". It is of the second kind because of the presence of the mass conservation term. Given an input glaciation history of the continents and a viscoelastic relative sea level Green function the Fredholm equation may be exactly inverted (in principle) to determine the solution. Of course, neither of these inputs are known exactly on a

priori grounds implying that the SLE (Eq. (59)) actually poses an inverse problem for both of these properties of the solution, namely for the glaciation history of the continents and for the depth dependence of mantle viscosity. The strategy that has been developed to construct solutions to this complex inverse problem will be commented upon extensively in what follows. Given observations of relative sea level history and other observational constraints we will describe how these observations may be inverted to determine both glaciation history and the depth dependence of mantle viscosity. The fact that errors in these two characteristics of the solution are correlated places significant demands upon the strategy employed in the process of constructing solutions to the GIA problem.

In order to make the integral equation nature of the SLE more explicit we note that, in general, a surface mass loading history of the Earth's surface will consist of two components: namely the space-time variation of continental ice thickness represented by the function "I" in Eq. (58), and the variation of water thickness (bathymetric depth change and thus the change of sea level) "S". The surface mass load per unit area therefore has the composite form "L" where:

$$L(\theta,\lambda,t)=\rho_I I(\theta,\lambda,t)+\rho_W S(\theta,\lambda,t), \qquad (58)$$

in which $\rho_I$and $\rho_W$are the densities of ice and water respectively (which differ by approximately 10%) and in which "S" is the space-time variation of the bathymetry of the oceans, thus relative sea level. The independent variables θ,λ and t in Eq. (58), represent co-latitude, longitude and time respectively. The first term in the complete SLE in Eq. (59), is also multiplied by the function "C" which is the so-called "ocean function" of Munk and McDonald (1960),

$$S(\theta,\lambda,t)=C(\theta,\lambda,t)\left[\int_{-\infty}^{t} dt' \iint_{\Omega} d\Omega' \left\{L(\theta',\lambda',t')G^{L}{}_{\phi}(\varphi,t-t')+\Psi^{R}(\theta',\lambda',t')G^{T}{}_{\phi}(\varphi,t-t')\right\}+\frac{\Delta\Phi(t)}{g}\right] \qquad (59)$$

which is unity over the oceans and zero over the continents. The Green function $G^{L}_{\phi}(\varphi,t)$ is that which, when convolved with surface mass loading translates these loads into the impact upon the

gravitational potential field measured with respect to the deforming surface of the solid Earth, an equipotential surface of which defines the surface of the equilibrium ocean, the geoid of classical geodesy. This relative sea level Green function follows from Eq. (19), together with recognition of the normal mode expansions for the surface load Love numbers and the fact that each of the individual Green functions involve a potentially infinite sum over spherical harmonic degree in Eqs. (15a,b). The angle φ in this RSL Green function is the angular separation between the source point $(\theta', \lambda'$ and the field point $(\theta, \lambda$. This simple dependence is a consequence of the assumption that the Earth model is spherically symmetric in its viscoelastic properties. The function $\frac{\Delta\Phi(t)}{g}$ is the time dependent but space independent correction that must be included in Eq. (59), in order to ensure that the dynamical system conserves mass in the sense that the mass lost by land ice melting translates precisely into a corresponding and equal mass gain by the oceans and vice-versa. This mass conservation correction must be determined in the course of the construction of solutions to the SLE. The solution of Eq. (59), answers the question as to where in the ocean basins the water that is produced by land ice-melting must be distributed, in order that the surface of the equilibrium ocean (sea level) remains an equipotential surface. The same holds in reverse during periods the growth of ice cover on the continents.

4.1. Comments upon the initial analyses of the SLE

It is important to understand that in the initial calculations of sea level history that were performed in Clark, Farrell and Peltier (1978), and Peltier, Farrell and Clark (1978) based only upon the first of the convolution integrals in Eq. (59), a number of strong assumptions were made. Specifically, concerning (i) the fact that the Green functions for both radial displacement and the gravitational potential perturbation did not include the influence of a surface lithosphere

in which the viscosity is effectively infinite, an influence that we have shown to be critical in the previous analysis of the Fennoscandian relaxation spectrum, and (ii) the ocean function "C" was assumed to be constant, meaning that coastlines were assumed to be fixed and equal to their modern positions. The latter assumption is also clearly incorrect as when water is added to the ocean basins as a consequence of the disintegration of grounded ice on the continents, the coastline will be forced to migrate inland in regions where the topographic gradient at the coast is sufficiently shallow. Finally, (iii) it was also assumed in these early analyses that the continental ice load at the maximum of glaciation was assumed to be in isostatic equilibrium with the deformation of the Earth's surface that this load had induced. At the time of these early analyses this approximation was based upon the untested assumption that the glaciation phase of a typical 100,000 year ice age cycle was sufficiently long that this would be a reasonable expectation. The accuracy of the latter assumption will of course depend upon the viscosity of the mantle, such that the higher this viscosity the more questionable this assumption becomes. As we will see in what follows all of these assumptions in the initial calculations of Clark, Farrell and Peltier (1978) and Peltier, Farrell and Clark (1978), led to errors in the computation of postglacial relative sea level histories, but did not undercut the value of these results as further development of the theoretical structure continued. It is also worth commenting that these early analyses also made use of an assumed (first guess) glaciation history of the continents that had been tabulated in Peltier and Andrews (1976) and which has often been referred to in the literature as ICE 1.

As important as were these assumptions made in the initial RSL history calculations was the methodology that was employed to solve the SLE. This method, as described in detail in Peltier et al. (1978), was a finite element method in which the triple convolution integral in Eq. (59),

was evaluated using a “look-up” table based upon the computation of a matrix of interaction coefficients between different regions of the surface that were “tiled” on a priori grounds with a large number of spherical caps between each of which the interactions were computed off line but invoked as the solution was time-stepped forward from the assumed initial conditions. These interaction coefficients were produced by integrating the Green functions over the range of spherical caps of different radii in terms of which the surface oceans and ice sheets were discretized. This method was eventually replaced by a spherical harmonics-based methodology, the initial version of which was described in Mitrovica and Peltier (1991), based upon the same “semi-spectral” methodology employed in spectral models of the atmospheric general circulation In order to describe the nature of the solutions for post glacial relative sea level history delivered by this early version of the SLE we will have to assume an appropriate version of the glaciation and deglaciation history of the continents, a history we know to have been forced by the action of gravitational n-body effects in the solar system.It is appropriate to note that considerable work has been undertaken internationally to produce “benchmarks” foe results that should be obtained as solution to the sea level equation as a means of ensuring that there is agreement within the international community as to the results that should be obtained for specific choices of the input viscosity structure and glaciation history. Although somewhat limited in their generality, exampls of such bwnchmark analyses are those of Spada et al , 2011) and Martinec et al (, 2018).

4.2. Rotational feedback in the Sea level Equation

The second of the three dimensional convolution integrals in the SLE (Eq. (59)), describes the feedback onto sea level associated with the rotational response of the Earth to the loading and unloading of the continents by glacial ice. The first step in the recognition that this feedback

could be important was achieved in the papers by Peltier (1983) and Wu and Peltier (1984), who demonstrated that there existed two previously unexplained rotational observables that they demonstrated to be unambiguously related to the GIA process, respectively the true polar wander of the instantaneous location of the north pole of rotation relative to the surface geography and the so-called nontidal acceleration of the rate of planetary rotation and thus the length of the day (l.o.d). Fig. 4.2 shows the original International Latitude Service (ILS) data for the period ending at the beginning of the satellite era in 1976. This shows the photo zenith tube derived time series for the x and y coordinates of the position of the north pole of rotation relative to the Conventional International Origin (CIO). These time series are clearly dominated by the 7-year quasi-periodic beat between the 14-month Chandler wobble and the 12-month annual wobble associated with the exchange of mass between the hemispheres. Clearly this dominant quasi-periodic motion is superimposed upon a steady drift of the pole at a rate near 1 degree per million years along the approximately 76 degree west meridian of longitude, towards what was the centroid of the position of Laurentide ice sheet that covered all of the Canadian land mass at the LGM.

The non tidal acceleration of planetary rotation, on the other hand, the second of the rotational observables shown by Peltier (1982) and Wu and Peltier (1984), to be explicable as a consequence of the GIA process is especially clearly observable in the timing of total eclipses of the Sun and Moon over the past 2000 years as these were recorded by naked eye astronomers over this period of time. These data, illustrated in Fig. 4.3, have been carefully compiled in Stephenson and Morrison (1995). Because corner reflectors were positioned on the surface of the Moon by Apollo programme astronauts, this has enabled continuous tracking of the distance between the Earth and the Moon by Lunar Laser Ranging and thus a direct measurement of the

friction due to the tides raised in the oceans by the gravitational attraction of the Moon. Conservation of angular momentum requires that the decrease in the Earth's rate of axial rotation and the related spin angular momentum, be compensated by an increase in the orbital angular momentum of the Moon and thus an increase in the Earth-Moon distance. If this measurement of tidal friction is assumed constant then, as shown on Fig. 4.3, one makes an error in the predicted timings of total eclipses that increases the further back in time the inferred timing of these eclipses. This misfit implies the action of a nontidal acceleration of the rate of planetary rotation which acts in such a way as to oppose the impact of tidal friction. That this effect is also associated with the GIA process was corroborated using a modern satellite measurement of the changing length of day using orbital data for the Laser Geodynamics Satellite (LAGEOS) in Peltier (1983, 1985).

Fig. 4.4, illustrates the importance of these rotational observables insofar as the inference of mantle viscosity is concerned for a series of models in which the viscosity is parameterized by a two-layer structure beneath the surface lithosphere just as in the previous interpretation of the Fennoscandian relaxation spectrum. These results have employed a simplified but, nevertheless, accurate representation of the surface mass loading history based upon the assumption of multiple 100,000 year cycles of glaciation and deglaciation. With the upper mantle viscosity held fixed the results are shown as a function of the viscosity of the lower mantle. Inspection of these comparisons demonstrates that both rotational observables are fit by the same upper mantle/lower mantle viscosity contrast and that this contrast is low just as was found to be the case based upon formal inversion of the Fennoscandian relaxation spectrum. Although the nontidal acceleration observable allows a high contrast viscosity model, the same is apparently not the case for true polar wander constraint.

More recent analyses of modern Earth orientation data in Roy and Peltier (2011), not only reconfirmed the importance of these inferences of the GIA connection to the rotational observables, but also demonstrated, as shown in Fig. 4.5, that beginning in the early 1990's a striking departure became evident between the connection of the rotational observables to the glacial isostatic adjustment process in continuing response to the last ice-age cycle. It was suggested and is now confirmed that the departure of both of the rotational observables from GIA-based expectations due to the last ice-age, is a consequence of the ongoing global warming process, due to the increasing concentration of carbon dioxide and other greenhouse gases in the atmosphere. Because the Great Polar Ice Sheets on Greenland and Antarctica are currently losing significant mass to the oceans (e.g. see Shepherd et al., 2018, 2020), this mass redistribution is having a marked effect upon the planet's moment of inertia tensor and thus on its rotational state. This constitutes the onset of a modern cycle of glacial isostatic adjustment, the impacts of which are to be described by the Sea Level Equation – based theory embodied in Eq. (59), above.

As previously noted, the influence of rotational feedback upon sea level history is embodied in the second of the three dimensional convolution integrals in Eq. (59). The function $\Psi^R(\theta,\lambda,t)$ is the variation of the centrifugal potential due to the changing rotational state of the Earth that is caused by the surface loading and unloading process associated with the ice-age cycle. Following Dahlen (1976), this may be expressed, to first order in perturbation theory, in terms of the following spherical harmonic expansion, as:

$$\Psi^R(\theta,\lambda,t) = \Psi_{00} Y_{00}(\theta,\lambda,t) + \sum_{m=-1}^{+1} \Psi_{2m} Y_{2m}(\theta,\lambda,t) \quad , \tag{60}$$

with,

$$\Psi_{00} = \frac{2}{3}\omega_3(t)\Omega_0 a^2 \quad , \tag{61a}$$

$$\Psi_{20} = -\frac{1}{3}\omega_3(t)\Omega_0 a^2\sqrt{4/5} \quad , \tag{61b}$$

$$\Psi_{2,-1} = (\omega_1 - i\omega_2)(\Omega_0 a^2/2)\sqrt{2/15} \quad , \tag{61c}$$

$$\Psi_{2,+1} = -(\omega_1 + i\omega_2)(\Omega_0 a^2/2)\sqrt{2/15} \quad . \tag{61d}$$

The ω_i in the above equations are to be obtained as solutions to the equation for the conservation of angular momentum as follows:

$$\frac{d}{dt}\left(J_{ij}\omega_i\right) + \in_{ijk} \omega_j J_{kl}\omega_l = \tau_j \quad . \tag{62}$$

In which the J_{ij} are the elements of the moment of inertia tensor and $\in_{ijk}$ is the Levi-Civita (alternating) tensor. Restricting attention to small departures from a modern state of steady rotation with angular velocity Ω_o, we may construct a solution to Eq. (62), accurate to first order in perturbation theory, by expanding:

$$\omega_i = \Omega_o\,(\delta_{i3} + m_i)\,;\, m_i = \omega_i/\Omega_o \quad , \tag{63a}$$

$$J_{11} = A + I_{11} \quad , \tag{63b}$$

$$J_{22} = B + I_{22} \quad , \tag{63c}$$

$$J_{33} = C + I_{33} \quad , \tag{63d}$$

$$J_{ij} = I_{ij}, i \neq j. \tag{63e}$$

Substitution of these expansions into Eq. (62), keeping only terms of first order, leads to the standard set of governing equations for polar wander and the length of day, respectively (see, e.g. Munk and McDonald, 1960), as:

$$\left.\begin{aligned} \frac{dm_1}{dt} + \frac{(C-B)}{A}\Omega_o\, m_2 &= \Psi_1 \\ \frac{dm_2}{dt} + \frac{(C-A)}{B}\Omega_o\, m_1 &= \Psi_2 \end{aligned}\right\} \text{ polar wander} \tag{64a,b}$$

$$\left.\frac{dm_3}{dt} = \Psi_3\right\} \text{ length of day}, \tag{64c}$$

in which the "excitation functions" are defined as:

$$\Psi_1 = \left(\frac{\Omega_o}{A}\right) I_{23} - \frac{(dI_{13}/dt)}{A} + \tau_1, \tag{65a}$$

$$\Psi_2 = -\left(\frac{\Omega_o}{B}\right) I_{13} - \frac{(dI_{23}/dt)}{B} + \tau_2, \tag{65b}$$

$$\Psi_3 = -\left(\frac{I_{33}}{C}\right) + \tau_3. \tag{65c}$$

In solving this set of equations to determine the components of the angular velocity vector for insertion into Eq. (61), and thus into the second of the three dimensional convolution integrals in the SLE (Eq. (59)), we take the external applied torques τ_i to be identically zero and compute the excitation functions on the basis of the appropriately adjusted perturbations to the elements of the moment of inertia tensor that would obtain if the Earth were perfectly rigid (see e.g., Peltier,

2015 for the details). It should be clear, however, that since the Cartesian components of the perturbations to the angular velocity vector are required to compute the strength of the rotational feedback on sea level history, the complete solution of the SLE must be computed iteratively. First, we solve the SLE by neglecting rotational feedback entirely. This delivers a solution for the complete time dependent loading history consisting of both the input ice loading component and the output ocean loading component. Given this complete history with its continental ice sheet loading history input component and its ocean water output component we can proceed to solve Eq. (62), to determine a first approximation for the Cartesian components of the angular velocity vector. We then employ this first approximation to construct the second of the convolution integrals that appear in the SLE. The solution of this complete SLE leads to a second approximation to the water loading component of the complete loading history. This is then employed to recompute the solution to Eq. (62), to obtain an improved approximation to the rotational response needed to construct an improved approximation to the SLE. This iterative procedure has been shown to converge rapidly in less, typically, than 5 iterations. Given this methodology for the computation of the rotational forcing due to the time varying centrifugal potential, the remaining terms in the Sea Level Equation consist of the surface mass loading and tidal potential loading Green functions, the first of which we described qualitatively above, which have been shown in Peltier (1976) and Peltier et al. (2012), to have the mathematical representations:

$$G_\phi^L(\phi,t) = \frac{a}{m_e}\sum_{l=0}^{\infty}(1+k_l^L(t)-h_l^L(t))P_l(\cos\theta) \tag{66a}$$

$${}_R G_\phi^T(\phi,t) = \frac{1}{g}\sum_{l=0}^{\infty}\frac{(2l+1)}{4\pi}(1+k_l^T(t)-h_l^T(t))P_l(\cos\theta) \tag{66b}$$

in which k_l^T, h_l^T are the visco-elastic tidal potential loading Love numbers and k_l^L, h_l^L are the corresponding surface mass loading Love numbers of Peltier (1974). The renormalization factor $(2l+1)/4\pi$ in (66b), is needed to ensure that the centrifugal potential introduces only local influence as discussed in detail in Peltier et al. (2012). Peltier (1976,1985), has shown that the time domain viscoelastic Love numbers that appear in (66a,b), may be expressed, in the case of impulsive point mass or centrifugal potential loading at the surface of the planet, in the form of the following normal mode expansions:

$$k_l^T(t) = k_l^{T,E}\delta(t) + \sum_{j=1}^{M} q'^{l}_{j} e^{-s_j^l t} \quad , \tag{67a}$$

$$h_l^T(t) = h_l^{T.E}\delta(t) + \sum_{j=1}^{M} r'^{l}_{j} e^{-s_j^l t} \quad , \tag{67b}$$

$$k_l^L(t) = k_l^{L,E}\delta(t) + \sum_{j=1}^{M} q_j^L e^{-s_j t} \quad , \tag{67c}$$

$$h_l^L(t) = h_l^{L,E}\delta(t) + \sum_{j=1}^{M} r_j^L e^{-s_j^l t} \quad . \tag{67d}$$

In these normal mode expansions the $k_l^{T,E}, h_l^{T,E}, k_l^{L.E}$ and $h_l^{L,E}$ are the elastic surface mass load and tidal potential loading Love numbers of Farrell (1972), the s_j^l are the inverse relaxation times of a discrete set of normal modes of visco-elastic gravitational relaxation determined as the zeros of an appropriate secular function (Peltier, 1985) or by collocation (Peltier, 1974, 1976), and the amplitudes $q'^{l}_{j}, r'^{l}_{j}, q_j^l, r_j^l$ are the residues at these poles. In so far as understanding of

the polar wander component of the rotational response of the planet to the GIA process is concerned the parameter k_2^T plays an especially crucial role, as discussed in detail in Peltier (2015) but which will not be repeated herein.

4.3. Continental surface mass loading histories and an initial implementation of the complete SLE

In order to make adequately close contact with the observational constraints the SLE (Eq. (59)), must be implemented by employing a fully realistic model of the surface loading and unloading of the continents by ice. Although it has been suggested that variations of surface nass loading associated with sediment might also play a role during a typical ice age cycle (eg Whitehouse, 2018), this effect is expected to be negligible, except perhaps in highly localized regions. The overwhelmingly dominant ice component of the GIA model has been under continuous revision since the initial ICE-1 version of this history was first described in Peltier and Andrews (1976). For the present purposes of illustrating the results obtained on the basis of complete solutions of the SLE, we will primarily employ the recent ICE-6G_C_D (VM5a) model of Peltier et al. (2015, 2018). In these versions of the Toronto model of the GIA process explicit descriptions of grounded continental ice cover are provided for North America, Northwestern Eurasia including the Barents Sea, Greenland and Iceland, Antarctica and Patagonia, all regions for which detailed information is available concerning the extent of ice cover at LGM and its diminishing area of ice cover as a function of time during the deglaciation process. For both North America and Northwestern Eurasia this information includes “deglaciation isochrones” describing the receding position of ice sheet margins as a function of time which enables the construction of spatially accurate descriptions of the main concentrations of glacial ice as deglaciation proceeds. In other regions such as Antarctica and Greenland the available

constraints upon the deglaciation process must rely more directly upon the nature of the fits provided by the SLE to local histories of relative sea level change. Even in regions where there exist strong constraints on the location of grounded ice, it is only through fits to local RSL histories that one may determine what the thickness of ice must have been as in these regions we may employ the fit of the SLE predictions to the data as a means of "weighing" the local ice cover, and thereby constraining its thickness.

In Fig. 4.6, we illustrate the primary concentrations of northern hemisphere ice according to the ICE-5G (VM2) model of the GIA process together with predicted fits of the SLE predictions to specific RSL observation at sites that were one ice covered by grounded glacial ice but which are now located on modern coastlines. These include sites that were located near the centers of postglacial rebound of both the Fennoscandian Ice Sheet and the Laurentide Ice Sheet of North America. Also shown is the model fit to the extremely important Barbados coral record of relative sea level history of Fairbanks (1979), but in the extended version of Peltier and Fairbanks (2006). The latter record continues to occupy a uniquely important position in the literature concerning the glacial isostatic adjustment process because it has been shown to provide an accurate local measurement of the globally averaged (eustatic) measurement of the total amount of grounded continental ice that was eliminated from all geographical regions during the transition from full glacial to interglacial conditions. Fig. 4.7 provides a comparison between the contribution to ice equivalent eustatic sea level from all regions between the ICE-5G (VM2) model of Peltier (2004) and the ICE-6G_C(VM5a) model of Peltier et al. (2015). Inspection of this figure will show that, in terms of the net eustatic sea level rise, the variations between these models were relatively modest.

Focusing next upon the differences between the largest scale features of solutions of the SLE that do or do not include the influence of rotational feedback, we show in Fig. 4.8 appropriate comparisons for the earlier ICE-4G (VM2) model. Part (a) of this figure illustrates the solution of the SLE that includes the influence of rotational feedback in the model prediction of the present day rate of relative sea level rise. For comparison purposes part (b) of the figure shows the prediction back of the same field for the same model but excluding the influence of rotational feedback. Part (c) of the figure shows the difference (a)-(b). Inspection of either (a) or (b) demonstrates that in the northern hemisphere regions that were initially covered by the grounded Laurentide and Fennoscandian ice sheets the present day rate of relative sea level change is negative as relative sea level in these regions is dominated by the postglacial rebound of the crust of the solid Earth causing relative sea level to fall as the land is continuously rising out of the sea. In the regions peripheral to those that were once ice covered, the opposite is the case as these regions RSL record is dominated by the collapse of the peripheral bulge in which the local radius of the solid Earth was increased by the viscous “flow” of mantle material out from under the ice covered region that is involved in the initial glaciation phase of the isostatic adjustment process. During and following deglaciation this bulge begins to collapse as material begins to flow back beneath the once ice covered region. The difference between plates (a) and (b) shown in (c), represents the influence of rotational feedback and this is clearly dominated by a spherical harmonic of degree 2 and order 1. Inspection of Eq. (61), demonstrates that the dominance of this spherical harmonic constituent is due to the dominance of the polar wander component of the rotational response to the glacial isostatic adjustment process.

Inspection of part (d) of this figure, depicts what is in many ways a much more fundamental characterization of the present day rate of sea level rise. This is the present day rate of change of

geoid height, the geoid being defined in terms of the gravitational potential that overlaps the surface of the sea in the absence of tides and currents. Its present daytime rate of change is uniquely accessible through the SLE analyses we are discussing. This may be computed simply by adding to the present day rate of sea level rise measured with respect to the deforming surface of the solid Earth the rate of radial displacement of the solid Earth measured with respect to the center of mass of the planet. Inspection of part (d) of the figure demonstrates that this field is strongly dominated by the same degree 2 and order 1 spherical harmonic constituent that we previously identified in part c of Fig. 4.8, as associated with domination of the influence of rotational feedback by the polar wander component of the rotational response to the GIA process.

In order to compute part (d) of Fig. 4.8, we have had to compute the present day rate of radial displacement due to the GIA process. Although this result is not a direct byproduct of the solution of the SLE, the results of the solution of the SLE provide what is needed to compute the present day rate of radial displacement as it provides a complete time dependent result for the surface mass loading of the oceans which, when combined with the initially assumed known history of the surface mass loading of the continents provides a complete history of the surface mass loading of the entire surface of the Earth. When convolved with the radial displacement Green function this delivers the result required. By invoking the convolution theorem this result may be written as follows, where for the sake of completeness we are showing the result for tangential displacement as well as for radial displacement.

Radial Displacement:

$$U(\theta,\lambda,t)=\sum_{l=0}^{\infty}\sum_{m=l}^{+l}\left[\frac{4\pi a^3}{(2l+1)m_e}\left(L_{lm}r_l^{E,L}+\sum_{k=1}^{k(l)}r_k^l\beta_{lm}^k\right)\right]Y_{lm} \quad (68)$$

$$+\sum_{l=0}^{\infty}\sum_{m=l}^{+l}\left[\frac{1}{g}\left(T_{lm}h_l^{E,T}+\sum_{k=1}^{k(l)}q_{lm}^{lk}\beta'^{k}_{lm}\right)\right]Y_{lm}.$$

Tangential Displacement:

$$V(\theta\lambda,t)=\sum_{l=0}^{\infty}\sum_{m=l}^{+l}\left[\frac{4\pi a^3}{(2l+1)m_e}\left(L_{lm}l_l^{E,L}+\sum_{k=1}^{k(l)}r_k^l\beta_{lm}^k\right)\right]\overline{\nabla}Y_{lm}$$

$$+\sum_{l=0}^{\infty}\sum_{m=l}^{+l}\left[\frac{1}{g}\left(T_{lm}l_l^{E,T}+\sum_{k=1}^{k(l)}t'^{l}_{k}\beta'^{k}_{lm}\right)\right]\overline{\nabla}Y_{lm}$$

In which $\beta_{lm}^k(+)=\int_{-\infty}^{t}L_{lm}(t')e^{-s_k^l(t-t')}dt'\,\beta_{lm}^k(-)=\int_{-\infty}^{t}T_{lm}(t)e^{-s_k^l(t-t')}dt'$.

In these expressions the L_{lm} and T_{lm} are the time dependent spherical harmonic coefficients delivered by the solution of the SLE for the surface mass loading and for tidal potential loading respectively and the r(l,k) and q(l,m,k) are the residues at the poles in the surface mass load and tidal potential loading Love numbers. As we will see, these radial and tangential three-dimensional displacement fields are both directly observable by the space geodetic technique that relies upon the Global Positioning System (GPS) constellation of Earth orbiting satellites. Prior to shifting our focus to such local measurements and their interpretation it will be important to make one further comment concerning the large-scale features of the solutions for the response of the planet to the GIA process. Namely, that in order for the time dependence of geoid height shown in Fig. 4.8d to be physically relevant, it requires a global model of the glaciation-deglaciation process. To reinforce this fact, we show Fig. 4.9; a three-part figure.

Part a of Fig. 4.9 (top) shows the prediction of the vertical motion of the crust for the North American continent for model ICE-6G_C (VM5a) of Peltier et al. (2015). This model is one of the most recent from the Toronto group, one that has been validated in detail by both GPS observations and Gravity Recovery and Climate Experiment (GRACE), time dependent gravity observations (see the recent paper by Argus et al., 2021 for detailed discussion). Clearly evident in this vertical motion prediction part of the figure are the three primary extrema in the present day post glacial rebound process. These were the regions of thickest ice in the Laurentide ice sheet at LGM. Part b of the figure, center, shows the present day prediction of the rate of relative sea level change to be compared with the rate of postglacial rebound of the crust. Whereas vertical motion of the crust is now occurring over the entire region that was once ice covered, relative sea level is currently falling over the same region, simply because relative sea level is strongly dominated by the vertical motion of the crust. In the figure, these two fields are labeled dRad and dRSL respectively. As discussed in connection with Fig. 4.8, the sum of these two fields is the time dependence of geoid height, labeled dGeoid on Fig. 4.9. Notable is the fact that although the two fields contributing to the sum are almost exactly opposite in sign they do not exactly cancel when added, leading to the prediction that the geoid height, sea level as measured with respect to the center of mass of the planet, is inflating over the once ice covered region. This characteristic of present day geoid height time dependence is extremely important. As discussed in Peltier et al. (2018), it is only given an accurate model of geoid height time dependence that one is able to make an accurate prediction of the vertical motion of the crust given only geoid height time dependence. In the following Section 5 of this paper we will begin to discuss such local features of the GIA process and the conclusions concerning deep Earth physics and surface

climate processes that can be drawn by comparing model predictions to the corresponding observations.

5. Model Predictions and Observations of the GIA Process and Inferences from them

Our purpose in this section is to begin discussing the different data sets that can be brought to bear to constrain the parameters of a global model of the GIA process. Each of these individual data sets is typically most used in constraining particular properties of the model whereas there is at least one that is able to constrain the collective contributions of all elements. We will begin in the next subsection with a discussion of this unique data set.

5.1. The Barbados coral record of postglacial RSL history

The primary data that began to become available as a means of constraining models of the GIA process consisted of the histories of the evolution of relative sea level for which age control was provided by ^{14}C dating. Initially ^{14}C age was determined by conventional counting of sample beta decays, but this method was eventually replaced by accelerator mass spectrometry (e.g. Litherland, 1980). As previously discussed this method of determining the age of individual Sea Level Index Points (SLIPS), (e.g. see Shennan and Horton, 2002 for a discussion of the modern methodology) is now widely employed for the purpose of compiling and assigning an indicative meaning to individual SLIPS. Because the carbon clock does not measure time in calendar years, since the ^{14}C production rate varies with time, this timescale requires calibration and the most recent version of this calibration (CALIB) is that of Stuiver and Reimer (1993). Such calibrated SLIPS are clustered into tight geographical groups so as to define individual sea level history curves that may define local relative sea level history if the set of individual samples span a sufficiently long interval of time. The global database of such histories, most of which are confined to the Holocene interval of time (most recent 10,000 calendar years), has evolved

considerably from the initial global compilations produced by the Toronto group (e.g. see Fig. 16 of Peltier, 2007). This global compilation is gradually being replaced by combining the results of a series of regional recompilations in which the methodology of Shennan and Horton (2002) has been rigorously applied. The current state of this new global recompilation is discussed in Khan et al. (2019).

Fig. 5.1 provides a comparison between RSL histories contained in the original Toronto global compilation and RSL predictions for the ICE-5G (VM2) model of the GIA process. Comparisons are shown for six globally distributed sites for which high quality observational constraints are available. The locations of these sites are shown against a background of the predicted present day rate of relative sea level rise (fall). Clearly apparent once more is the degree 2 and order 1 spherical harmonic overprint in the background field caused by the impact of rotational feedback on sea level history due to the dominance of the polar wander component of the rotational response to the GIA process. Notable also is the fact that there exist dramatically different RSL signatures of the sea level response to the glacial loading and unloading of the continents by glacial ice. Where the surface was initially covered by grounded ice, sea level is currently falling, whereas in the peripheral region, it is rising due to the collapse of the glacial forebulge. Further afield the response is highly variable due to the complexity of the coastline and to the proximity to one of the four extrema of the degree two and order one pattern associated with the influence of rotational feedback.

Among all of the sites from which such RSL histories are available there is one that has proven to be especially important, namely that from the island of Barbados in the Caribbean Sea which is located just off the North coast of Venezuela, but well south of the region of strong forebulge collapse. The island is comprised entirely of corals and since it has been continuously

uplifted out of the sea tectonically by the interaction between the eastward moving Caribbean plate and the subduction zone that forms its eastern margin, the coral-based record is one that reaches back in time for hundreds of thousands of years. This covers several of the 100,000 year ice age cycles that were discussed in the Introductory section of this paper, a record previously discussed by Broecker and van Donk (1970). The individual coral samples that make up the original record of Fairbanks (1989) and the extension of it in Peltier and Fairbanks (2006) are shown in plate c of Fig. 5.2. Also shown on the inset is the inference based upon the succession of uplifted high stands of the sea based upon data from the three locations shown on part a of the rate of uplift of the island of 0.34 mm/yr. This implies that the island has risen out of the sea by ~7 m in the past 21,000 years. This means that to obtain the correct history of RSL at Barbados, the raw depths of the individual samples must be adjusted to greater depth by the product of sample age and this rate of uplift of the island. At Barbados it is also critical to understand that the ages of the individual coral samples that comprise the record are determined by the application of U/Th dating, not radiocarbon dating. This is important because U/Th age is essentially sidereal age. In fact, by separately dating the same samples using both methods, the radiocarbon clock has been very effectively calibrated!

After application of this tectonic correction, the adjusted data at Barbados are replotted in Fig. 5.3, where they are compared to several distinct predicted and inferred measures of sea level history including the prediction of the ICE-6G_C (VM5a) model, which is shown as the black line. The first comparison of interest is that shown as the red step-discontinuous sea level history. This history clearly provides a very accurate approximation to the black line. The red discontinuous curve is what has been referred to in the literature by Peltier (2002) as the “ice-equivalent” sea level history. This is derived by computing, at the nominal 500 year sampling

interval of the glaciation history of grounded continental ice in the model, the individual increments of globally averaged sea level on the basis of the assumption that the surface area of the oceans remained fixed to the modern area. Because the average rise of sea level is not adjusted for the variations of ocean area that accompany the growth and decay of continental ice sheets, this record is dependent only upon the volume of grounded ice and its variation through time. This implies that the Barbados record is providing, from a single site on Earth's surface, what appears to be an accurate estimate of "ice equivalent" eustatic sea level history.

The third curve on Fig. 5.3, and shown on the inset, is the eustatic sea level history constructed by Waelbroeck et al. (2002) based upon temperature corrected benthic $\delta^{18}O$ as discussed in the Introductory section of this paper and shown for the complete most recent ice-age cycle of the Late Quaternary period. Also shown on the inset is the complete ice age cycle of the ICE-6G_C (VM5a) model as the black curve. In the range of time prior to 30 ka this model was tuned to the SPECMAP deep sea oxygen isotope stack record (shown in red) of Imbrie et al. (1979) which, as shown on the inset, is extremely close to that of Waelbroeck et al. (2002). Notable is the fact that this oxygen isotope-based eustatic sea level source closely matches the RSL history at Barbados predicted by the ICE-6G_C (VM5a) model. Especially important is that the tectonically corrected coral-based SLIPS of age near 30,000 years based upon Acropora Palmata samples, a species that, in the modern ecology, lives within 5 m of local sea level, are essentially coincident in depth with the $\delta^{18}O$-based eustatic curve in the youngest segment of Marine Isotope Stage 3 and with the predicted RSL history determined by solving the SLE given the ICE-6G_C loading history and the VM5a model of the depth dependence of viscoelasticity of the lithosphere-mantle system.

In recent years, there have been several attempts to undermine the implications of these model fits to the Barbados coral-based record of RSL history. Different authors have argued either that the ICE-6G_C loading history of the continents contains too little grounded ice at LGM (e.g. Austerman et al., 2013; Simms et al., 2019), i.e., that there is "missing ice" in the model, or, on the contrary, that the model contained far too much ice at LGM (e.g. Gowan et al., 2021). It will be useful here to discuss the arguments that the authors of these papers have presented in favor of these conflicting views.

In the paper by Austerman et al. (2013), the authors described the application of a model of the GIA process that included the influence of lateral heterogeneity of viscosity in which this lateral heterogeneity was estimated on the basis of a three dimensional seismic tomography-based model of S-wave velocity. Based upon the assumption that this lateral heterogeneity was due entirely to the lateral heterogeneity of temperature and using the assumption of a particular S-wave to temperature conversion factor, and the further assumption of a temperature to viscosity relationship, the authors made a prediction of sea level history at Barbados. Their prediction was that RSL at LGM was 7 m shallower than that required by the Barbados coral record corrected for the tectonic uplift of the island.

It was noted in Peltier et al. (2015), that this result precisely canceled the 7m increase in sample depth at LGM due to the influence of tectonic uplift! This result may not have been a coincidence and in any event no further argument in its favor has ever been presented! Initially believing in the validity of their argument the authors concluded that there was "missing ice" in the Toronto models. This would require that the amount of missing ice would be equivalent to the size of the Greenland Ice Sheet. The authors had no suggestion as to where this missing ice might have been located. A significant further weakness of this result is that the predictions of

the model with lateral heterogeneity of viscosity seems not to have been tested for its ability to reconcile data from other locations and so the model of the influence of lateral heterogeneity of viscosity on the GIA process is highly suspect. As will be discussed in Part II of this paper to follow, Li et al. (2020) have recently employed their own GIA model incorporating the influence of lateral heterogeneity of viscosity and found that such models may dramatically misfit RSL data from the Hudson Bay region of the Laurentian platform. An acceptable model of the global GIA process must reconcile the global database of constraints.

A second recent paper that tended to reinforce this notion that there was "missing ice" in the existing models of LGM to modern glaciation history was the paper by Simms et al. (2020). These authors, on the basis of an attempted objective accounting of the total LGM mass of grounded continental ice in each of the ice sheets known to have existed at this time, concluded that the missing contributions to global sea level rise amounted to 18.1 +-9.6 m. They estimated that 2.4 +- 0.3 m could have been provided by the thermal expansion of ocean volume due to warming across the glacial-interglacial transition and an additional perhaps 1.4 m could have been due to the release of groundwater. This suggests that the authors believe that the missing grounded continental ice must have amounted to approximately 13.8 m of global sea level rise equivalent, in other words two Greenland equivalents of grounded ice! The authors accept as required to close the LGM ice volume budget a total of 132 m. Unfortunately, their analysis appears to have been based upon the assumption that LGM occurred at 21 ka whereas, accounting to the Barbados sea level record, LGM actually occurred 5000 years earlier at 26 ka. In the Toronto ICE-6G_C (VM5a) model the ice equivalent eustatic sea level depression at actual LGM is approximately 130.8 m. (see Fig. 4.7). As shown previously, this model fits the Barbados constraint on total ice equivalent eustatic sea level with high accuracy. The conclusion

that follows from close inspection of both of these papers that have advocated for the validity of the idea that there is "missing ice" is that they are incorrect insofar as the Toronto models are concerned.

The opposite argument has also been recently made by Gowan et al. (2021) to the effect that there is not only no "missing ice" in the Toronto models, but that they contain far too much. It will also be worthwhile to consider their argument in detail as it is primarily based upon the suggestion that deep sea sedimentary core records of oxygen isotopic variability do not provide an accurate proxy for the time dependent volume of grounded ice on the continents. In what follows we will demonstrate that this notion is at best "misguided". The Gowan et al. paper is actually motivated by the recognition that the GIA model of Lambeck et al. (e.g. 2017), was incapable of reconciling GPS measurements of the present day vertical motion of the crust over the North American continent because it is based upon a model of the depth dependence of mantle viscosity in which a large increase in the value of this parameter is assumed to exist across the 660 km depth seismic discontinuity. The impossibility of fitting the GPS observations with a viscosity model of this kind was explicitly accepted by Gowan et al. (2019) unless the surface mass load associated with the Laurentide ice sheet was dramatically reduced. The Gowan et al. (2021) paper is therefore an attempt to argue that an ice loading model of this kind is plausible. Unfortunately, the authors of the Gowan et al. (2021) paper seems to think that the Barbados constraint on eustatic sea level history consists only of the oxygen isotopic data from deep sea sedimentary cores, as represented by the temperature corrected benthic foraminifera record of Waelbroeck et al. (2002) or the entirely independently produced SPECMAP stack of Imbrie et al. (1979).

In Fig. 5.4, we show detailed reconstructions of three of the modified versions of the loading history of the continents compared to observations of the relative sea level record at Barbados and the eustatic sea level record of Waelbroeck et al. (2002). Inspection of the intercomparisons will establish several critical facts. First, based upon the cluster of four Acropora palmata (Ap) samples of U/Th age near 30 ka, the oxygen isotopic record of eustatic sea level agrees very closely with the deep sea core estimate of RSL at this time. This is very important because in the modern ecology of the Caribbean Sea Ap lives within 5 m of sea level. In Gowan et al. (2021) the coral derived estimate of RSL at 30 ka, which agrees with the oxygen isotopic estimate is entirely ignored. The misfit of the Gowan et al. models to the RSL constraint at 30 ka is 21.5 m as listed in Table 1. Also ignored are the RSL estimates provided by the series of Montastrea Annularis samples in the age range between 21 ka and 26 ka (26 ka being the age of LGM according to the Barbados coral record. These samples also cannot be ignored. The prediction of the ICE-6G_C (VM5a) model passes through the shallow water tips of these samples for which the vertical error bars are of length 10 m. These error bars are accurately determined on the basis of a pressure induced shape transition that occurs in Ma (e.g. Fairbanks and Dodge, 1979) that is visible in electron micrographs. Any viable RSL record must also satisfy these Ma constraints and these also agree with the oxygen isotopic eustatic sea level inference. Inspection of the re-constructed RSL history predictions for three of the Gowan et al. (2021) in Fig. 5.4, demonstrates that these models dramatically misfit both the RSL estimates based upon oxygen isotopes but also those based upon direct coral-based RSL measurements. As also shown in Table 1 the misfit to these constraints at 26 ka (LGM) is 36.5 m, which is entirely unacceptable. These models, as previously noted, are actually based upon an attempt to salvage the ANU preferred model of the depth dependence of viscosity, a model which is characterized by a large

increase in this Earth property across the 660 km seismic discontinuity. These models are entirely rejected by both direct and proxy estimates of the time dependence of sea level at the critical Barbados location. In subsection 5.2, we will on the basis of the constraints provided by both relative sea level histories other than that at Barbados and especially in combination with Global Positioning System (GPS) measurements of the present day vertical motion of the crust of the North American continent, review the arguments on the basis of which high contrast viscosity models of this kind must be rejected. Prior to presenting this discussion, in the next subsection we present a brief review of the history of attempts to resolve the question of the depth dependence of mantle viscosity.

5.2. The mantle viscosity inverse problem for spherically symmetric viscoelastic models: A brief history

It will be useful to begin this discussion by reviewing the history of the many decades of work that has been devoted to developing a consensus view of mantle viscosity depth dependence. The continued attention that has been devoted to this issue is a clear measure of the importance that geophysical science has attached to it. As previously discussed, this is connected to the fact that this physical parameter exerts a primary control on the efficiency of heat transfer from the Earth's interior to the surface and therefore upon the thermal evolution of the planet. Also important in this process, as previously discussed, are the pressure induced phase transitions that occur in mantle mineralogy as depth increases and the presence of the surface lithosphere which is broken into a series of surface plates which may act to inhibit radial heat transport out of the interior. The issue of mantle viscosity is probably more important to our understanding of Earth evolution than any of these additional characteristics of the system.

The first argument to the effect that the contrast in viscosity between the upper mantle and transition zone on the one hand, and the viscosity of the lower mantle on the other, had to be high, was that by Munk and MacDonald (1960). They argued that there was "something special" about the "equatorial bulge" of the Earth and that this was to be interpreted as being due to the fact that the current bulge was a fossil relict of a time when the Earth was rotating faster than it is at present due to the continued action of tidal friction. Only if the effective viscosity of the deep Earth were sufficiently high, it was argued, could the equatorial bulge have resisted relaxation back towards a less anomalous value. On this basis Munk and MacDonald concluded that lower mantle viscosity would have to be equal to a value near 7.9×10^{24} Pa s, much higher than the value of upper mantle and transition zone viscosity previously inferred by Haskell (1935), on the basis of his analysis of the postglacial rebound of Fennoscandia. Goldreich and Toomre (1969) pointed out soon thereafter that the basis of this inference was incorrect. There was nothing in fact special about Earth's equatorial bulge, its non-hydrostatic form was to be interpreted as being dynamically supported by the internal mantle convection process.

The original conclusion of Munk and MacDonald was almost immediately reinforced by McKenzie (1966, 1967, 1968), who argued similarly in this series of papers that the viscosity of the lower mantle had to have a value of approximately 2.4×10^{26} Pa s, higher still than the Munk and MacDonald estimate. Very recently, McKenzie (2018) has commented on the analyses presented in his papers as follows: "I now think that the whole enterprise is unlikely to be correct because there is nothing special about the nonhydrostatic equatorial bulge, it is simply part of the Earth's gravity field that is sustained by mantle convection", thereby echoing the argument of Goldriech and Toomre 50 years earlier. Attention was drawn to the importance of the paper of Goldreich and Toomre (1969) in Peltier (1974), at the beginning of the development

of the modern theory of the glacial isostatic adjustment process. Although the latter paper did not advocate for any particular model of viscosity depth dependence, resolution of this issue was seen to be an important one that analyses of the constraints on the GIA process might finally resolve.

The argument in favor of appreciable viscosity contrast between the upper mantle and transition zone and the lower mantle beneath was nevertheless taken up thereafter and sympathetically by Walcott (1973, 1978, 1980). Walcott also argued for the necessity of a large contrast between the viscosity of the upper mantle and transition zone on the one hand and the lower mantle on the other on the basis of what he believed to be a strong correlation between the large free air gravity anomaly centered over Hudson Bay, as revealed by satellite observations of the planet's gravitational field, and what he assumed had been the thickness distribution of the Laurentide ice sheet that had covered all of Canada at the Last Glacial Maximum. At that time, it was generally believed that the LGM thickness of the Laurentide ice sheet was mono-domal with the single extremum of ice thickness centered upon Hudson Bay as in the ICE-1 reconstruction of Peltier and Andrews (1976). This satellite observed anomaly was shown most recently in Fig. 6a of Peltier (1998), and its interpretation was the focus of attention earlier in Peltier et al. (1992). Believing that the Laurentide ice sheet had been a mono-domal structure, also centered on Hudson Bay, Walcott argued that the satellite observed free air anomaly must represent the uncompensated uplift of the crust that had yet to be eliminated by continuing postglacial rebound. This implied to him that the viscosity of the deep Earth, i.e., the lower mantle, had to be extremely high so that the rate of relaxation would be sufficiently slow. His argument was therefore similar to that of Munk and MacDonald and MacKenzie, but based not upon an Earth rotation related effect, but rather upon glacial isostasy. On this basis, Walcott inferred a lower

mantle viscosity in the range of 10^{23} Pa s, lower than the values misinterpreted by Munk and MacDonald and MacKenzie but still significantly higher than the then accepted value of the upper mantle and transition zone viscosity inferred by Haskell (1935), whose preferred value for this shallower region was 10^{21} Pa s. Walcott's early work reinforced the view that a "channel flow" model characterized by effectively infinite lower mantle viscosity was to be preferred in which isostatic adjustment involved only the upper mantle and transition zone. This model had originally been introduced by Van Bemmelen et al. (1935).

It is now well understood, but still insufficiently aired in the literature, that Walcott's argument is also incorrect. Although it was initially assumed in the early ICE-4G (VM2) GIA model of Peltier (e.g., 1998), that the Laurentide ice sheet had indeed been mono-domal and centered on Hudson Bay, as Walcott had assumed (e.g. see Plate 6, part b of Peltier, 1998), in later analyses (e.g. Peltier et al., 2004), it was recognized that in fact the North American ice sheet was multi-domed in accord with the original geomorphology-based inferences of Dyke and Prest (1987). Once data became available from the GRACE satellites, this fact became irrefutable. The ICE-6G_C (VM5a) model of Peltier et al. (2015; see Fig. 8 of that paper) accurately predicts the observed time dependence of the gravity field anomaly over North America to consist of two primary extrema, one over SE Hudson Bay and the other to the northwest of the bay over what Dyke and Prest (1987) referred to as the Keewatin Dome in their model of LGM ice thickness. A third less prominent extrema also exists in the Foxe basin off the south west coast of Baffin Island. As shown in Peltier et al. (1992) and reviewed in Peltier (1998a) the satellite observed free air gravity anomaly is not caused by uncompensated glacial isostatic adjustment but rather exists as a consequence of the pattern of normal stress at Earth's surface associated with the mantle convection process. This was established by employing the

internal loading theory for the mantle convection process as developed in the doctoral theses at Toronto of both Alessandro Forte and Giovanni Pari (e.g., see Pari and Peltier, 1996), work in which the internal load was determined based upon seismic tomographic reconstructions of elastic shear wave heterogeneity in the mantle that could be mapped into density heterogeneity (see plate 6 in Peltier (1998a). These 3D tomographic reconstructions were inferred as superimposed upon the background spherically symmetric elastic PREM model of Dziewonski and Anderson (1981). The convection model predicted the satellite observed "static" free air gravity anomaly almost perfectly, as shown here in Fig. 5.5.

The fourth person to investigate the validity of the original Munk and MacDonald and McKenzie and Walcott requirement for high upper mantle and transition zone viscosity contrast with the lower mantle, has been Lambeck et al. (e.g., 2017 most recently) in many papers based upon use of a partial reconstruction and independently produced form of the Toronto theory of the GIA process. His first attempt to establish the need for a high contrast solution was based upon analyses of data from Fennoscandia (e.g., Lambeck et al., 1998 a,b). In these papers, it was argued that the glacial isostatic adjustment signal centered over the Gulf of Bothnia of Fennoscandia required a similarly high viscosity contrast as that which McKenzie and Walcott had previously advocated. The difficulty with this suggestion is that, although such models are indeed able to reconcile the data if based upon an appropriately thin surface mass load and a sufficiently thin lithosphere, the data themselves have only very modest resolving power below the depth of the 660 km seismic discontinuity. This is demonstrated explicitly in Mitrovica and Peltier (1993 and 1995, op. cit. and Peltier et al., 2015) who, as mentioned previously, show that the Fennoscandia data are all well fit by the same VM5a viscosity model if the overly thin ice load preferred by Lambeck et al. is somewhat increased and a thicker lithosphere also employed.

The Fennoscandian ice load is simply too small in horizontal scale for the GIA response to its removal to be adequately sensitive to the viscosity of the lower mantle.

It is only the rebound induced by removal of the load of much larger horizontal scale that was associated with the vast Laurentide Ice Sheet (LIS) that is able to provide the resolving power needed to accurately estimate the viscosity of the upper part of the lower mantle and therefore, when taken together with the constraint of the viscosity of the upper mantle and transition zone provided by Fennoscandian rebound, the contrast in viscosity across the 660 km seismic discontinuity. In the next two subsections we present results from the most recent series of original analyses that have enabled very firm conclusions to be drawn.

5.3. Recent work on the Mantle Viscosity Inverse problem based upon the interpretation of relative sea level data

Formal inversions of the data sets that may be invoked to constrain the depth dependence of mantle viscosity began with the papers of Mitrovica and Peltier (1993, 1995), which dealt respectively with the inversion of the McConnell (1968) relaxation spectrum for the rebound of Fennoscandia and with the rebound in response to the emplacement and removal of the Laurentide ice sheet that was centered on and around Hudson Bay. As previously discussed, the formal inversion of the Fennoscandian relaxation spectrum was relatively straight forward as there existed the analytical formulae for the derivatives describing the sensitivity of the GIA model prediction of the relaxation time characteristic of a particular spherical harmonic degree in the relaxation spectrum to the depth dependence of viscosity. Unfortunately, the inverse problem for mantle viscosity based upon data pertaining to the rebound of the crust and related relative sea level variations associated with the deglaciation of the vast Laurentide ice sheet complex with its extensive Cordilleran and Innuitian flanking ice sheets does not allow for such a simple mathematical parameterization of the response. The inversion of the Fennoscandian data relied

upon the accurate assumption that the horizontal scale of the ice sheet was sufficiently small that only the fundamental M0 mantle mode of the relaxation spectrum of the full spherical model was efficiently excited by the loading history. For the North American loading history, because of its horizontal extent, all modes are excited including the C0 mode that exists because of the density contrast across the core-mantle boundary. A new parameterization of the viscoelastic response to load removal was required for this purpose. What might serve as an appropriate parameterization was suggested by the observed relative sea level histories from sites near the centers of rebound on the coasts of Hudson Bay. The locations of sites in this region from the recently recompiled database of Vacchi et al. (2018), hereafter V18, are shown on Fig. 5.6 and the collection of data from sites 4 and 5 is shown on Fig. 5.7. The data on Fig. 5.7 are color coded according to the regions from which the data are derived, namely the east coast of James Bay and Richmond Gulf on the east coast of Hudson Bay. Clear even by visual inspection of this data set is that a simple parameterization of the form $RSL=A[exp(-t/T)-1]$ should provide a high quality fit to the observations. The two parameters of this fit, namely the amplitude "*A*" and relaxation time parameter "*T*", provides a potentially powerful means of separating the influence of viscosity which primarily determines relaxation time from that due to the magnitude of the ice load whose removal has induced the observed amount of uplift which is represented by the amplitude parameter "*A*". (Sensitivity) kernels for the sensitivity of the inferred relaxation time at a specific geographical location may be inferred numerically by inserting a delta function-like perturbation in viscosity as a function of depth in the prescribed radial discretization of the model and for each such insertion computing the shift in the relaxation time caused by each such insertion. At each site from which a relative sea level curve is available, application of this procedure delivers a distinct derivative for that site. As it happens, the variation of the kernels for

Laurentian rebound thereby inferred do not vary significantly. At all sites these sensitivity kernels have the form shown in part b of Fig. 3.5, where the numerically inferred kernel for the Bathurst Inlet site is compared with the result obtained by following the same procedure for the Angermanland River site on the coast of Sweden. For all sites like Bathurst Inlet the depth of maximum sensitivity to the depth dependence of viscosity is located in the top ~500 km or so of the lower mantle, exactly the region of the mantle for which the viscosity has been most energetically debated. Prior to showing results for the formal inversion of the Laurentide rebound data, it will be useful to first focus upon a demonstration of the ability of this simple parameterization to discriminate between the various viscosity models that have been proposed in the past.

According to Dyke et al. (2005), the data shown in Fig. 5.7 from SE Hudson Bay are those from the center of rebound in which the height of the Marine Limit (ML) is highly correlated with the model predictions of the extremum in the rate of present day crustal uplift. It is also important to note that the data available from these two locations actually come from several points within each of these distinct regions and so it is an issue as to whether it would be possible to define a single relative sea level curve based upon them. In order to explicitly address this issue, we will in what follows compute complete RSL histories for each point in the individual cluster of points in each region and employ the spread of predicted RSL histories from each set of points to represent the curve that may be constructed from them. As a starting point for the following discussion, we have shown on Fig. 5.7 the raw data from these two sites superimposed, with those from the east coast of James Bay and Richmond Gulf color coded as are these individual regions in the boxes on Fig. 5.6. Also shown on this figure, as a circle enclosing error bars for an additional data point, which is the so-called ML as surveyed most

fully in Hillaire-Marcel (1976) and Hillaire-Marcel and Fairbridge (1978) and later reviewed in Dyke et al. (2005) at 275 m +-15m above present sea level with an age in the range 7.8 ka – 8.2 ka. This is a data point not included in the V18 compilation as it cannot be characterized as a SLIP according to the definition employed by Shennan and Horton (2002). A detailed discussion of the constraints on this ML data point is provided in the Appendix of the recent paper by Argus et al. (2021). In plotting these data from the V18 compilation, we are showing primarily SLIPS which by definition are points through which any viable model prediction of RSL history should pass (e.g. Shennan and Horton, 2002). It is important to recognize that this compilation of SE Hudson Bay data represents a highly significant improvement over the compilation from the same region originally published in Peltier (1998a) based upon data provided by Professor Claude Hillaire-Marcel of UQAM University. Although the earlier compilation contained only limiting data, bounding the actual elevation of sea level either from above (terrestrial limiting) or below (marine limiting), the recompilation of V18 contains 34 SLIPS, 11 of which were data in the Peltier et al. (1998a) data set that were described as limiting data but recognized in V18 as SLIPS. This expanded data set will therefore provide much firmer constraints upon models of the GIA process in this region than has previously been possible. It is important to note from Fig. 5.7, that the SLIPS from these two regions lie quite precisely on the same RSL curve and that this curve has a strikingly exponential form.

It is also important to understand why several of the other regions from which SLIPS have been compiled in the V18 database for other coastal regions of Hudson Bay will not be employed in the analyses to be presented herein. It is especially notable, for example, that all of the data from the Richmond Gulf region of Hudson Bay lie very close to the present day coastline and that those from eastern James Bay do not lie far off it. This is critical for the purpose of model-

185

data comparisons because, in the topographically self-consistent form of the solutions to the SLE described in Peltier (1994), it is assumed that all of the data points employed to define a curve have been collected from points that are not only sufficiently closely clustered geographically, but are also closely connected to the present position of the coastline. Evident on Fig. 5.7, is that at all of the other coastal Hudson Bay locations the individual SLIPS are widely distributed, especially in terms of distance from the present day location of the coast and are not particularly numerous. Because the position of the coastline is strongly time dependent in Hudson Bay following establishment of the direct connection of the Bay to the Atlantic, with the initial coastal location being significantly inland from its present location (see Peltier, 1998), the data from these other regions are not suitable for the sort of detailed analysis to be described herein, as they are unable to adequately constrain the present day rate of RSL fall.

Fig. 5.8a shows the fit of the predictions of the ICE-6G_C (VM5a) and ICE-7G_NA (VM7), (see Roy and Peltier, 2018) models to the southeast Hudson Bay collection of SLIPS. Fig. 5.8b shows the depth dependence of viscosity for these two models. It will be important to further recognize in all that follows, that the model fits we show relative to the data that have been collected from a particular region to make a “curve”, are not, as previously commented, simply predictions for a single longitude-latitude point within the given region. Rather we make separate predictions for every longitude-latitude point in the cluster that might have been employed to define a single curve. We then employ the “spread” of RLS predictions for all of the points in a given cluster relative to error bars on the individual SLIPS as a measure of the true misfit between observations and model predictions. Comparison of the predictions of the two Toronto models to the V18 compilation of SLIPS for SE Hudson Bay demonstrates that both models fit the dense collection of SLIPS of age <~4 ka quite accurately. For age >~ 4 ka but less than the

age of the marine limit, however, a modest misfit exists such that the model predictions lie somewhat above the SLIPS in this range. This suggests that the effective viscosity of the model, in the range of depths to which these data are sensitive, which detailed formal resolving power analyses (e.g. Peltier, 1998b for a review), have shown lies primarily in the upper part of the lower mantle or in the lowest part of the mantle transition zone, may be slightly too high (assuming that the spherically symmetric viscoelastic parameterization remains adequate). Also notable in these comparisons of model predictions and the V18 observations is that the Toronto models also fit the Marine Limit observation of Hillaire-Marcel (1976), Hillaire-Marcel and Fairbridge (1978) and Dyke et al. (2005). Because these models also fit the present-day GPS observations of vertical motion of the crust extremely well (see what follows for further analyses of this data) and because the Late Holocene RSL data are dominated by this motion, it should not be a surprise that the Late Holocene RSL data are so well reconciled by these models.

The latter point turns out to be so important to the logical structure of this section of the paper that it is worth explicitly demonstrating the truth of it before proceeding. In the previously shown Fig. 4.9, we have shown the predicted present day rate of uplift of the crust in frame dRad, the present day rate of relative sea level fall in frame dRSL and their sum in frame dGeoid, all having units of mm/yr. These fields are especially interesting for present purposes because dGeoid=dRad+dRSL, where dGeoid is the time rate of change of geoid height, the “d” in these expressions representing time differentiation. Notable from the figure is the fact that |dGeoid|<< |dRad| or |dRSL| and that in the previously ice covered region, including that near SE Hudson Bay, dRad and dRSL are of opposite sign with dRSL<0 and dRad>0. Because dGeoid>0 in this region this means that dRad is slightly greater in magnitude than dRSL. Specifically at the position marked on each frame of Fig. 4c we have dRad=13.3 mm/yr. dRSL = -12.2 mm/yr and

dGeoid = 1.11 mm/yr. Because |dGeoid|/|dRad|= ~0.1 in SE Hudson Bay this means that in SE Hudson Bay an overly strong predicted rate of RSL fall implies an overly large rate of vertical displacement of the crust. Therefore, the fact that the Toronto models fit the V18 SLIPS at a young age means that these data are also accurately- constraining the rate of radial displacement. As we will see in what follows, the other models whose predictions we will examine predict an overly high rate of RSL fall in SE Hudson Bay, and therefore are also predicting an overly high rate of present day vertical uplift of the crust. We will show that this interpretation based upon the available RSL observations is confirmed as correct by GPS observations. Although the RSL data only enable us to make this argument for a single region, our analysis of the GPS data will enable us to show that the same conclusion follows for all sites on the Laurentide platform that were previously covered by thick ice.

In Fig. 5.9, we show the fits of two additional models to the same set of SLIPS from SE Hudson Bay. These two models differ radically in terms of their viscosity structures which are shown in Fig. 5.9b. The first of these comparison models is a simple two layer model of the type preferred by the group at the Australian National University, as most recently re-confirmed by them in Lambeck et al. (2017), whereas the second is one of the much more complex models suggested by Mitrovica and Forte (2004), which is referred to on Fig. 5.9b as MFA. The predictions of these two models for the V18 collection of SLIPS, shown on Fig. 5.9a, have been made on the basis of the assumption that the glaciation history is fixed to that of ICE-7G_NA. Inspection of the fit of these models to the data shows that they both significantly misfit the observations but, interestingly, their predictions are almost identical. The nature of the misfits to the data are such that model predictions lie above all of the data both in the age range <~4 ka and above this age, such that they are predicting a far too rapid rate of sea level fall. However, both

models also reconcile the Marine Limit observation. One might argue that a GIA model with either of these depth dependent viscosity structures might be reinstated as plausible by significantly reducing the mass of the ice load. This has been explicitly advocated in Gowan et al. (2021), but such models lead to unacceptable misfits to the Barbados constraint on eustatic sea level history. As it turns out, such high viscosity contrast models with small ice loads may also be ruled out directly on the basis of the parameterization we have introduced as the basis for the formal inversion of the observations.

The explanation of this interesting circumstance (that two models that differ radically in their viscosity structure nevertheless make predictions of RSL history that are essentially identical through the Late Holocene) may be understood by considering a single property of the set of SE Hudson Bay SLIPS and the various model predictions that are intended to fit them. Attention has been drawn in the past (e.g. see Mitrovica and Peltier, 1995), to the utility of the fact that RSL curves from the centers of postglacial rebound of the crust have a simple exponential form. It has been pointed out that high quality fits to such data with a two parameter model, involving only an amplitude and an exponential relaxation time, provide a means of producing a parameterization of the data that separates one parameter that depends primarily upon the amount of ice that has been removed to induce the observed crustal uplift, namely the amplitude parameter “A”, from another that depends almost exclusively upon the viscosity model, the relaxation time parameter “T”, if the rebound data being parameterized are taken from the period of free decay of the surface deflection when the ice load has ceased to vary. As we will show in what follows, by invoking this parameterization of both the data and the predictions of the various models, we will be led to a clear understanding of a further reason why the specific viscosity models illustrated in Fig. 5.9b must be seen as unacceptable.

In order to extract exponential fits to both the SE Hudson Bay SLIPS and the predictions of the models that are under consideration to this point, we have employed standard software. All fitting of simple exponential relaxation functions to the SE Hudson Bay SLIPS plus the Marine Limit datum and to the output of the models, for which results are provided in what follows, have been performed using a Levenberg-Marquardt nonlinear least-squares algorithm, as implemented in the fit python package (Newville et al., "LMFIT: Non-Linear Least-Square Minimization and Curve-Fitting for Python," doi:10.5281/zenodo.11813). The error estimates from exponential fits to the data are 1 sigma for both amplitude and relaxation time. Our results based upon this analysis for both the raw data of V18 and for 5 model predictions of the SE Hudson Bay data set are tabulated in Table 2 (the fifth model in the set has yet to be described but will be discussed in what follows). Furthermore, the exponential fits to the data both including and excluding the Marine Limit data point are also provided in the same table. On Figures 5.8a and 5.9a, we have also included the results of the exponential model fit to the data when the Marine Limit is included as the thin black line. Inspection of the data in Table 2 will show that the results for the two Toronto models are strikingly differentiated from the results of both the Lambeck et al. (2017) 2-layer model and those for the complex MFA model of Mitrovica and Forte (2004) in terms of the exponential relaxation time inferred to be characteristic of the best fitting exponential model. Whereas the relaxation times found to be characteristic of the Toronto models are found to be in the near vicinity of 4000 years, those of both the Lambeck and MFA models are in the near vicinity of 5500 years, a significant difference. Because the inferred relaxation times are primarily dependent upon viscosity (e.g. Mitrovica and Peltier, 1995), these results confirm that the effective viscosity of the deep Earth of the Lambeck et al. (2017) and Mitrovica and Forte (2004) models is too high to adequately fit

the data from this region near the dominant SE Hudson Bay center of postglacial rebound of the crust. When the relaxation time is too high this means that early in the rebound process the relaxation is occurring too slowly whereas late in the relaxation process the relaxation is occurring too quickly so that over the most recent few thousand years sea level near the center of rebound is falling too quickly and therefore as previously demonstrated, postglacial uplift of the solid surface is rising too rapidly using this parameterization form the region once covered by the Laurentide ice sheet

Before proceeding to implement this parameterization in a formal inversion of all available constraints on the GIA process, it will be important to further investigate an additional issue. In particular it remains a question concerning the meaningfulness of relative model fits to the data as to whether, with an appropriate adjustment to the loading history away from that of either ICE-6G_C or ICE-7G_NA, one could not recover an equally good fit to the critical V18 data from SE Hudson Bay, using the "stiffer" versions of the viscosity structure represented by either the model of Lambeck et al. (2017) or that of Mitrovica and Forte (2004). Fortunately for the purpose of this discussion there are now publicly available data (http://rses.anu.edu.au/data/ANU_ice_model(LW-6+E-6).tar.gz) consisting of sea level history predictions from all sites across the Laurentian platform for the model of Lambeck et al. (2017). Based upon an interpolation of these data from the grid provided, we have extracted RSL curves for both regions 4 and 5 of the V18 database plus the ML and the results of the comparison between observations and these model predictions are shown on Fig. 5.10. These authors are employing a loading history significantly modified from the publically available loading history of Peltier et al. (2015) for the ICE-6G_C model as is clear on the basis of a detailed analysis (not shown). These results demonstrate that, with this apparently preferred adjustment to the loading

history, the fit to the data is only further degraded from that delivered using the ICE-7G_NA loading history for the same high contrast viscosity model. In particular, the high viscosity contrast model continues to predict a far too rapid rate of fall of sea level near the center of rebound in SE Hudson Bay and therefore, it will also be predicting a far too rapid rate of vertical motion of the crust. Because the present day rate of vertical crustal motion is now recorded on hundreds of GPS receivers distributed across the North American continent, as we will demonstrate in the next subsection, this fatal problem with the high viscosity contrast models will be found to be the case at all of the previously ice covered regions of the North American continent.

Before describing the important constraint that GPS observations provide on the depth dependence of viscosity, when combined with a loading history sufficient to reconcile the constraint on eustatic sea level history provided by the coral-based record from the island of Barbados, it will be useful to first provide results from a formal inversion of relative sea level data from both Fennoscandia and Laurentia in combination with the constraints provided by the previously discussed Earth rotation. For Fennoscandia, we will employ the previously discussed relaxation spectrum of McConnell (1968), together with the kernels of Peltier (1976). For Laurentia, we will employ the site specific relaxation times inferred on the basis of exponential fits to RSL data from the large number of sites for which analyses were presented in Peltier (1998b) with associated kernels also provided in this paper. Finally, we will also employ the rotational data for the non tidal acceleration of rotation and for the rate of true polar wander. The derivatives for the latter data are also shown in part c of Fig. 3.5. The results of the simultaneous inversion of all of these data were described in detail in Peltier (1998b) and were shown

previously as VM2 in Fig. 3.2. The viscosity model VM5a is simply a multilayer approximation to VM2, a model that delivers essentially identical results for all GIA constraints as model VM2.

In Fig. 5.11, we show a comparison between most Toronto viscosity models and others that have been suggested in the recent literature. Also noted in this figure, which is from Argus et al. (2021), is the range of depths for which the different data sets employed in the simultaneous inversion of all data are providing constraints upon viscosity. The strategy employed in the construction of the Toronto models has been to exploit the fact that the data from each geographical region or different data types provide information on viscosity depth dependence that is sensitive to a particular range of depths. Thus, the strongest constraints upon lithospheric thickness are provided by data that come from the region once covered by the Scottish Ice Sheet and also from Fennoscandia if there are independent constraints on LGM ice thickness. The Fennoscandian relaxation spectrum, on the other hand, provides the best available constraint upon upper mantle and transition zone viscosity. Relative sea level data from the region once covered by the Laurentide ice sheet are most strongly influenced by the viscosity of the upper part of the lower mantle. The Earth rotation observations, on the other hand, most strongly constrain the viscosity of the lower part of the lower mantle adjacent to and above the core-mantle boundary. The Toronto strategy for model construction is then akin to peeling an onion. When we invert all of the data simultaneously, the strategy follows from the non-overlap between the derivatives for each data type.

Comparing the different viscosity models on Fig. 5.11, the latest versions of the Toronto viscosity model, namely VM5a and VM7, the latter from Roy and Peltier (2017) are very close except in the lowermost part of the lower mantle where the viscosity in VM7 is higher than in VM5a. However, it is also somewhat lower at the top of the lower mantle, the volume average

over the lower mantle being almost identical. As described in Roy and Peltier (2017), this slight modification was driven by the recognition that, in the absence of this adjustment, there existed a robust misfit to RSL data from the southernmost region of the US east coast and the state of Florida based upon the interpretation of mangrove deposits from the region. In Roy and Peltier (2017), it was shown that the adjustment from VM5a to VM7 reconciled this otherwise evident misfit. This model also eliminated a condensed matter physics related flaw in the VM5a model. Because the mantle solidus and adiabat diverge strongly as a function of depth and because viscosity is expected to increase, on the basis of an homologous temperature argument, monotonically as depth increases, VM7 is to be preferred over VM5a (VM2). Returning to consideration of Fig. 3.2, it will be clear, comparing Model VM3 on this figure to VM7 on Fig. 5.11 that these are quite similar, at least by virtue of the fact that the lower mantle viscosity in each is quite high. Comparing both of these models to that of Lau et al. (2016, 2018) demonstrates that they are extremely close, unsurprisingly as all were produced by simultaneous inversion of the same data, differing primarily on the basis of the argument used to infer a model in which viscosity increases continuously with depth. Argus et al. (2021) have drawn attention to a flaw in the argument of Lau et al. that has apparently led to a model of the VM7 kind. Also shown on Fig. 5.11 is the model of Lambeck et al. (e.g., 2017) that is firmly ruled out by all of these results based upon the formal inversion of the totality of the GIA constraints. There cannot exist a large increase in viscosity across the 660 km depth seismic discontinuity. This is very strongly confirmed by the GPS constraints as we demonstrate in what immediately follows.

5.4. Space geodetic constraints on models of the GIA process: Very Long Baseline Interferometry (VLBI), Global Positioning System (GPS), and both static and time dependent gravity (GRACE)

The final data sets that the theory of the GIA process has enabled us to make contact with include those being provided by various space geodetic measurement systems. The first of these to be considered consisted of Very Long Baseline Interferometric (VLBI) measurements of horizontal motion using radio telescopes situated along the US east coast (Argus et al., 1999), in the region of postglacial forebulge collapse. These analyses showed there to be a significant difference between these observed horizontal motions and those predicted using the prevalent GIA model of the time, ICE-4G (VM2), the predictions of which were reviewed in Peltier (1998a). This misfit was later shown in Peltier and Drummond (2008) to be explicable if the radial viscosity profile was simply adjusted by incorporating explicit lithospheric viscosity stratification as would be expected to exist on *a priori* grounds based upon the increase of temperature with depth through the lithosphere into the upper mantle.

The second application of the theoretical structure to the understanding of space geodetic observations was to observations of the static free air gravity anomalies inferred on the basis of satellite orbit analysis. A particular focus of this work was upon the large negative anomaly centered over Hudson Bay shown previously in Fig. 5.5, which Walcott (1978) had interpreted as requiring a very large contrast in viscosity between the upper mantle and transition zone and the lower mantle below. In Peltier and Solheim, (1992), Pari and Peltier (1996) and Peltier (1998a), it was explicitly shown that the ICE-4G (VM2) model predicted a free air anomaly over Hudson Bay that was an order of magnitude too small to explain this satellite-based inference. This implied either that the mono-domal model of LGM ice cover over Laurentia that still characterized the Toronto models at this time was incorrect, or that the large free air gravity

anomaly over Hudson Bay was not a consequence of uncompensated glacial isostatic adjustment as Walcott had assumed. In Peltier et al. (1992) and Pari and Peltier (1996) it was shown that both the magnitude and form of the free air gravity anomaly over Hudson Bay were entirely reconciled by a model of mantle convection in which the internal density heterogeneity was inferred on the basis of seismic tomography. It was not until GRACE observations of time dependent gravity became available, as is discussed further in what follows, that the validity of the Peltier et al. (1992) interpretation was established as correct. The GRACE data firmly established that the LGM North American ice sheet had been multi-domed and that the observed time dependence of the gravitational field was accurately predicted by a GIA model with the same VM2 (VM5a), viscosity structure if the ICE-4G loading history was appropriately modified away from the earlier mono-domal form.

The third application of space geodetic measurements to understanding the GIA process involved the use of Global Positioning System (GPS) measurements of both horizontal and vertical crustal motions. The initial GIA application of this system was to constrain the present-day crustal motion in Fennoscandia, work that was conducted in the context of the BIFROST project as described in Milne et al. (2004). This was followed later by the work of Argus et al. (2010), Argus et al. (2014) and Peltier et al. (2015). Argus et al. (2010) discussed the application of GPS data to constrain the much larger scale pattern of crustal motions associated with the rebound of the North American continent in response to removal of the Laurentide, Cordilleran, and Innuitian ice sheet complex that had covered all of Canada at LGM. Their analysis revealed a significant error in the ICE-5G (VM2) model of the GIA process described in Peltier (2004), the first to address the importance of the forthcoming GRACE observations as providing a further constraint on GIA models. This error was traced to the presence in this model of

excessive ice thickness in the region to the west of Hudson Bay. The required adjustment to the loading history needed to reconcile the GPS observations was described in Vettoretti and Peltier (2013). This led to the development of the most recent ICE-6G_C (VM5a) model of Peltier et al. (2015) and Argus et al. (2014). In Peltier et al. (2015) the theory was applied to the analysis of GPS observations of vertical and horizontal motion from the entire North American continent but also to the Fennoscandian data set originally analyzed by Milne et al. (2004) and to the equivalent data set for Antarctica.

Comparison of the two models for Fennoscandia developed by Milne et al. (2004) and Peltier et al. (2015) to explain the GPS observations provided insight concerning the problem of uniqueness in model fits to GIA observations. In the Milne et al. (2004) paper it was concluded that a particular viscosity model, essentially the same as that which has most recently been further advocated in Lambeck et al. (2017), was to be preferred over that in Peltier (2004) and Peltier et al. (2015). In the latter paper, however, it was shown that the data could be equally well fit with the same viscosity profile as that which Peltier (1998a, 2004) found to be preferred for the North American data (VM2, to which VM5a was simply a multi-layer approximation), taken together with an appropriate regional loading history and lithospheric thickness. This raised a key point concerning the issue of non-uniqueness of the inferences of the depth dependence of mantle viscosity that are made using the theory of the GIA process. Inputs to this theory include both a model of the depth dependence of viscosity and a model of the surface mass loading of the continents by grounded ice. Significant tradeoffs between these distinct components of the model exist, leading to a significant source of non-uniqueness of interpretation of GIA-related observations, unless means are available through which this non-uniqueness may be mitigated if not entirely eliminated. The same issue has more recently arisen in connection with the

interpretation of GPS and relative sea level data from Antarctica as discussed in Argus et al. (2014) who comment at length upon the interpretation of sub-lithospheric viscosity in this region by Whitehouse et al. (2012), arguing that this interpretation also failed to recognize this source of non-uniqueness.

We will end this subsection, and Part I of this paper, by discussing the important role that the GPS observations have begun to play in further cementing the accuracy of the VM5a model of the depth dependence of viscosity which has been inferred on the basis of formal Bayesian inversion of the totality of the GIA observables excluding those provided by space geodetic measurements. In this, GPS observations of vertical motion over the North American continent are playing an extremely important role. This is, at least in part, because of the extremely dense coverage of the continent by GPS receivers shown on Fig. 5.12. Although the distribution of GPS receivers is thinner over the region that was once covered by the Laurentide Ice Sheet (LIS), the Canadian Base Network (CBN) is sufficiently dense when considering both permanent and regularly re-occupied campaign stations that these data well sample the predicted vertical motion pattern of amplitudes predicted by the ICE-6G_C (VM5a) model of the GIA process which is illustrated in color on the scale shown as background to the site distribution of stations.

In order to provide detailed comparisons between model predictions and observations, we will present explicit comparisons along the sequence of labeled traverses shown on Fig. 5.13. Fig. 5.14a,b,c, from Peltier et al. (2015) provides these detailed comparisons on which we compare the predictions of models ICE-5G (VM2), ICE-6G_C (VM5a) and a model by A et al. (2013), the latter of which employed exactly the ICE-5G loading history and the VM2 viscosity structure but a different computational methodology. The two versions of ICE-5G (VM2) produce essentially identical results but both differ significantly insofar as their vertical motion

predictions are concerned from the observations and from the predictions of the ICE-6G_C (VM5a) model which well fits the data on essentially all transects.

As discussed previously in the section concerning model fits to the SE Hudson Bay relative sea level record, there is the expectation that the GPS observations of vertical crustal motion will provide a useful means of further discriminating between models of viscosity depth dependence. That this turns out to be extremely useful in this regard is demonstrated in Fig. 5.15, which is from Argus et al. (2021), in which we show the differential fits of the ICE-6G_C (VM5a) and Lambeck et al. (2017) models to the GPS observed data set over the entire North American continent. Whereas the ICE-6G_C (VM5a) has been shown to fit the GPS observations with high accuracy, the fit of the Lambeck et al. (2017) is extremely poor at all sites that were previously ice covered with the magnitude of the misfit being essentially identical to that expected on the basis of the misfit of the model to the relative sea level data from SE Hudson Bay. This simply reinforces the conclusion that has been clear for more than a decade that high contrast models of viscosity depth dependence cannot fit the observational constraints. Fig. 5.16 presents a comparison of the fits of these two models to the Gravity Recovery and Climate Experiment (GRACE) inferences of the present day rate of change of continental water storage according to these two models of the GIA process. Whereas ICE-6G_C (VM5a) predicts no significant present day change in the rate of water storage over the continent, that predicted by the model of Lambeck et al. (2017) is physically implausible.

This subsection completes Part I of this paper for which we will provide a brief summary before moving on to Part II in which we discuss the ability of an alternative model to similarly reconcile the observational constraints. It should be clear on the basis of the discussion in the preceding sections that the spherically symmetric linear Maxwell viscoelastic model has

provided self-consistent explanations of all of the primary observational constraints on the GIA process. Special solutions are not required for different geographical regions when attention is restricted to the large-scale characteristics of this dynamical process. Exceptions to this general rule include regions like Iceland on the mid-Atlantic Ridge which is a region of active volcanism in which deep Earth viscosity is anomalously low, the Basin and Range Province of the western US where heat flow is anomalously high and regions within the dynamical sphere of influence of subduction zones. It has proven possible to demonstrate this fact because of the methodology employed to construct the model demonstrated by Fig. 5.11, in which GIA observations from different geographical regions which exhibit strongly differential sensitivity to viscosity depth dependence are exploited to determine the depth dependence of this physical property using GIA response characteristics (relaxation times) that are only weakly dependent upon the history of surface mass loading. Given an initial best fit to the viscosity structure determined in this way, one infers an initial best global fit to the constraints upon the characteristics of the GIA response that are most strongly dependent upon the loading history. The past several decades of work by the Toronto group has clearly established that this iterative process is convergent using the spherically symmetric Maxwell model of the GIA process. Whether the converged structure can survive in competition with a more general nonlinear and spherically asymmetric model of the same physical phenomenon is addressed in Part II of this paper to follow.

Part II: The Nonlinear Laplace Finite Element Maxwell Rheological Model of the Glacial Isostatic Adjustment Process.

6. Introduction to the Nonlinear Finite Element Model

In Section 6, we shall review GIA models that can take into account the effects of lateral

heterogeneity and nonlinear rheology. The spectral normal mode method works well under the assumptions that there are no lateral heterogeneities and that mantle rheology is linear. The existence of lateral heterogeneity causes modes to be coupled. In other words, a harmonic load of a certain wavelength can induce deformation of many other wavelengths simultaneously, and not just the wavelength of the load as in the case of lateral homogeneity. Since a large number of modes are coupled by lateral heterogeneity (Wu, 2002a), this makes the spectral method more difficult to be used efficiently and accurately except when lateral heterogeneity is very weak (see Section 7.2 for more details). Fortunately, mode coupling is weak for degree 2 deformation (Wu and Wang, 2006), because the degree 2 component of lateral heterogeneity from seismic tomographic models is not strong, thus spectral formulation of the rotational motion and its rotational feedback to the Sea Level Equation (SLE) on a laterally homogeneous Earth with the background viscosity can be applied. As we shall see below in Eq. (82), nonlinear rheology implies lateral heterogeneity because the effective viscosity depends on stress which varies laterally (Wu, 2002d). Thus, the same difficulty exists when the rheology is nonlinear. Again, mode coupling for degree 2 is also weak for nonlinear rheology (Wu, 2002a).

Several numerical techniques have been introduced to study the effect of lateral heterogeneity. These include the Finite-Element or FE method (Wu, 1992a, 2002b, 2004; Zhong et al., 2003; A et al., 2013), spectral-finite element (SFE) computations (Martinec, 2000; Tanaka et al., 2011), and a finite-volume (FV) formulation (Latychev et al., 2005a). Of these, most are dedicated codes that are not publicly available. Only the Coupled Poisson-Finite Element technique (Wu, 2004) can be easily implemented using commercial FE packages that are well tested, highly efficient and the results of which are very reliable (see Appendix B in Wong and Wu, 2019). For the review to follow we will focus on the FE method. However, as we shall see

below, commercial FE packages need to be modified by using a simple stress transformation in order to take into account the important effects of pre-stress advection (Wu, 1992a,b and the previous Section 3) and self-gravitation. Since the transformation is applied iteratively, this Coupled Poisson-Finite Element technique is also called the Iterative Stress Transform Method or IST.

6.1. IST and the Equations of Motion

The reason stress transformation is required is because commercial FE packages do not solve the full equation of momentum balance (see Eq. 14 in Part I), but instead the equation of zero stress divergence of the FE stress $\bar{\bar{t}}$ (i.e. $\bar{\nabla}\cdot\bar{\bar{t}}=0$) is solved. Thus, the equation that commercial FE codes use neglects the important effects of pre-stress advection and self-gravitation. However, under the transformation $\bar{\bar{t}}=\bar{\bar{\tau}}-\left(\rho_o g_o u_r+\rho_o\phi_1\right)\bar{\bar{I}}$, the physical stress $\bar{\bar{\tau}}$ is transformed to the FE stress $\bar{\bar{t}}$. One advantage of this transform is that it does not affect the strain nor the displacement. Using this, the equation of momentum balance within elements of constant density of an incompressible Earth with $\Delta=\bar{\nabla}\cdot\bar{u}=0$ becomes:

$$\bar{\nabla}\cdot\bar{\bar{t}}=\bar{\nabla}\cdot\bar{\bar{\tau}}-\bar{\nabla}\cdot\left(\rho_o g_o u_r\right)+\rho_o\bar{\nabla}\phi_1=0\,, \tag{71}$$

which is identical to the equation solved by the commercial FE method for an incompressible Earth. Theoretically, this assumption of incompressibility means that the constitutive equation in the domain of the Laplace transform variable "s" becomes $\tau_{kl}=\Pi\,\delta_{kl}+2\mu\,e_{kl}$ where Π is pressure and $\lambda\Delta=\Pi$. But in practice, all one needs to do in using commercial FE codes (e.g. ABAQUS) is to define material properties by their Poisson's ratio ν and Young's modulus E. So, for an incompressible Earth, one takes $E=3\mu$ for given shear modulus μ and take $\nu=0.499$ (since the value 0.5 may not be allowed).

For $\Delta=0$, Poisson's equation for self-gravitation becomes the homogeneous Laplace equation and the perturbed gravitational potential $-\phi_1$ can be obtained as follows: Assume the Earth to be composed of a homogeneous core of radius r_1 and density ρ_1 overlaid by N-1 layers of spherical shells with uniform density ρ_k between $r_{k-1} \le r \le r_k$ (k =2,3, …, N). See Fig. 6.1. Note that r_N refers to the surface of the Earth. Then Φ_1, the coefficients of the spherical harmonic decomposition of the perturbed gravitational potential, can be computed from the "homogeneous" solutions to Poisson's equation Φ_h (Wong and Wu 2019; Wu, 2004):

$$\Phi_h(r) = C_k r^n + C_k' r^{-(n+1)} \tag{72a}$$

with:

$$C_k = \left(\frac{4\pi G}{2n+1}\right)\left[-\Gamma_n r_N^{-(n-1)} + \sum_{i=k}^{N}\left(\overline{\rho}_{i+1} - \overline{\rho}_i\right) U_n(r_i) r_i^{-(n-1)}\right] \tag{72b}$$

and

$$C_k' = \left(\frac{4\pi G}{2n+1}\right)\left[\sum_{i=1}^{k-1}\left(\rho_{i+1} - \rho_i\right) U_n(r_i) r_i^{(n+2)}\right], \tag{72c}$$

where U_n and Γ_n are the spherical harmonic coefficients of radial displacement and surface load of degree n, respectively.

In reality, the mantle is not incompressible and the value of Poisson's ratio ν in the mantle lies between 0.25 and 0.32. In that case, the material properties in the commercial FE codes are taken to be $E = 2\mu(1+\nu)$ where the actual values of ν and μ are used. Solutions to Poisson's equation for a self-gravitating compressible Earth can be obtained from $\Phi_1 = \Phi_h + \Phi_p$ where Φ_h is the "homogeneous solution" given in Eq. (72) for an incompressible Earth and the "particular solution" (Wong and Wu, 2019):

$$\Phi_p = \frac{4\pi G}{2n+1}\int_{r_1}^{r_N} \rho_o \chi_n^m(r') \frac{r_<^n}{r_>^{n+1}} (r')^2 dr'. \tag{73}$$

Here χ_n^m are the spherical harmonic coefficients of the dilatation $\Delta = \bar{\nabla} \cdot \bar{u}$ and can be computed from the sum of the diagonal elements of the strain tensor – i.e. from the output of the FE model (see Wong and Wu, 2019). If one also uses Eq. (71), as the equation of momentum balance with compressibility included in the material properties of the $\bar{\nabla} \cdot \bar{\bar{\tau}}$ term (computed by the FE code) and in Poisson's equation of self-gravitation $\nabla^2 \phi_1 = -4\pi G \rho_o \Delta$, then the solution is called the "material compressible" approximation (Klemann et al., 2003), because only the internal buoyancy force $(\rho_o g_o \Delta \hat{r})$ term is neglected. If this internal buoyancy term is included, then the full equation needs to be solved by another technique (see Wong and Wu, 2019), but that may require intensive computation as the solution can be slow to converge. This is because gravitational instability can arise if the effect of dilatation near the top of a compressible uniform thick layer is large enough to cause a density inversion inside that layer (see Appendix A). The advantage of this "material compressible" approximation is that the computation is very fast and stable because gravitational instabilities are completely eliminated. The validity of using this "material compressible" approximation in the computation of GIA induced relative sea levels and uplift rates is demonstrated in Appendix A.

6.2. IST and the Boundary Conditions

In the above, we reviewed how the equations of motion are adapted for the FE method using the IST technique. Here we summarize only the boundary conditions that are affected by the stress transformation – the continuity of normal and tangential displacement and shear stress across the interfaces are not affected so will not be listed (see Wu, 2004 for details).

First, the surface boundary condition for normal FE stress is:

$$t_{rr} + \rho_o g_o u_r = -(\sigma g_o + \rho_o \phi_1), \tag{74}$$

where σ is the surface mass density of the applied load. In the FE method, the second term on the left can be simulated by the Wrinkler foundation (or elastic springs for inclined material surfaces, see Schmidt et al., 2012) with spring constant $\rho_o g_o$ on the surface of the FE grid and the term on the right side of Eq. (74), is the downward load applied to the surface where $\rho_o \phi_1$ is the potential load. Second, at internal boundaries,the difference between the normal FE stress above and below the boundary is:

$$\left[t_{rr}\right]_{-\square^{+}} = t_{rr}\big|_{+} - t_{rr}\big|_{+} = \Delta\rho\left(g_o u_r + \phi_1\right) \tag{75}$$

where $\Delta\rho = \rho_{-} - \rho_{+}$ is the density jump across the boundary. Again, in the FE method, the terms $\Delta\rho\, g_o u_r$ can be simulated by Wrinkler foundation with spring constant $\Delta\rho\, g_o$ at the boundary and the potential load $\Delta\rho\,\phi_1$ must be applied there. Finally, at the Core-Mantle Boundary (CMB), the FE stress above is:

$$t_{rr}\big|_{+} = \Delta\rho\, g_o u_r - \rho_{+}\phi_1. \tag{76}$$

Again, the first term on the right can be simulated by Wrinkler foundation with spring constant $\Delta\rho\, g_o$ at the CMB and the potential load $\rho_{+}\phi_1$ must be applied there too.

6.3. The IST procedure for Earth Deformation Computation

The procedure to compute the deformation of a spherical, self-gravitating Earth using commercial FE codes can be summarized as follows:

(i) First, a FE grid should be set up for the spherical Earth which consists of a viscoelastic mantle overlying a spherical fluid core (for example, see Figs. 6.2 and 6.3 below). Next, the material properties *E*, *v*, background density $\rho_o$and viscosity η of the layers must be defined. Whenever there is a density contrast between the upper and lower layers, springs that act only in the radial direction (Winkler Foundation) with spring constant $\Delta\rho\, g_o$ must

be applied at the boundary (see discussion in the last section). Note that both radial and lateral variations in E, ν and/or η within the mantle layers are allowed (see Section 6.5 for details). Lateral variations in the thickness of the layers are also allowed as long as the slope of the surface is small and the surfaces of the gravitational potential remain approximately spherical so that the computation of gravitational potential in Section 6.2 remains valid.

(ii) In the initial step of the iteration, the Earth is taken to be non-self-gravitating, so set $\phi_1 = 0$ in all the boundary conditions. With springs (or Wrinkler foundations) set up across boundaries to simulate density contrasts in the radial direction as described in (i), we only need to be concerned with the applied load at the Earth's surface (eq. 74) because the potential load everywhere is zero (see equations 75, and 76). In Eq. (74), the normal stress is due to the downward pressure of the applied load (ρg_o) which can change with time during the whole load/unload process. This non-self-gravitating FE model is then used to compute all the stresses, strains and displacements at all time steps during the load/unload process.

(iii) From the output of the FE computation, the radial displacement $u_r(r_i, \theta, \psi, t)$ and dilatation Δ and their spherical harmonic coefficients $U_n^m(r_i, t)$ and $\chi_n^m(r_i, t)$at all interfaces and at all times are computed. These can then be used to compute $\Phi_1 = \Phi_h + \Phi_p$ (see equations 72 and 73) and thus $-\phi_1(r_i, \theta, \psi, t)$for the next iteration.

(iv) Substituting this computed $\phi_1(r_i, \theta, \psi, t)$ into the boundary conditions in equations 74-76, gives a new load to be applied at the interfaces in the FE model. These new loads will be used for the FE calculation in the next iteration.

(v) The last two steps are repeated until the solution converges to an acceptable level. Usually, it takes about 4 to 5 iterations to reach convergence.

The validation of this procedure is demonstrated in Wu (2004) and Wong and Wu (2019), for Heaviside loading of harmonic loads, but it can also be used to compute any realistic time and space dependent loads. However, if realistic loads are applied, one needs to make sure that the degree-one component of the load be removed before applying it to the boundary conditions of the FE model because degree-one load causes a rigid shift in the center of mass (Farrell, 1972; Peltier, 1974; Cathles, 1975) and that is not allowed in commercial FE codes. In GIA problems, the conservation of mass of the surface loads ensures that the degree-zero of the combined ice and water load is zero.

The FE grid on the surface of the spherical Earth model typically has spatial resolution of 0.5^ox0.5^o, but for illustration purposes, a 2^ox2^o FE grid is shown in Fig. 6.2a. By comparing Fig. 6.2c and d, it can be seen that a 0.5^ox0.5^o grid can give a more reasonable representation of the features in the Great Lakes area in North America. However, if such resolution is maintained at all depths, then the memory required would be extremely high and the run time would be extremely slow even for a high performance computer today. To reduce the memory requirement, the spatial resolution of the deeper layers must have increasingly coarse resolution. How this can be achieved is illustrated in Fig. 6.3.

6.4. Lateral Viscosity Variations and Seismic Tomography

In the last sub-section, it is mentioned that material properties of the FE Earth model can vary both in the radial direction and also laterally. The 3D variations of the elastic properties are provided by standard 1D Earth models such as PREM (as discussed in Section 2 above) in

combination with seismic tomography models. This subsection is concerned with estimating the 3D viscosity variations $\eta(r,\theta,\phi)$ from seismic tomography models.

Currently, a number of high resolution seismic tomography models are available. In general, their long wavelength patterns are fairly well established, but their short wavelength patterns may differ from one another, since their technique of inversion, data type, source and reference models are different. Instead of focusing on any one of these seismic tomography models here, we follow Milne et al. (2018), and take the average of the following four seismic tomography models: S362ANI+M (Moulik and Ekstrom, 2014), SEMum (Lekic and Romanowicz, 2011), SGLOBE-rani (Chang et al., 2015) and TX2019slab (Lu et al., 2019), since that will show their common features. We also compute the standard deviation of these four models to see the location and magnitude of the uncertainties of the Mean Seismic Tomography model. Fig. 6.4 shows the mean lateral shear velocity anomalies $\frac{\delta v_S}{v_S}$ of the Mean Seismic Tomography model at the four layers below the lithosphere: shallow upper mantle UM1 (100-400 km depth), deep upper mantle UM2 (400-670 km depth), shallow lower mantle LM1 (670-1271 km depth) and deep lower mantle LM2 (1271-2891 km depth). Inspection of Fig. 6.4, shows that the lateral variations in $\frac{\delta v_S}{v_S}$ is about 6.4% in layer UM1, 3.2% in UM2, and around 2.4% in LM1 and LM2. The uncertainties of the shear velocity anomalies and the consequence will be discussed in Section 7.3. To find the lateral viscosity structure, $\eta(r,\theta,\phi)$, we take it to be the superposition of the radial and lateral viscosity structures logarithmically, i.e.

$$\log_{10}[\eta(r,\theta,\phi)]=\log_{10}[\eta_o(r)]+\log_{10}[\Delta\eta(r,\theta,\phi)]. \quad (77)$$

The radial viscosity structure is given by the 1D background viscosity model $\eta_o(r)$ from 1D GIA Earth models such as VM5a, VM6, VM7 etc. respectively of Peltier (2004), Peltier et al. (2015)

and Roy and Peltier (2016). The lateral viscosity perturbations $\Delta\eta(r,\theta,\phi)$ are estimated from the lateral shear velocity anomalies $\frac{\delta v_S}{v_S}$ from a seismic tomography model by employing scaling relationships from microphysics of rocks that convert seismic velocity anomalies to temperature anomalies and then to viscosity anomalies. The scaling relation can be derived using the Arrhenius relation for viscosity: $\eta = \eta_o \exp\left[\frac{E^* + pV^*}{RT_o}\right]$ where E^*, V^*, p, R, and T_o are the activation energy, activation volume, pressure, gas constant and background temperature profile, respectively (e.g. Ivins and Sammis, 1995). For a temperature anomaly of δT, the perturbed viscosity can be derived from the Arrhenius relation as: $\frac{\Delta\eta}{\eta} = -\left\{\frac{E^* + pV^*}{RT_o^2}\right\}\delta T$. To complete the scaling relationship, one needs a relationship between $\frac{\delta v_S}{v_S}$ and δT. Ivins and Sammis (1995) neglected the effect of anelasticity during thermal heating and used $\delta T = \frac{-1}{\alpha}\frac{\partial \ln(\rho)}{\partial \ln(v_S)}\frac{\delta v_S}{v_S}$, where α is the thermal expansion coefficient and $\frac{\partial \ln(\rho)}{\partial \ln(v_S)}$ has a value around 0.3. On the other hand, Wu et al., (2013) used the relation: $\delta T = \frac{1}{\left[\frac{\partial \ln(v_S)}{\partial T}\right]_{ah+an}}\frac{\delta v_S}{v_S}$, where both the important effects of anharmonicity (ah) and anelasticity (an) are included during thermal heating (Karato, 2008). Note that in the approach of Wu et al., shear velocity anomalies are related to temperature anomalies directly – without the need to introduce a density conversion as an intermediate step which introduces more uncertainties in both parameters α and $\frac{\partial \ln(\rho)}{\partial \ln(v_S)}$. Thus,

unless one is interested in obtaining density perturbations from seismic anomalies, one can obtain the scaling relationship of Wu et al. (2013), which is given by:

$$\log_{10}\left[\Delta\eta(r,\theta,\phi)\right]=\frac{-0.4343}{\left[\frac{\partial \ln(v_S)}{\partial T}\right]_{ah+an}}\frac{\left(E^*+pV^*\right)}{RT_o^2}\frac{\delta v_S}{v_S}\beta. \quad (78)$$

The values of the parameters in Eq. (78), are given in Karato (2008). Note that β represents the fractional contribution of the thermal effect on seismic anomalies because physically, lateral variation of seismic velocity can be partly caused by non-thermal effects. The importance of including it will be further explained below.

The application of the scaling relationship Eq. (78) is illustrated in Fig. 6.5, which shows $\log_{10}\left[\Delta\eta(r,\theta,\phi)\right]$ of the four layers in the Mean Seismic Tomography model with $\beta=1$. Note that the largest lateral viscosity perturbation is in UM1 with variations of about six orders of magnitude, while that in UM2 and LM2 are about three orders of magnitude and slightly smaller in LM1. Also, note that below western Hudson Bay in Eastern Canada, both the shear velocity anomaly (Fig. 6.4), and the lateral viscosity perturbation (Fig. 6.5) are positive in UM1. Then they become slightly negative in UM2, but become slightly positive again in LM1 and LM2. This "reversal of lateral viscosity perturbation" under Eastern Canada in UM2 when compared to the other layers, will be discussed in Section 7.2.

Given the background viscosity model $\eta_o(r)$, the seismic tomography model $\left(\frac{\delta v_S}{v_S}\right)$ and the assumed temperature profile $T_o(r)$ (e.g. Leitch and Yuen, 1989; Tackley et al., 1993; Schubert et al., 2001), β is the remaining unknown parameter in the scaling relationship Eq. (78). In other words, the 3D viscosity variations $\eta(r,\theta,\phi)$ can be determined if the value of β is known. Since $\eta(r,\theta,\phi)$ affects the misfit between model predictions and observations related to the GIA

process, one can search for the value of β that can give the best fit between model predictions and GIA observations. Physically, β represents the fractional contribution of the thermal effect on seismic anomalies. When $\beta=0$, the Earth model would be laterally homogeneous. When $\beta=1$, the above equation assumes that seismic anomalies are entirely due to thermal effects. However, lateral variations in seismic velocity can also have contributions from non-thermal sources such as lateral changes in chemical composition, degree of hydration, partial melting or non-isotropic pre-stress effects. So, $\beta<1$ in general and the non-thermal contributions are in non-thermal contribution is represented by$(1-\beta)$. Thus, theoretically, the observations of GIA can be used to constrain the thermal contribution to seismic anomalies (Wu et al., 2013). As we shall see in Section 7.2, there is ample evidence that using $\beta=1$ can overcorrect the GIA predictions, while using $\beta<1$ can lead to a better fit between the predictions and the observations.

It should be noted that the value of β in the upper mantle is probably different from that in the lower mantle. The reason is that in the shallow upper mantle, the good correlation between isotropic wave speed and surface tectonics suggests that the thermal effect is dominant there (Hager et al., 1985). But non-thermal effects appear to be dominant in the lower mantle (Karato and Karki, 2001; Trampert and van der Hilst, 2005). Thus, the search for the best 3D viscosity model involves searching for the combination (β_{UM}, β_{LM}) where the subscripts UM and LM stand for upper and lower mantle respectively. If there is need to further refine the layers in the upper and lower mantle, then the combination (β_{UM1}, β_{UM2}, β_{LM1} β_{LM2}) can also be considered. It should also be noted that for regional GIA studies, there is a trade-off between the background viscosity and the value of β (Li et al., 2018, 2020) because both can lead to similar local viscosity required to fit the local GIA data. We note, however, that the issue of how to construct a best mapping between seismic tomography and mantle viscosity remains an important issue for

future research. This issue has already been highlighted in Section 5, which described the results of directly mapping seismic heterogeneity into density, and as shown in connection with Fig. 5.5, that if the s-wave heterogeneity was mapped directly into density with a partial derivative that converted positive s-wave heterogeneity into high density, then one could fit the free air gravity anomaly over North America essentially perfectly. This is consistent with the idea that cratons have high density roots.

Alternatively, one can compute the 3D change in viscosity in the shallow part of the upper mantle with the microphysical approach, where linear (diffusion creep) or nonlinear (dislocation creep) flow laws with appropriate creep parameters are used. The first step of this approach is to estimate the 3D thermal structure of the upper mantle from geotherms and borehole heat flow data (Artemieva, 2006), while the thermal structure in the rest of the upper mantle can be estimated from seismic tomography data based on the assumption that anomalies in seismic velocities are entirely due to thermal effects and the spatial changes in chemical composition or other non-thermal causes have negligible effects. Goes et al. (2000) inverted both P and S seismic velocities using an iterative approach that compares the observed and the synthetic P and S wave velocities, while van der Wal et al. (2013) inverted using S wave alone with the simple scaling law and the assumption of thermal origin for the seismic anomalies :

$$\delta T = \frac{1}{\left[\frac{\partial \ln(v_S)}{\partial T}\right]_{ah+an}} \frac{\delta v_S}{v_S} \quad . \tag{79}$$

The temperature structure can then be obtained by superposing δT on the background temperature profile.

An example of the thermal structure underneath Fennoscandia at three representative depths obtained from van der Wal et al. (2013) are shown in Fig. 6.6. The thermal structure at 80 km

depth is obtained from geotherms and borehole heat flow data, while that at 150 km and 220 km depths are obtained from the S wave tomography model of Grand (2002). Note that a relatively cold thermal structure that extends to at least 220 km depth exists east of Sweden and the Gulf of Bothnia. On the other hand, a relatively warm structure exists in the west and the warm structure moves towards the Norwegian coast at 220 km depth.

In the second step of the microphysical approach, the 3D viscosity can be obtained from the appropriate steady state creep law of the mantle: $\eta = \frac{\sigma'^{(1-n)}_E}{2A}$ where $\sigma'_E = \sqrt{\frac{(\sigma_{ij}\sigma_{ij})}{2}}$ is the effective shear stress, σ'_{ij} is the deviatoric stress and n is the stress exponent. Note that, in general, the creep parameter A is a function of pressure p, temperature T, grain size d, water fugacity f_{H_2O}, melt fraction φ, melt constant α ,grain size exponent m, water fugacity exponent r, pre-exponential factor B and can be written as (Hirth and Kohlstedt, 2003):

$$A = B d^{m} f_{H_2O}^{-r} \exp(\alpha\varphi) \exp\left(\frac{E^* + pV^*}{RT}\right). \quad (80)$$

Note that when n =1 the flow law is linear and $\eta = \frac{1}{(2A)}$ is independent of the stress σ'_E. But for nonlinear creep (n >1) , η is inversely dependent on $\sigma'^{(n-1)}_E$. The case of nonlinear creep will be discussed in more detail in the next subsection and in the rest of this subsection, our attention continues to focus on linear (diffusion) creep. Given the lateral temperature variations at the three different depths in Fig. 6.6, the lateral viscosity variations can be computed using the creep law with appropriate data.

To illustrate this, we assumed that the mantle under old cratons is dry and without melting, then for diffusion creep with a given grain size, each value of temperature maps into a value of viscosity and thus the lateral temperature variation map in Fig. 6.6 can be interpreted as a lateral

viscosity variation map. The converted viscosity values can be read from the color scale bars below each map in Fig. 6.6. An inspection of this figure shows that the red and orange regions at 80 to 150 km depth, with viscosities around 10^{21} Pa s, generally lie on the north and west of the Norwegian coast, and the regions with lower viscosities (reddish white color) in all these depths can be considered as the asthenosphere. On the east side of the maps, the viscosities are higher. These results are consistent with that shown in Fig. 6.5a. If one considers the regions with viscosity higher than 10^{24} Pa s as part of the elastic lithosphere (e.g. Kaufmann et al., 2005; van der Wal et al., 2015; Nield et al., 2018), then Fig. 6.6 shows that the lithosphere on the east side exists above 220 km depth. Similarly, one may deduce the 3D variation of the asthenosphere. Thus, an advantage of this microphysical approach is that the 3D structure of the elastic lithosphere and asthenosphere can be automatically determined from the 3D temperature structure. This is true not only for linear creep but also for nonlinear creep. The disadvantage of this approach is that the assumption of thermal origin of seismic anomalies may not be correct, and thus δT and its effect on viscosity can be overestimated.

6.5. Linear, Nonlinear and Composite Rheology

In general, for viscoelastic material, the steady state linear or nonlinear creep law, in tensor form, can be written as (e.g. Ranalli, 1995):

$$\dot{\varepsilon}_{ij} = A\,\sigma'^{\,n-1}_{E}\,\sigma'_{ij}, \tag{81}$$

where $\dot{\varepsilon}_{ij}$ is the deviatoric strain rate, n is the stress exponent and the creep parameter A is determined from shear experiments (see discussion in last subsection). For GIA modeling with commercial FE packages, it is useful to define the effective viscosity as :

$$\eta_{eff} = \frac{1}{\sqrt{3^{2n+1}}}\,\frac{1}{A^{*}\,\sigma'^{\,n-1}_{E}} \tag{82}$$

where A* is the creep parameter determined from uniaxial experiments and is related to the parameter A by (Ranalli, 1995) :

$$A^* = \left(\frac{2}{3^{\frac{(n+1)}{2}}} \right) A . \tag{83}$$

This is because in commercial FE packages (e.g. ABAQUS), the steady state (time-independent) creep of Maxwell rheology is defined by the inputs A^* and n. So, for linear rheology, the inputs are n=1 and $A^* = \frac{1}{3\eta_{eff}}$ and for a 3D Earth, with viscosity structure $\eta(r,\theta,\phi)$, the latter input is $A^*(r,\theta,\phi) = \frac{1}{3\eta(r,\theta,\phi)}$.

Laboratory study of olivine polycrystals shows that diffusion creep, which gives rise to linear rheology, can become the dominant creep mechanism in the mantle if the stress level is relatively low, or the grain size is small, or both (e.g. Karato and Wu, 1993). On the other hand, if the stress level is high, or grain size is large, dislocation creep is the dominant creep mechanism, giving rise to nonlinear rheology (e.g. Goetze and Kohlstedt, 1973; Li et al., 1996; Cordier et al., 2004; Mainprice et al., 2005).

From creep experiments of olivine polycrystals, the stress exponent for dislocation creep is found to have values around 3 (e.g. Karato and Wu, 1993). Using GIA models with power-law creep, Wu (2002a) found that the effects of stress exponents n=2, 3 and 4 are not large enough to be easily discriminated by the RSL and uplift rate data.

For dislocation creep, the value of A^* under the cold and dry centers of GIA in Laurentia and Fennoscandia can be estimated from the findings of microphysics as follows: Using Table 1 in Karato and Wu (1993) with (i) activation energy $E^{\square}$= 540 kJ/mol and activation volume $V^{\square}$= 1.5×10^{-5} m^3/mol, (ii) with shear modulus μ and pressure p from standard Earth models like

PREM, and (iii) reasonable mantle temperature profile in the mantle (e.g. Leitch and Yuen, 1989; Tackley et al., 1993; Schubert et al., 2001), the value of A^* can be estimated to be of the order of 10^{-40} to 10^{-30}. Using GIA models with nonlinear creep in the mantle, Wu (1999, 2001) found that values of A^* in the order of 10^{-35} $Pa^{-3}s^{-1}$ give predicted land emergence curves that are reasonably consistent with the observational data around Laurentia.

Early studies of GIA modeling with power law rheology are summarized in Wu (1998b), and Steffen and Wu (2011). One important question is whether GIA observations can tell whether the rheology of the mantle is linear or nonlinear, and if so, which part of the mantle is nonlinear? Based on seismic anisotropy data, which indicates that the flow in the shallow upper mantle may be nonlinear, Karato and Wu (1993) showed that if the region with power-law rheology that lies below the elastic lithosphere is thin (< 200 km), then the RSL predictions can fit the observed RSL data in Laurentia for a simple ice model where the ice margin does not migrate with time. However, if the region with power law extends to greater depth, then the radial deformation is characterized by the presence of a "viscously stationary zone", which is incompatible with the RSL data near the Laurentide ice margin. Later studies with realistic ice history, that includes the migration of ice margin and ocean loading, are able to mitigate this problem of a "viscously stationary zone" and if the region with power-law rheology is restricted to lie in the lower mantle, reasonable fit to RSL data around Laurentia can be obtained (e.g. Wu 2001, 2002b,c,d; Wu and Wang, 2008).

It is important to note that for power-law creep with $n \neq 1$, the effective viscosity (Eq. 82) is dependent on both space and time because the stress level evolves in both space and time. The spatial dependence of stress level means that nonlinear creep law results in lateral heterogeneity in effective viscosity. In addition, higher stress level (e.g. below load center at glacial maximum

to the early phase of deglaciation) implies low effective viscosity, so deformation proceeds quickly (Wu, 1992a, 1993). On the other hand, low stress level (e.g. below load center today - long after deglaciation ended) implies higher effective viscosity and so the deformation proceeds much slower (e.g. Wu, 1993; Barnhoorn et al., 2011). Consequently, RSL curves near the center of rebound should show faster uplift rate at the end of deglaciation than today (Wu, 1993,1995) if mantle rheology is nonlinear. Since ambient tectonic stress may also contribute to the stress level, one expects that the ambient tectonic stress also needs to be included in GIA studies (Schmeling, 1987). By including the tensorial interaction between tectonic and GIA induced stress in a mantle with power-law creep, Wu (2001), found that (i) if ambient tectonic stress level is low (<1 MPa), then tectonic stress can be neglected; (ii) if the ambient tectonic stress level is high (>100 MPa), then the creep law becomes incompatible with observed sea levels data around Laurentia; and (iii) if the ambient tectonic stress level is of the order of 10 MPa, then the sea level data around Laurentia can be explained provided that A^* has value around 10^{-35} $Pa^{-3}s^{-1}$.

However, Karato (1998), questioned the importance of stress interaction between tectonic stress and GIA induced stress because the strain rate induced by GIA is orders of magnitude smaller than that due to tectonics and the time scale of the GIA process is comparably short, thus the distance that dislocations move during the GIA process is small and the dislocation density is unlikely to change appreciably to cause interaction. In the studies of Wu (2002b,c) and Wu and Wang (2008), this position of no interaction is taken, also the mantle is assumed to be made up of uniform layers satisfying either a linear or a nonlinear flow law.

On the other hand, there is no reason why linear diffusion creep and nonlinear dislocation creep cannot operate simultaneously in the same region of space. When that happens, the creep

rate is the sum of the creep rates from linear flow with viscosity $\eta$and nonlinear flow laws with A^* and $n \neq 1$. Therefore, the stress-strain relationship becomes:

$$\dot{\varepsilon}_{ij} = \frac{1}{2}\left(\frac{1}{\eta} + \sqrt{3^{n+1}} A^* \sigma'^{n-1}_E\right)\sigma'_{ij} \quad (84)$$

This is called "composite rheology" (van der Wal et al., 2010, 2013; Huang et al., 2019) and its effective viscosity is given by: $\eta_{eff} = \left\{\frac{1}{\eta} + \sqrt{3^{n+1}} A^* \sigma'^{n-1}_E\right\}^{-1}$. With $A^*=0$, the flow law for composite rheology becomes the flow law for linear rheology but when $A^* \neq 0$ and $\eta = \infty$, it becomes the flow law for nonlinear rheology.

Note that the creep law (Eq. (84)), for composite rheology here is different from that used in Gasperini et al. (1992, 2004), Dal Forno and Gasperini (2007) and Giunchi and Spada (2000). In their formulation, the value of nonlinear creep A^* (or A), which can be determined from microphysics, is not used directly but is represented by a combination of ambient tectonic stress, GIA stress and transition stress. Unfortunately, the values of the ambient tectonic stress and the transition stress are not well known. Moreover, the interaction between ambient tectonic stress and the GIA induced stress in their formulation is approximated by the scalar addition of the second invariant of the interacting deviatoric stress tensors in lieu of tensor addition between tectonic and GIA induced stresses. This approach is modified by Kang et al. (2021) to express the effective viscosity as a function of ambient tectonic stress, GIA stress, transition stress and the creep parameter A, which they assumed to vary in the radial direction only - but scalar addition between the interacting stresses is still assumed. Since the transition stress is unknown, different magnitudes of the transition stress were used in these studies and Gasperini et al. (1992) showed that large transition stress makes the media with composite rheology behave like a Newtonian fluid. In the following discussion, we will continue to use Eq. (84), where the

interaction between ambient tectonic stress and the GIA induced stress is via tensor addition and knowledge of transition stress is not required because that is determined by the strain rate of the linear diffusion creep and nonlinear dislocation creep mechanisms.

From the flow law for composite rheology (Eq. 84), it can be seen that nonlinear creep becomes dominant if $\sigma'_E > \frac{1}{3\sqrt{A^* \eta}}$ for n=3. For example, take A^* = 3.3x10^{-35} Pa^{-3}s^{-1} and $\eta = 3x10^{21} Pas$, so $\frac{1}{3\sqrt{A^* \eta}} \approx 1.06$ MPa. Since σ'_E evolves in both space and time during a glacial cycle, wherever $\sigma'_E > 1.06$ MPa, nonlinear creep becomes dominant. But wherever $\sigma'_E < 1.06$ MPa, then linear creep with $\eta = 3x10^{21} Pas$ will become dominant. Typically, the zone where nonlinear creep becomes dominant occurs in the vicinity below the edge of large glacial loads and extends to deeper layers under the center of the load especially before the end of deglaciation (see Fig. 6.7). Fig. 6.7, also shows that in the far field of the ice load, linear creep becomes dominant. In reality, the situation is slightly more complicated than shown in Fig. 6.7, because both A^* and η are not constants in the mantle but both are dependent on mantle temperature, grain size, water content and the degree of melting - and they all can vary in both space and time. A slightly more realistic case is considered in Barnhoorn et al. (2011) which also confirms that the effective viscosity in the regions below the ice load are strongly affected by the stress level which is time-dependent. Consequently, the surface deformation history, as recorded in RSL data, in the vicinity of the glacial load for nonlinear/composite rheology is quite different from that for linear rheology.

This is confirmed by the study of Kang et al. (2021). What that means is that the ice thickness history models constructed with the assumption of linear rheology may not be applicable, or

need to be modified, before they can be used to model the GIA process for nonlinear or composite rheology.

In view of this, Huang et al. (2019) constructed an ice thickness history model that is based on ICE-6G_C but modified for an Earth model that has composite rheology in the upper mantle (UM) that differs from the composite rheology in the lower mantle (LM). They found that the predictions of the Earth model with $A^*_{UM} = 1.67 \times 10^{-35}$ Pa^{-3} s^{-1}, $\eta_{UM} = 3 \times 10^{21}$ Pa s, $A^*_{LM} = 8.87 \times 10^{-36}$ Pa^{-3} s^{-1}, $\eta_{LM} = 1.6 \times 10^{22}$ Pa s is able to give good fit to the observed uplift rate and gravity-rate-of-change data in North America, Northern Europe and the global RSL data (from the present to at least 12 ka BP) simultaneously. This is an important achievement because previous work that assumes that composite rheology is uniform throughout the mantle, found it impossible to fit the RSL data and observed peak uplift rate or peak gravity rate-of change simultaneously (van der Wal et al., 2010). Huang et al. (2019) also showed in their Appendix F, that these values of A^*_{UM} and A^*_{LM} are consistent with laboratory findings of microphysics, if reasonable mantle temperatures are used.

6.6. The IST procedure for Gravitationally Self-Consistent Sea Level Computation

Given the ice history model and the Earth model, one may proceed to solve the gravitationally self-consistent Sea Level Equation (SLE) of Farrell and Clark (1976; and see Part I for a detailed discussion of the origins of this) structure and its mathematical components using the IST (or Coupled Poisson-FE) method. This can be done without solving for Earth deformation first (Wu, 2004). Below, we outline how the SLE that includes time-dependent ocean margins (Peltier, 1994), near-field water influx and Earth rotational feedback (see e.g. Peltier, 2007, 2015 and Part I of this paper for detailed review based upon the linear spherically

symmetric Maxwell model) can be solved by the iterative approach until the desired accuracy is achieved.

Since the time dependent ocean function $O(\theta,\phi,t)$ is central to the SLE, we will outline how this can be determined. First, take the ocean function $O(\theta,\phi,t_p)$ to be time independent and coastlines to be the same as the present time t_p, so that sea level is approximated by the ice-equivalent sea level:

$$S_o(t)=\frac{-M_I(t)}{\rho_o A_o(t_p)}O(\theta,\phi,t_p), \tag{85}$$

where $M_I(t)$is the mass loss history of the ice at time *t*, and $A_o(t_p)$is the area of the ocean basins today. Thus, using $S_o(t)$, with given ice history and the present-day land and ocean topography, we can get an estimate of the time-dependent ocean function $O_1(\theta,\phi,t)$. For example, if the ice-equivalent sea level rose by *w* meters from time *t* to the present, then the first order ocean function at that time is given by the coastline when the sea level is dropped eustatically by *w* meters from today's land and ocean topography. From that, we can determine where (i) glaciated regions become inundated by the sea (e.g. Hudson Bay) or (ii) exposed continental shelf becomes inundated by the sea due to melting of continental ice (e.g. Grand Banks). Thus, the first order effect of time-dependent ocean margin and near-field water influx can be included. The ocean function obtained this way is just an approximation because the vertical motion of the land and the geoid have not been taken into account. When one solves the SLE iteratively (see below), first without rotational feedback, and then with rotational feedback, the time dependent ocean function and the near-field water influx effect estimate become more and more realistic.

As mentioned above, the SLE without rotational feedback is solved first. The equation is:

$$S(\theta,\phi,t)=\left[\frac{\phi_1(\theta,\phi,t)}{g-U(\theta,\phi,t)+c(t)}\right]O_1(\theta,\phi,t), \tag{86}$$

where $c(t)=\frac{-M_I(t)}{\rho_o A_o(t)}-\frac{1}{A_o(t)}\langle\frac{\phi_1}{g}-U\rangle_{ocean}$ and $\langle\rangle_{ocean}$ represents integration over the ocean basin. This together with the ice load history defines the surface load. After removing the degree-one component, this load can be applied to the non-self-gravitating spherical Earth (i.e. taking $\phi_1=0$) and let the FE model compute the displacements, strains and stresses at all time steps. This is just step (ii) in Section 6.3. So, by following through the steps (iii) and (iv) in Section 6.3, $\phi_1(\theta,\phi,t)$, $U(\theta,\phi,t)$ and thus $c(t)$ and $S(\theta,\phi,t)$at all time steps can be computed and that gives the updated boundary conditions for the next iteration. Through the iteration, the effect of self-gravitation can be included in the results. Usually, the solution converges after 3-4 iterations (Wu, 2004). The result can also be used to update and refine the time dependent ocean function $O(\theta,\phi,t)$. In addition, the time evolution of surface mass density can also be used to compute the perturbed moments of inertia and the time rates of polar wander $[\dot{m}_1,\dot{m}_2]$as described in Section 4.2. This prepares for the next stage of including rotational-feedback in the SLE computation.

Next, the SLE with rotational feedback is solved. The equation is:

$$S(\theta,\phi,t)=\left[\frac{\phi_1(\theta,\phi,t)}{g-U(\theta,\phi,t)+G^T\bigotimes\Lambda+C(t)}\right]O_n(\theta,\phi,t), \quad (87)$$

where $C(t)=\frac{-M_I(t)}{\rho_o A_o(t)}-\frac{1}{A_o(t)}\langle\frac{\phi_1}{g}-U+G^T\bigotimes\Lambda\rangle_{ocean}$. The extra term $G^T\bigotimes\Lambda$is the tidal or rotation induced sea level change obtained by convoluting $\Lambda(\theta,\phi,t)$, the perturbed rotational/ centrifugal potential, with G^T, the Green function for tidal induced sea level change. This term can be computed, for example, using the formalism described in Section 4.2, for a laterally homogeneous Earth, because the degree 2 component of lateral heterogeneity from seismic tomographic models or nonlinear rheology is weak, so mode coupling can be neglected. The

procedure for iteration is the same as that described for the SLE without rotational feedback, except the extra term is included in this sea level computation. Again, the time dependent ocean function, the perturbed moments of inertia and the time rates of polar wander can be updated and the SLE with rotational feedback solved repeatedly until convergence is achieved.

Section 7. A Brief Review of GIA Analyses that Include Lateral Heterogeneity or Composite Rheology

In the following subsections, we will briefly review models of the GIA process which include complexities such as lateral heterogeneity and composite rheology.

7.1. Sensitivity and Optimal Location of GIA data for a Laterally Heterogeneous Earth

Paulson et al. (2005) studied the sensitivity of present-day uplift rate in a laterally heterogeneous mantle forced by a point load. They defined the sensitivity by: $\frac{\int |u_i(t) - u_a(t)| dt}{\int |u_i(t)| dt}$, where u_i is the uplift rate for a homogeneous (iso-viscous) mantle and $u_a(t)$ is the uplift rate at the same observation location when the mantle has a viscosity anomaly at a given location. Note that the integral is over 60 Maxwell times (about 27 kyr), so their sensitivity is not for the present-day uplift rate. They concluded that the areas of highest sensitivity are beneath the point load and beneath the observational site. However, for sites far from the point load, the denominator in their definition of sensitivity may have magnitudes close to zero and that can greatly magnify the sensitivity of the anomalous region that is far from the point load. Recently, Crawford et al. (2018) used the adjoint method to compute sensitivity in a laterally heterogeneous mantle at certain RSL sites, but there is no mention of where the load is located relative to the sites, nor the size of the load or its time history. The latter indicates that a point load is also assumed. The methods of Paulson et al. (2005) and Crawford et al. (2018) are

borrowed from Earthquake seismology, where the source can be approximated by a point load. However, this is not entirely correct for GIA studies as glacial loads have much larger horizontal dimensions than its thicknesses, and cannot be treated as a point source. Also, a point load cannot reveal the important relationship between the width of the load and how deep GIA data can see into the mantle. This relationship is valid for both laterally homogeneous and heterogeneous Earth models, and can be illustrated using the results of a simple GIA model, which we will describe in the next paragraph. After that, we will see that sensitivity also depends on the type of GIA data, the age of the data, the background viscosity profile and the depth of the viscosity anomaly.

To see the relationship between the width of the load and the depth it can see, we consider an incompressible uniform half-space, loaded by a harmonic load with wave-number k. The solution of such a problem is well known: The vertical displacement w at depth z ($z<0$) is given by: $w=(kz-1)e^{kz}$, while the shear stress S is proportional to $-kze^{kz}$. For an elliptical load with characteristic lengths of L and M, $k \cong 1.7\sqrt{\frac{1}{L^2}+\frac{1}{M^2}}$ and $k \propto 1/L$ if $L \approx M$ (Cathles, 1975). Since Peltier (1976) pointed out that the sensitivity kernel is mainly determined by the shear energy distribution (see section 3.5), the normalized shear energy profile, which is proportional to S^2, is plotted as a function of normalized depth (kz) in Fig. 7.1. The normalization of the shear energy distribution removes any time dependence in a viscoelastic half-space. From Fig. 7.1, we see that both the depth of the peak $\left(at \frac{-1}{k}\right)$ and its half-peak values (at $\frac{-0.38}{k}$ and $\frac{-2.08}{k}$) depend on the value of the wave-number k. Thus, a wider load can have higher sensitivity at greater depth.

In order to study sensitivity for a laterally heterogeneous mantle, we follow the perturbation method (Wu, 2006; Steffen et al., 2007; Steffen and Wu, 2014) which gives sensitivity kernel

just like the Fréchet kernel in section 3.5 (Peltier, 1976; Mitrovica and Peltier 1991, 1993, 1995; Milne et al., 2004):

Consider the forward problem: $\underline{p}=I(\underline{m})$, where $\underline{m}=[m_1,\ldots,m_M]^T$ contains the M parameters of the Earth model and $\underline{p}=[p_1,\ldots p_N]^T$ contains the N predictions of the forward problem operator I for a certain ice model input (see Fig. 7.2). Suppose that the predictions of this initial Earth model already give a reasonably good fit to the GIA observations so that the problem can be linearized. If one perturbs the material property m_j (e.g. effective viscosity) *only* in the j-th region of the Earth (e.g. at a certain depth and at a certain angular distance from a reference position - like the center of an ice load) with magnitude δm_j and the volume of the perturbed region is ΔV_j, then the sensitivity kernel K_{lj}, for the l-th observation and the j-th region of the Earth, can be obtained from the changes in the N model predictions δp_l (Wu, 2006; Steffen et al., 2007; Steffen and Wu, 2014):

$$K_{lj}=\frac{\delta p_l}{\delta m_j \Delta V_j}. \tag{88}$$

Given the sensitivity kernel defined in Eq. (88), one may ask whether a certain type of GIA data (e.g. RSL, crustal rate of motion, gravity-rate-of-change) at a certain location (on or above the Earth's surface), is able to resolve the change in material property at a certain depth inside a 1D Earth, or at a certain region inside the 3D Earth.

An example of the sensitivity kernel for uplift rate on a laterally homogeneous Earth with simple ice load history is shown in Fig. 7.3. The left diagram plots the kernel as a function of depth just like Peltier (1976), Mitrovica and Peltier (1991, 1995) and Milne et al. (2004). It shows that for the uplift rate observed at the center of the load with size comparable to the Laurentide ice sheet (blue dotted curve), the sensitivity is highest in LM1, followed by UM2. For

observations at the edge of the ice load (green dashed), the sensitivity is highest in UM1 and UM2, but the magnitude of sensitivity is much lower than that at the ice center. If the uplift rate is observed 10° outside the ice edge (purple line), the sensitivity is highest in LM1, but the magnitude of sensitivity is even lower. Fig. 7.3a, gives the sensitivity kernel at only three locations. If one is interested in how the sensitivity varies with distance from the load center, one can replot the sensitivity as in Fig. 7.3b, where the four curves represent the values of the kernel at the four homogeneous layers UM1, UM2, LM1 and LM2. It can be seen that sensitivities in the lower mantle (LM1 and LM2) peak around the center of the load and broaden with depth. On the other hand, for the upper mantle (UM1 & UM2), sensitivity peaks around 10° from the load center and a trough exists just outside the ice load. At an angular distance of more than 30° from the load center, the sensitivity for uplift rate becomes very low.

If the Earth model above has an anomalous viscosity region of limited horizontal and radial extent, then the sensitivity kernels for uplift rate and tangential velocity at different observation points along the Earth's surface for this laterally heterogeneous model are given in Fig. 7.4. The depth of the anomalous region can be one of UM1, UM2, LM1 or LM2. Similarly, anomalous regions with increasing angular distance from the load center are labeled regions A, B, C, D, E, (see Fig. 7.4). Region A is under the load center; region B is close to the ice margin but still underneath the ice load; region C is just outside the ice margin, etc. Regions A to D have width of 7.5° while regions E to I (not shown in Fig. 7.4) have a width of 30°. The column on the left of Fig. 7.4 plots the sensitivity for uplift rate at the four different depths and angular distances, while the column on the right is for tangential velocity.

In general, the magnitude of sensitivity for uplift rate is localized mainly within regions A, B and C, with the largest magnitude underneath the load, and as the anomalous region moves

farther away outside the load the magnitude of sensitivity decreases. Also, the observation is most sensitive to anomalous regions directly below. (This was later confirmed by Steffen and Wu (2014) for very small anomalous regions in Fennoscandia). On the other hand, the sensitivity for tangential velocity extends much further away – for example, an anomalous viscosity in regions A or B can be felt by tangential velocity measurements at region E and beyond, and with magnitude more than an order higher than that for uplift rate. Fig. 7.4 also shows that if the anomalous viscosity region is in the lower mantle, the magnitude of sensitivity decreases, but its width increases with depth.

Using these simple Earth and ice models, Wu (2006) also showed that the sensitivity kernel depends on the type of GIA observations – for RSL data, the sensitivity kernel also depends on the age of the data. These are confirmed with more realistic ice and Earth models, which we will discuss below.

With the more realistic ICE-6G_C model and lateral viscosity variations inferred from seismic tomography, the sensitivities in laterally heterogeneous upper mantle (UM) and lower mantle (LM) for present-day gravity-rate-of-change (e.g. from GRACE measurements), uplift rate (e.g. from GPS measurements), and relative sea level changes are shown in Fig. 7.5 and Fig. 7.6. From these, Wu (2006) and Li et al. (2018), summarized their findings as:

(i) Sensitivity depends on the type of observational data – while the sensitivity kernels for uplift rate from GPS, gravity-rate-of change and RSL data within the last 6 ka BP show a similar pattern. (This is clearly seen by comparing Fig. 7.5a,b and Fig. 7.6g; same for Fig. 7.5c,d and Fig. 7.6h.) The sensitivity for tangential velocity is higher for viscosity variations in the upper mantle and the effect of anomalous viscosity on tangential velocity can be seen at greater distance from the ice load (Fig.7.4);

(ii) Sensitivity depends on the location of the data relative to the ice sheet – higher sensitivity if the site of the observation lies closer to the ice center (this can be clearly seen in Figs. 7.4, 7.5 and 7.6, where the sites with high sensitivity are around the ice sheet centers.) Also, observations near the ice margin have higher sensitivity to the shallower part of the mantle (e.g. Figs. 7.4, 7.5a and b);

(iii) Sensitivity depends on the horizontal dimension of the ice sheet, which determines how deep the observations near the center of the ice load can see (As shown in Fig. 7.5c,d and Fig. 7.6h, sensitivity in the lower mantle peaks under the center of the Laurentide ice sheet but is much weaker elsewhere including under Fennoscandia. Because the Fennoscandian ice sheet has a smaller horizontal extent than Laurentia, its sensitivity peaks in the upper mantle.)

(iv) Sensitivity depends on the age of the RSL data – as the age increases, the amplitude of sensitivity at different depths also changes (Wu 2006; Li et al., 2018, also Fig. 7.6);

(v) Sensitivity depends on the background viscosity profile – a large viscosity increase in the lower mantle causes the amplitude of sensitivity to increase in the upper mantle but decrease in the lower mantle.

(vi) In the presence of lateral viscosity variations, sensitivity is highest if the anomalous region lies directly below the observation site, however, as the depth of the viscosity anomaly increases, the width of its influence increases and can be detected in neighboring regions. However, the amplitude of sensitivity decreases with increasing depth (see Fig. 7.4).

Another useful application of the sensitivity kernel is in the planning of new GPS or absolute gravimetry stations or in the search of new high quality RSL data. For example, we

want to find the optimal locations of new GIA data, where the sensitivity of the data exceeds the observational error of the data and that can resolve one or more of the following 4 main GIA parameters: (i) lithospheric thickness, (ii) background viscosity, (iii) lateral viscosity variations and (iv) ice thickness. The preliminary findings of optimal location for GPS, absolute gravity, GRACE data and RSL data can be found in Wu et al. (2010) and Steffen et al. (2012, 2014d). Below, we give a brief summary of their work.

To compute the sensitivity to ice thickness, we follow the same principle as for the other Earth parameters, that is, by taking the difference between the predictions of two models that only differ in that particular parameter. So, to study the sensitivity to ice history, we compare the predictions of ICE-4G and ICE-5G in North America, but ICE-4G and FBKS8 (Lambeck et al., 1998) in Fennoscandia because this gives a higher sensitivity there. For the sensitivity to lithospheric thickness, the Earth models only differ in the lithosphere i.e. we compare one with a 115 km uniform thickness with one that thickens from 75 km below the oceans to over 200 km thick at the continental craton. For the sensitivity to background viscosity, we compare 1D Earth models that only differ in the background viscosity of the lower mantle, where the value changes from $6\text{x}10^{21}$ Pa s to 10^{22} Pa s. For the sensitivity to lateral viscosity variations, we compare laterally homogeneous with laterally heterogeneous Earth models – the latter has $\beta_{UM}= \beta_{LM}=0.6$ in the determination of $\log_{10}[\Delta\eta(r,\theta,\phi)]$.

Fig. 7.7b and c, maps the GRACE g-dot sensitivity that exceeds the uncertainty of g-dot measurements to the four GIA parameters in Laurentia and Fennoscandia today. They show that g-dot data in the green shaded areas in Laurentia and Fennoscandia have high enough sensitivity to resolve lateral variations in lithospheric thickness. These areas mostly lie around the past ice margin of these ice sheets, but also near the center of GIA in Fennoscandia. On the other hand,

the purple shaded areas that can resolve lateral viscosity variations in the mantle lie near the center of GIA in Laurentia but on the northern part of the ice margin in Fennoscandia. The areas with blue dots can resolve background viscosity profiles, and are found near the centers of GIA in Laurentia and Fennoscandia and cover a larger area than the green and purple areas. The areas shaded with red can resolve the changes in the assumed ice histories. Thus, g-dot data in certain areas can have sensitivity to one, two, three or all four parameters of GIA. Theoretically, one can then choose GIA data from different areas to separate the effects of the individual GIA parameters.

Since the sensitivity kernels for land uplift rate and RSL data within the last 6 ka BP are similar to g-dot, the sensitivity of uplift rate data and recent RSL data to the four GIA parameters in Laurentia and Fennoscandia show some similarity to Fig. 7.7b and c. Also, the sensitivity of RSL data changes with time. Fig. 7.7a, shows the situation for RSL data at 10 ka. Inspection of this figure shows that RSL data at 10 ka with 1 m error has enough sensitivity to resolve lateral variations in lithospheric thickness for only limited sites – mostly those around the ice margins of the large ice sheets in North America, Greenland, Eurasia and Antarctica. However, the RSL sites that can resolve the background viscosity profile and lateral viscosity variations can be found in much broader areas around the large ice sheets in North America, Greenland, Eurasia and Antarctica. With 1 m error, RSL sites in most areas around the globe can potentially resolve large ice history variations - thus recent improvement on the quality of RSL data can improve the sensitivity even more.

7.2. Lateral Heterogeneities in the lithosphere, asthenosphere and mantle

In this subsection, we review briefly the development in GIA studies of lateral heterogeneities.

Evidence from surface geology and seismic tomography since the late 1970s clearly show that material properties inside the Earth vary not only radially, but also laterally (e.g. Kennett and TkalCi´c, 2008). From Section 6.5, we have seen that this may involve lateral viscosity changes of three to five orders of magnitude! Later, the study of land emergence data using 1-D GIA models also suggests the presence of lateral variations in viscosity and lithospheric thickness (e.g. Nakada and Lambeck, 1991; Breuer and Wolf, 1995; Kaufmann and Wolf, 1996).

Can lateral heterogeneity be studied with the traditional spectral (Normal Mode) approach? It is well known that for a non-rotating spherically symmetric Earth, a harmonic load of degree l and order m induces deformation of the same harmonic order and degree. However, in the presence of lateral heterogeneity or nonlinear rheology, not only is degree l and order m excited, but modes of other degrees and orders are excited as well (Wu, 2002a). The cause of the coupling is revealed in Fig. 7.8, which compares the normalized radial displacement Ur of a laterally homogeneous Earth and that of a laterally heterogeneous Earth, where the mantle viscosity increases sharply by two orders of magnitude at colatitude $\psi = 45^o$ (Fig. 7.8a). On the extreme left side of Fig. 7.8b (with colatitude ~ 0^o), the viscosity of the laterally heterogeneous model is the same as that for the laterally homogeneous model, so the amplitudes of $Ur(\psi)$ for both Earth models are close together. However, as colatitude increases in the laterally heterogeneous model, the effect of the higher viscosity at colatitude > 45^o is felt, resulting in a delayed response and hence smaller magnitude for $Ur(\psi)$. For example, the normalized magnitude of Ur at $\psi = 90^o$ and 180^o are reduced from -0.5 and 1.0 to -0.34 and 0.65 respectively. Thus, the curve $Ur(\psi)$ for the laterally heterogeneous model cannot be represented by a single harmonic, but needs the superposition of other harmonics as well (see Fig. 7.8c). The existence of mode coupling means that the solution of the surface loading problem for a laterally

heterogeneous model must be expressed as the superposition of all the modes involved, and if the effect of lateral heterogeneity is weak, then the number of modes involved may be greatly reduced, and the relative amplitude of these modes can be computed iteratively. D'Agostino et al. (1997) assumed that the coupling involves 10 neighboring modes in their study of the effects of a laterally heterogeneous lithospheric craton on a non-self-gravitating Earth. They found that the effects of lateral heterogeneity do not greatly affect the long wavelength vertical displacements, but the effects are large on the tangential displacements. Kaufmann and Wolf (1999) used the perturbation method and obtained the solution in analytical form for an incompressible flat-Earth. However, their formulation involves only two harmonics – one for the load and the other for the lateral heterogeneity whose spectral amplitude depends on the magnitude of the viscosity contrast. They found that for loading by the Fennoscandian ice sheet, the harmonic variations of the shear modulus and viscosity can modify the vertical surface displacement by several tens of meters – and the modification increases in proportion to the amplitude of the lateral variations. However, Wu (2002a) found that a sharp transition of the lateral viscosity contrast may involve more than 10 modes (see Fig.7.8c). In addition, the number of modes involved and their strength of coupling also depend on the harmonic of the load (l, m) and the location and the magnitude of the viscosity contrast. Furthermore, mode coupling also plays an important role if mantle rheology is nonlinear. Now, as more modes are included, the spectral (or perturbation) method can become computationally more intensive and the solution may lose its accuracy. Thus, the spectral/normal mode method works well only if the lateral change in viscosity is very gradual and the magnitude of lateral viscosity variation is extremely weak. For most practical considerations, other more sophisticated techniques, such as the finite-element (FE) method, need to be used.

Early studies of the effects of lateral heterogeneity on GIA, using the FE method, assumed an axisymmetric (2D) Earth with simple structures, that is forced by simple ice history models with horizontal dimension comparable to or larger than the Fennoscandian ice sheet (e.g. Sabadini et al.,1986; Gasperini et al., 1991; Kaufmann et al., 1997; Wu et al., 1998). Their main concern was to identify the locations within the former Fennoscandian ice sheet where the effects of certain assumed lateral variations in lithospheric properties, asthenospheric viscosity and mantle viscosities on GIA predictions are large enough to be detected. They found that inside formerly glaciated areas, the effects of these lateral heterogeneities significantly influence the predicted velocities, horizontal displacement and gravity, although RSL data there are less sensitive to their effects. On the other hand, these lateral heterogeneities can be resolved from RSL and other geodetic data around and outside the former ice margin. In addition, the effects of lateral viscosity variations in the lower mantle can be detected both within and outside the former Laurentide ice margin. However, the effects of lateral density variations are small for RSL and other geodetic data.

Kaufmann et al. (1997) also studied the question whether lateral heterogeneities in the lithosphere and asthenosphere can be inferred and modeled correctly by using a suite of laterally homogeneous Earth models, just as in Nakada and Lambeck (1991), Breuer and Wolf (1995) or Kaufmann and Wolf (1996). They found that if lateral heterogeneity only exists in the lithosphere, then the lateral change in lithospheric thickness can be accurately resolved by considering a suite of 1-D models with different lithospheric thickness, but if lateral heterogeneity in the asthenosphere is also involved, then 1-D models cannot resolve both the lateral changes accurately. This result was later confirmed by Kaufmann and Wu (2002) using 3-D flat Earth models for Fennoscandia. Wu et al. (1998) also showed that the effect of removing

the assumption of axisymmetry is small. They further showed that the results from these 2-D models can be extended to 3-D flat Earth models.

In the next stage, compressible 3D-flat Earth FE models with realistic ice histories were used to study the effects of lateral heterogeneity on GIA in local regions such as Barents Sea (Kaufmann and Wu, 1998), Fennoscandia (Kaufmann et al., 2000; Steffen et al., 2006), Antarctica (Kaufmann et al., 2005), and Laurentia (Wu, 2005). In these studies, the ocean load is approximated by the eustatic sea levels. Again, the aim of these studies was to confirm that the effects of given lateral heterogeneities can be large enough to be detected by GIA observations such as free air gravity, RSL data and observed vertical and horizontal velocities. It is important to note that there was also progress in how the lateral changes in Earth structure were obtained. In Kaufmann and Wu (1998) and Kaufmann et al., (2000), the lateral changes in lithospheric thickness and asthenospheric viscosity were deduced from earlier 1-D GIA modeling results or from geophysical data with limited coverage. But in Kaufmann et al. (2005), Wu (2005) and Steffen et al. (2006), lateral viscosity changes were deduced from seismic tomography model S20A, with the assumption that the seismic anomalies are caused by thermal effects alone, and that the effect of anelasticity can be neglected in the scaling law between seismic anomalies and viscosity perturbations (see Section 6.5). Kaufmann et al. (2005) found that lateral heterogeneities in the mantle have small effects on the uplift pattern, but their effects on the magnitude of uplift are significant (see Figs. 7.9a and c). On the other hand, lateral heterogeneities affect not only the magnitude of horizontal velocity but also the pattern and direction of flow – instead of divergence from the center of deglaciation as in the laterally homogeneous case, the flow for the laterally heterogeneous case is from the high viscosity area beneath East Antarctica to the less viscous upper mantle below West Antarctica (Figs. 7.9b and

d). Wu (2005) studied the effects of lateral heterogeneity in Laurentia, and also the contributions of lateral heterogeneities from individual layers in the lithosphere, shallow upper mantle UM1 (sub-lithosphere to ~400 km depth), transition zone UM2 (400-670 km) and lower mantle (see Fig. 7.10). He found that the results from Antarctica also applies to Laurentia, except that the changes in vertical and horizontal velocities are smaller in magnitude under Laurentia, so that the lateral heterogeneities only distort the horizontal divergent motion found in the laterally homogeneous case, but are not large enough to overprint it as in Antarctica. One reason is that there is a "reverse lateral viscosity variation" under the center of Laurentia (see Fig. 6.5) – meaning that the low viscosity in UM2 is sandwiched between higher viscosities in UM1 and the lower mantle (LM1 and LM2). Steffen et al. (2006) also used seismic tomography under Fennoscandia to infer the Earth's structure and they also studied the contribution of individual layers of lateral heterogeneity in the upper mantle. They confirmed that lateral viscosity structure can significantly influence RSL, uplift rate and horizontal velocity in Fennoscandia. In addition, lateral heterogeneity in the upper mantle has a strong influence on horizontal motion. However, the effect of lateral heterogeneity is too strong to fit GIA observations while laterally homogeneous models can better fit the data (see Fig. 7.11). One explanation is that the FBKS8 ice model (Lambeck et al.,1998) used in the model is tuned for laterally homogeneous models. Another possibility is that the assumption of thermal origin of seismic anomalies (i.e. $\beta=1$) is not correct. If seismic anomalies are partially caused by compositional heterogeneities or non-isotropic stress, then the lateral viscosity variations would be smaller ($\beta<1$) and the tangential motion could fit the observations better.

In the third development stage, the spherical shape of the Earth and the effects of self-gravity in the solid Earth and the oceans (i.e. gravitationally consistent sea-levels) were also

included. The FE model of Giunchi and Spada (2000) included the spherical shape of the Earth but not the effect of self-gravity in the solid Earth and oceans. The FE-spectral model of Martinec (2000) and the FE model of Zhong et al. (2003) both included the spherical shape and self-gravity in the solid Earth, but ignored the effect of self-gravity in the oceans. Note that these models all assumed that Earth material is incompressible. Compressibility affects the magnitude of tangential velocity significantly (Mitrovica et al., 1994), but its effect on vertical velocity is small (Tanaka et al., 2011) and does not significantly affect RSL predictions except for the early phase of deglaciation (Wolf, 1985). Latychev et al. (2005a) used the finite volume method and included compressibility, sphericity and self-gravity in the solid Earth, but not self-gravity in the oceans. However, self-gravity in the solid Earth is important for deformations of the low harmonics (Wu, 2002a) and self-gravity in the oceans is important for RSL computations near the former ice margins (Wu and van der Wal, 2003), and that is especially important for the interpretation of lateral heterogeneity since the RSL data near the former ice margins are most sensitive to the effects of lateral variations in lithospheric thickness and asthenospheric viscosity. Wu (2004) developed the IST method to include the effects of self-gravity in the solid Earth and the oceans for spherical incompressible Earth (see Sections 6.2, 6.4 and 6.6). Using this model for simple ice loads and axisymmetric Earth structure, Wu and van der Wal (2003), studied the effects of lateral heterogeneity on RSL curves. They found that for RSL data near the center of deglaciation in Laurentia, the effect of lateral viscosity variations in the lower mantle can be masked to a great extent by the “reverse lateral viscosity variations” in UM2 (400-670 km depth), but that is not the case for RSL data just outside the former ice margin. Using the same FE model, Wu et al. (2005) confirmed that results of spherical Earth with axisymmetry remain valid for 3-D spherical case. They also found that both geoid rates and RSL data near the center

of deglaciation in Laurentia cannot resolve lateral variations in lithospheric thickness and asthenospheric viscosity, but land uplift rate and RSL rates there can. As in the discussion on sensitivity (Section 7.1 and Wu 2006), RSL, geoid rate, land uplift rate or RSL rate near the center of deglaciation in Laurentia can resolve lateral viscosity variations in the lower mantle, while tangential velocity data can distinguish lateral heterogeneities near the surface and in the lower mantle.

Wang and Wu (2006a,b,c), used the IST method to further study the effects of lateral heterogeneity in a spherical, 3-D, self-gravitating Earth and oceans, where seismic anomalies from tomography model S20A (Ekstrom and Dziewonski, 1998) are assumed to have thermal origin (i.e. $\beta=1$) and the effect of anelasticity is neglected in the scaling relationship. Wang and Wu (2006a) studied the effects of lateral heterogeneity on present-day crustal motion, especially the interaction between individual ice sheets (see Fig. 7.12). They found that the uplift rate pattern in most areas is localized, with little interaction with its neighboring ice sheets, except for the area between western Greenland and North America. However, the tangential motions in North America, Greenland and Eurasia strongly interact with each other and dominate the motion in the Arctic, although their interaction with Antarctica is weak (see Fig.7.12 and Fig. 7.13d). Wang and Wu (2006a) also studied the contributions from individual layers of lateral heterogeneities in the mantle as in previous 3-D flat Earth models (Kaufmann et al., 2005; Wu, 2005), and confirmed that lateral heterogeneities have only small effects on the pattern of present-day uplift rate, but can strongly affect their magnitude (see Fig. 7.13 a and c). The pattern of uplift rate is mainly determined by the ice model. In general, a higher viscosity perturbation under the ice load results in larger present-day uplift rates and the net uplift rate is controlled by the interaction between different layers of lateral heterogeneities in the mantle. On

the other hand, the effects of lateral heterogeneities on tangential motion are large and can overprint the divergent pattern of flow predicted by laterally homogeneous layers (see Fig. 7.13 b and d). In general, if the center of deglaciation is situated over a gradient of lateral viscosity change, then the incremental tangential motion is from the area of high viscosity towards areas of low viscosity. The net tangential velocity is due to the interaction between different ice sheets and also between the different layers of laterally heterogeneity. Wang and Wu (2006b) found that the model with lateral heterogeneity can give a better match to the observed RSL data at a certain age than laterally homogeneous models - by adjusting β, the thermalcontributions of the different layers of lateral heterogeneity, to the RSL prediction. The contribution of the layers varies with age of the RSL data, the location of the site relative to the ice sheet and the size of the ice sheet – because it is controlled by the sensitivity of the GIA prediction on lateral viscosity variations (see Section 7.1 and Fig. 7.6). Wang and Wu (2006b) also showed that the main contribution of lateral heterogeneities on the zonal harmonics of the geopotential $\dot{J}_l$ and the secular rate of change of gravity (e.g. g-dot data from GRACE) in Laurentia and Greenland come from the deep mantle and their effects are significant but the values are also affected by the background 1-D viscosity profile.

Wang and Wu (2006c), further studied the relationship between lateral heterogeneity and the background viscosity profile $\eta_o(r)$. They found that a low viscosity contrast between upper and lower mantle in $\eta_o(r)$ gives a stronger divergent tangential motion in North America which can also affect the tangential motion in Fennoscandia (see Fig. 7.14a). On the other hand, higher viscosity contrast gives converging tangential velocity motion outside the peak of the peripheral bulge in North America and a divergent tangential motion in Fennoscandia, except for the southern part (see Fig. 7.14c). They concluded that both lateral heterogeneity and viscosity

contrast between the upper and lower mantle can affect the magnitude of uplift rates in centers of rebound, but lateral heterogeneity can strongly affect the direction and magnitude of tangential motion (see Fig. 7.14b and d).

Using the finite volume method, Latychev et al. (2005b) and Whitehouse et al. (2006) investigated the effects of a weak zone along plate boundaries on uplift rate and tangential velocity. Latychev et al. (2005b) found that the effects of plate boundaries on uplift rates are generally small except along the plate boundaries (e.g. Iceland). On the other hand, the weak zones strongly limit long wavelength stress transmission. Whitehouse et al. (2006) confirmed that the effects of plate boundaries on uplift rate are small in Fennoscandia, but the effects on tangential motion in Fennoscandia are more significant. They also found that the effect of lower mantle viscosity and far field structure strongly influence the tangential motion in Fennoscandia. These confirm the findings of Wang and Wu (2006a, b and c) and are supported by the findings of Tanaka et al. (2011).

Paulson et al. (2005) improved on the spherical, self-gravitating, incompressible, 3-D FE model of Zhong et al. (2003) and included both effects of self-gravity in the oceans and rotational feedback. Their 3-D Earth model is inferred from seismic tomography assuming pure thermal origin of the seismic anomalies. Like Kaufmann et al. (1997), they investigated the possibility of using 1-D Earth models to fit the predictions from 3-D Earth models, but their approach of obtaining 1-D models is different – the 1-D models are obtained by a weighted lateral average of the 3-D Earth model. They confirmed that 1-D models have difficulties in reproducing the GIA predictions of 3-D Earth models (including RSL and gravity anomaly in Eastern Canada, $\dot{J}_2$, polar wander rate and GRACE gravity coefficients). Later, A et al. (2013) improved on the 3-D GIA model of Paulson et al. (2005) by including the effect of

compressibility. They found that incompressibility reduces the GIA-induced Antarctic GRACE mass gain estimates by roughly 2 percent and reduces the present-day uplift rate in Antarctica by about 5 percent. Like Paulson et al. (2005), they also studied the possibility of using 1-D Earth models to fit the RSL relaxation times and uplift rate predictions from 3-D Earth models in Eastern Canada and Antarctica. They concluded that the effects of lateral heterogeneity in Antarctica on present-day uplift rate can be significant and that can complicate the interpretation of ice-mass balance derived from satellite gravimetry, because GIA has significant contribution to GRACE signal, it must be removed to reveal ice-mass balance. Their finding is supported by the study of van der Wal et al. (2015).

Nield et al. (2018) focused on the impact of lateral variations in lithospheric thickness on GIA in West Antarctica because a spatially variable lithospheric thickness and the viscosity below could affect bedrock slope via uplift and thus the stability of marine based ice sheets there (Gomez et al., 2015, 2018). In addition, the difference in spatial gradient of uplift rate between 1-D and 3-D models often reflects the local thickness of the lithosphere. Nield et al. (2018) used two main approaches in estimating the lateral lithospheric thickness variation in the 3-D model. The first one is to infer the thickness of the elastic lithosphere from seismic studies. However, the thickness of this seismic lithosphere can be significantly thicker than the mechanically strong elastic lithosphere seen by the GIA process. The second one uses the microphysics approach and the temperature derived from seismic velocity anomalies is used to determine the effective viscosity of a certain mantle flow law (van der Wal et al., 2013). As illustrated in Fig. 6.6, any part of the shallow upper mantle with effective viscosity exceeding a critical value (e.g. 10^{24} Pa s) is considered as part of the elastic lithosphere. Due to the lack of GIA observations in Antarctica, no definite conclusion can be made, but Nield et al. (2018) prefer the second

approach, which when combined with the lateral variation in mantle viscosity below Antarctica (e.g. Kaufmann et al., 2005), could be useful for estimating ice-mass balance and ice sheet stability there.

As pointed out in Steffen et al. (2006) and Wang and Wu (2006a), the introduction of lateral heterogeneity inferred from seismic tomography with β=1, can sometimes help model predictions better fit the observed data, but can also overcorrect it. One reason is probably due to the erroneous assumption that seismic anomalies are induced by thermal effects alone (β=1). If seismic anomalies are partially caused by lateral changes in chemical compositional, water content, partial melting or non-isotropic prestress, then the lateral viscosity variations would have smaller contribution (β< 1) and that may help to fit the GIA data even better. Thus, by searching for the value of β which can give the best fit to GIA observations (e.g. RSL, uplift rate, tangential velocity and gravity-rate-of-change from GRACE) simultaneously, a constraint can be put on the thermal contribution of seismic anomalies in the mantle. However, there are several hurdles that need to be overcome before one can unambiguously constrain the role of thermal effects in the mantle. First, a good estimate of the background viscosity profile $\eta_o(r)$ is important for the study of lateral heterogeneities (Wang and Wu, 2006c). Second, the uncertainties of seismic tomography models (e.g. Milne et al., 2018), the uncertainties in the scaling parameters between $\frac{\delta v_S}{v_S}$ and $\Delta\eta(r,\theta,\phi)$ (Wu et al., 2013), and the uncertainties in ice thickness history can all affect the conclusion. In addition, the value of β should be able to vary from the upper mantle to the lower mantle and may even be different under different geologic provinces.

Nevertheless, Wang et al. (2008) did a feasibility study to understand the impact of varying the value of β on GIA predictions (e.g. RSL, uplift rate, tangential velocity and gravity-rate-of-change from GRACE). They used the GIA model of Wang and Wu (2006a,b,c), but included

material compressibility and assumed that the value of β is the same throughout the whole mantle. They found that the changes in GIA predictions due to variation of the value of β are large enough to be detected and constrained by the observations. They also found a tradeoff between the contributions from different layers of lateral viscosity variations in the mantle (UM1, UM2, LM1 and LM2) - however, the assumption of constant β value throughout the whole mantle limits further study of the tradeoff.

Wu et al. (2013) included the effects of anelasticity in the scaling law in addition to the effect of material compressibility and extended the study of Wang et al. (2008) by allowing the value of β in the upper mantle (β_{UM}) and lower mantle (β_{LM}) to be different. They searched the (β_{UM}, β_{LM}) parameter space for the Earth model that can best fit the three types of GIA observations simultaneously with the χ-statistics and their confidence parameter Ψ as follows: The misfits between prediction and observation are quantified by

$$\chi = \sqrt{\frac{1}{N}\sum_{i=1}^{N}\left[\frac{\{o_i - p_i(m_j)\}}{\Delta o_i}\right]^2} \quad , \tag{89}$$

where N is the number of data, o_i is the i-th observation with uncertainty Δo_i, and $p_i(m_j)$ are the i-th prediction for model m_j. Suppose model m_b gives the minimum value of $\chi$and is thus the best fitting model, then the confidence parameter:

$$\Psi = \sqrt{\frac{1}{N}\sum_{i=1}^{N}\left[\frac{\{p_i(m_b) - p_i(m_j)\}}{\Delta o_i}\right]^2} \le 1 \tag{90}$$

can be computed to bracket all the Earth models in (β_{UM}, β_{LM}) parameter space that can give similar fit (e.g. within 2σ uncertainty) to the observations like model m_b. Their results are summarized in Figs. 7.15 and 7.16.

Inspection of Fig. 7.15a, shows that the Earth model that can best fit 127 global RSL sites with long time record length has (β_{UM}, β_{LM}) ~(0.3,0.0). Since the contour lines for $\Psi \le 0.5$ and $\Psi \le 1$are nearly vertical, it means that the global data cannot resolve the value of β_{LM}. The reason is because the sensitivity of RSL data in the lower mantle is generally small except around the Hudson Bay area (see Fig. 7.6b,d,f and h). In view of this, only the RSL data in the Hudson Bay area are used in Fig. 7.15b, where the best fitting model has (β_{UM}, β_{LM}) ~(0.65,0.7). But all the models in the (β_{UM}, β_{LM}) parameter space give similar misfit to this best model to within 1σ uncertainty (see area with $\Psi \le 1$. Thus, RSL data alone is not able to resolve the thermal effect very well.

In Fig. 7.16a and b, the present-day peak uplift rate and the g-dot values of GRACE in the GIA centers of Laurentia and Fennoscandia are used to constrain the best fitting model. The contribution of recent melting and hydrology on g-dot has been removed using observational data directly (Wang et al., 2013, 2015) – this avoids the uncertainty in using g-dot from GIA models. It is found that the best solution has $\beta_{UM} \sim 0.65$, and β_{LM} is between 0.8 and 0.9. Comparing with the values found for RSL data in Hudson Bay (Fig. 7.15b), the values of $\beta_{UM}$are approximately the same and the values for β_{LM} are also close together. Also, the area of $\Psi \le 1$ in Fig. 7.16a and b, are also similar. Fig. 7.16c and d, show the results in Fennoscandia. There, the best solution also gives $\beta_{UM} \sim 0.65$, but the values of β_{LM} are close to zero. Again, the contour lines of $\Psi \le 0.5$ or $\Psi \le 1$ in Fig. 7.16a and b, are nearly vertical, meaning that the data cannot resolve the value of β_{LM}. Again, the reason is that the data in Fennoscandia has very low sensitivity in the lower mantle (see Fig. 7.5 and 7.6). Wu et al. (2013) also searched for the best solution in the lower mantle, i.e. $(\beta_{LM\,1}, \beta_{LM\,2})$ parameter space with β_{UM} fixed at 0.65. They found that the best solution has $\beta_{LM\,1}$ between 0.7 and 0.8, but the area for $\Psi \le 1$ is very large for

β_{LM2}. The reason is that even GIA data in the center of Laurentia cannot resolve the deep part of the lower mantle clearly. Thus, Wu et al. (2013) concluded that thermal effect on seismic anomalies increases from about 65 per cent in the upper mantle to about 75 percent in the shallow part of the lower mantle and can be up to 100 per cent in the deep lower mantle. However, the uncertainty increases from about 10 percent in the upper mantle to about 40 per cent in the shallow upper mantle, and is not well constrained at all in the deep lower mantle. Wu et al. (2013) demonstrated that the uncertainties in the scaling parameter including the background temperature do not strongly affect the estimated values of (β_{UM}, β_{LM1}, β_{LM2}). However, the effects of other model inputs were not studied. These model inputs include the ice model (given by ICE-4G), the background viscosity profile (given by a simplified version of VM2), and the seismic tomography model (given by model S20A of Ekstrom and Dziewonski, 1998). The effects of using different model inputs are demonstrated in Li et al. (2018) and Li and Wu (2019) – although their real aim was to search for the laterally heterogeneous structure under Laurentia and Fennoscandia that can best fit GIA observations such as global RSL data, uplift rate and g-dot in Laurentia and Fennoscandia.

Li et al. (2018) and Li and Wu (2019) improved on the GIA model of Wu et al. (2013) by including time-dependent coastlines and rotational feedback in the sea level computation. Other improvements include a finer spatial resolution finite-element grid (0.5^o x 0.5^o instead of 2^o x 2^o grid); a higher spatial resolution seismic tomography model (Bunge and Grand, 2000) instead of S20A; and an expanded RSL data set and updated GIA induced g-dot maps in Eastern Canada and Northern Europe. They fixed the ice input to be ICE-6G_C and used VM5a as the starting background viscosity model. After some fine tuning, Li et al. (2018) found that to give the best fit to the GIA data, the background viscosity in the upper mantle should be around 0.3×10^{21} Pa s

with $(\beta_{UM}, \beta_{LM}) \sim (0.05, 0.6)$. This value of background viscosity in the upper mantle is close to that in VM5b and also in Lau et al. (2016), but may also be a consequence of tuning with the ICE-6G model (see Steffen et al., 2006). The low value of β_{UM} found is contrary to the fact that lateral heterogeneity is strongest in the shallow upper mantle (see Fig. 6.5a) since there is good correlation between isotropic wave speed in the layer and near surface tectonics with thermal origin. Such low value of β_{UM} is probably due to the trade-off between the background viscosity and the value of β which can be understood as follows: Suppose $\eta_{ave}(UM\,1, \varnothing)$ is the actual averaged viscosity in the shallow upper mantle (UM1) under location $\varnothing$(e.g. Eastern Canada or Fennoscandia) that can result in the observed GIA values. From Section 6.5, it is known that $\log_{10}[\eta_{ave}(UM\,1, \varnothing)] = \log_{10}[\eta_o(UM\,1)] + \log_{10}[\Delta\eta(UM\,1, \varnothing)]$. Since Fig. 6.5a, shows that the viscosity perturbations in UM1 are positive under Eastern Canada and Fennoscandia, a small value of β_{UM} will result in a small $\Delta\eta(UM\,1, \varnothing)$ which may be smaller than the actual value $\eta_{ave}(UM\,1, \varnothing)$. However, this can be compensated by a larger background viscosity $\eta_o(UM\,1)$, so that the sum of the log terms gives the same value as $\log_{10}[\eta_{ave}(UM\,1, \varnothing)]$. On the other hand, a larger value of β_{UM} will need a smaller background viscosity $\eta_o(UM\,1)$ to achieve the same actual value.

Li and Wu (2019) tried to constrain sub-lithospheric properties (such as depth, thickness and viscosity), lateral lithospheric variations and asthenospheric properties using observed GIA data. They confirmed that the inclusion of lateral variation of sub-lithospheric and asthenospheric properties (see Fig. 7.19) can significantly improve the fit to observed RSL data, but their effects on uplift rate and g-dot are less significant. They also found a trade-off between the thickness of the elastic lithosphere and sub-lithospheric properties (viscosity or thickness). Their results prefer an elastic lithosphere that has a maximum thickness of 140 km under continental cratons

but reduces to about 60 km under the oceans. The preferred depth of the asthenospheric bottom is around 190-200 km with asthenospheric viscosity around 10^{20} Pa s. When these are combined with the best laterally heterogeneous mantle model in Li et al. (2018), the best fit to global RSL, peak uplift rate and g-dot data in Laurentia simultaneously is found.

7.3. Uncertainties of GIA predictions

Geodetic observations (e.g. tide-gauge and gravity-rate-of-change data) often contain signals not only from GIA, but also from other sources (e.g. related to recent climate change). In order to study the signal from the other sources, the contribution of the GIA signal must be removed. Due to the imperfect knowledge of GIA model inputs such as the ice history and mantle rheology, it is desirable to quantify the uncertainties of GIA predictions.

Love et al. (2016) studied the uncertainties of sea level changes along the Atlantic and Gulf coasts of North America by computing 12,705 GIA models that consist of different combinations of 35 different ice histories with 363 different 1D Earth models. Based on 28 RSL records, with the majority of their ages younger than 8 ka, optimal GIA models are found for three geographic subsets: (i) Canadian sites near the ice margin, (ii) US Atlantic coast and (iii) US Gulf coast. However, the ice models, lithospheric thickness, and upper and lower mantle viscosities in the optimal models of each geographic region are different. To find the uncertainty range, they used a nominally Bayesian approach and estimated one-sided bounds from these 1-D models by isolating models that bound the data from above and below. Four extra GIA models with 3-D Earth structure were also computed to explore the influence of lateral viscosity variations.

Caron et al. (2018), computed the uncertainties by varying the GIA model parameters: The ice history variations are obtained by scaling the different large ice sheet thickness histories with a different scaling parameter for each ice sheet. The Earth models used are laterally

homogeneous and there are three parameters for each 1-D Earth model: the thickness of the elastic lithosphere and the viscosities in the upper and lower mantle. However, instead of choosing the optimal model with the least misfit to the RSL and uplift rate data, Caron et al. (2018) chose the optimal model based on the expected value of these scaling parameters for the ice sheets and Earth parameters. As a consequence, some of the models included in the computation of GIA uncertainties may not fit all the observed RSL and uplift rate data well simultaneously. Also, as pointed out in Argus et al. (2021), the expected values of the ice and Earth model of Caron et al. (2018) do not produce the expected values of uplift rate on the Earth's surface.

Milne et al. (2018) computed the uncertainties of GIA predictions in Greenland by varying the inputs of 3D mantle viscosities derived from different seismic tomography models (with $\beta=1$) and lithospheric models with different lateral thickness variations. They found that the uncertainties of the seismic tomography models and lithospheric models can have significant influence on the GIA predictions in Greenland. On the other hand, Li et al. (2018) compared their results of using S20A (Ekstrom and Dziewonski, 1998) and Bunge and Grand's (2000) model, and found that the difference in seismic tomography model do not significantly affect their best solution (β_{UM}, β_{LM}) for RSL data in Laurentia and Fennoscandia. In Fig. 6.4, the average of four seismic tomography models is shown although the tomography models differ from those used in Milne et al. (2018). The 2σ uncertainties of the shear velocity anomalies in the four depth layers are shown in Fig. 7.17, which shows that the uncertainty is largest in UM1, and decreases with increasing depth. The 2σ uncertainties of $\log_{10}[\Delta\eta(r,\theta,\phi)]$ in the four layers of the Mean Seismic Tomography model are shown in Fig. 7.18. Just like in Fig. 6.5, the largest uncertainties are found in UM1 and UM2. If $\beta=1$, then the uncertainty of $\log_{10}[\Delta\eta(r,\theta,\phi)]$

under Eastern Canada can range from 0.4 to 1.6 in UM1, 0 to 1.8 in UM2 and 0 to 0.8 in LM1 and LM2, respectively. Under Fennoscandia, the range of the uncertainties are slightly smaller. If β<1, then the uncertainties would also be smaller. Thus, future improvement of seismic tomography models and a good handle on the value of β will help to reduce the uncertainties of lateral viscosity perturbations in 3D GIA models.

Vestøl et al. (2019) developed NKG2016LU, a new land uplift model for Fennoscandia and the Baltic Region. In the uplift model, the geodetic empirical model is combined with a GIA model to give a semi-empirical model. The geodetic approach uses observed precise leveling and GNSS data from the BIFROST project to compute the empirical model using the Least Square Collocation method. The uncertainty of the empirical model is determined by using linear propagation of errors. The GIA model tested more than 11,000 ice and 1-D Earth model combinations and the selected model is able to give the best overall fit to the GNSS and RSL data in northern Europe. The uncertainty grid of the optimal GIA model (see Fig. 7.19) reflects our limited knowledge of the input (ice and Earth) model parameters together with other types of error, which can be due to limitations in the assumed rheology, 1-D model, non-GIA effects (e.g. tectonic motion in fitting the observed data). The combined semi-empirical model is created in a remove-interpolate-restore approach. The combined uncertainty of the uplift model can also be obtained from the standard propagation of the uncertainty grid using the two-step procedure, but a new one-step method is preferred from the statistical point of view.

Melini and Spada (2019) divide the GIA uncertainty into two types, type 1 (T1) uncertainty associated with limited knowledge of input model parameters (e.g. ice and Earth model – the latter includes the background viscosity profile, the seismic tomography model, the scaling parameters and the value of β), and type 2 (T2) uncertainty associated with structural differences

in GIA models (e.g. methodological differences). They found that the two types of uncertainty are of significant amplitude and of comparable importance.

Li et al. (2020) subdivided the T1 classification of Melini and Spada (2019) into T1A, T1B and T1C uncertainties by requiring the models included to be able to fit the observational RSL, g-dot and u-dot data reasonably well simultaneously. In T1A uncertainties, the ice model is assumed to be fixed, but Earth model parameters (including 3D structures) can be varied. In T1B uncertainties, the Earth model is fixed, but the variations in ice thickness history is studied. For T1C uncertainties, both ice and Earth rheology variations are included.

Li et al. (2020) studied T1A type uncertainties in North America using ICE-6G_C in combination with a whole variety of 3D Earth structures. These include 250 models with different combinations of elastic lithospheres, sub-lithospheric and asthenospheric properties. The elastic lithosphere can be either uniformly thick or have thick continental lithosphere under the old craton that changes gradually to thin oceanic lithosphere (see Fig. 7.20). The range of thicknesses considered is summarized in Table 3. Beneath the elastic lithosphere is a uniformly thick sub-lithosphere, and below that lies the asthenosphere, whose thickness changes laterally. The range of values considered for the thickness, depth and viscosity for the sub-lithosphere and asthenosphere are summarized in Table 3. Below the asthenosphere is the laterally heterogeneous mantle with different (β_{UM}, β_{LM}) combinations. From these 250 different combinations of lithosphere, sub-lithosphere, asthenosphere and mantle viscosity models, they found 10 models that give the best fit to the observed RSL, g-dot and uplift rate data, and from them the mean prediction and the 2σ uncertainties are obtained. The results for RSL, present-day uplift rate and g-dot are shown in Figs. 7.21 to 7.23. Li et al. (2020) have also compared the mean and 2σ uncertainties from the best 5 or 20 models, and found that the mean prediction does

not change significantly. For the uncertainties, the differences between 5 and 10 models are almost the same, but the uncertainties for 20 models are slightly larger because the 10 added models cannot fit the GIA data as well as the original 10. Just as Li et al (2020) has investigated the extent to which lateral heterogemeit of viscosity may be accommodated beneath Laurentia, finding it to be modest and not required by the data,, in Li et al (2022) the authors investifated the extent to which large misfits of the Toronto spherically symmetric models to local White Sea RSL data could be eliminated by lateral heterogeneity. Although this proved to be possible, the necessity of this was essentially eliminated by a modest adjustment to the regional ice loading history which had been unconstrained in the Toronto models.

Inspection of the left panel of Fig. 7.21, reveals that the mean of the 10 best fitting GIA models from Li et al (2020) shows two peaks in western and eastern Hudson Bay whose amplitudes decrease from the Last Glacial Maximum to the present. These are the expected results of ICE-6G_C. The 2σ uncertainties of RSL predictions at 15 ka BP show larger uncertainties west and east of Hudson Bay and near the previous ice margins along the northern Atlantic and Pacific coasts. From 15 to 11 ka BP, the amplitudes of the uncertainties generally decrease with time except for those of the peaks west of Hudson Bay and in the north Pacific coast which increases due to the rapid melting related to the Meltwater Pulses 1A and 1B in the ICE-6G_C reconstruction (see Supplementary Material in Li et al., 2020 for more details). From about 8 ka BP to the present, the amplitudes of the uncertainties further decrease and merge into one broad peak that stretches from southwest Hudson Bay to Saskatchewan. In addition, there are peaks around the LGM ice margin along the coasts and on land. These changes in the spatial distribution of the 2σ uncertainties of RSL predictions are mostly controlled by the 3D viscosity structures in the upper and lower mantle (see Fig. 7.6g and h).

Fig. 7.22, compares the mean RSL predictions of the 10 best-fitting models (purple curves) with the predictions of the best fitting Earth model (green curves) and the RSL data at six sites in North America. This best fitting model has laterally heterogeneous mantle with upper mantle background viscosity of $3\text{x}10^{20}$ Pa s, $\beta_{UM}=0.05$ and β_{LM} =0.6 under a 20 km thick sub-lithosphere with viscosity 10^{22} Pa s below a uniformly thick 110 km elastic lithosphere. Notice that predicted RSL from the mean with 3σ uncertainties and the best fitting model fit most of the RSL data. Also, the RSL uncertainties are small compared with the much larger RSL magnitudes in the near field (e.g. sites 1, 4 and 5 in Fig. 7.22) and also in the intermediate field of the Laurentide ice margin at LGM (e.g. sites 20 and 24 in Fig. 7.22). The largest RSL uncertainties are found in sites close to the ice margin (e.g. site 16 in Fig. 7.22).

Fig. 7.23, shows that the mean of the uplift-rate and g-dot predictions of the 10 best-fitting models have peaks west and east of Hudson Bay just like that in Fig. 7.21e. In particular most predicted uplift-rates at GNSS stations fit within the 2σ uncertainties of the observed data. The 2 σ uncertainties of uplift-rate and g-dot show similar patterns and are broadly similar to Fig. 7.21f. When these results are compared with those of Caron et al. (2018), one can see that the patterns of the 2σ uncertainties are different and the amplitudes in Li et al. (2020) are smaller. One reason for their difference is due to the fact that Caron et al. (2018) used 1D Earth models, while Li et al. (2020) used 3D Earth models. Another reason is that the models of Li et al. (2020) can simultaneously fit the RSL histories and observed present-day uplift rate and g-dot data, while this may not be the case in Caron et al. (2018).

When Li et al. (2020) compared their uncertainties with the estimate from 20% of the mean signal rule, they found that this 20% rule overestimates the uncertainties in western and eastern

Hudson Bay, but underestimate the uncertainties near the ice margins, especially in southwestern Hudson Bay, where the largest g-dot uncertainties exist (see Fig. 7.23d).

Currently, there are four ways to estimate GIA uncertainties (Simon and Riva, 2020). The first one is parameter variation, which is used in Milne et al. (2018), Caron et al. (2018) and Li et al. (2020). The second one is the ±20% GIA mean signal rule, which Li et al. (2020) found to be too simplistic and unrealistic. The other two ways are residual analysis and the semi-empirical method. Simon and Riva (2020) noted that analyzing residuals between predictions and the constraining data is not a true measure of uncertainty since only one model result is considered. The semi-empirical method uses the inversion of constraining data sets to obtain the formal measure of GIA uncertainty (Riva et al., 2009; Hill et al., 2010; Sasgen et al., 2012; Simon et al., 2017) – and the advantage of this method is that it should be completely free of uncertainties of the forward models. However, the constraining data sets may contain signals from sources other than GIA (e.g. from recent climate change), and the semi-empirical method works well only if the non-GIA signals in the constraining data are completely removed. However, the reason why there are interests in estimating GIA uncertainties is to remove the GIA signal from the data, so that the signal from the other sources can be studied. So, any inability to separate GIA and other contributions to the observed data become the shortcoming of the semi-empirical method. For the method of parameter variation, the effects of non-GIA signals in the constraining data may also lead to unreliable results. So, perhaps a combination of iterative use of the semi-empirical method with "cleaned" data and the method of parameter variation and using variations of 3D Earth models and variations of ice model combinations that can fit the "cleaned" GIA observations will be employed in future estimation of GIA uncertainties. The uncertainties of Li et al. (2020) are realistic in that they require models to fit all the data in North America, the

relative sea level data, the GPS vertical displacement data, and the GRACE gravity data, but the uncertainties of Caron et al. (2018) are unrealistic in that the optimal parameter values predict GPS vertical displacement and GRACE gravity rates that do not fit the data.

7.4. GIA induced Viscous Heating and Volcanism

GIA induces viscous flow in the mantle, and the heat dissipation due to frictional interaction between neighboring viscous elements is called "viscous heating". Such heating can potentially change the temperature and thus material properties of mantle rocks (e.g. seismic velocity and viscosity). There is speculation that glacial cycle induced heating could be large enough to (i) trigger volcanism during the Quaternary (e.g. Nakada and Yokose, 1992), (ii) affect seismic velocities and the interpretation of seismic tomography, (iii) affect mantle viscosity which determines the rate and style of Earth dynamics including GIA and mantle convection (e.g. Balachandar et al., 1995), and (iv) cause transient heat flux at the Earth's surface that can affect the stability of ice sheets by basal heating (e.g. Pattyn, 2010) and thus paleoclimate. In addition, if viscous heating leads to a decrease in mantle viscosity near the surface, then this could lead to faster GIA induced land uplift and that may help to stabilize marine ice sheets (Gomez et al., 2015).

The rate of viscous dissipation for shear deformation H (hereafter called "viscous heating") can be computed from the deviatoric stress σ_D and the deviatoric strain rate $\dot{\epsilon}_D$:

$$H = \sigma_D : \dot{\epsilon}_D = \frac{\sigma_D : \sigma_D}{(2\eta_{eff})}. \quad (91)$$

This shows that low effective viscosity η_{eff} results in high viscous heating. This can also be expressed as: $H = 2\eta_{eff}\dot{\epsilon}_D : \dot{\epsilon}_D$, which shows that viscous heating should increase with larger effective viscosity provided that the deviatoric strain rate $\dot{\epsilon}_D$ is nearly constant. However, for

the GIA process, $\dot{\epsilon}_D$, varies significantly in both space and time with $\dot{\epsilon}_D : \dot{\epsilon}_D = \left(\frac{\sigma_D}{\eta_{eff}}\right)^2$, thus Eq. (91) is used instead. For the interpretation of results, it is useful to normalize the computed viscous heating by the chondritic magnitude of radiogenic heating of 3×10^{-9} W/m^3 (Leitch and Yuen, 1989), just as in the study of viscous dissipation in mantle convection (Balachandar et al., 1995).

To study the effects of viscous heating, Hanyk et al. (2005) considered axisymmetric parabolic ice loads with simple glacial histories on a spherical Earth with linear rheology. They found that the magnitude of viscous heating can generate observable transient heat flux on the surface of the Earth especially if a low viscosity zone is found below the ice margin. They also suggested that some degree of volcanism can be generated if the deglacial period is short and speculated that higher values of viscous heating can be generated if mantle rheology is non-linear.

Huang et al. (2018) followed the suggestion of Hanyk et al. (2005) and studied the effects of linear, nonlinear and composite rheologies on viscous heating. But they also improved on Hanyk's work by (i) using a realistic ice history model (ICE-6G_C) together with realistic, self-gravitating oceans, and (ii) estimating the effects of viscous heating on temperature changes inside the Earth, in addition to changes in surface heat flux. In what follows, we summarize their findings:

Huang et al. (2018) first studied uniform mantle models with linear, nonlinear and composite rheologies, and explored the effects of various values and combinations of (η, A^*) on viscous heating. The range of values of η studied was from 3×10^{20} to 3×10^{22} Pa s and the range of A^* is from 1.11×10^{-36} to 1.11×10^{-33} Pa^{-3} s^{-1}. They found that for uniform mantle, viscous

heating is largest (with normalized value of 11.64) when the combination η = 3x10^{20} Pa s with A^* =1.11x10^{-36} Pa^{-3} s^{-1} is used for composite rheology. This value of 11.64 can also be achieved for linear rheology when η = 3x10^{20} Pa s. They also found that compressibility increases viscous heating for linear rheology but only slightly for nonlinear or composite rheology. Huang et al. (2018) also studied stratified Earth models like VM5a (Peltier et al., 2015) and its variations with an ultra-low viscosity zone (η= 3x10^{18} Pa s) of different thickness (40 or 100 km) below the lithosphere; and also models similar to VM5a but having an ultra-low viscosity layer with nonlinear or composite rheology. For all the Earth models that they considered, the one that can produce the largest viscous heating of 118.81 is model M5, which is basically VM5a with a 100 km thick "ultra-low viscosity" layer with composite rheology (where $\eta = 3\,x10^{18}$ Pa s and A^* =1.11x10^{-36} Pa^{-3} s^{-1}) below the lithosphere.

The inclusion of a realistic ice model (ICE-6G_C) is important since it eliminates unreasonably fast or slow deglaciation histories. Together with realistic oceans, the interaction among ice sheets and ocean loads affects the spatial distribution of viscous heating. This is illustrated in Fig. 7.24 where normalized viscous heating for model M5 is shown at 13 ka BP, the time when viscous heating reaches its peak magnitude (see Figs. 7.25 and 7.26). Fig. 7.24 shows that viscous dissipation is generally important around the past ice margins, also it peaks between the past ice margins of Laurentia and the Cordilleran ice sheet in North America. The reason is that these ice sheets differ both in their horizontal scale and ice thickness, so the differential motions interfere constructively to give large shear stresses. Similarly, a smaller local peak is found between the past ice margins of Fennoscandia and the Barents Sea. On the other hand, there is very low viscous heating between the northeast coast of Canada and Greenland, and that is due to the destructive interference between ice and water loading there. The spatial distribution

of the normalized viscous heating for other Earth models show similar patterns, although the magnitudes of viscous heating are different.

Fig. 7.26 shows how viscous heating varies with time from 15, 13 and 10 ka BP below Laurentia and Fennoscandia for model M5. Note that for both regions, viscous heating is concentrated within the "ultra-low viscosity" composite layer of the Earth model and peaks around 150 km depth, but the magnitude under Laurentia is larger than that in Fennoscandia. In contrast, for the VM5a model, viscous heating is concentrated above 1300 km depth and peaks near 660 km depth (see Fig. 4 in Huang et al., 2018). Moreover, the peak viscous heating in VM5a is just below 20, and so is only about 15% of the peak value in model M5.

Huang et al. (2018) also estimated the upper bound of both the change in heat flux and temperature change due to viscous heating. They found that the change in heat flux due to viscous heating is observable and significant when compared to the mean continental heat flux of 65 mWm^{-2} (Jaupart and Mareschal, 2007). This confirms the finding of Hanyk et al. (2005). However, since the period of high heating is relatively short (see Figs. 7.25), the upper bound of temperature change due to viscous heating is of the order of 0.01 K. Even if there were 30 consecutive glacial cycles, the cumulated temperature change could only be about 0.3 K. Thus, the temperature change due to viscous heating is too small to induce widespread melting or volcanism or to affect mantle rock properties or ice sheet stability. This implies that the effect of viscous heating can be neglected in future models of the GIA process.

However, this conclusion does not imply that glacial cycles could not have triggered volcanism during the Quaternary, as other mechanisms, such as decompression (Jull and McKenzie, 1996; Slater et al., 1998) can explain the high lava production rate in Iceland and

Greenland, following deglaciation (Sigvaldason et al., 1992; Nakada and Yokose, 1992; Huyber and Langmuir, 2009, Uenzelmann-Neben et al., 2012).

7.5. GIA induced Earthquakes and Fault Stability

In the last 30 years or so, there has been much interest in the relation between GIA induced stress, the reactivation of Glacially Triggered Faults (GTF), and the generation of Earthquakes, which can also affect ice sheet stability. As we shall see below, glacial retreat can induce Earthquakes near the ice margin, and the ground shaking motion there can increase ice sheet calving and even reduce the basal coupling between the ice sheet and the ground. The geological evidence of GTFs and the modeling of their reactivation were reviewed in a recent book "Glacially-Triggered Faulting" (Eds. Steffen et al., 2021). Earlier reviews of modeling work to understand fault stability and GIA induced Earthquake can be found in Wu (1998c), Steffen and Wu (2011), Wu et al. (2021) and Steffen et al. (2021). In this subsection, we will briefly review the physics of Glacially-Triggered Faulting and discuss some recent modeling results.

From studies of rock mechanics, it is well known that the stress level required to rupture an intact rock in the crust is above 50 MPa and typically of the order of 100 MPa (Johnson and DeGraff, 1988). Since GIA induced stress levels are typically around 20-35 MPa, this is not high enough to create a new fault in intact rocks of the crust. But, if a pre-existing fault has already been created by earlier tectonic or other geological processes, then GIA can easily reactivate it since that only takes a few kPa if the fault is critically stressed (King et al., 1994). A fault is critically stressed if it is close to but not at failure when a fault can slip and Earthquakes can be generated. If the fault is critically stressed before the onset of glaciation, then the background stresses (e.g. tectonic and overburden stresses) must be able to keep it critically stressed. Thus,

both GIA induced stress and background stress, which defines the background stress regime, are important for the triggering of GTFs.

Early studies of GTF assumed that faults are reactivated by the "maximum stress difference" (e.g. Walcott, 1970; Spada et al., 1991), or the "maximum flexural stress" (e.g. Stein et al., 1979) or the strain-rate (e.g. James and Bent, 1994; Hetzel and Hampel, 2005). Actually, the stability of faults and their reactivation should be assessed by the Mohr-Coulomb Failure theory, which we shall briefly summarize below:

Consider a fault plane in the crust, the state of stress that acts on that fault at a fixed time can be represented by the normal stress σ_n and the shear stress τ, that act on the fault with fault orientation θ, which is the angle between the normal of the fault plane and the maximum principal stress direction. When one plots $\sigma_n$vs τ for different values of θ on the Mohr diagram then one gets the Mohr circle (see Fig. 7.27). If the maximum, intermediate and minimum (compressive) principal stresses are represented by $\sigma_1, \sigma_2, \sigma_3$ respectively, then the center of the Mohr circle is at $(\sigma_1+\sigma_3)/2$ and the radius of the Mohr circle is $(\sigma_1-\sigma_3)/2$. In other words, the left and right side of the Mohr circle are at $\sigma_n=\sigma_3$ and $\sigma_n=\sigma_1$ respectively (see Fig. 7.27).

Now, the normal stress pushes the fault surfaces together making the fault more difficult to slip, but the shear stress acts parallel to the fault plane and thus promotes fault slip. Therefore, the criteria for fault slip, or the failure envelope, is a relation between the shear stress τ and the normal stress σ_n. For upper crustal depth, the failure envelope can be approximated by the line of failure: $\tau=\tau_o+\mu\sigma_n$, where μ is the coefficient of friction and τ_o is the cohesive strength. From rock mechanics, μ has a value between 0.4 and 0.8 (Byerlee, 1978) and τ_o is generally assumed to be small and negligible for critically stressed pre-existing faults.

According to the Coulomb-Mohr failure theory, if the Mohr circle touches the failure envelope, then the fault becomes unstable and slip motion can occur along the fault which can in turn result in Earthquakes (see Fig. 7.28a). If the Mohr circle is not in contact with the failure envelope but lies below it (see Fig. 7.28b), then there is fault stability. The shortest perpendicular distance from the line of failure to the Mohr circle is defined as the Fault Stability Margin (FSM), which is related to the principal compressive stresses by (Johnston, 1987):

$$FSM = \frac{\sin\left[\tan^{-1}(\mu)\right]}{2\mu}\left[\mu(\sigma_1+\sigma_3)+2\tau_o\right]-\frac{1}{2}(\sigma_1-\sigma_3). \quad (92)$$

If the Mohr circle is very close to the failure envelope, but there is no contact, then the fault is critically stressed.

In the discussion of the Mohr diagram, the state of stress has contributions from GIA, tectonics, overburden and pore fluid pressure. During a glacial cycle, the changing weight of the ice/water load affects the vertical stress immediately (in time). On the other hand, the application (or removal) of the surface load causes the elastic lithosphere to bend (or unbend), but the effect is not immediate because any change in lithospheric flexure involves the flow of mantle rocks beneath the lithosphere and since mantle viscosity is high, the bending stress, which is tangential to the Earth's surface, takes thousands of years to respond to the changing surface load. But the time scale for the bending stress to change is still rapid compared to that for the tectonic stress and overburden pressure (by erosion or sedimentation) to change. On the other hand, pore fluid pressure fluctuates much more rapidly, can be affected by the glacial cycle and can affect the frictional properties of the faults. But fluctuations of pore fluid pressure are not well known and so their effects are generally neglected in preliminary studies.

In any case, the evolution of the state of the total stress at the fault location during a glacial cycle changes the position and radius of the Mohr circle, causing the FSM to change in time (see

Fig. 7.28). Wu and Hasegawa (1996a,b) defined this change to be $dFSM(t) = FSM(t) - FSM(t_o)$, where t_o is the time before the onset of glaciation and t is any time during or after the glacial cycle. Note that the dependence of $dFSM$ on location is suppressed in this equation. Also, if the fault is critically stressed at t_o, then $FSM(t_o)$ is very close to zero. Positive values of dFSM means that the Mohr circle moves away from the failure envelope and the fault is stabilized. On the other hand, negative values of dFSM means that the Mohr circle moves towards the failure envelope and the fault instability is promoted – whether the fault slip or not depends on the value of dFSM relative to the initial value of $FSM(t_o)$ and the orientation of the fault plane θ (see Fig. 2c in Wu, 1998a). In the literature, FSM is sometimes replaced by the Coulomb Failure Stress (CFS), which is just the vertical distance between the failure envelope and any point on the Mohr circle (e.g. Lund, 2005; Lund et al., 2009; Steffen, et al. 2021). But unlike dFSM, $dCFS$ is defined so that negative values imply increasing fault stability and positive values imply decreasing stability. But either choice of $dFSM$ or $dCFS$ do not affect the discussion below as long as the difference in sign is taken into account.

Wu and Hasegawa (1996a,b) described how the GIA model can be used to study fault stability using the FE method for 3D flat-Earths that can allow the inclusion of lateral heterogeneity (Wu and Mazzotti, 2007) or power-law rheology (Wu, 2002d). A recent review of the methodology is given in Wu et al. (2021). The 1-D results are validated using the spectral method for a spherical, compressible, self-gravitating, Maxwell Earth (Johnston et al., 1998; Wu and Johnston, 1998). Basically, it starts with a regular GIA model but the output also contains the time evolution of the GIA stresses induced by the changing surface ice and water loads. The GIA induced stresses near the surface (which includes the vertical and horizontal bending stresses in the lithosphere) are then superposed onto the given background tectonic stress and

overburden to give the "total stress" and its evolution, from which we can compute the temporal change of dFSM at any given spatial location. Since glacial induced stresses change much faster than tectonic stress and overburden pressure, the latter two are treated as time independent within the glacial cycle. Another useful simplification is to assume that the faults under consideration are "virtual faults" – meaning that the free fault surface does not affect the stress distribution. This allows the prediction of the onset timing of fault reactivation, but prevents the modeling of the evolution of fault slips. Recently, the FE method has been modified to include the effects of a physical fault surface and thus the amount of fault slip and the slip history can now be predicted (Steffen et al., 2014a,b,c, 2015). The new methodology by Steffen et al. (2014a) is more realistic than the model of Hetzel and Hampel (2005), which incorrectly predicts continuous fault slip over thousands of years (even before glaciation and long after the deglaciation event ended) and neglects the stress migration from the mantle to the lithosphere (see Steffen et al., 2015 for details).

Fig. 7.28 illustrates the physics of fault reactivation for a critically stressed fault, located within the ice margin of Laurentia. The background stresses here are due to ridge-push at the mid-Atlantic ridge (Richardson et al., 1997) thus the background stress regime is thrust. This means that the maximum and intermediate principal background stresses σ_1^{BG} and σ_2^{BG} are nearly horizontal (in the x and y directions respectively) but the minimum principal background stress σ_3^{BG} is nearly vertical (in the z-direction). Here the superscript BG stands for the "background stress Before Glaciation". The stress field before the onset of glaciation is shown in Fig. 7.28a with the Mohr diagram shown on the right. Note that the left side of the Mohr circle is at the minimum principal stress σ_3^{BG} while the right side of the circle is at the maximum principal stress

σ_1^{BG}. Since the fault is critically stressed, the Mohr circle is shown to be close to but not touching the line of failure.

During the glacial or deglacial phase with ice load on the Earth's surface, the vertical stress becomes $\sigma_3^{DG}=\sigma_3^{BG}+\sigma_z^{GIA}$,where the superscript "DG" stands for "during glaciation or deglacial" and σ_z^{GIA} is due to the weight of the ice load. The maximum horizontal principal stress becomes $\sigma_1^{DG}=\sigma_1^{BG}+\sigma_x^{GIA}$, where σ_x^{GIA} is the bending stress induced by the flexure of the lithosphere. For large ice sheets, the magnitude of the bending stress is comparable to the weight of the ice load and the Mohr circle is mainly shifted away from the line of failure and the change in the radius of the Mohr circle is small compared to the shift (see Fig. 7.28b). As a consequence, the fault becomes stabilized in the presence of glacial ice load (Johnston, 1987). This result is valid for ice sheets with size comparable to or larger than the Fennoscandian ice sheet. For smaller ice sheets there is horizontal stress amplification – meaning that the horizontal GIA induced bending stress becomes much larger than the vertically GIA induced stress. For example, for the ice load over Great Britain, the induced horizontal stress can be as large as six times the vertical stress. When there is horizontal stress amplification, the radius of the Mohr circle in Fig. 7.28b becomes so large that fault instability can occur even in the presence of the glacial ice load (Johnston et al.,1998, Wu et al., 1999).

During the deglacial phase, σ_z^{GIA}decreases with the same rate as the weight of the ice load, so that the vertical stress moves back towards σ_3^{BG}, and after the end of deglaciation ("AG") becomes $\sigma_3^{AG}=\sigma_3^{BG}$. But the horizontal bending stress σ_x^{GIA}decreases much more slowly due to viscous flow of mantle rocks below the lithosphere. At the end of deglaciation, the right side of the Mohr circle is at σ_1^{AG} which has value much greater than the initial value σ_1^{BG} while the left side of the Mohr circle is at σ_3^{BG}. As a result, the radius of the Mohr circle increases so much that

it can touch the line of failure at the end of deglaciation. This means that fault instability is promoted at the end of deglaciation (Wu and Hasegawa, 1996a,b). If the fault slips, then some of the stress will be released and this may stabilize the fault momentarily until GIA induced stress brings it back towards instability (see Fig. 7.30 and discussion below). This predicted timing of fault instability is found to be in agreement with the observed timing of GTFs inside Laurentia and Fennoscandia. For a retreating ice front, fault instability means that Earthquakes can be triggered soon after the ice load above the fault is removed. As time progresses after the end of deglaciation, the Mohr circle moves back towards its position before the initiation of the glacial cycle, until another glacial cycle starts again.

Using the Mohr-Coulomb theory as above, Steffen et al. (2021) investigated $dFSM(t)$ inside and outside the Fennoscandian ice margin and also for thrust, normal and strike-slip background stress regimes. They found that for normal or strike-slip background-stress regimes, fault stability is always promoted beneath the ice sheets (see Table 4). In contrast, only thrust regimes can trigger fault instability within the ice margin at the end of deglaciation. If the background-stress regime is normal or strike-slip, then fault instability can be promoted during the glacial and deglacial phase for faults just outside the ice margin, but as soon as deglaciation ends, then fault stability is promoted just outside the ice margin. For faults near the peripheral bulge, which is much farther away from the ice margin, the situation during the glacial and deglacial phase is like that just outside the ice margin, however after the end of deglaciation, fault stability is promoted for thrust background stress regime, but instability for normal or strike-slip background stress regimes.

Fig. 7.29 shows how the predicted $dFSM(t)$ near Lac Témiscouata (about 300 km northeast of Quebec City) evolves with time for five different viscosity models. Model RF22 (blue dashed

curve) is the reference model with linear mantle rheology and has viscosity of 10^{21} Pa s uniform mantle below a 125 km thick lithosphere. The model represented by the red dashed curve is similar to RF22 but is laterally heterogeneous, with a 200 km thick lithosphere underneath the craton that thins to 100 km thick with a low 10^{20} Pa s asthenosphere below the continental margin. The model represented by the green dashed curve is like model RF22 but has a 10^{19} Pa s ductile zone within the elastic lithosphere. The solid cyan line represents the model which is like RF22, but is laterally heterogeneous with a vertical ductile layer that goes from 20 km depth to the bottom of the lithosphere along the St. Lawrence valley. The model represented by the magenta curve is like RF22 but has a nonlinear lower mantle with n=3 and $A^*=3x10^{-36}$ Pa^{-3} s^{-1}. Fig. 7.29 shows that from 18 to about 9 ka BP, the *dFSM* curves for all the different Earth models are positive, meaning that fault stability is predicted, but their values decrease with time due to the thinning and retreat of the Laurentide ice sheet. Then, at the end of deglaciation around 9 ka BP, all the models predict a change to negative values of *dFSM*, implying that fault instability was promoted. Such prediction is consistent with the sediment record in Lac Témiscouata which indicates liquefaction or/and slumping induced by paleo-Earthquake at the time (Shilts et al., 1992).

Just like Lac Témiscouata, the onset timing of paleo-Earthquakes at other sites that lie within the ice margin of the Laurentide or Fennoscandian ice sheet are determined by the local deglaciation history as explained in Fig. 7.28 (Wu and Hasegawa, 1996b; Wu, 1997, 1998c; Wu et al., 1999). For paleo-Earthquakes that lie outside the Laurentide ice margin (e.g. Wabash Valley in Indiana and New Madrid in Missouri), Wu and Johnston (2000) found that their observed onset timing is also consistent with that predicted by the evolution of GIA induced stress. However, the magnitude of *dFSM* decays rapidly from the ice margin, so they may not be

large enough to trigger the M8 Earthquake near New Madrid in 1811, but it may be able to act as a switch that released other stresses stored up in the New Madrid Fault.

The next example is from a site along the Osning Thrust which lies just outside the Fennoscandian ice margin at the Last Glacial Maximum in north central Europe (Brandes et al., 2015, 2018). Here, beside the historical earthquake in 1612, a paleo-Earthquake also occurred around 11.5 ka BP with magnitude greater than 5.5, implying a fault slip of around 1 meter. This is summarized in Fig. 7.30. The predicted *dFSM* from the GIA model is shown by the red curve. From about 20 to 11.5 ka BP, the value of *dFSM* is positive meaning that there is fault stability. But due to the retreat of the Fennoscandian ice sheet, it became zero around 11.5 ka BP, and matches the observed onset time of the paleo-earthquake. If the fault slipped with magnitude around 1 m at 11.5 ka BP, then the stress release brought the fault back to stability as shown by the red curve. However, subsequent decay of *dFSM* brought it back to instability around the time of the historic Earthquake around 1612. The dotted lines indicate how the magnitude of the fault slip affects the timing of the second historic seismic event. If the slip magnitude is much smaller than 1 m, then the second event is predicted to occur much earlier, e.g. around 8 ka BP instead of 1612. On the other hand, if the fault slip is much greater than 1 m, then the second event would not have occurred.

The examples above are taken from areas around the ice sheets in Laurentia and Fennoscandia, both of them have deglaciated more than 8 ka ago. Kaufmann et al. (2005) studied the temporal-spatial variation of *dFSM* in Antarctica with and without the effect of lateral heterogeneity. They found that the large present-day ice cover there could suppress seismicity while fault instability can be promoted offshore – for example in Balleny Island (Henry et al., 2000). Steffen et al. (2020) also suggested that early Holocene Greenland ice-mass loss likely

triggered a large magnitude Earthquake or a series of smaller magnitude Earthquakes around 10,600 years ago offshore south-western Greenland. The causal relation between glacial melting and fault instability is also supported by recent seismic activities following rapid glacier melting in southern Alaska (Sauber and Molnia, 2004; Sauber and Ruppert, 2008; Johnson et al., 2020).

It has also been suggested that the Earthquakes induced by ice melting near the Laurentian ice margin in northeast Canada could have induced ice-rafting episodes and the deposition of North Atlantic sediments called Heinrich events (Hunt and Malin, 1998). However, Bassis et al. (2017) suggested Henrich events are driven by warm subsurface water near the calving edge, i.e. the "marine ice cliff instability", and the GIA of the bed.

Part III. A Brief Summary and Discussion of Future Directions

Section 8. Summary and Prospects

In part I of this paper a reasonably complete review was provided of the spherically symmetric Maxwell viscoelastic model of the glacial isostatic adjustment process. This theory is based upon the construction of viscoelastic Green functions for the surface mass load boundary value problem. These Green functions, a different such function may be constructed for each geophysical observable of interest, are expressed in the form of spherical harmonic expansions. In these expansions the time dependent amplitudes of each of the spherical harmonics consist of viscoelastic extensions of the so-called "Love numbers" first introduced by A.E.H. Love in his book "Some problems in Geodynamics". For elastic models of the Earth, the modern discussion of these Love numbers has been provided by Farrell (1972). In Peltier (1974) a methodology as described, based upon the so-called Correspondence principle of linear viscoelasticity, made it possible to convert the elastic Love number calculator employed by Farrell (1972), which was based upon the elastic gravitational normal mode software of Gilbert (1968). This analysis was

based upon the assumption that the rheology of the planet could be described as a three dimensional Maxwell solid, the stress-strain relationship for which had been discussed by Eringen (1963). Application of the Correspondence Principle for this model led directly to the determination of the required Love numbers as functions of the Laplace transform variable "s". Initially these Love number spectra were inverted using a colocation method but it quickly became clear that an exact method could be developed in which each Love number could be represented by a finite sum of "modes of viscous gravitation relaxation" plus a unique constant for each spherical harmonic degree in the relaxation spectrum. These constants were exactly the elastic Love numbers that had been computed by Farrell (1972). Given the now time dependent Green functions determined in this way, one could determine the response of the assumed spherically symmetric viscoelastic Earth to an arbitrary history of surface mass loading of the planet simply by convolution of the surface mass loading history with the appropriate Green function.

However, the surface mass loading history during the Late Quaternary ice age cycle is complicated by the fact that, the hydrological cycle being closed, when ice accumulates on the surface of a continent, this is accommodated by an equivalent loss of mass from the oceans. Furthermore, one of the primary observables of ice-age dynamical processes consists of inferred histories of relative sea level that had been accumulating in the same period of time by the application of the radiocarbon clock to the determine the histories of relative sea level change along all of the world's coastlines. In 1976 a series of three papers appeared in the same issue of what was then the geophysical *Journal of the Royal Astronomical Society*, respectively those of Peltier and Andrews (1976), Farrell and Clark (1976) and Peltier (1976). In the first of these papers were provided two Green functions, one for the gravitational potential perturbation and

another for radial displacement (as well as others). These two Green functions were provided to Farrell and Clark who noted that a relative sea level Green function would simply be the difference between the gravitational potential Green function and that for radial displacement. When this Green function is convolved over the entire surface mass load consisting of its ice and water components, it makes a prediction of relative sea level history. However, this is now an integral equation because relative sea level exists both in the triple convolution integral as well as one the left hand side. Farrell and Clark (1976) recognized that the result obtained by evaluating the convolution integral would have to be corrected so as to ensure that the solution for RSL history was mass conserving. This correction took the form of a time dependent but space independent function. It appears to have been first explicitly noted in Peltier et al. (2015), although this had been understood much earlier, that the Sea Level Equation (SLE) was an example of integral equations that are known as Fredholm integral equations of the second kind (see e.g., the second volume of the treatise "Methods of Mathematical Physics" by Courant and Hilbert, (1953). In 1980, Clark, Farrell and Peltier received the Kirk Bryan Award of the Geological Society of America for their collaborative efforts following publication of the first detailed global calculation of postglacial relative sea level history in Clark et al. (1978) and Peltier et al. (1978). These calculations also depended upon a second result in Peltier and Andrews (1976), which was a first model of continental glaciation history for a portion of the most recent ice-age cycle.

As detailed in Sections 3-5 of the present paper the form of the theory as it existed in 1978 was still extremely rudimentary, not only in terms of this model of glaciation history but also in terms of the radial viscosity profile. In terms of glaciation history, the model had no Antarctic component and in terms of the radial viscosity profile the model had no lithosphere! However,

the most important improvement has been that involved in modifying the structure of the Sea Level Equation itself to include the effects due to the changes in Earth rotation caused by the ice-age cycle of glaciation and deglaciation.

The demonstration that significant impacts upon Earth rotation were caused by the ice age cycle was provided in Peltier (1983) and Wu and Peltier (1984), who demonstrated that both the non-tidal acceleration of Earth's rate of axial rotation and the true polar wander of the spin axis relative to surface geography were both explained by the GIA process and that both provided strong constraints upon the radial viscosity profile. The next step in the further refinement of the theory was to investigate the strength of the feedback of these rotational effects onto sea level itself. These necessary analyses made use of the results of Dahlen (1976), for the relationship between changes in the Earth's rotation and the centrifugal potential. The final form of the SLE is that discussed in Section 4 of the present paper. Solution of this augmented SLE demonstrated that the influence of rotational feedback was extremely strong and controlled by the polar wander component of the rotational response to the ice age cycle.

As discussed in Section 5 of this paper, this final form of the Sea Level Equation has completed the formal structure of the normal mode theory for the GIA process for the spherical symmetric linear Maxwell model. Although there is remaining scope for its further refinement, especially concerning the loading history, this linear theory has been remarkably successful as there appears to be no major observational constraint that is not satisfied by the model. It also needs to be understood that this model is unique in that it is truly global in that it consists of a single time dependent history of glaciation and deglaciation and a single depth dependent profile of mantle viscosity. Why a single such viscosity profile might be expected to be adequate has been discussed in this paper in which attention has been drawn to the fact that the mantle

convective circulation operates at such a high Rayleigh number that the majority of the mantle is expected to be well mixed and the interior temperature to be adiabatic.

Although the spherically symmetric linear Maxwell model has been extremely successful, its assumptions, namely that the rheology is linear and that lateral heterogeneity of viscosity may be ignored, need to be investigated. In order to test the validity of these fundamental assumptions, a much more general model is clearly required and the most carefully tested of such models is the finite element model based upon the commercially available ABAQUS platform, which has been reviewed at length in Part II of this paper. Although the modifications required to ABAQUS that have been required to be able to apply it to the GIA problem are highly significant, the result has been carefully benchmarked against those from the spherically symmetric Maxwell model (see for example the detailed discussion in Li et al., 2020) and had been found to deliver essentially identical results. The fact that the model also enables the full influence of both nonlinear and composite rheology to be incorporated in the calculation as well that of lateral heterogeneity is especially important.

Part II of this review shows that lateral viscosity variations in the Earth can be large and can significantly affect the GIA process. The effects of lateral heterogeneity can be clearly detected by GIA observations in certain optimal locations. Furthermore, the lateral structure of a 3-D Earth cannot be accurately deduced from 1-D GIA models. Due to the effect of mode coupling, the spectral/normal mode method also has difficulty in modeling the GIA process if the lateral variation is strong, thus new methods have to be developed.

To study the effects of lateral heterogeneities on GIA, we need to construct a model of the lateral viscosity variations in the mantle. The best way to achieve that is to infer the lateral viscosity perturbations from seismic tomography models of shear wave velocity heterogeneity

and supplement such data with results of near-surface geophysical studies of the thermal-mechanical properties. More such near-surface geophysical studies will be particularly useful for local GIA studies in the future. The lateral viscosity perturbations obtained this way can be superposed on the 1-D (background) viscosity profile. As discussed in Section 7.2, the background viscosity profile can affect the interpretation of lateral heterogeneities, so it is important that the best-fitting background viscosity profile that is less dependent on the ice history model is desired. However, as discussed in Section 6.5, there are different ways to obtain the lateral viscosity perturbations from the laterally varying seismic anomalies. Future improvement in controlling the uncertainties of parameters in the scaling relationship (Eq. (78)), and in the creep parameters in Eq. (80), will definitely benefit future GIA studies. The choice of seismic tomography model may also be important especially for local GIA studies with lateral heterogeneities. Currently, there is good agreement on the long wavelength structures between the different shear wave tomography models, but future refinement of the short wavelength structures will definitely help to reduce the uncertainties of GIA studies of lateral heterogeneities. Section 7.2 also shows that, with the improvements mentioned above, it is possible to use GIA data to understand the role, or constrain the contribution, of thermal effects on the lateral seismic anomaly inferences. Also shown in recent work (Li et al., 2020), in which a large number of GIA models with tomographically lateral heterogeneity of viscosity were analyzed and those which misfit the observation were rejected, the only models retained were those in which the horizontally averaged depth dependent structure was consistent with this property of the spherically symmetric Maxwell model. These results appear to be unique in the literature and strongly reinforce the recently published results of Argus et al., (2021) to the effect that the increase in viscosity across the mantle phase transition at 660 km depth cannot be large.

In Section 3.4, it is shown that sensitivity kernels can be used in the inversion of the radial viscosity variations in a 1-D mantle. Using the perturbation method, Section 7.1 shows that sensitivity kernels can also be found for a 3-D Earth with lateral viscosity variations. It is further shown that these kernels depend on the characteristic width of the load, the type of GIA data, the age of the data, the 1-D background viscosity profile and the depth of the viscosity anomaly. In particular, the wider the load, the deeper the GIA data near the center of the load can "see" and the magnitude of sensitivity is generally higher for observations closer to the ice load center. Also, the sensitivity kernels for present-day uplift rate, gravity-rate-of change, and RSL data within the last 6 ka BP are similar, but the kernel for tangential motion is different in that the magnitude of sensitivity extends much further away from the load and is more concentrated in the upper mantle.

Section 7.1 also shows that sensitivity kernels can be useful in the planning of new GPS or absolute gravimetry stations or in search of new high quality RSL data. The aim is to search for the optimal locations of the new data, so that the sensitivity of the data exceeds the observational error of the data and can resolve GIA related issues such as ice thickness, lithospheric thickness, background viscosity and lateral viscosity variations.

In recent years, there has been a great deal of interest in quantifying the uncertainties of GIA predictions because geodetic measurements do not just contain signals from the GIA process, but also from other sources such as recent climate change. In order to study the signal from the other source, the contribution of the GIA signal must be removed. Due to the imperfect knowledge of GIA model inputs such as the ice history and mantle rheology, it is desirable to quantify the uncertainties of GIA predictions. Section 7.3 has provided a brief survey of some recent progress in this area. This is illustrated by the results of a recent study of the Type 1A

uncertainties in North America that includes a large variety of 3D Earth structures that can fit a large number of GIA observations well simultaneously. So far, there have not been many serious efforts in quantifying Type 1B (related to the ice history model) and 1C (both ice and Earth models) uncertainties. Current studies either include variations in ice thickness history in local regions only (Love et al., 2016; Vestol et al., 2019) or represent the variation of each large ice sheet of the globe by a single scaling parameter (Caron et al., 2018). Clearly, a single parameter is far from enough to describe any local variations in the timing and rate of rapid ice melting or readvancing events which may lead to the modification of the ice profile. Also, any modification of the ice margin that is not well constrained by terminal moraine data is not permitted in a single scaling parameter. In order to understand why Type 1A uncertainties are easier to study than Type 1B and 1C uncertainties, we briefly mention the challenges in one of the many ways to reconstruct ice sheet histories based on GIA data - since the main challenges are probably the same among the other approaches. In the inversion of ice thickness history, it is common to subdivide the ice sheets into ice grids where the ice thickness is assumed uniform within the grid but the thickness values can change with time. The spatial resolution of the ice model is determined by the number of ice grids, which together with the number of time steps in the ice history specifies the number of unknown parameters to be determined by the inversion. Now, the thickness values at a local ice grid can be affected by the spatial resolution of the ice model and is also affected by the amount of geological, geophysical and geodetical data that has enough resolving power to constrain the local ice thickness history accurately. Generally, the sensitivity of the observational data decreases with distance from the ice grid, so for first order estimates of the thickness history of any local grid, one only needs to consider the observational data closeby. Next, the amount of observational constraints available for that ice grid and the number of

unknown parameters needs to be considered. If the number of unknown parameters is less than the number of constraints, then the problem is overdetermined. In the inversion of the Laurentide ice-sheet history, Clark (1980) only used eight large ice grids to represent the whole ice sheet, because he only had a limited amount of RSL data and he wanted the inversion problem to be overdetermined. If the number of unknown parameters is more than the number of constraints, then the problem becomes underdetermined and the local ice thickness history thus determined is non-unique. This means that the predictions of some variants of the ice thickness history can give similar overall misfit values to the observational constraints, and thus the inferred ice history has larger uncertainty. This can happen to ice grids that are located far inland where RSL observations are few or not available. Of course, these sites can have observational constraints from present-day rate-of-change (e.g. land uplift rate, gravity-rate-of-change), but present-day rate-of-change data is only sensitive to the integrated ice history in addition to mantle rheology - it cannot resolve the ice thickness values at the specified time steps as well as RSL data. Fortunately, recent developments of thermo-mechanical models of ice sheets coupled with climate input, in addition to GIA data (Tarasov et al., 2012) may also provide extra constraints to the ice sheet reconstruction, but the uncertainties of such models also need to be considered. For places like Antarctica and Greenland, where current loading and unloading events do play a significant role, and where RSL data are sparse, the uncertainties of ice history deduced are very large (Peltier, 2004; Whitehouse et al., 2012; Ivins et al., 2013). Thus, the uncertainties of ice history models depend strongly on both space and time. The inversion described above is only for the first order estimate of the local ice history. In reality, the adjustment of loading and unloading events in neighboring ice and ocean grids can also affect the local ice thickness history – so they need to be considered together in subsequent iterations of refinement. For distant ice

and ocean grids, the effects of the "long wavelength" variation of surface mass redistribution (including rotational feedback on sea levels in the oceans) may also have secondary effects on the local ice thickness history and that also need to be considered too in the refinement process. Of course, the global ice model must be able to fit the RSL at distant sites like Barbados (see Section 5.1). In short, the reconstruction of global ice history (with all the ice grids taken as a whole) involves many iterations of refinement, until most of the observational constraints can be fitted by the predictions simultaneously. Any randomly large modifications of the constructed global ice model (as may appear in Monte Carlo technique) may seriously destroy the fit already obtained between the predicted and the observed GIA data. But in the study of Type 1B uncertainties, it is desirable to deduce the uncertainties from a large number of different global ice models, provided that all of them are able to give predictions that can fit most of the observational GIA data simultaneously. Thus, much effort in reconstructing different ice models is required for Type 1B (and also Type 1C) studies. In contrast, in the study of Type 1A uncertainties, the global ice model is fixed, and the lateral viscosity variations can be deduced from models of seismic tomography for given scaling parameters that control the magnitude of lateral heterogeneity (Eq. (78)). Thus the variations in Earth models involve variations in the scaling parameters, the choice of the seismic tomography model (which mainly affects the short wavelength lateral variation of viscosity) and the radial background viscosity profile. Thus, it is easier to keep the number of unknown Earth parameters smaller than the number of observational constraints, and the inversion problem remains overdetermined. The study of Type 1C uncertainties is more challenging, because both the Earth model and the ice model are modified, and the interaction/trade-off between Type 1A and 1B uncertainties means larger parameter space to be searched. This appears to be one of the future research directions on GIA

uncertainties.

GIA models should also investigate the effect of nonlinear rheology because creep experiments on mantle rocks show that both diffusion (linear) and dislocation (nonlinear) creep can operate in the mantle. It is well known that the dominant creep mechanism depends on the stress level and the grain size. For nonlinear or power-law creep, the effective viscosity is both space and time dependent. Thus, for sites below the ice sheet, the effective viscosity in the early stage of deglaciation is relatively low but it increases with time. Consequently, if mantle rheology is nonlinear, RSL sites within the ice margin may be characterized by a rapid uplift rate at the early stage of deglaciation but the uplift rate decreases with time. On the other hand, if mantle rheology is linear, then the value of the effective viscosity remains constant through time. This difference in the vertical deformation under the ice sheet means that ice sheet history models constructed for linear rheology need to be modified if the mantle rheology is nonlinear. It remains unclear as to whether the required adjustments to the loading history will be able to maintain the excellent fit to the constraints on eustatic sea level history provided by the Barbados data set and deep sea core oxygen isotopic constraint. Another characteristic of a nonlinear mantle is the existence of a "viscously stationary zone" near the ice margin if the ice margin does not migrate with time and the effect of ocean loading is neglected. With more realistic ice models that include the migration of the ice margin and the inclusion of ocean loading, the effect of "viscously stationary zone" is mitigated, and the predicted RSL curves near the Laurentide ice margin can fit the observed data provided that the zone with nonlinear rheology is thin or must lie in the lower mantle. However, the latter scenario is not compatible with seismic anisotropy observations, which suggest that the rheology of the shallow upper mantle is nonlinear. This problem can be resolved if the rheology of the mantle is taken to be

composite. In particular, if the creep parameters of the composite rheology in the upper mantle are different from those creep parameters of the composite rheology in the lower mantle, then not only the global RSL data but, also the observed uplift rate and gravity-rate-of-change within the ice margin can mostly be explained after the ice history (e.g. ICE-6G_C) is allowed to be modified (see Section 6.6). Another complication for nonlinear or composite rheology is the effect of the interaction between GIA induced stress and the background tectonic stress. It is found that the GIA observations can be explained only if the effect of the interaction between GIA stress and tectonic stress is small. This confirms the viewpoint from microphysics of rocks, which suggested that effects of such stress interaction cannot be large.

There has been speculation that the GIA process can affect volcanism in Iceland or Greenland and trigger Earthquakes near the ice margins. Section 7.4 reviews the issue whether viscous dissipation from GIA induced mantle flow can generate enough heat to cause volcanism, affect mantle rock properties such as seismic wave speed or mantle viscosity and also affect ice sheet stability. The GIA models in such studies include the effects of linear, nonlinear and composite rheologies. The results demonstrate that previous arguments suggesting that this effect of viscous dissipation could be important are not supported because the increase in temperature due to viscous dissipation is too small. Thus, future models of GIA do not need to include viscous heating. However, GIA can still affect volcanic activity via the effect of decompression which can affect the lava production rate in Iceland and Greenland following deglaciation.

Section 7.5 reviews the physics of GIA reactivating faults formed by earlier tectonic processes. The FE method described in Section 6 has been extended to model GIA induced stress and Earthquakes. The success of such models in predicting the onset timing and the slip

magnitude of some recent and paleo-Earthquakes inside and outside the ice margin have also been discussed.

By way of final comments and to provide an apology for having to eliminate detailed discussion of at least two major areas of research that have become deeply connected to work on the problem of glacial isostatic adjustment, we offer the following abbreviated comments: The first area of GIA research that we have not been able to adequately represent in our text concerns the regional comparison of relative sea level observations with the predictions of the model. Modern examples of this work includes that of Rostami et al. (2000), for the east coast of South America, that of Engelhart et al. (2012) for the east coast of the USA, that of Khan et al. (2017) for the coastlines surrounding the Caribbean Sea, that of Vacchi et al. (2018) for the east and Arctic coast of Canada, including Hudson Bay, that of Baranskaya et al. (2018) for the eastern Russian Arctic and the Barents Sea, and that of Roy and Peltier (2018) for the Western Mediterranean. These regional analyses are providing the data that are driving continuous improvements of the model. Eventually they will be assembled into a new global database that will replace that originally produced by Tushingham and Peltier (1991).

The second area that has become strongly dependent upon output of GIA modeling concerns its use as input for fixing the boundary conditions needed in the application of modern coupled climate models for the reconstruction of past ice-age climates. Work of this kind has included the use of paleobathymmetric reconstructions as input in the reconstruction of the ocean tidal regime of the glacial oceans as in Griffiths and Peltier (2008, 2009), Velay-Vitow and Peltier (2020), and Velay-Vitow et al. (2020, 2021) and, as importantly, for the reconstruction of complete ice age surface boundary conditions as in Ivanovic et al. (2016) and Kagayama et al. (2021). One of the most recent contributions of this kind has involved the demonstration that the boundary

conditions provided by the ICE-6G_C (VM5a) model have provided, for the first time, an explanation of the Dansgaard-Oeschger oscillation of millennium timescale that dominated climate variability during Marine Oxygen Isotope Stage 3 (Peltier and Vettoretti, 2014; Vettoretti and Peltier, 2015, 2016, 2018; Peltier et al., 2020). Finally, the predictions of present day GIA influence in both Antarctica and Greenland are proving to be indispensable to the accurate inference of the ongoing rates of mass loss from these great polar ice sheets due to the ongoing global warming due to the increasing concentration of atmospheric greenhouse gases (Shepherd et al., 2018, 2020). To do adequate justice to work in both of these areas of application of GIA research would have required much more space than that of a single paper such as this. It is expected that the level of interdisciplinary activity in these areas will become increasingly important as physical models of the GIA process become increasingly refined.

Acknowledgements

We are very grateful to all of our colleagues who have contributed to the research that has been discussed in this paper and especially those whose work we have been obliged to describe much more succinctly than otherwise would have been ideal. We thank Pingping Huang for providing the figures in Section 7.4, and also Holger Steffen for providing Fig. 7.19 and for his constructive comments on Sections 7.1 and 7.3. Tanghua Li is supported by the Singapore Ministry of Education Academic Research Fund MOE2019-T3-1-004 and MOE2018-T2-1-003, the National Research Foundation Singapore, and the Singapore Ministry of Education, under the Research Centers of Excellence initiative. This work comprises Earth Observatory of Singapore contribution no. 428. Jesse Velay-Vitow is supported by NSERC grant CGSD3 - 547034 – 2020 as well as by the Walter C. Sumner Mmeorial Foundation.

Appendix A. Compressible and Incompressible Earth Models

PREM shows that, apart from the fluid outer core and the oceans, Earth's material is compressible. However, in the development of GIA modelling, both incompressible and compressible Earth models are widely used. The aim of this Appendix is to explain this and briefly review the following issues: (i) The advantages and limitations of incompressible Earth models; and (ii) The effects of unstable modes and the dilatation D-modes due to compressible Earth models. In particular, can ultra-low viscosity in the asthenosphere (e.g. Gomez et al., 2015) promote such instability in the GIA process? (iii) Demonstrate that the RSL and uplift rates computed for ICE-6G_C(VM5a) using the Coupled-Laplace-Finite-Element (CLFE) method, that includes material compressibility, agree quite well with that computed using the conventional normal mode method that includes the full effects of compressibility.

To understand the usefulness of incompressible Earth models, we note that analytical solutions exist for incompressible uniform shells and cores and thus their solutions can be obtained by analytical matrix propagation technique (e.g. Sabadini et al., 1982; Wu, 1990; Spada et al., 1992). Since analytical solutions are not affected by errors introduced during numerical integration, this method is generally considered to be most accurate. However, for compressible Earths, analytical solutions only exist for a uniform sphere, but not for compressible uniform shells above the core (Cambiotti et al. 2009). Thus, the solution for a radially stratified compressible Earth has to be obtained by the numerical integration method such as the Runge-Kutta-Gill scheme with variable step size (Peltier 1974). To check the accuracy of the numerical integration scheme, one can compare its results with that from the analytical matrix propagation

technique for an incompressible Earth. Wong and Wu (2019) showed that the comparison is very good especially when the number of layers in the mantle is larger than about four.

However, compressibility causes instabilities (Plag and Jüttner, 1995; Hanyk et al., 1999). This effect is illustrated in Fig. A1 where the effect of compressibility on the Love number spectrum $h_n(s)$ for harmonic degree n=2 and 5 is shown. The diagrams on the top row are for a two-layer Earth, which consists of a uniform mantle over a uniform core. The diagrams on the bottom row are for a six-layer Earth, consisting of a 115 km thick uniform lithosphere, four uniform mantle layers and a uniform core. Inspection of Fig. A1b shows that a number of singularities are found at s smaller than $s=10^{-1}$. The locations of these singularities correspond exactly to the eigenvalues of the unstable modes. This supports the finding of Plag and Jüttner (1995). Fig. A1c shows that the presence of a lithosphere and a few more compressible layers can suppress some of these singularities. On the other hand, no singularity exists for the Love number spectrum for an incompressible Earths (see figures on the left column). The effect of compressibility on the Love number spectrum for n=5 for the six-layer Earth model is shown in Fig. A1d, where it can be seen that the difference is largest in the elastic limit, but as s decreases, the difference become very small since in the viscous limit, the Maxwell constitutive relation ensures that the compressible solid mantle becomes an incompressible fluid. The difference between the time histories of these Love numbers will be considered near the end of this Appendix.

Next, let us consider the effect of compressibility on the number of modes. For an incompressible Earth, the normal modes are either buoyancy modes caused by the density contrast between adjacent layers (e.g. M0 mode at the earth's surface, C0 mode at the core–mantle boundary), or viscoelastic modes caused by the contrast between viscoelastic layers with

different values of Maxwell time, (including the L0 mode caused by the elastic lithosphere over a viscoelastic mantle). The number of buoyancy and viscoelastic modes are finite and are well known for an incompressible earth (Wu and Ni 1996). Also, these modes are always stable. The excitation strength of the viscoelastic mode is generally small when compared to the M0 mode.

Compressible Earths have the same number of buoyancy and viscoelastic modes as the incompressible case, but the relaxation times and excitation strengths of these modes are both affected by the presence of compressibility. However, compressible Earths have two extra series of modes: the stable dilatation D-modes (Han and Wahr, 1995; Vermeersen et al., 1996; Vermeersen and Sabadini, 1998) and the unstable Rayleigh–Taylor or RT modes (Plag and Jüttner, 1995; Hanyk et al. 1999; Vermeersen and Mitrovica, 2000) which grow exponentially with time. In the incompressible limit, the relaxation time of the stable D-modes becomes the Maxwell time, showing that they are due to dilatation in a compressible Earth. The excitation strengths of the D-modes are generally negligible (Vermeersen et al., 1996). Cambiotti and Sabadini (2010) found that for Earth models with continuous variations of the initial bulk modulus and when the initial density profile that follows the Darwin-law, then the compositional C-mode exists. Actually, the RT-modes are the unstable subclass of the C-modes, while the stable class of the C-modes affect the tangential motion in a way that makes the tangential fluid limit diverge. Since we are not concerned with Darwin-law density profile nor tangential motion, we will focus on the unstable RT modes in the following.

The RT modes are due to unstable density stratification induced by compressional deformation. Consider a thick layer with uniform density near the Earth's surface which is subjected to a surface load. When the top part of this uniform layer become more compressed than the bottom part, gravitational instability due to density inversion tends to be induced in this

uniform thick layer unless this is countered by other body forces (Wong and Wu, 2019). But if the density gradients in the mantle are represented by thinner uniform layers, then the effect of density inversion may become suppressed. In general, the strengths of the RT modes are at least an order of magnitude smaller than the stable fundamental mode M0. However, unstable modes with very small excitation strength can still become dominating if the time of loading is long compared with the growth time of the mode (Wong and Wu, 2019). Thus, the importance of the RT modes is determined by their time scale of growth.

Since the unstable modes grow exponentially with time, only the RT1 mode, which has the fastest growth time among the RT modes, needs to be considered in practice. Vermeersen and Mitrovica (2000) also showed that the growth time of the RT1 mode decreases with increasing angular order. In the absence of any ultra-low viscosity in the mantle, the growth time of the RT1 mode is longer than the age of the Earth for degree 2, and is of the order of 10 Myr for degree 50. However, the Earth's stratification and also material properties such as viscosity, affect the growth time of the unstable modes (Vermeersen and Mitrovica, 2000; Wong and Wu, 2019).

An important question is whether an ultra-low viscosity asthenosphere such as that proposed in Gomez et al. (2015) can promote any instabilities during the GIA process. Based on the PREM model, Wong and Wu (2019) constructed a stratified Earth with 30-layers that includes a 100 km thick ultra-low viscosity ($5x10^{18}$ Pa s) asthenosphere below a 120 km thick lithosphere, and in their Fig. D3, showed that the RT1 modes have growth time of more than 10 Myrs at degree 2 and growth time of around 1 Myrs for degree 50 (see also Figure A2). So, for degrees less than 50, the growth time of the fastest RT mode is much longer than the period of a glacial cycle (around 100 kyrs), thus the effects of the unstable modes can be ignored even if a few glacial cycles are considered. This is in agreement with the conclusion of Vermeersen and

Mitrovica (2000). However, the growth time continues to decrease to less than 1 Myrs at degree 100 (Wong and Wu, 2019), and it is not clear if the growth time will further decrease at even higher degrees. Since instability can develop during the deformation of a compressible planet if the fastest growth time of the planet is short when compared to the period of loading, future study should include the growth time of RT1 modes for harmonic degrees much higher than 120, especially in Antarctica where the period of consecutive glacial cycles is of the order of 3 Myrs.

Next, we consider the effects of incompressibility on the Heaviside Love number histories $h_n^H(t)$,its time-rate of-change $\frac{d}{dt}h_n^H(t)$ and relative Love number histories $h_n^H(t)-h_n^H(t_o)$ where t_o is the time of reference. The last two quantities are related to the computation of land uplift rate and relative sea level curves.

It is well known that incompressibility can significantly affect the elastic asymptote, the excitation strengths, and the relaxation times (e.g. Wu and Peltier, 1982; Vermeersen et al., 1996). Thus, it is not surprising that the effect of incompressibility on the Heaviside Love number histories $h_n^H(t)$ is also significant. This is illustrated in Fig. A3a for the six-layer Earth model of Fig. A1, where the growth time of the unstable modes of the compressible model greatly exceeds the period of Heaviside loading which is set at 100 kyrs, so the effect of instability can be neglected. Note that the percentage error for $h_5^H(t)$ is more than 50% at t=0, but it decreases rapidly to about 10% around t=20 kyrs after Heaviside loading, and then decrease much slower afterwards. The percentage errors for $h_2^H(t)$ and $h_{15}^H(t)$ are similar. For the other Lover numbers, similar result is also found. This has led to the conclusion that the effect of compressibility is significant for some GIA variables such as long-term polar wander (Vermeersen et al., 1996) and horizontal velocities (Tanaka et al., 2011). However, Fig. A3b

shows that the difference between $\frac{d}{dt}h_n^H(t)$ for compressible and incompressible Earth models are much smaller – below 5% during the first 5 kyrs and then the differences become much smaller. In Fig. A3c, $h_n^H(t)-h_n^H(t_o)$ is computed for n=2, 5 and 15 with t_o = 15 kyrs after Heaviside loading. It can be seen that apart from the first 5 kyrs, the agreement between the compressible and incompressible results become very good. If n=5 and $t_o$is decreased to 10 or 5 kyrs - as in Fig. A3d, then one can see that the agreement becomes even better. This supports the finding of Wolf (1985) that the effect of compressibility is only significant for relative sea levels during the initial phase of glacial loading or unloading, but becomes not very significant afterwards.

Finally, we want to demonstrate that the RSL and uplift rates computed for ICE-6G_C(VM5a) by the Coupled-Laplace-Finite-Element (CLFE) method, agree quite well with that computed using the conventional normal mode method of Peltier et al. (2015). Note that an important difference of the two methods is that the full effects of mantle compressibility is included in Peltier et al. (2015), but in the CLFE method, only "material compressibility" (Klemann et al., 2003) is included. In other words, in the equation of motion:

$$\vec{\nabla}\cdot\hat{\tau}-\vec{\nabla}\left(\vec{u}\cdot\rho_o g_o\hat{r}\right)-\rho_1 g_o\hat{r}-\rho_o\vec{\nabla}\phi_1=0.$$

only the third (internal buoyancy) term is not included the CLFE method - otherwise everything is the same as the fully compressible case. The reason for the exclusion is that density reversal that induce Rayleigh-Taylor instability is driven by the internal buoyancy term (Wong and Wu, 2019). Without this internal buoyancy term, the solution converges much faster. Also, since the Heaviside responses (e.g. $h_n^H(t)$) of "material compressibility" is intermediate between the response of a fully compressible Earth and an incompressible Earth, the predicted RSL and uplift rate that assumes material compressibility is expected to give a better approximation to the fully

compressible case than shown in Fig. A3. This is confirmed in Fig. A4 which shows that the predicted shape and amplitude of $\dot{U}$ (or land uplift rate) from both methods agree quite well - the main differences are outside the edge of the ice margin along the east coast near the Canada-US border where the amplitudes of the uplift rate are low. Comparison of the predicted RSL curves at two representative sites (inside and outside the ice margin) also show that the differences are much less than the uncertainties of the RSL data.

In summary, compressibility can induce unstable modes that grow in time – especially in simple Earth models made up of a few layers. For more realistic stratified Earth models that has no ultra-low viscosities in the mantle, the growth time of the unstable modes are much longer than the glacial period, and thus can be neglected. However, future studies should investigate the effect of an ultra-low viscosity asthenosphere on the growth time of unstable modes for deformation of high angular degrees, to see if the effect of the unstable modes can also be neglected. Incompressible Earth models do not have unstable modes, but the effect of incompressibility is significant in the computation of the Load Love Numbers. However, the effect of incompressibility on uplift rate and relative sea levels are only significant during the initial phase of glacial loading or unloading, and the difference can become insignificant afterwards. With the inclusion of material compressibility, the predictions of RSL and uplift rate from the CLFE method give reasonably good agreement with that from the conventional normal mode method.

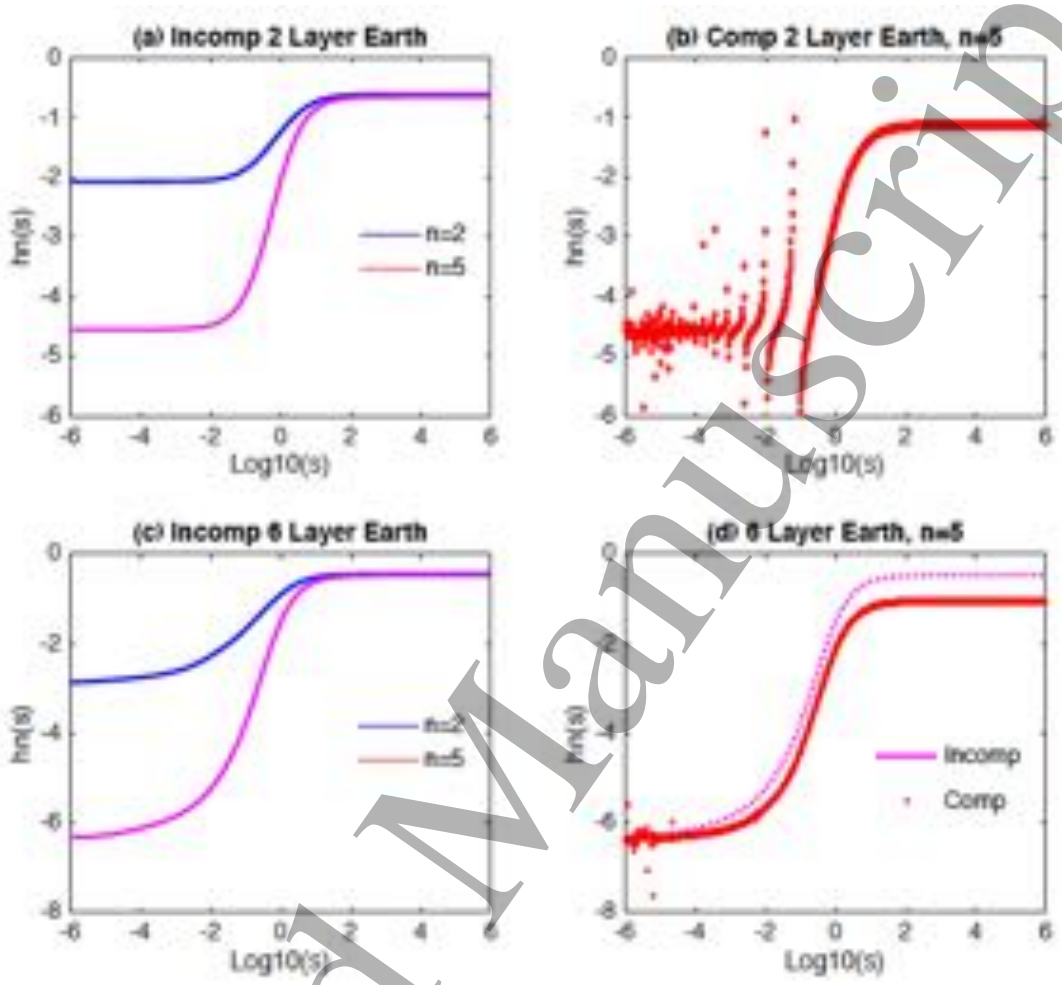

Figure. A1 Love number spectrum $h_n(s)$ for the two-layer and six-layer Earth models. From results of Wong and Wu (2019).

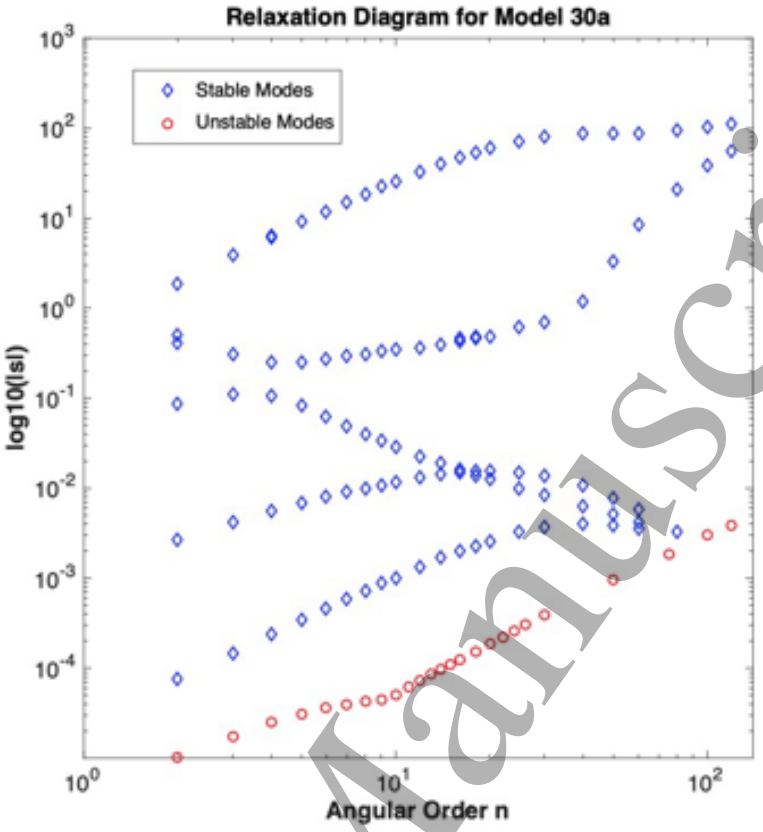

Figure A2. Relaxation diagram that includes both stable (blue diamonds) and unstable (red open circles) RT modes of a compressible 30-layer Earth model. Note that only the dominant modes are shown. After Wong and Wu (2019).

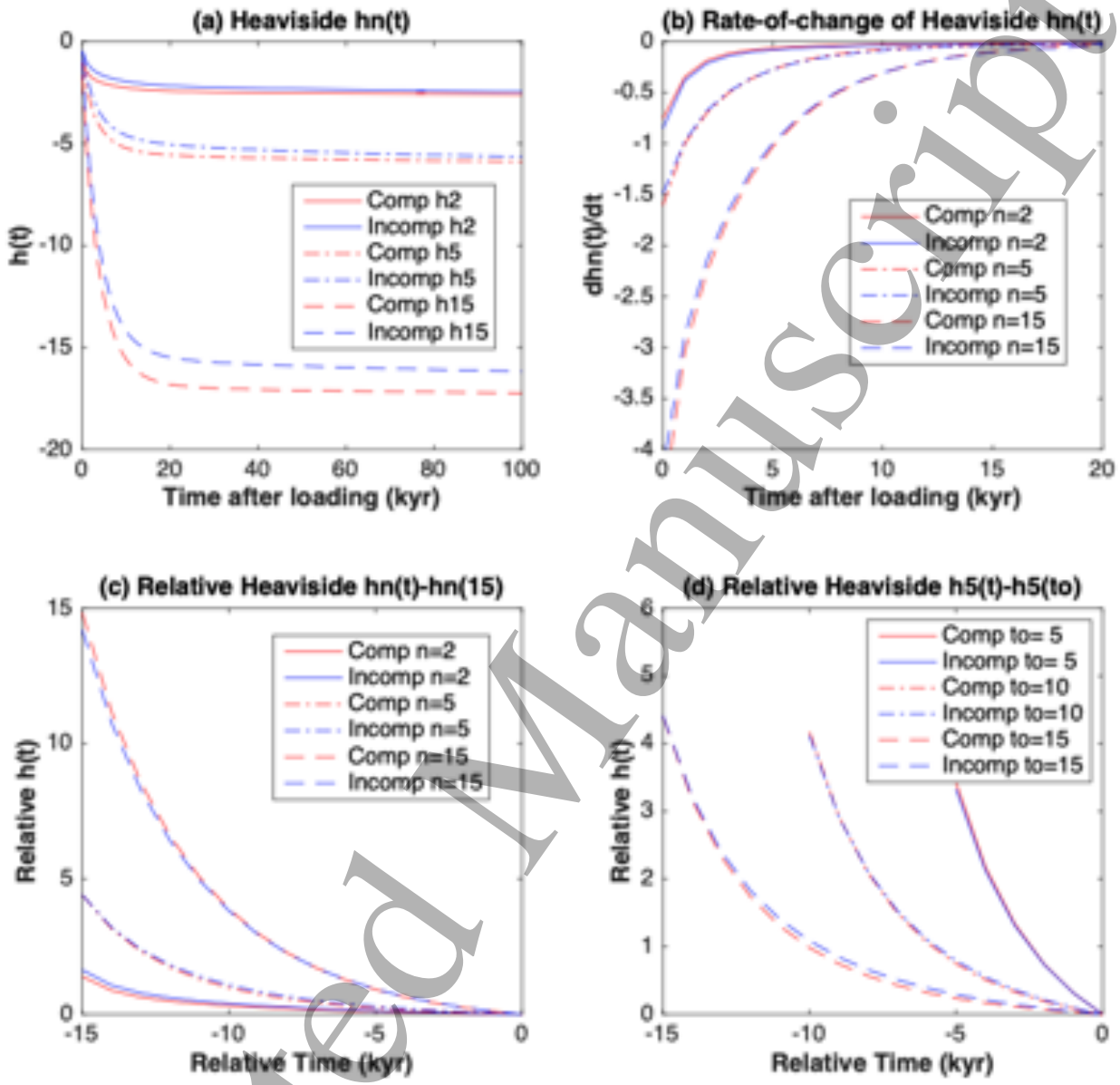

4335

Figure A3. (a) Comparing the Heaviside load Love number histories $h_n^H(t)$ of compressible (red curves) and incompressible (blue curves) six-layer earth models for harmonic degrees n=2, 5 and 15. (b) Comparing $\frac{d}{dt}h_n^H(t)$ = time-rate-of-change of Heaviside load Love numbers of compressible (red curves) and incompressible (blue curves) six-layer earth models for n=2, 5 and 15. (c) Plot of $h_n^H(t) - h_n^H(t_o)$ = Relative Love number histories for t_o = 15 ka after Heaviside loading and n = 2, 5 & 15. (d) Plot of $h_n^H(t) - h_n^H(t_o)$ where n=5 and t_o = 10, 15 & 20 ka after Heaviside loading. From results of Wong and Wu (2019).

4340

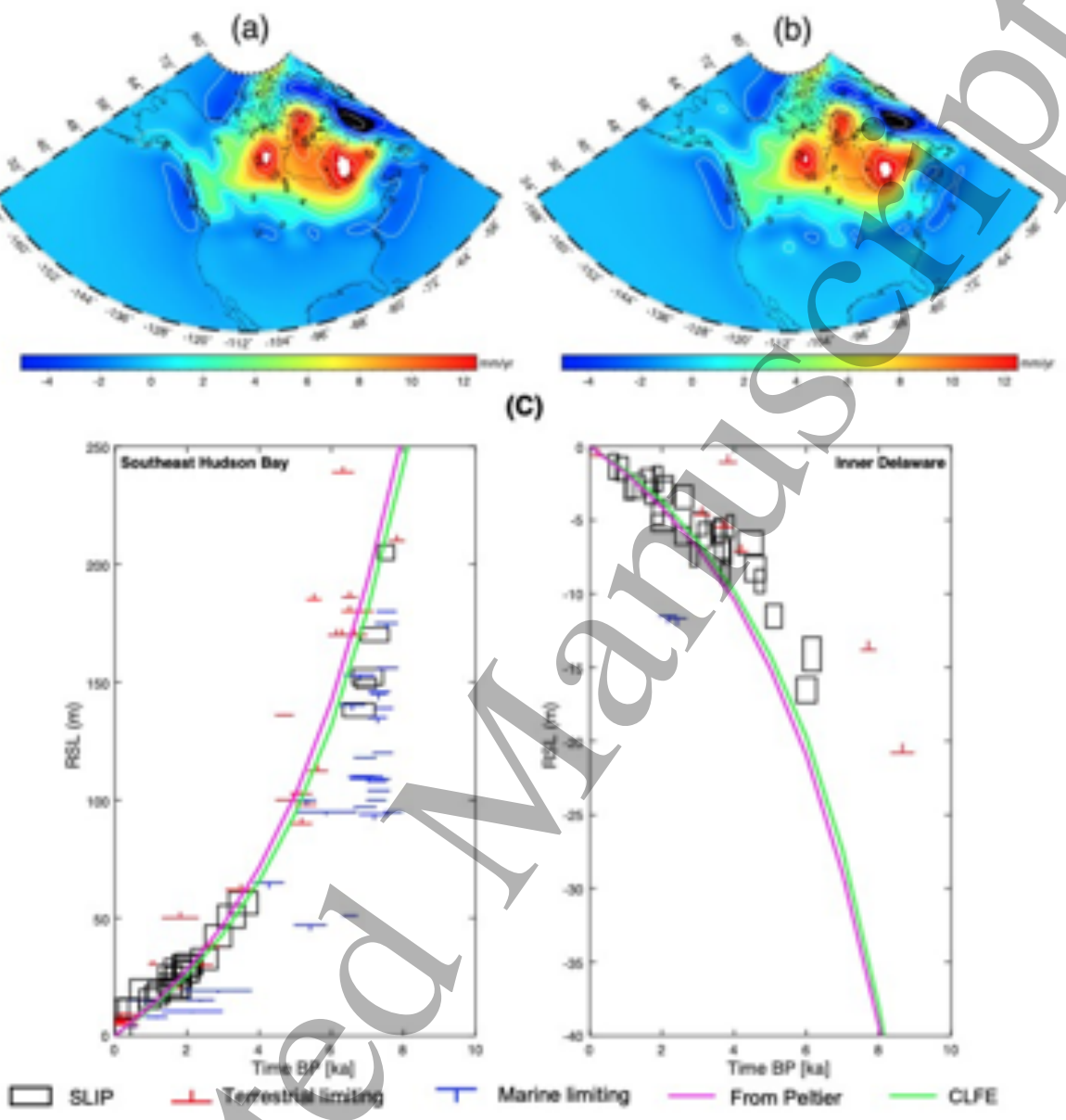

Figure A4. Comparison of predictions computed with the Peltier's spectral-normal mode method for a fully compressible Earth with that from the CLFE method where material compressibility is included. Both methods use the ICE-6G_C (VM5a) model combination. (a) Present-day uplift rate $\dot{U}$ in North America as computed by Peltier (b) $\dot{U}$ computed with CLFE method. (c) Comparison of RSL at Southeast Hudson Bay and Inner Delaware provided by Peltier (magenta solid line) and that computed with CLFE method (green solid line). From Li et al. (2020).

Appendix B. Table of Symbols

This Appendix contains table 5.

References (Mar_15-2022)

A, G., Wahr, J., and S. Zhong, Computations of viscoelastic response of a 3D compressible Earth to surface loading: An application to glacial isostatic adjustment in Antarctica and Canada, J. Int., 192, 557-572, 2013.

Alterman, Z., H. Jarosch, and C.L. Pekeris, Oscillations of the earth, *Mathematical, Physical and Engineering Sciences*, 1959.

Alterman, Z., H. Jarosch, and C.L. Pekeris, Propagation of Rayleigh waves in the earth, *Geophys. J. astr. Soc.*, **4**, 219, 1961.

Argus, D.F., W.R. Peltier and Watkins, M.M., Glacial isostatic adjustment observed using very long baseline interferometry and satellite laser ranging geodesy, J. Geophysical Res. **104**(B12), 29077-29,093, 1999.

Argus, D.F., and W.R. Peltier, et al., The angular velocities of the plates and the velocity of Earth's Centre from space geodesy, *Geophysical Journal International*, **180**(3), 913-960, 2010.

Argus, D.F., W.R. Peltier, R Drummond and A.W. Moore, The Antarctica component of postglacial rebound model ICE-6G_C (VM5a) based on GPS positioning, exposure age dating of ice thicknesses, and relative sea level histories, *Geophys. Journal International*, **198**(1), 537-563, 2014.

Argus, D.F., W.R. Peltier, G. Blewitt and C. Kreemer, The Viscosity of the Top Third of the Lower Mantle Estimated Using GPS, GRACE, and Relative Sea Level Measurements of Glacial Isostatic Adjustment, *Journal of Geophys. Res.: Solid Earth*, **126**(5)**,** 2021.

Artemieva, I.M., Global 1 ◦ ×1 ◦ thermal model TC1 for the continental lithosphere: implications for lithosphere secular evolution, *Tectonophysics*, **416**, 245–277, 2006.

Austerman, J., J.X. Mitrovica, K. Latychev and G.A. Milne, Barbados-based estimate of ice volume at Last Glacial Maximum affected by subducted plate, *Nature Geoscience*, **6,** 553-557, 2013.

Backus, G. E., Converting vector and tensor equations to scalar equations in spherical co-ordinates, *Geophys. J.*, **13**, 71, 1967.

Backus, G.E., and J.F. Gilbert, Numerical applications of a formalism for geophysical inverse problems, *Geophys. J. Roy. Astron. Soc*., **13**, 247, 1967.

Backus, G.E., and J.F. Gilbert, The resolving power of gross earth data, *Geophys. J. Roy. Astron. Soc*., **16**, 169, 1968.

Baksi, K., A geomagnetic polarity timescale for the period 0-17 Ma, based on 40/Ar/39Ar plateau ages for selected field reversals, *Geophys. Res. Letters*, **20**(15), 1607-1610, 1993.

Balachandar, S., Yuen D.A., Reuteler, D.M., Kauer, G.S., Viscous dissipation in three-dimensional convection with temperature-dependent viscosity, *Science*, **267**, 1150-1153, 1995.

Baranskaya, A. V., Khan, N. S., Romanenko, F. A., Roy, K., Peltier, W. R., & Horton, B. P. A postglacial relative sea-level database for the Russian Arctic coast. *Quaternary Science Reviews*, **199**, 188-205, 2018.

Barnhoorn A. W. van der Wal, B.L.A. Vermeersen and M.R. Drury, Lateral, radial, and temporal variations in upper mantle viscosity and rheology under Scandinavia, *Geochem., Geophys., Geosystems*, **12**(1), 2011.

Bassis, J.N., S.V. Petersen, and L.M. Cathles, Heinrich events triggered by ocean forcing and modulated by isostatic adjustment, *Nature*, **542**, 332-334, 2017.

Brandes, C., H. Steffen, R. Steffen, P. Wu, Intraplate seismicity in northern Central Europe is induced by the last glaciation, *Geology*, **43**, 611-614, 2015.

Brandes, C., H. Steffen, P. Sandersen, P. Wu, J. Winsemann, Glacially induced faulting along the NW segment of the Sorgenfrei-Tornquist Zone, northern Denmark: implications for neotectonics and Lateglacial fault-bound basin formation, *Quaternary Sci. Reviews*, **189**, 149-168, 2018.

Berger, A., Long term variations of daily and monthly insolation during the Last Ice Age, *EOS*, **57**(4), p. 254, 1976a.

Berger, A., Obliquity and general precession for the last 5 000 000 years, *Astronomy and Astrophysics*, **51**, 27-135, 1976b.

Bina, C.R., and B.J. Wood, Olivine-spinel transitions: Experimental and thermodynamic constraints and implications for the nature of the 400-km seismic discontinuity, *Journal of Geophys. Res.: Solid Earth*, **92**(B6), 4853-4866, 1987.

Biot, M.A., Theory of stress-strain relations in anisotropic viscoelastic and relaxation phenomena, *J. Appl. Phys*., **25**(11), 1385, 1954.

Biot, M.A.,Variational principles in irreversible thermodynamics with application to viscoelasticity, *Phys. Rev*., **97**, 1463, 1955a.

Biot, M.A., Dynamics of viscoelastic anisotropic media, in *Proceedings of the Second Midwestern Conference on Solid Mechanics, Res. Ser*., vol. **129**, Engineering Experiment Station, Purdue University, Lafayette, Ind., 1955b.

Bretangnon, P., *Astron. & Astrophys.*, **30**, 141-154, 1974.

Broecker W.S., and van Donk, J., Insolation Changes, Ice Volumes, and the 018 Record in Deep-Sea Cores, *Reviews of Geophys. And Space Physics*, **8,** 169, 1970.

Breuer, D. and Wolf, D., Deglacial land emergence and lateral upper-mantle heterogeneity in the Svalbard Archipelago-I. First results for simple load models, *Geophys. J. Int.*, **121,** 775-788, 1995.

Bunge, H.-P. and Grand, S.P., Mesozoic plate-motion history below the northeast Pacific Ocean from seismic images of the subducted Farallon slab, *Nature*, **405**(6784), 337–340, 2000.

Busse, F., and G. Schubert, Convection in a fluid with two phases, *J. Fluid Mech.*, **46**, 801, 1971.

Byerlee, J.D., Friction of rock. *Pure and Applied Geophysics*, **116**, 615–626, 1978.

Cambiotti, G., Barletta, V. R., Bordoni, A. and Sabadini, R. A comparative analysis of the solutions for a Maxwell Earth: the role of the advection and buoyancy force. *Geophysical Journal International*, **176**(3), 995-1006, 2009.

Cambiotti and Sabadini, The compressional and compositional stratifications in Maxwell earth models: the gravitational overturning and the long-period tangential flux. *Geophysical Journal International*, 180.2, 475-500, 2010.

Caron, L., Ivins, E. R., Larour, E., Adhikari, S., Nilsson, J., and Blewitt, G., GIA model statistics for GRACE hydrology, cryosphere, and ocean science. *Geophysical Research Letters*, **45**(5), 2203–2212, 2018.

Cathles, L.M., Viscosity of the Earth's mantle, Princeton University Press, New Jersey, USA, 1975.

Chang, S.J., A.M.G. Ferreira, J. Ritsema, H.J. van Heijst, J.H. Woodhouse, Joint inversion for global isotropic and radially anisotropic mantle structure including crustal thickness perturbations, *Journal of Geophysical Research: Solid Earth*, 120, 4278-4300, 2015.

Cheng, M. and Tapley, B. D. Variations in the Earth's oblateness during the past 28 years. *Journal of Geophysical Research: Solid Earth*, **109**(B9), 2004.

Christensen, U.R. and D.A. Yuen, Layered convection induced by phase transitions, *Journal of Geophys. Res.: Solid Earth*, **90**(B12)**,** 10,291-10,300, 1985.

Christensen, U., Effects of Phase Transitions on Mantle Convection, *Annual Review of Earth and Planetary Sciences*, **23**, 65-87, 1995.

Clark, J.A., W.E. Farrell, and W.R. Peltier, Global Changes in Postglacial Sea Level: A Numerical Calculation, *Quaternary Research*, **9,** 265-287, 1978.

Clark, J. A. The reconstruction of the Laurentide Ice Sheet of North America from sea level data: Method and preliminary results. *Journal of Geophysical Research: Solid Earth*, **85**(B8), 4307-4323, 1980.

Cordier, P., T. Ungar, L. Zsoidos and G. Tichy, Dislocation creep in MgSiO3 perovskite at conditions of the Earth's uppermost lower mantle, *Nature*, **428**, 837-840, 2004.

Courant, R., and Hilbert, D., Methods of Mathematical Physics, Volume 1, Elsevier Science.

Crawford, O., D. Al-Attar, J. Tromp, J.X. Mitrovica, J. Austermann, and H.C.P. Lau, Quantifying the sensitivity of post-glacial sea level change to laterally varying viscosity. *Geophys. J. Int.*, **214**, 1324-1363, 2018.

D'Agostino, G., G. Spada, and R. Sabadini, Postglacial rebound and lateral viscosity variations: a semi-analytical approach based on a spherical model with Maxwell rheology, *Geophys. J. Int.*, **129**, F9-F13., 1997.

Dahlen, F.A., The Passive Influence of the Oceans Upon the Rotation of the Earth, *Geophys. Journal International*, **46**(2), 363-406, 1976.

Dal Forno, G. and Gasperini, P., Modelling of mantle postglacial relaxation in axisymmetric geometry with a composite rheology and a glacial load interpolated by adjusted spherical harmonics analysis, *Geophys. J. Int.*, **169**, 1301–1311, 2007.

Deblonde, G., and W.R. Peltier, A model of late Pleistocene ice sheet growth with realistic geography and simplified cryodynamics and geodynamics, *Climate Dynamics*, **5**, 103-110, 1990.

DeMets, C., R.G. Gordon, D.F. Argus and S. Stein, Effect of Recent Revisions to the Geomagnetic Reversal Time-Scale on Estimates of Current Plate Motions, *Geophys. Res. Letters*, **21**(20)**,** 1994.

Dyke, A. and Prest, V., Late Wisconsonian and Holocene history of the Laurentide ice-sheet, *Geogr. Phys. Quaternaire*, **41**(2), 237-263, 1987.

Dyke, A.S., Dredge, L.A., and Hodgson, D.A., North American deglacial marine and lake-limit surfaces. *Géographie physique et Quaternaire*, **59**(2-3), 155-185, 2005.

Dziewonski, A.M. and D.L. Anderson, Preliminary reference Earth model, *Physics of the Earth Planetary Interiors*, **25**(4), 297-356, 1981.

Ekström, G., Dziewonski, A.M., The unique anisotropy of the Pacific upper mantle. Nature 394, 168–172, 1998.

Emiliani, C., Pleistocene temperatures, *J. Geol.*, **63**, 538, 1955.

Engelhart, S. E., & Horton, B. P. Holocene sea level database for the Atlantic coast of the United States. *Quaternary Science Reviews*, **54**, 12-25, 2012.

Eringen, A.C., Linear Theory of Micropolar Elasticity, *Journal of Mathematics and Mechanics*, **15**(6), 909-923, 1966.

Fairbanks, R. G. A 17,000-year glacio-eustatic sea level record: influence of glacial melting rates on the Younger Dryas event and deep-ocean circulation. *Nature*, **342**(6250), 637-642, 1989.

Fairbanks, R.G., and Dodge, R.E., Annual periodicity of the skeletal oxygen and carbon Stable isotopic composition in the coral Montastrea Annularis, *Geochimica et Cosmochimica Acta*, **43**(7), 1-10, 1979.

Farrell, W.E., Deformation of the earth by surface loads, *Rev. Geophys. Space Phys*., **10**, 761-797, 1972.

Farrell, W.E., and Clark, J.A., On postglacial sea level, *Geophys. J.R. astr. Soc*., **46**, 647-667, 1976.

Gasperini, P., Sabadini, R., & Yuen, D. A. Deep continental roots: the effects of lateral variations of viscosity on post-glacial rebound. In Glacial Isostasy, Sea-Level and Mantle Rheology (pp. 21-32). Springer, Dordrecht, 1991.

Gasperini, P., Yuen, D. and Sabadini, R., Postglacial rebound with a non-Newtonian upper mantle and a Newtonian lower mantle rheology, *Geophys. Res. Lett*., **19**, 1711–1714, 1992.

Gasperini, P., Dal Forno, G., and Boschi, E., Linear or nonlinear rheology in the Earth's mantle: the prevalence of power-law creep in the postglacial isostatic readjustment of Laurentia, *Geophysical Journal International*, **157**(3), 1297-1302, 2004.

Gilbert, F. and G. Backus, Propagator matrices in elastic wave and vibration problems, *Mathematics*, 1966.

Gilbert, F. and G. Backus, The Resolving Power of Gross Earth Data, *Geophysical Journal of the Royal Astronomical Society*, **16(2)**, 169-205, 1968a.

Gilbert, F., and G. Backus, Elastic-gravitational vibrations of a radially stratified sphere, in *Dynamics of Stratified Solids*, edited by G. Hermann, p. 827, American Society of Mechanical Engineers, New York, 1968b.

Gilbert, F., Excitation of the normal modes of the Earth by earthquake sources, *Geophys. J.R. astr. Soc.*, **22**, 223, 1970.

Giunchi, C. and Spada, G., Postglacial rebound in a non-Newtonian spherical Earth, *Geophys. Res. Lett.*, **27**, 2065–2068, 2000.

Goes, S., Govers, R. and Vacher, P., Shallow mantle temperatures under Europe from P and S wave tomography, J. Geophys. Res., **105**(B5), 11 15311 169, 2000.

Goetze, C., and Kohlstedt, D.L., Laboratory study of dislocation climb and diffusion in olivine, *J. Geophys. Res*. **78**, 5961–5971, 1973.

Goldreich, P., and A. Toomre, Some remarks on polar wandering, *J. Geophys. Res*., **74**, 2555-2567, 1969.

Goldsby, D.L. and D.L. Kohlstedt, Gain Boundary Sliding in Fine-Grained Ice I, *Scripta Materialia*, **37**(9), 1399-1406, 1997.

Goldsby, D.L. and D.L. Kohlstedt, Superplastic deformation of ice: Experimental observations, *Journal of Geophysical Res*., **106**(B6), 11,017-11,030, 2001.

Gomez, N., D. Pollard and D. Holland, Sea –level feedback lowers projections of future Antarctic Ice-Sheet mass loss, *Nature Communications*, **6**:8798, 2015.

Gomez, N., Latychev, K., and Pollard, D., A Coupled Ice Sheet--Sea Level Model Incorporating 3D Earth Structure: Variations in Antarctica during the Last Deglacial Retreat. *Journal of Climate*, **31**(10), 4041–4054, 2018.

Gowan, E.J., and X. Zhang, et al., Global ice sheet reconstruction for the past 8000 years. PANGAEA,

Nature Communications, **12**, 1199, 2019.

Gowan, E.J., X. Zhang, et al., A new global ice sheet reconstruction for the past 80 000 years, *Nature Communications*, **12**, 2021.

Grand, S.P., Mantle shear-wave tomography and the fate of subducted slabs, *Phil. Trans. R. Soc. Lond., A*, **360**, 2475–2491, 2002.

Griffiths, S. D., & Peltier, W. R. Megatides in the Arctic Ocean under glacial conditions. *Geophysical research letters*, **35**(8), 2008.

Griffiths, S. D., & Peltier, W. R. Modeling of polar ocean tides at the Last Glacial Maximum: Amplification, sensitivity, and climatological implications. *Journal of Climate*, **22**(11), 2905-2924, 2009.

Hager, B.H., Clayton, R.W., Richards, M.A., Comer, R.P. and Dziewonski, A.M., Lower mantle heterogeneity, dynamic topography and the geoid, *Nature*, **313**, 541–545, 1985.

Han, D. and Wahr, J. The viscoelastic relaxation of a realistically stratified earth, and a further analysis of postglacial rebound. *Geophysical Journal International*, **120**(2), 287-311, 1995.

Hanyk L, Moser J, Yuen D A, et al. Time-domain approach for the transient responses in stratified viscoelastic Earth models. *Geophysical research letters*, 22(10): 1285-1288, 1995.

Hanyk, L., Matyska, C. and Yuen, D. A. Secular gravitational instability of a compressible viscoelastic sphere. *Geophysical research letters*, **26**(5), 557-560, 1999.

Hanyk, L., Matyska, C., and Yuen, D. A., Short time-scale heating of the Earth's mantle by ice-sheet dynamics. *Earth, planets and space*, **57**(9), 895-902, 2005.

Haskell, N.A., The motion of a viscous fluid under a surface load, 1, *Physics*, **6**, 265, 1935.

Hays, J.D., J. Imbrie and N.J. Shackleton, Variations in the Earth's Orbit: Pacemaker of the Ice Ages, *Science, New Series*, **194**, 1121-1132, 1976.

Henry, C., Das, S., and Woodhouse, J.H., The March 25, 1988 M w = 8.1 Antarctic Plate earthquake: moment tensor and rupture history, *J. Geophys. Res*. **105**, 16097–16119, 2000.

Herring, C., Diffusional viscosity of a polycrystalline solid, *J. appl. Phys*., **21**, 437, 1950.

Hetzel, R., and Hampel, A., Slip rate variations on normal faults during glacial-interglacial changes in surface loads. *Nature*, **435**, 81–84, 2005.

Hibbitt, D., Karlsson, B., Sorensen, P., Getting Started with ABAQUS – Version (6.11). Hibbitt, Karlsson & Sorensen, Inc., 2011.

Hill, E. M., Davis, J. L., Tamisiea, M. E., and Lidberg, M., Combination of geodetic observations and models for glacial isostatic adjustment fields in Fennoscandia, *Journal of Geoph. Res*., **115,** 2010.

Hillaire-Marcel, C., La glaciation et le relevement isostatiqu sur le cote est de la Baie d'Hudson, *Cahier de Geographie de Quebec*, **20**(50), 185-220, 1976.

Hillaire-Marcel, C. and R.W.F. Fairbridge, Isostasy and eustasy of Hudson Bay, *Geology*, **6(2),** 117-122, 1978.

Hirth, G. and Kohlstedt, D., Rheology of the Upper mantle and the mantle wedge: a view from the experimentalists, in Inside the Subduction Factory, *Geophysical Monograph Series*, Vol. **138**, pp. 83–105, ed. Eiler, J., American Geophysical Union, Washington, DC., 2003.

Huang, P., P. Wu, and H. Steffen, In search of an ice history that is consistent with composite rheology in Glacial Isostatic Adjustment modeling, *Earth & Planet. Sci. Lett.*, **517**, 26-37, 2019.

Huang, P., P. Wu, and W. van der Wal, Effects of mantle rheologies on viscous heating induced by Glacial Isostatic Adjustment, *Geophys. J. Int*., **213**:157-168, 2018.

Hughes, A. L. C., R. Gyllencreutz, Ø. S. Lohne, J. Mangerud, J.I. Svendsen, The last Eurasian ice sheets – a chronological database and time-slice reconstruction, DATED-1. Boreas, 45, 1–45, 2016.

Hunt, A.G. and P.E. Malin, Possible triggering of Heinrich events by ice-load-induced earthquakes, *Nature*, **393**, 155-158, 1998.

Huybers, P., and Langmuir, C., Feedback between deglaciation, volcanism, and atmospheric CO_2. *Earth and Planetary Science Letters*, **286**(3), 479-491, 2009.

Ivanovic, R. F., Gregoire, L. J., Kageyama, M., Roche, D. M., Valdes, P. J., Burke, A., ... & Tarasov, L. Transient climate simulations of the deglaciation 21–9 thousand years before present (version 1)–PMIP4 Core experiment design and boundary conditions. *Geoscientific Model Development*, **9**(7), 2563-2587, 2016.

Ivins, E.R., Sammis, C.G., On lateral viscosity contrast in the mantle and the rheology of low frequency geodynamics, *Geophys. J. Int*., **123**, 305–322, 1995.

Ivins, E. R., James, T. S., Wahr, J., O. Schrama, E. J., Landerer, F. W., & Simon, K. M. Antarctic contribution to sea level rise observed by GRACE with improved GIA correction. *Journal of Geophysical Research: Solid Earth*, **118**(6), 3126-3141, 2013.

Ivins, E. R., Caron, L., Adhikari, S., Larour, E., & Scheinert, M. A linear viscoelasticity for decadal to centennial time scale mantle deformation. *Reports on Progress in Physics*, **83**(10), 106801, (2020).

Imbrie, J. and K.P. Imbrie, Ice Ages: Solving the Mystery, *Geological Magazine*, 224 pp., 1979.

Ito, E. and E. Takahashi, Postspinel transformations in the system Mg2Si04-Fe2Si04 and some geophysical implications, *Journal of Geophysical Research*, 1989.

Ishii, T. R. Huang, et al, Complete agreement of the post-spinel transition with the 660-km seismic discontinuity, *Scientific Reports*, **8**, 2018.

James, T.S., and Bent, A.L., A comparison of eastern North American seismic strain-rates to glacial rebound strain-rates. *Geophysical Research Letters*, **21**, 2127–2130, 1994.

Jarvis. G.T. and W.R. Peltier, "Mantle convection as a boundary layer phenomenon", *Geophys. J.R. astr. Soc*., **68,** 389-427, 1982.

Jaupart, C., and Mareschal, J. C., Heat Flow and Thermal Structure of the Lithosphere-6.05, 2007.

Johnson, R.B. and DeGraff, J.V., Principles of Engineering Geology. Wiley, 1998.

Johnson, C.W., Y. Fu and R. Bürgmann, Hydrospheric modulation of stress and seismicity on shallow faults in southern Alaska, *Earth & Planet. Sci. Lett*., **530**, 115904, 2020.

Johnston, A.C., Suppression of earthquakes by large continental ice sheets. *Nature*, **330**, 467–469, 1987.

Johnston, P., P. Wu and K. Lambeck, Dependence of horizontal stress magnitude on load dimension in glacial rebound models, *Geophys.J.Int*., **132**, 41-60, 1998.

Jull, J. & McKenzie, D., The effect of deglaciation on mantle melting beneath Iceland. *J. Geophys. Res*., **101** (B10), 21,815-21,828, 1996.

Kachuck, S. B., & Cathles III, L. M. Benchmarked computation of time-domain viscoelastic Love numbers for adiabatic mantles. *Geophysical Journal International*, **218**(3), 2136-2149, 2019.

Kageyama, M., Harrison, S. P., Kapsch, M. L., Lofverstrom, M., Lora, J. M., Mikolajewicz, U., ... & Zhu, J. The PMIP4 Last Glacial Maximum experiments: preliminary results and comparison with the PMIP3 simulations. *Climate of the Past*, **17**(3), 1065-1089, 2021.

Kang, K., S. Zhong, G. A, W. Mao, The effects of non-Newtonian rheology in the upper mantle on relative sea level change and geodetic observables induced by Glacial Isostatic Adjustment process, *Geophys. J. Int*., in press, 2021.

Karato, S-I, and P. Wu, Rheology of the Upper Mantle: A Synthesis, *Science*, **260**(5109), 1993.

Karato, S., Micro-Physics of Post Glacial Rebound. In: Wu, P. (Ed.), Dynamics of the Ice Age Earth: A Modern Perspective. Trans Tech Publ., Switzerland, pp. 351–364, 1998.

Karato, S.I., Deformation of Earth Materials: An Introduction to the Rheology of Solid Earth, Cambridge University Press, 2008.

Karato, S. and B. Karki, Origin of lateral variation of seismic wave velocities and density in the deep mantle, *Journal of Geophysical Research: Atmospheres*, **106**(B11), 21771–21784, 2001.

Karato, S. and P. Wu, Rheology of the upper mantle: a synthesis, *Science*, **260:** 771-778, 1993.

Kaufmann, G. and D. Wolf, Deglacial land emergence and lateral upper-mantle heterogeneity in the Svalbard Archipelago – II. Extended results for high-resolution load models, *Geophys. J. Int*., **127**, 125-140, 1996.

Kaufmann, G. and D. Wolf, Effects of lateral viscosity variations on postglacial rebound: an analytical approach, *Geophys. J. Int*., **137**, 489-500, 1999.

Kaufmann, G. and P. Wu, Lateral asthenospheric viscosity variations and postglacial rebound: a case study for the Barents Sea, *Geophys. Res Lett*., **25**, 1963-1966, 1998.

Kaufmann, G., P. Wu and G. Li, Glacial isostatic adjustment in Fennoscandia for a laterally heterogeneous earth, *Geophys. J. Int*., **143**: 262-273, 2000.

Kaufmann, G., P. Wu and D. Wolf, Some effects of lateral heterogeneities in the upper mantle on postglacial land uplift close to continental margins, *Geophys.J.Int.*, **128**, 175-187. 1997.

Kaufmann, G. and P. Wu, Glacial isostatic adjustment in Fennoscandia with a three dimensional viscosity structure as an inverse problem, *Earth and Planetary Science Letters*, **197**, 1-10, 2002.

Kaufmann, G., P. Wu and E.R. Ivins, Lateral viscosity variations beneath Antarctica and their implications on regional rebound motions and seismotectonics, *J. Geodyn*. **39**(2), 165-181, 2005.

Kaula, W.M., Elastic models of the mantle corresponding to variations in the external gravity field, *J. Geophys. Res*., **68**, 4967, 1963.

Kennett, B. and TkalCi´c, H, Dynamic Earth: crustal and mantle heterogeneity, *Aust. J. Earth Sci*., **55**(3), 265–279, 2008.

Khan, N. S., Ashe, E., Horton, B. P., Dutton, A., Kopp, R. E., Brocard, G., ... & Scatena, F. N. Drivers of Holocene sea-level change in the Caribbean. *Quaternary Science Reviews*, **155**, 13-36, 2017.

Khan, C., S. Muliyil and B.J. Rao, Genome Damage Sensing Leads to Tissue Homeostasis in Drosophila, *Int. Rev. Cell Mol. Biol*., **345**, 173-224, 2019.

King, G.C.P., Stein, R.S., and Lin, J., Static stress changes and the triggering of earthquakes. *Bulletin of the Seismological Society of America* **84**(3), 935-953, 1994.

Klemann, V., P. Wu, and D. Wolf, Compressible viscoelasticity: stability of solutions for homogeneous plane earth models, *Geophys. J. Int*., **153**, 569-585, 2003.

Kuo, J.T., Static response of a multilayered medium under inclined surface loads, *J. Geophys. Res*., **74**, 3195, 1969.

Lambeck, K., C. Smither and P. Johnston, Sea-level change, glacial rebound and mantle viscosity for northern Europe, *Geophys. Journal International*, **134**(1), 102-144, 1998.

Lambeck, K., On the choice of timescale in glacial rebound modelling: mantle viscosity estimates and the radiocarbon timescale, *Geophys. J. Int*., **134**(2), 647-651, 1998.

Lambeck, K., A. Purcell and S. Zhao, The North American Late Wisconsin ice sheet and mantle viscosity from glacial rebound analyses, *Quaternary Science Reviews*, **158,** 172-210, 2017.

Laskar, J., Accurate methods in general planetary theory, *Astronomy and Astrophysics*, **144**, 133-146, 1985.

Latychev, K., Mitrovica, J.X., Tromp, J., Tamisiea, M.E., Komatitsch, D. and Christara, C.C., Glacial isostatic adjustment on 3-D Earth models: a finite-volume formulation, *Geophys. J. Int*., **161**, 421222, 2005a.

Latychev, L., Mitrovica, J.X., Tamisiea, M.E., Tromp, J. and Moucha, R., Influence of lithospheric thickness variations on 3-D crustal velocities due to glacial isostatic adjustment, *Geophys. Res. Lett.*, **32**, L01304, 2005b.

Lau, H. C. P., Austermann, J., Holtzman, B. K., Havlin, C., Lloyd, A. J., Book, C., & Hopper, E. Frequency dependent mantle viscoelasticity via the complex viscosity: Cases from Antarctica. Journal of Geophysical Research: Solid Earth, 126, e2021JB022622, 2021.

Lau, H. C. P., & Holtzman, B. K. "Measures of dissipation in viscoelastic media" extended: Toward continuous characterization across very broad geophysical time scales. Geophysical Research Letters, 46, 9544–9553, 2019GL083529, 2019.

Lau, H. C. P., Austermann, J., Mitrovica, J. X., Crawford, O., Al-Attar, D., & Latychev, K. (2018). Inferences of mantle viscosity based on ice age data sets: The bias in radial viscosity profiles due to the neglect of laterally heterogeneous viscosity structure. Journal of Geophysical Research: Solid Earth, 123(9), 7237-7252.

Lau, H. C., Mitrovica, J. X., Austermann, J., Crawford, O., Al-Attar, D., & Latychev, K. (2016). Inferences of mantle viscosity based on ice age data sets: Radial structure. Journal of Geophysical Research: Solid Earth, 121(10), 6991-7012.

Leitch, A.M., and Yuen, D.A., Internal heating and thermal constraints on the mantle, *Geophys. Res. Lett,*. **16**, 1407–1410, 1989.

Lekic, V. and B. Romanowicz, Inferring upper-mantle structure by full waveform tomography with the spectral element method, *Geophys. J. Int*., **185**, 799-831, 2011.

Li, P., Karato, S., Wang, Z., High-temperature creep of fine-grained polycrystalline CaTiO 3, *Phys. Earth Planet. Inter.*, **95,** 19–36, 1996.

Li, Y., M. Bao, M. Ferndahl and A. Cathelin, 23GHz front-end circuits in SiGe BICMOS technology, *IEEE Symposium*, 2003.

Li, T., P. Wu, H. Steffen, H.S. Wang, In search of laterally heterogeneous viscosity models of Glacial Isostatic Adjustment with the ICE-6G_C global ice history model, *Geophys. J. Int*., **214**, 1191-1205, 2018.

Li, T., and Wu, P., Laterally heterogeneous lithosphere, asthenosphere and sub-lithospheric properties under Laurentia and Fennoscandia from Glacial Isostatic Adjustment. *Geophysical Journal International*, **216**(3), 1633–1647, 2019.

Li, T., P. Wu, H.S. Wang, H. Steffen, N.S. Khan. S.E. Engelhart, M. Vacchi, T.A. Shaw, W.R. Peltier, B.P. Horton, Uncertainties of Glacial Isostatic Adjustment model predictions in North

America associated with 3D structure, *Geophys. Res. Lett*., **47**, 2020.

Li, Tanghua, Nicole S. Khan, Alisa V. Baranskaya, Timothy A. Shaw, W. Richard Peltier, Gordan R. Stuhne, Patrick Wu, and Benjamin P. Horton. "Influence of 3D Earth structure on Glacial Isostatic Adjustment in the Russian Arctic." *Journal of Geophysical Research: Solid Earth*, 2020.

Li, Y., W. Cai and L. Zhu, Numerical simulations for plates under ice impact based on a concrete constitutive ice model, *International Journal of Impact Engineering*, **143**(17-18), 2020.

Lindén, R., Den senkvartara strandförskjutningens förloop och kronologi i Angermanland, *Geol. Foeren. Stokholm Foerh*, **60**, 397-404, 1938.

Litherland, A.E., Ultrasensitive mass spectrometry with accelerators, *Annu. Rev. Nucl. Sci.*, **30**, 437-473, 1980.

Longman, I.M., A Green's function for determining the deformation of the earth under surface mass loads, 1, *Theory. J. Geophys. Res*., **67**, 845, 1962.

Longman, I.M., A Green's function for determining the deformation of the earth under surface mass loads, 2, Computations and numerical results, *J. Geophys. Res*., **68**, 485, 1963.

Love, A.E.H., IX. The stress produced in a semi-infinite solid by pressure on part of the boundary, *Mathematical, Physical and Eng*. Sciences, 1929.

Love, T., G.A. Milne, L. Tarasov, S.E. Engelhart, M.P. Hijma, K. Latychev, B.P. Horton, and T.E. Törnqvist, The contributions of glacial isostatic adjustment to projections of sea-level change along the Atlantic and Gulf coasts of North America, *Earth's Future*, **4**, 2016.

Lu, C., S.P. Grand, H. Lai, and E.J. Garnero, TX2019slab: a new P and S Tomography Model incorporating subducting slabs, *Journal of Geophysical Research: Solid Earth*, **124**(11), 11549–11567, 2019.

Lund, B., *Effects of deglaciation on the crustal stress field and implications for end glacial faulting: a parametric study of simple earth and ice models*. Swedish Nuclear Fuel and Waste Management Co., Stockholm, Technical Report TR-05-04, 68 pp., 2005.

Lund, B., Schmidt, P., and Hieronymus, C., *Stress evolution and fault stability during glaciation*. Swedish Nuclear Fuel and Waste Management Co., Stockholm, Technical Report TR-09-15, 101 pp., 2009.

Mainprice, D., A. Tommasi, H. Couvy and P. Cordier, Pressure sensitivity of olivine slip systems and seismic anisotropy of Earth's upper mantle, *Nature*, **433**(7027), 731-733, 2005.

Martinec, Z., Spectral-finite element approach to three-dimensional viscoelastic relaxation in a

spherical Earth, *Geophys. J. Int*., **142**, 117–141, 2000.

Martinec, Z., Klemann, V., van der Wal, W., Riva, R. E. M., Spada, G., Sun, Y., ... & James, T. S. A benchmark study of numerical implementations of the sea level equation in GIA modelling. *Geophysical Journal International*, *215*(1), 389-414, 2018.

McConnell, R.K., Viscosity of the mantle from relaxation time spectra of isostatic adjustment, *J. Geophys. Res*., **73**(22), 7089-7105, 1968.

McKenzie, D.P., The viscosity of the lower mantle, *J. Geophys. Res*., **71**, 3995, 1966.

McKenzie, D.P., The viscosity of the mantle, *Geophys. J. Roy. Astron. Soc*., **14**, 297, 1967.

McKenzie, D.P., The geophysical importance of high temperature creep, in *The history of the Earth's crust*, ed. R.A. Phinney, Princeton University Press, Princeton, New Jersey, 1968.

McKenzie, D.P., A geologist reflects on a long career, *Ann. Rev. Earth Planet. Sci*., **46**, 1-20, 2018.

Melini, D., and Spada, G., Some remarks on Glacial Isostatic Adjustment modelling uncertainties. *Geophysical Journal International*, **218**(1), 401–413, 2019.

Milankovic, M., Kanon der Erdbestrahlung und Seine Anwendung auf das Eiszeitenproblem, Königlich Serbische Akademie, 1941.

Milne, G.A., J.X. Mitrovica, J.L Davis, H.-G. Scherneck, J.M. Johansson, M. Ekman, and H. Koivula, Continuous GPS Measurements of Postglacial Adjustment in Fennoscandia, 2. Modeling Results, *J. Geophys. Res*., **109**, 2004.

Milne, G. A., Latychev, K., Schaeffer, A., Crowley, J. W., Lecavalier, B. S., and Audette, A., The influence of lateral Earth structure on glacial isostatic adjustment in Greenland. *Geophysical Journal International*, **214**(2), 1252–1266, 2018.

Mitrovica, J.X. and A.M. Forte, A new inference of mantle viscosity based upon joint inversion of convection and glacial isostatic adjustment data, *Earth and Planetary Science Letters*, **225(1-2)**, 177-189, 2004.

Mitrovica, J.X. & Peltier, W.R., A complete formalism for the inversion of post glacial rebound data: resolving power analysis, Geophys. J. Int., 104, 267–288, 1991.

Mitrovica, J.X. and W.R. Peltier, On postglacial geoid subsidence over the equatorial oceans", *J. Geophys. Res*.**, 96**, 20053-20071, 1991.

Mitrovica, J.X., and W.R. Peltier, "The inference of mantle viscosity from an inversion of the Fennoscandian relaxation spectrum", *Geophys. J. Int*., **114**, 45-62, 1993.

Mitrovica, J. X., Davis, J. L., Mathews, P. M. and Shapiro, I. I. Determination of tidal h Love number parameters in the diurnal band using an extensive VLBI data set. *Geophysical research letters*, **21**(8), 705-708, 1994.

Mitrovica, J.X. and W.R. Peltier, "Constraints on Mantle Viscosity based upon the inversion of post-glacial uplift data from the Hudson Bay region, *Geophys. J. Int*., **122,** 353-376, 1995.

Moulik, P. & G. Ekström, An anisotropic shear velocity model of the Earth's mantle using normal modes, body waves, surface waves and long-period waveforms, *Geophys. J. Int*., **199**, 1713-1738, 2014.

Munk, W.H. and MacDonald, J.F., *The rotation of the Earth*, Cambridge University Press, New York, 1960.

Murakami, M., K. Hirose, K. Kawamura, N. Sata and Y. Ohishi, Post-perovskite phase transition in MgSi03, *Science*, **7**(304), 2004.

Nakada, M. and Lambeck, K. Late Pleistocene and Holocene sea-level change; evidence for lateral mantle viscosity structure?. In Glacial Isostasy, Sea-Level and Mantle Rheology (pp. 79-94). Springer, Dordrecht, 1991.

Nakada, M., and Yokose, H., Ice age as a trigger of active Quaternary volcanism and tectonism. *Tectonophysics*, **212**(3-4), 321-329, 1992.

Nield, G. A., Whitehouse, P. L., van der Wal, W., Blank, B., O'Donnell, J. P., and Stuart, G. W., The impact of lateral variations in lithospheric thickness on glacial isostatic adjustment in West Antarctica. *Geophysical Journal International*, **214**(2), 811–824, 2018.

Pan, E., Chen, J. Y., Bevis, M., Bordoni, A., Barletta, V. R., & Molavi Tabrizi, A. An analytical solution for the elastic response to surface loads imposed on a layered, transversely isotropic and self-gravitating Earth. *Geophysical Supplements to the Monthly Notices of the Royal Astronomical Society*, **203**(3), 2150-2181, 2015.

Pari, G. and W.R. Peltier, The heat flow constraint on mantle tomography-based convection models: towards a geodynamically self-consistent inference of mantle viscosity, *Oceano. Literature Review*, **43**, 1996.

Parsons, B.E., *Changes in the Earth's shape*, PhD thesis, Cambridge University, Cambridge, 1972.

Pattyn, F., Antarctic subglacial conditions inferred from a hybrid ice sheet/ice stream model, *Earth and Planetary Science Letters*, **295**(3), 451-461, 2010.

Paulson, A., Zhong, S. & Wahr, J., Modelling post-glacial rebound with lateral viscosity variations, *Geophys. J. Int*., **163**(1), 357–371, 2005.

Peltier, W.R., Penetrative convection in the planetary mantle, *Geophys. Fluid Dyn*., **3**, 265, 1972.

Peltier, W.R., The impulse response of a Maxwell earth, *Rev. Geophys. Space Phys*., **12**, 649, 1974.

Peltier, W.R. and Andrews J.T., Glacial-Isostatic adjustment-I. The Forward Problem, *Geophys. J.R. astr. Soc*., **46**, 605-646, 1976.

Peltier, W.R., Glacial isostatic adjustment-II. The inverse problem, *Geophys. J.R. astr. Soc.*, **46**, 669-705, 1976.

Peltier, W.R., W.E. Farrell and J.A. Clark, Glacial isostasy and relative sea level: a global finite element model, *Tectonophysics*, **50**, 81-110, 1978.

Peltier, W.R., Constraint on deep mantle viscosity from LAGEOS acceleration data, *Nature*, **304**, 434-436, 1983.

Peltier, W.R., The LAGEOS constraint on deep mantle viscosity: results from a new normal mode method for the inversion of viscoelastic relaxation spectra, *J. Geophys. Res*., **90**, 9411-9421, 1985.

Peltier, W.R., R.A. Drummond and A.M. Tushingham, Postglacial rebound and transient lower mantle rheology, *Geophys. J.R. astr. Soc*., **87**, 79-116, 1986.

Peltier, W.R., and L.P. Solheim, Mantle phase transitions and layered chaotic convection, *Geophys. Res. Lett*., **19**, 321-324, 1992.

Peltier, W.R., A.M. Forte, J.X. Mitrovica and A.M. Dziewonski, Earth's gravitational field: Seismic tomography resolves the enigma of the Laurentian anomaly, *Geophys. Res. Lett.*, **19**, 1555-1558, 1992.

Peltier, W.R., Ice Age Paleotopography, *Science*, **265**, 195-201, 1994.

Peltier, W.R., "Postglacial variations in the level of the sea: Implications for climate dynamics and solid-Earth geophysics", invited paper, *Reviews of Geophysics*, **36**, 603-689, 1998.

Peltier, W.R., Postglacial variations in the level of the sea: Implications for climate dynamics and solid-Earth geophysics, invited paper, *Reviews of Geophysics*, **36**, 603-689, 1998a.

Peltier, W.R., The inverse problem for mantle viscosity, invited paper, *Inverse Problems*, **14**, 441-478, 1998b.

Peltier, W.R., On eustatic sea level history, Last Glacial Maximum to Holocene, *Quat. Sci., Rev*., **21**, 377-396, 2002.

Peltier, W.R., Global glacial isostasy and the surface of the ice-age Earth: the ICE-5G (VM2) model and GRACE, *Ann. Rev. Earth and Planet. Sci*. **32**, 111-149, 2004.

Peltier, W.R. and L.P. Solheim, The climate of the Earth at Last Glacial Maximum: statistical equilibrium state and a mode of internal variability, *Quat. Sci. Rev.*, **23,** 335-357, 2004.

Peltier, W.R. and R.G. Fairbanks, Global glacial ice volume and Last Glacial Maximum duration from an extended Barbados sea level record, *Quaternary Science Reviews*, **25,** 3322-3337, 2006.

Peltier, W.R., Rapid climate change and Arctic Ocean freshening, *Geology*, **35,** 1147-1148, 2007.

Peltier, W.R., History of Earth Rotation, in *Volume 9 of The Treatise On Geophysics*, G. Schubert ed., pp. 243-293 Elsevier Press, 2007.

Peltier, W.R. and R. Drummond, The rheological stratification of the lithosphere: A direct inference based upon the geodetically observed pattern of the glacial isostatic adjustment of the North American continent, *Geophys. Res. Lett.*, **35**, 2008.

Peltier, W.R., R. Drummond and K. Roy, "Comments on the paper of Chambers et al. (2010) concerning the influence of rotational feedback on geoid height time-dependence in glacial isostatic adjustment", *J. Geophys. Res.-Solid Earth*, **117,** B11403, 2012.

Peltier, W. R. and Vettoretti, G. Dansgaard-Oeschger oscillations predicted in a comprehensive model of glacial climate: A "kicked" salt oscillator in the Atlantic. *Geophysical Research Letters*, **41**(20), 7306-7313, 2014.

Peltier, W.R., Argus, D.F. and Drummond, R., Space geodesy constrains ice-age terminal deglaciation: the global ICE-6G_C (VM5a) model, *J. Geophys. Res. – Solid Earth*, **120**(1), 450-487, 2015.

Peltier, W.R. "The history of the Earth's rotation: Impacts of deep Earth physics and surface climate variability", In: Gerald Schubert (editor-in-chief) Treatise on Geophysics, 2nd edition, Vol. 9., Oxford:Elsevier, p. 221-279, 2015.

Peltier, W.R., Argus, D.F., Drummond, R., Comment on "An assessment of the ICE-6G_C (VM5a) glacial isostatic adjustment model" by Purcell et al., *J. Geophys. Res.- Solid Earth*, **123**, 2018.

Peltier, W. R., Ma, Y. and Chandan, D. The KPP trigger of rapid AMOC intensification in the nonlinear Dansgaard-Oeschger relaxation oscillation. *Journal of Geophysical Research: Oceans*, **125**(5), e2019JC015557, 2020.

Plag, H. P., & Jüttner, H. U. Rayleigh-Taylor instabilities of a self-gravitating *Earth. Journal of geodynamics*, **20**(3), 267-288, 1995.

Quinn, T.R., Tremaine, S. and M. Duncan, A Three Million Year Integration of the Earth's Orbit, *Astronomical Journal*, **101**, p.2287, 1991.

Ranalli, G., Rheology of the Earth. 2nd ed., Chapman & Hall, London, 1995.

Ratcliff, J. T., & Gross, R. S. Combinations of Earth orientation measurements: SPACE2008, COMB2008, and POLE2008. Pasadena, CA: Jet Propulsion Laboratory, National Aeronautics and Space Administration, 2010.

Reiss, M.C., G. Rumpker, F. Tilmann, et al., Seismic anisotropy of the lithosphere and asthenosphere beneath southern Madagascar from teleseismic shear wave splitting analysis and waveform modeling, *Journal of Geophys. Res.: Solid Earth*, **121,** 6627-6643, 2016.

Richter, F.M., Dynamic models for sea floor spreading, *Rev. Geophys. Space Phys*., **11**, 223, 1973.

Riva, R. E. M., Gunter, B. C., Urban, T. J., Vermeersen, B. L. A., Lindenbergh, R. C.,and Helsen, M. M., et al., Glacial isostatic adjustment over Antarctica from combined ICESat and GRACE satellite data, *Earth and Planetary Science Letters*, **288**(3-4), 516–523, 2009.

Rostami, K., Peltier, W. R., & Mangini, A. Quaternary marine terraces, sea-level changes and uplift history of Patagonia, Argentina: comparisons with predictions of the ICE-4G (VM2) model of the global process of glacial isostatic adjustment. *Quaternary Science Reviews*, **19**(14-15), 1495-1525, 2000.

Roy, K. and W.R. Peltier, GRACE era secular trends in Earth rotation parameters: A global scale impact of the global warming process, *Geophys. Res. Lett.*, **38**, L10306, 2011.

Roy, K., Peltier, W.R., Space geodetic and water level gauge constraints on continental uplift and tilting over North America: Regional convergence of the ICE-6G_C (VM5a/VM6) models, *Geophys. J. Int*., **210**(2), 1115-1142, 2017.

Roy, K., & Peltier, W. R. Relative sea level in the Western Mediterranean basin: a regional test of the ICE-7G_NA (VM7) model and a constraint on late Holocene Antarctic deglaciation. *Quaternary Science Reviews*, **183**, 76-87, 2018.

Sabadini, R., Yuen, D. A. and Boschi, E. Polar wandering and the forced responses of a rotating, multilayered, viscoelastic planet. *Journal of Geophysical Research: Solid Earth*, **87**(B4), 2885-2903, 1982.

Sabadini, R., Yuen, D.A. and Portney, M., The effects of upper-mantle lateral heterogeneities on post-glacial rebound, *Geophys. Res. Lett*., **13**, 337–340, 1986.

Sasgen, I., Klemann, V., and Martinec, Z., Towards the inversion of GRACE gravity fields for present-day ice-mass changes and glacial-isostatic adjustment in North America and Greenland, *Journal of Geodynamics*, **59**-60, 49–63, 2012.

Sauber, J. M., and Molnia, B.F., Glacier ice mass fluctuations and fault instability in tectonically active Southern Alaska, *Global and Planetary Change*, **42**, 279–293, 2004.

Sauber, J. M., and Ruppert, N., Rapid Ice Mass Loss: Does it Have an Influence on Earthquake Occurrence in Southeast Alaska? American Geophysical Union: Active Tectonics and Seismic Potential of Alaska, *Geophysical Monograph Series*, **179**, 2008.

Sauramo, M., Land uplift with hinge lines in Fennoscandia, *Ann. Acad. Sci. Fenn., Ser. A*, **344**, 1-25, 1958.

Schapery, R.A., *Irreversible thermodynamics and variational principles with applications to viscoelasticity*, PhD thesis, Calif. Inst. of Technol., Pasadena, 1962.

Schmeling, H., On the interaction between small- and large-scale convection and postglacial rebound flow in a power-law mantle, *Earth planet. Sci. Lett*., **84**, 254–262, 1987.

Schmidt, P., Lund, B., and Hieronymus, C., Implementation of the glacial rebound prestress advection correction in general-purpose finite element analysis soft-ware: springs versus foundations. *Computers & Geosciences*, **40**, 97–106, 2012.

Shackleton, N., Oxygen Isotope Analyses and Pleistocene Temperatures Re-assessed, *Nature*, **215**, 15-17, 1967.

Shackleton, N.J., A. Berger, and W.R. Peltier, An alternative astronomical calibration of the lower Pleistocene timescale based on ODP site 677, *Transactions of the Royal Society of Edinburgh: Earth Sciences*, **81**, 251-261, 1990.

Shahnas, H. and Peltier, W.R., The impacts of mantle phase transitions and the iron spin crossover in ferropericlase on convective mixing – is the evidence for compositional convection definitive?: New results from a Yin-Yang overset grid-based control volume model, *J. Geophys. Res.-Solid Earth*, **120,** 5884-5910, 2015.

Shennan, I. and B. Horton, Holocene land- and sea-level changes in Great Britain, *Journal of Quaternary Sci*., **17**, (5-6), 511-526, 2002.

Shepherd, A., et al., Mass balance of the Antarctic Ice Sheet from 1992 to 2017, *Nature*, **558**, 219-222, 2018.

Shepherd, A., et al., Mass balance of the Greenland Ice Sheet from 1992 to 2018, *Nature*, **579**(7798), 223-239, 2020.

Shilts, W.W., Rappol, M. & Blais, A., Evidence of late and postglacial seismic activity in the Temiscouata-Madawaska Valley, *Quebec-NewBrunswick,Canada, Can.J.EarthSci.*, **29**, 1043-1059, 1992.

Sigvaldason, G. E., Annertz, K., and Nilsson, M., Effect of glacier loading/deloading on volcanism: postglacial volcanic production rate of the Dyngjufjöll area, central Iceland. *Bulletin of Volcanology*, **54**(5), 385-392, 1992.

Simms, A.R., and L. Lisiecki, et al., Balancing the last glacial maximum (LGM) sea-level budget, *Quat. Sci. Reviews*, **205**, 143-153, 2019.

Simms, A.R., Interactive comment on "Last interglacial sea levels within the Gulf of Mexico and northwestern Caribbean Sea", *Earth Syst. Sci. Data Discuss.*, **253,** 2020.

Simon, K. M., and Riva, R. E. M., Uncertainty estimation in regional models of long-term GIA uplift and sea level change: An overview, *Journal of Geophysical Research: Solid Earth*, **125**(8), e2019JB018983, 2020.

Simon, K. M., Riva, R. E. M., Kleinherenbrink, M., and Tangdamrongsub, N., A data-driven model for constraint of present-day glacial isostatic adjustment in North America, *Earth and Planetary Science Letters*, **474,** 322–333, 2017.

Slater, L., Jull, M., McKenzie, D., and Gronvöld, K., Deglaciation effects on mantle melting under Iceland: results from the northern volcanic zone, *Earth Planet. Sci. Lett.*, **164**, 151-164, 1998.

Solheim, L.P. and W.R. Peltier, "Avalanche effects in phase transition modulated thermal convection: a model of the earth's mantle", *J. Geophys. Res*., **99**, 6997-7018, 1994a.

Solheim, L.P. and W.R. Peltier, "660 km phase boundary deflections and episodically layered isochemical convection", *J. Geophys. Res*., **99**, 15861-15875, 1994b.

Spada, G., Yuen, D.A., Sabadini, R. and Boschi, E., Lower-mantle viscosity constrained by seismicity around deglaciated regions, *Nature*, **351,** 53-55, 1991.

Spada, G., Sabadini, R., Yuen, D. A. and Ricard, Y. Effects on post-glacial rebound from the hard rheology in the transition zone. *Geophysical Journal International*, **109**(3), 683-700, 1992.

Spada, G, and Boschi, L. "Using the Post—Widder formula to compute the Earth's viscoelastic Love numbers." *Geophysical Journal International* 166.1 309-321, 2006.

Spada, G., Antonioli, A., Cianetti, S. and Giunchi, C., Glacial isostatic adjustment and relative sea level changes: the role of lithospheric and upper mantle heterogeneities in a 3D spherical Earth, *Geophys. J. Int*., **165**, 692–702, 2006.

Spada, G., Barletta, V. R., Klemann, V., Riva, R. E. M., Martinec, Z., Gasperini, P., ... & King, M. A. A benchmark study for glacial isostatic adjustment codes. *Geophysical Journal International*, *185*(1), 106-132, 2011.

Steffen, H., G. Kaufmann and P. Wu, Three dimensional finite-element modeling of the glacial isostatic adjustment in Fennoscandia, *Earth and Planetary Science Letters*, **50**: 358-375, 2006.

Steffen, H., P. Wu and G. Kaufmann, Sensitivity of crustal velocities in Fennoscandia to radial and lateral viscosity variations in the mantle, *Earth and Planetary Science letters*, **257**, 474-485, 2007.

Steffen, H., and P. Wu, Glacial isostatic adjustment in Fennoscandia - a review of data and modeling. *J. Geodyn.*, 52, 169-204, 2011.

Steffen, H., P. Wu, and H.S. Wang, Optimal locations for absolute gravity measurements and sensitivity of GRACE observations for constraining glacial isostatic adjustment on the northern hemisphere, *Geophys. J. Int*., **190**, 1483-1494, 2012.

Steffen, H. and P. Wu, The sensitivity of GNSS measurements in Fennoscandia to distinct three-dimensional upper-mantle structures, *Solid Earth*, **5**, 557-567, 2014.

Steffen, H., P. Wu, and H.S. Wang, Optimal locations of sea-level indicators in glacial isostatic adjustment investigations, *Solid Earth*, **5**, 511-521, 2014d.

Steffen, R., P. Wu, H. Steffen, and D.W. Eaton, On the implementation of faults in finite element glacial isostatic adjustment models, *Computers & Geosciences*, **62**, 150-159, 2014a.

Steffen, R., P. Wu, H. Steffen, and D.W. Eaton, The effect of earth rheology and ice sheet size on fault-slip and magnitude of postglacial earthquakes, *Earth & Planet. Sci. Lett*., **388**, 71-80, 2014b.

Steffen, R., H. Steffen, P. Wu, and D.W. Eaton, Stress and fault parameters affecting fault slip magnitude and activation time during a glacial cycle, *Tectonics*, **33**, 1461-1476, 2014c.

Steffen, R., H. Steffen, P. Wu, and D.W. Eaton, Reply to comment by Hampel et al. on "Stress and fault parameters affecting fault slip magnitude and activation time during a glacial cycle", *Tectonics*, **34**(11), 2359-2366, 2015.

Steffen, R., Steffen, H., Weiss, R., Lecavalier, B.S., Milne, G.A., Woodroffe, S.A., and Bennike, O., Did deglaciation of the Greenland ice sheet cause a large earthquake and tsunami around 10,600 years ago?, 2020.

Steffen, R., P. Wu, and B. Lund, Geomechanics of Glacially-Triggered Faulting, in "Glacially-Triggered Faulting" edited by H. Steffen, O. Olesen & R. Sutinen, p. 20-39, 2021.

Stein, **S.,** Sleep, N.H., Geller, R.J., Wang, S.C. and Kroeger, G.C., Earthquakes along the passive margin of Eastern Canada, *Geophys. Res. Lett.*, **6,** 537-540, 1979.

Stephenson, E.R. and L.V. Morrison, Long terms fluctuations in the Earth's rotation: 700 B.C. to A.D. 1990, *Philos. Trns. R. Soc. London, Ser. A*, **351**, 165-202, 1995.

Stuiver, M. and P.J. Reimer, Extended ^{14}C data base and revised calib. 3.0 ^{14}C age calibration program, *Radiocarbon*, **35,** 215-230, 1993.

Tackley, P.J., Stevenson, D.J., Glatzmaier, G.A., Schubert, G., Effect of an endothermic phase transition at 670 km depth in a spherical model of convection in the earth's mantle, *Nature*, **361**, 699–704, 1993.

Tackley, P.J., et al. including G. Schubert, Effects of multiple phase transitions in a three-dimensional spherical model of convection in Earth's mantle, *Journal of Geophys. Res.: Solid Earth*, **99**(B8), 1994.

Tanaka, Y., Klemann, V., Martinec, Z. & Riva, R., Spectral-finite element approach to viscoelastic relaxation in a spherical compressible Earth: application to GIA modelling, *Geophys. J. Int*., **184**(1), 220–234, 2011.

Tanaka Y, Klemann V, Okuno J. Application of a numerical inverse Laplace integration method to surface loading on a viscoelastic compressible Earth model. *Pure and applied geophysics*, **166**(8): 1199-1216, 2009.

Tang, H, and Sun, W. "New method for computing post-seismic deformations in a realistic gravitational viscoelastic earth model." *Journal of Geophysical Research: Solid Earth* **124**.5: 5060-5080, 2009.

Tarantola, A., and B. Vallette, Inverse problems = Quest for information, *Journal of Geophysics*, **50(1)**, 1981.

Tarantola, A., and B. Vallette, Generalized nonlinear inverse problems solved using the least squares criterion, *Reviews of Geophysics and Space Physics*, **20(2)**, 219-232, 1982.

Tarasov, L., Dyke, A. S., Neal, R. M., & Peltier, W. R. A data-calibrated distribution of deglacial chronologies for the North American ice complex from glaciological modeling. *Earth and Planetary Science Letters*, **315**, 30-40, 2012.

Trampert, J. and R.D. van der Hilst, Towards a quantitative interpretation of global seismic tomography, in Earth's Deep Mantle: Structure, Comosition, and Evolution, *Geophysical Monograph Series*, **160**, AGU, 2005.

Tushingham, A., & Peltier, W. R. Ice-3G: A new global model of late Pleistocene deglaciation based upon geophysical predictions of post-glacial relative sea level change. *Journal of Geophysical Research: Solid Earth*, **96**(B3), 4497-4523, 1991.

Uenzelmann-Neben, G., Schmidt D.N., Niessen, F., and Stein, R., Intraplate volcanism off South Greenland: caused by glacial rebound? *Geophys. J. Int.*, **190**, 1-7, 2012.

Urey, H.C., The thermodynamic properties of isotopic substances, *The Journal of the Chemical Society*, 562-581, 1947.

Vacchi, M., S.E. Engelhart, including W.R. Peltier, et al., Postglacial relative sea-level histories along the eastern Canadian coastline, *Quaternary Sci. Reviews*, **201**, 124-146, 2018.

Van Bemmelen, R.W., Berlage, H.P., and Gerlands Beitr. Z. *Geophys*. 43, 19-55, 1935.

van der Wal, W., P. Wu, H.S. Wang, and M.G. Sideris, Sea levels and uplift rate from composite rheology in Glacial Isostatic Adjustment modeling, *J. Geod.* 50:38-48, 2010.

van der Wal, W., A. Barnhoorn, P. Stocchi, S. Gradmann, P. Wu, M. Drury, and B. Vermeersen, Glacial Isostatic Adjustment Model with Composite 3D Earth Rheology for Fennoscandia, *Geophy. J. Int.*, **192**(3), 1109-1115, 2013.

van der Wal, W., P.L. Whitehouse, and E.J.O. Schrama, Effect of GIA models with 3D composite mantle viscosity on GRACE mass balance estimates for Antarctica, *Earth and Planetary Science Letters*, **414**, 134-143, 2015.

Velay-Vitow, J., Peltier, W. R., & Stuhne, G. R. The tides of the glacial ocean and their possible connection to Heinrich event instabilities of the Laurentide ice sheet. *Journal of Geophysical Research: Oceans*, **125**(1), e2019JC015444, 2020.

Velay-Vitow, J., & Richard Peltier, W. Out of the ice age: Megatides of the arctic ocean and the Bølling-Ållerød, Younger Dryas transition. *Geophysical Research Letters*, **47**(23), e2020GL089870, 2020.

Velay-Vitow, J., Peltier, W. R., & Stuhne, G. R. An investigation of the possibility of non-Laurentide ice stream contributions to Heinrich event 3. *Quaternary Research*, **101**, 13-25, 2021.

Vermeersen, L. L. A., Sabadini, R. AND Spada, G. Compressible rotational deformation. *Geophysical Journal International*, **126**(3), 735-761, 1996.

Vermeersen, L. L. A. AND Sabadini, R. Effects of compressibility and stratification on viscoelastic relaxation: the analytical perspective. In Retrospective Collection (Vol. 24, pp. 123-134). Trans Tech Publications, 1998.

Vermeersen, L. L. A. and Mitrovica, J. X. Gravitational stability of spherical self-gravitating relaxation models. *Geophysical Journal International*, **142**(2), 351-360, 2000.

Vestøl, O., J. Ågren, H. Steffen, H. Kierulf, and L. Tarasov, NKG2016LU: a new uplift model for Fennoscandia and the Baltic Region, *Journal of Geodesy*, 2019.

Vettoretti, G. and Peltier, W.R., Last Glacial Maximum ice-sheet impacts on North Atlantic climate variability: The importance of the sea ice lid, *Geophys. Res. Lett*., **40**(24), 6378-6383, 2013.

Vettoretti, G. and Peltier, W. R. Interhemispheric air temperature phase relationships in the nonlinear Dansgaard-Oeschger oscillation. *Geophysical Research Letters*, **42**(4), 1180-1189, 2015.

Vettoretti, G. and Peltier, W. R. Thermohaline instability and the formation of glacial North Atlantic super polynyas at the onset of Dansgaard-Oeschger warming events. *Geophysical Research Letters*, **43**(10), 5336-5344, 2016.

Vettoretti, G. and Peltier, W. R. Fast physics and slow physics in the nonlinear Dansgaard–Oeschger relaxation oscillation. *Journal of Climate*, **31**(9), 3423-3449, 2018.

Waelbroeck, C., and L. Labeyrie, et al., Sea-level and deep water temperature changes derived from benthic foraminifera isotopic records, *Quaternary Science Reviews*, **21**, 295-305, 2002.

Walcott, R.I., Isostatic response to loading of the crust in Canada. *Canadian Journal of Earth Sciences*, **7**, 716–727, 1970.

Walcott, R.I., Structure of the Earth from glacio-isostatic rebound, *Annual Review of Earth and Planetary Sciences*, **1**(15-37), 1973.

Walcott, R.I., Geodetic strains and large earthquakes in the axial tectonic belt of North Island, New Zealand, *Journal of Geophysical Research*, **83**, pp. 4419, 1978.

Walcott, R.I., Rheological models and observational data of glacio-isostatic rebound. In Earth Rheology, Isostasy ad Eustasy, edited by N.A. Morner, pp. 3-10, John Wiley, New York, 1980.

Wang, H.S. and P. Wu, Effects of lateral variations in lithospheric thickness and mantle viscosity on glacially induced surface motion on a spherical, self-gravitating Maxwell Earth, *Earth and Planetary Science Letters*, **244**, 576-589, 2006a.

Wang, H.S. and P. Wu, Effects of lateral variations in lithospheric thickness and mantle viscosity on glacially induced relative sea levels and long wavelength gravity field in a spherical, self-gravitating Maxwell Earth, *Earth and Planetary Science Letters*, **249,** 368-383, 2006b.

Wang, H.S. and P. Wu, Role of background viscosity in the investigation of postglacial induced crustal motion in a laterally heterogeneous mantle, *J. Geod*., **42**, 85-94, 2006c.

Wang, H.S., P. Wu and W. van der Wal, Using postglacial sea level, crustal velocities and gravity-rate-of-change to constrain the influence of thermal effects on mantle lateral heterogeneities, *J. Geod*., **46**, 104-117, 2008.

Wang, H. S., L. Jia, H. Steffen, P. Wu, L. Jiang, H. Hsu, L. Xiang, Z. Wang, and B. Hu, Increased water storage in North America and Scandinavia from GRACE gravity data, *Nature Geoscience*, **6**(1), 38-42, 2013.

Wang, H.S., L. Xiang, L. Jia, P. Wu, H. Steffen, L. Jiang, and Q. Shen, Water storage changes in North America retrieved from GRACE gravity and GPS data, *Geodesy and Geodynamics*, 6(4),267-273, 2015.

Whitehouse P.L Glacial isostatic adjustment modelling: historical perspectives, recent advances, and future directions, *Earth surface dynamics*, 6(2): 401-429, 2018.

Whitehouse, P.L, Bentley, M.J., and Le Brecq, A.M., A deglacial model for Antarctica: geological constraints and glaciological modelling as a basis for a new model of Antarctic glacial isostatic adjustment, *At. Sci. Rev*., **32**, 1-24, 2012.

Whitehouse, P., Latychev, K., Milne, G.A., Mitrovica, J.X. and Kendall, R., Impact of 3-D earth structure on Fennoscandian Glacial Isostatic Adjustment: implications for space-geodetic estimates of present-day crustal deformations, Geophys. Res. Lett., 33, L13502, 2006.

Wolf, D., The normal modes of a uniform, compressible Maxwell half-space. *Journal of Geophysics*, **56**, 100–105, 1985.

Wong, M.C.K, and P. Wu, Using commercial finite element packages for the study of Glacial Isostatic Adjustment on a compressible self-gravitating spherical earth - 1. Harmonic Loads, *Geophys. J. Int.*, **217**, 1798-1820, 2019.

Wu, P., The response of a Maxwell Earth to applied surface mass loads: glacial isostatic adjustment, 171 pp, 1978.

Wu, P. Deformation of internal boundaries in a viscoelastic earth and topographic coupling between the mantle and core. *Geophysical Journal International*, **101**(1), 213-231, 1990.

Wu, P., Deformation of an incompressible viscoelastic flat earth with Power Law Creep: a Finite Element approach, *Geophys. J. Int.*, **108**, 136-142, 1992a.

Wu, P., Viscoelastic vs. Viscous deformation and the advection of prestress, *Geophys.J.Int*., **108**: 35-51, 1992b.

Wu, P. Postglacial Rebound in a Power-law medium with Axial symmetry and the existence of the Transition zone in Relative Sea Level data. *Geophys.J.Int.*, **114**: 417-432, 1993.

Wu, P., Can observations of postglacial rebound tell whether the rheology of the mantle is linear or nonlinear? *Geophys.Res.Lett.*, **22**, 1645-1648, 1995.

Wu, P., Effect of viscosity structure of fault potential and stress orientations in eastern Canada, *Geophys. J. Int.*, **130**, 365-382, 1997.

Wu, P., Will earthquake activity in Eastern Canada increase in the next few thousand years? *Can. J. Earth Sci*., **35**, 562-568, 1998a.

Wu, P., Postglacial rebound Modeling with Power Law Rheology, In "Dynamics of the Ice Age Earth: A Modern Perspective" edited by P.Wu, Trans Tech Publ., Uetikon-Zuerich, Switzerland, p.365-382, 1998b.

Wu, P., Intraplate earthquakes and Postglacial Rebound in Eastern Canada and Northern Europe. in "Dynamics of the Ice Age Earth: A Modern Perspective" edited by P. Wu, Trans Tech Publ., Uetikon-Zuerich, Switzerland, p.603-628, 1998c.

Wu, P., Modeling Postglacial Sea-Levels with Power Law Rheology and Realistic Ice Model in the Absence of Ambient Tectonic Stress, *Geophys. J. Int*., **139**, 691-702, 1999.

Wu, P., Postglacial induced surface motion and gravity in Laurentia for uniform mantle with Power-law rheology and ambient tectonic stress, *Earth and Planetary Science Letter*, **186**, 427-435, 2001.

Wu, P., Mode coupling in a viscoelastic self-gravitating spherical earth induced by axisymmetric loads and lateral viscosity variations, *Earth and Planetary Science Letters*, **202**, 49-60, 2002a

Wu, P., Effects of nonlinear rheology on degree 2 harmonic deformation in a spherical self-gravitating earth, Geophys. Res. Lett., 29(8), 40-1-40-4, 2002b.

Wu, P., Effects of Stress Exponent in Mantle Flow Law on Postglacial Induced Surface Motion and Gravity in Laurentia, Geophysical Journal International, 148, 677-687, 2002c.

Wu, P., Postglacial induced surface motion, gravity and fault instability in Laurentia: evidence for power law rheology in the mantle? In Ice Sheets, Sea Level and the Dynamic Earth, Edited by J.X. Mitrovica & L.L.A. Vermeersen, AGU Geodynamics Series, 29, 219-231, 2002d.

Wu, P., Using Commercial Finite Element Packages for the Study of Earth Deformations, Sea levels and the State of Stress, Geophys. J. Int., 158, 401-408, 2004.

Wu, P., Effects of lateral variations in lithospheric thickness and mantle viscosity on glacially induced surface motion and seismotectonics in Laurentia, Earth and Planetary Science Letters, 235, 549-563, 2005.

Wu, P., Sensitivity of relative sea levels and crustal velocities in Laurentide to radial and lateral viscosity variations in the mantle, Geophys. J. Int., 165, 401-413, 2006.

Wu, P. and Peltier, W. R. (1982). Viscous gravitational relaxation. *Geophysical Journal International*, **70**(2), 435-485.

Wu, P. and W.R. Peltier, Glacial isostatic adjustment and the free air gravity anomaly as a constraint on deep mantle viscosity, *Geophys. J.R. Astron. Soc*., **74**, 377-449, 1983.

Wu, P., & Peltier, W. R. Pleistocene deglaciation and the Earth's rotation: a new analysis. Geophysical Journal International, 76(3), 753-791, 1984.

Wu, P. and Ni, Z. Some analytical solutions for the viscoelastic gravitational relaxation of a two-layer non-self-gravitating incompressible spherical earth. *Geophysical Journal International*, **126**(2), 413-436, 1996.

Wu, P. and H.S. Hasegawa, Induced stresses and fault potential in Eastern Canada due to a disc load: a preliminary analysis, *Geophys.J.Int*., **125**, 415-430, 1996a.

Wu, P. and H.S. Hasegawa, Induced stresses and fault potential in Eastern Canada due to a realistic load: a preliminary analysis, Geophys.J.Int., 127, 215-229, 1996b.

Wu, P., Z. Ni and G. Kaufmann, Postglacial Rebound with Lateral Heterogeneities : from 2D to 3D modeling. in "Dynamics of the Ice Age Earth: A Modern Perspective" edited by P.Wu, Trans Tech Publ., Uetikon-Zuerich, Switzerland, p.557-582, 1998.

Wu, P. and P. Johnston, Validity of using Flat-Earth Finite Element Models in the study of Postglacial Rebound, in "Dynamics of the Ice Age Earth: A Modern Perspective" edited by P.Wu, Trans Tech Publ., Uetikon-Zuerich, Switzerland, p.191-202, 1998.

Wu, P., P. Johnston and K. Lambeck, Postglacial rebound and fault instability in Fennoscandia, Geophys. J.Int., 139, 657-670, 1999.

Wu, P., and P. Johnston, Can deglaciation trigger earthquakes in N. America? Geophys. Res. Lett., 27: 1323-1326, 2000.

Wu, P., and W. van der Wal, Postglacial Sea levels on a Spherical, Self-gravitating Viscoelastic Earth: Effects of lateral viscosity variations in the upper mantle on the inference of viscosity contrasts in the lower mantle, Earth and Planetary Science Letters, 211, 57-68, 2003.

Wu, P., H.S. Wang and H. Schotman, Postglacial Induced Surface Motions, Sea-levels & Geoid Rates on a Spherical, Self-gravitating Laterally Heterogeneous Earth, Earth, J. Geodyn., 39 (2), 127-142, 2005.

Wu, P. and H.S. Wang, Effects of Mode Coupling and Location of Rotational Axis on Glacial Induced Rotational Deformation in a Laterally Heterogeneous Viscoelastic Earth, Geophys. J. Int., 167, 853-859, 2006.

Wu, P. and S. Mazzotti, Effects of a lithospheric weak zone on postglacial seismotectonics in Eastern Canada and Northeastern USA, GSA Special Paper 425: Continental intraplate earthquakes: science, hazard and policy issues, Ed. S. Stein & S. Mazzotti, p.113-128, 2007.

Wu, P. and H.S. Wang, Postglacial Isostatic Adjustment in a Self-Gravitating Spherical Earth with Power-law rheology, J. Geod., 46, 118-130, 2008.

Wu, P., H. Steffen and H.S. Wang, Optimal locations for GPS measurements in North America and northern Europe for constraining Glacial Isostatic Adjustment, Geophys. J. Int., 181, 653-664, 2010.

Wu, P., H.S. Wang and H. Steffen, The role of thermal effect on mantle seismic anomalies under Laurentia and Fennoscandia from observations of Glacial Isostatic Adjustment, Geophy. J. Int., 192(1), 7-17, 2013.

Wu, P., R. Steffen, H. Steffen, and B. Lund, Glacial Isostatic Adjustment Models for Earthquake Triggering, in "Glacially-Triggered Faulting" edited by H. Steffen, O. Olesen & R. Sutinen, p. 383-401, 2021.

Zhong, S., Paulson, A. and Wahr, J., Three-dimensional finite element modelling of Earth's viscoelastic deformation: effects of lateral variations in lithospheric thickness, Geophys. J. Int., 155, 679–695, 2003.

Table 1: Compares the predicted eustatic sea level at Barbados relative to modern of the ICE6G_C (vm5a) model of Argus et al. (2014) and 72-73-74-75 (ehgr) of Gowan et al. (2021) to RSL observations derived from depth corrected coral records (Peltier and Fairbanks, 2006) at selected times, highlighted in orange. The misfit between predicted values and observations at 30ka, 26ka and 14.5ka is substantially higher in the Gowan et al. model than in ICE6G_C.

Time(kya)	ICE6G_C (vm5a)	72-73-74-75 (ehgr)	Difference (I6G – Gowan)	Coral Samples
-40.0	-82.84	-26.61	-56.23	N/A
-38.0	-85.23	-33.42	-51.82	N/A
-36.0	-86.10	-38.06	-48.05	N/A
-34.0	-84.51	-43.27	-41.24	N/A
-32.0	-81.53	-49.97	-31.56	N/A
-31.0	-80.07	-53.59	-26.48	N/A
-30.0	-78.68	-57.21	-21.47	-83.00
-29.0	-87.19	-64.10	-23.09	N/A
-28.0	-99.99	-70.98	-29.01	N/A
-27.0	-111.10	-77.51	-33.58	N/A
-26.0	-119.33	-83.69	-35.65	-122.00
-25.0	-116.86	-89.86	-27.00	N/A
-24.0	-113.71	-96.06	-17.66	N/A
-23.0	-112.05	-102.25	-9.80	N/A
-22.0	-110.25	-106.54	-3.70	N/A
-21.0	-109.42	-108.93	-0.49	N/A
-20.5	-108.71	-110.12	1.42	N/A
-20.0	-108.03	-111.32	3.29	N/A
-19.5	-107.23	-109.86	2.63	N/A
-19.0	-106.56	-108.40	1.85	N/A
-18.5	-105.64	-106.94	1.30	N/A
-18.0	-104.42	-105.49	1.07	N/A
-17.5	-102.99	-104.03	1.04	N/A
-17.0	-101.65	-99.20	-2.46	N/A
-16.5	-99.93	-94.36	-5.57	N/A
-16.0	-98.05	-89.53	-8.52	N/A
-15.5	-94.57	-84.69	-9.87	N/A
-15.0	-91.63	-79.86	-11.77	N/A
-14.5	-88.22	-75.02	-13.21	-92.00
-14.0	-69.59	-70.17	0.59	N/A
-13.5	-63.91	-65.33	1.43	-69.00
-13.0	-60.30	-60.49	0.19	N/A
-12.5	-58.10	-55.65	-2.45	N/A
-12.0	-56.83	-50.81	-6.02	N/A
-11.5	-49.80	-45.97	-3.83	N/A
-11.0	-36.38	-41.13	4.75	N/A
-10.5	-31.32	-36.29	4.97	N/A
-10.0	-26.50	-31.45	4.95	N/A

Table 2. Lists the parameters of exponential fits to both the observed relative sea level constraints at site 4 and 5 of the Vacchi et al. (2018) compilation. These two parameter exponential relaxation fits are characterized by an amplitude "A" and a relaxation time "T" with the fit constrained to fit a relative sea level height RSL= 0 m at present day (t=0). Comparisons are shown to predictions of the ICE-

6G_C (VM5a) model and the ICE-7G_NA (VM7) model of the Toronto group, as well as to predictions of models MFA of Mitrovica and Forte and the two layer model of Lambeck et al. (2017). Notable is the fact that the latter two models misfit the observations in exactly the same way and have characteristic relaxation times that are excessive implying that mantle viscosity at the top of the lower mantle is too high.

Vacchi 4,5 (No ML) (Exponential fits to observations: A = 58 ± 9 m, T = 5.3 ± 0.5 kyr)			
Vacchi 4,5 (8000 kyr ML) (Exponential fits to observations: A = 23 ± 5 m, T = 3.3 ± 0.3 kyr)			
Value	A (m)	T (kyr)	RMS Error (m)
ICE6G (VM5a)	45.55 ± 0.15	4.23 ± 0.01	20.03
I7G	43.30 ± 0.23	3.99 ± 0.01	27.59
I7G (MFA)	90.97 ± 1.23	5.73 ± 0.05	32.95
I7G (2layer)	97.35 ± 1.55	6.14 ± 0.06	29.50
ICE7G NA (VM7TZ1)	28.50 ± 0.14	3.36 ± 0.01	25.48

Table 3 Lithospheric, sub-lithospheric and asthenospheric parameter space searched.

	Thickness (km)	Viscosity (Pa s)	Depth of bottom (km)
Elastic Lithopsphere	Lat. Homo.: 50 to 130 Lat. Hetero: 50 to 220	~	~
Sub-lithosphere	30 to 90	10^{18} to 10^{24} or elastic	50 to 130
Asthenosphere	5 to 80	10^{18} to 10^{21}	125 to 200

Table 4 Promotion of Fault stability/instability at 3 locations and 3 time stages for Thrust, Normal & Strike-Slip background stress regime. (Results summarized from Steffen et al., 2021)

Background Stress Regime	*Thrust*			*Normal*			*Strike-Slip*		
Location	*Beneath ice sheet*	*Between ice margin & bulge*	*Around peripheral bulge*	*Beneath ice sheet*	*Between ice margin & bulge*	*Around peripheral bulge*	*Beneath ice sheet*	*Between ice margin & bulge*	*Around peripheral bu*
During Glaciation	*Stable (dFSM Increase)*	*Stable (dFSM Increase)*	*Stable (dFSM Increase)*	*Mostly Stable (dFSM Increase)*	*Unstable*	*Unstable*	*Stable (dFSM Increase)*	*Unstable*	*Unstable*
During Deglaciation	*Stable (dFSM Decrease)*	*Stable (dFSM Decrease)*	*Stable (dFSM Decrease)*	*Stable*	*Unstable (dFSM Increase)*	*Unstable (dFSM Increase)*	*Stable (dFSM Decrease)*	*Unstable (dFSM Increase)*	*Unstable (dFSM Increase*
After Deglaciation	*Unstable*	*Unstable*	*Stable (dFSM Decrease)*	*Stable (dFSM Decrease)*	*Stable*	*Unstable (dFSM Increase)*	*Stable (dFSM Decrease)*	*Stable*	*Unstable (dFSM Increase*

Table 5. List of Symbols for the paper entitled Glacial Isostatic adjustment

Symbol	Definition
Introduction	
$\delta^{18}O$	Ratio of the stable isotopes of Oxygen
t	Time
$\delta Q(t)$	Summertime seasonal insolation anomaly
$\varepsilon(t)$, $e(t)$	Orbital obliquity and eccentricity
ω_p	Angular frequency of orbital precession
λ, μ	Elastic Lam´e parameters
e_{ij}, τ_{ij}	Strain and stress tensors
V_p, V_s	Primary and secondary shear wave velocity
ρ	Density
v	Viscosity
δ_{ij}	Kronecker Delta
s	Laplace transform variable
$\sim$	Indicates Laplace transform of variable
$\cdot$	Indicates time derivative of variable
K	Boltzmann's constant
T	Absolute temperature
a	Mean grain radius
V_a	Activation volume
E	Activation energy for self diffusion
p	Pressure
D_0	Self diffusion coefficient
Ω	Atomic volume
Ra	Rayleigh number
κ	Thermal conductivity
Pr	Prandtl number
$\dot{\varepsilon}_{ij}, \sigma_{ij}$	Deviatoric strain rate and stress
A^*	Creep parameter
V_{eff}	Effective viscosity
r, θ, φ	Radius, latitude and longitude

Part A	
G	Universal gravitation constant
g	Constant of gravity on Earth
$P_n(\cos(\theta))$	Legendre polynomial of degree n
U_n, V_n	Radial and tangential displacement
φ_n	Perturbation to the gravitational potential
T_{rn}, T_θ	Normal and tangential components of stress tensor
Q_n	Vertical derivative gravitational potential
a	Radius of the Earth
h_n, l_n, k_n	Love numbers
h^V_n, h^E_n	Viscous and elastic components of a Love number
$\delta(t)$	Dirac Delta
α_i, τ_i	Amplitude and time constant
Y_{lm}	Normalized spherical harmonic
ρ_I, ρ_w	Density of ice and water
θ, λ, t	Colatitude, longitude and time
$L(\theta, \lambda, t)$	Surface load function
$S(\theta, \lambda, t)$	Sea level function
$C(\theta, \lambda, t)$	Ocean function
$\Psi^r(\theta, \lambda, t)$	Variation of centrifugal potential
$G^L(\varphi, t)$, $G^T(\varphi, t)$	Surface loading and tidal Green functions
Part B	
A, A*	Creep Parameter
β	Fractional contribution of thermal effect
η	Viscosity
$\dot{\varepsilon}_{ij}, \sigma_{ij}$	Deviatoric strain rate and stress
σ_1, σ_2, σ_3	maximum, intermediate and minimum principal stresses
V_p, V_s	Primary and secondary shear wave velocity
E^*, V^*	Activation energy and volume
R	Gas constant
T_0	Background temperature profile
d	Grain size
f_{H2O}	Water fugacity
α, φ	Melt constant and fraction
$\Lambda(\theta, \varphi, t)$	Perturbed rotational/centrifugal potential
χ-statistics	Measurement of misfit between prediction and Observation
Ψ	Confidence Parameter
$\mathcal{H}$	Viscous dissipation of heating
FSM, dFSM	Fault Stability Margin and change in Fault Stability Margin

Figure Captions

Figure 1.1a. Oxygen isotope ratio $\delta\,^{18}O$ from the ODP 677 deep sea sedimentary core from the Panama Basin in two segments, respectively 2Ma – 1Ma and 1Ma-now. (b) Power spectra of the two segments of the IDP 677 record in (a). (c) Summertime seasonal insolation anomaly for 65 degrees north latitude for the same two periods of time for which the oxygen isotope time series are shown in (a). (d) Power spectra of the insolation anomaly time series segments shown in (c).

Figure 1.2. The graphics in the left column of this figure illustrate schematically the primary contributions to the variations of earth's orbital geometry that are responsible for the changing latitude dependence of solar insolation that are responsible for the growth and decay of continental ice cover. In the right column the time series shown are for the variation of the orbital elements over the most recent 140,000 years. Several important times are noted in the figures of the right hand column, notably the time of onset of the most recent 100 kyr glacial cycle (PEGI) and the time of Last Glacial Maximum (LGM) (a) orbital eccentricity varies on two primary timescales of ~413 thousand years and ~100 thousand years. (b) orbital obliquity varies on a timescale of 41,000 years and (c) orbital precession with a period of ~21,000 years is amplitude modulated by the variation in orbital eccentricity.

Figure 1.3ab. (a) The relative sea level record at the island of Barbados in the Caribbean Sea as analysed by Broecker and van Donk (1970), from whose paper this figure has been redrawn. The coral-based record from this island, which is being uplifted out of the sea by plate tectonic processes records sub-aerially a sequence of high stands of the sea as a function of time moving back in time from the Last Glacial Maximum at ~26,000 years before present back to the time of onset of the most recent 100 kyr glacial cycle at ~116,000 years ago. These high stands are separated by approximately 20 000 years in the earliest part of the record, i.e., by a complete

processional cycle. (b) Oxygen isotopic time series from deep sea sedimentary core P6304-9 of Emiliani (1966) which is to be compared to the Barbados sea level record in Figure 1.3a. is also from Broecker and van Donk (1979). as redrawn for present purposes Taken together these two parts of Figure 1.3 clearly established that individual ice-age cycles of glaciation and deglaciation were of "sawtooth" form with the process of glaciation being much slower than the process of deglaciation.

Figure 1.3c. Multiple deep sea sedimentary core oxygen isotopic records illustrating the fact that the ice age cycle of ice volume variations has a distinctly sawtooth form characterized by a slow and relatively long-lived glaciation process, followed by a relatively fast deglaciation process. The figure is from Broecker and Van Donk (1970) but it has also been redrawn.

Figure 1.4 (a) Variation of Top of the Atmosphere (TOA) received polar insolation as a function of latitude and month of the year through a typical annual cycle. (b) Insolation anomaly (difference from modern) for the mid-Holocene period at 6000 years before present. Notable is the fact that northern hemisphere summers are anomalously warm which explains why the summer monsoon circulations in the northern hemisphere were intensified at this time. (c) insolation anomaly at the Last Glacial Maximum demonstrating that the difference from the modern insolation regime was very modest (d) insolation anomaly for 116,000 years ago demonstrating that at this time summer seasonal insolation was anomalously weak, thus confirming that it is the weakness of summer insolation forcing that enables the continental glaciation process to begin.

Figure 2.1. Depth dependent physical properties of the Earth according to the Preliminary Reference Earth Model (PREM) of Dziewonski and Anderson (1981) shown both on a depth from surface scale and on a pressure scale. As this is a model in which the Earth is taken to be a

Hookean elastic solid that is unable to flow. Important for the purpose of this paper are the discontinuities in physical properties at 420 and 660 km depth that are due to pressure induced phase transition in mantle mineralogy, respectively the Olivine-Spinel and the Spinel to Perovskite plus Magnesiowustite transitions. Also important is the transition from the solid state mantle to the liquid outer core across the Core-Mantle Boundary (CMB).

Figure 2.2. Redrawn from Goldsby and Kohlstedt (1997) illustrates the solid state creep properties of fine grained ice with a grain size of 1 mm for two different temperatures, respectively 350 degrees kelvin and 373 degrees kelvin. Since ice melts at 373.15 degrees kelvin the comparison between (a) and (b) provides direct evidence of the fact that as the melting temperature of a solid is approached the solid has an increased ability to flow like a liquid. The mechanism though which flow occurs, however, is a strong function of differential stress. Parts (a) and (b) of the figure plot strain rate (flow speed) as a function of differential stress. These log-log plots demonstrate that for this ice analogue to earth's mantle there are three distinct regimes, each characterized by a different stress exponent "n". At highest differential stress n=4, at intermediate stress levels the exponent n=2 whereas at lowest differential stress n=1 and the solid has begun to flow like a Newtonian viscous fluid. See the text for further discussion.

Figure 2.3. Spherical shell convection model results as a function of the effective Rayleigh number of the shell over the range that extends from a lowest Raleigh number for which significant thermal instability has yet to occur to the highest Rayleigh numbers that are in the Earth-like range. These calculations are all from the work of Shahnas and Peltier (e.g., 2015) and this series is for models with fixed rate of internal heating associated with radioactive decay processes, termed H1 on the individual plates of the figure. Evident is that as the Rayleigh number increases the horizontal scale of the upwelling and downwelling plumes which dominate

the circulation dramatically decreases. These results have been obtained for models in which neither the Olivine-Spinel or the Spinel-post Spinel phase transitions are includes.

***Figure 2.4**. Mollweide projection image of the interior temperature field of a mantle convection simulation in which both the Olivine-Spinel and the Spinel-post-Spinel phase transitions are included. This image demonstrates that the influence of the latter endothermic transition is to cause the formation of an internal boundary layer in the mantle at the depth of the 660 km seismic discontinuity. This boundary layer is episodically unstable, leading to the formation of "avalanche-like" downwellings that cause episodic localized increases of heat loss from the core when they strike this boundary.

Figure 3..1 (a). The viscoelastic "h" Love number as a function of spherical harmonic degree "n" and Laplace transform variable "s" for the simple Earth model discussed in Peltier (1974) in which the elastic Earth model 1066B of Gilbert and Dziewonski (1971) was employed and a viscosity structure consisting of a constant viscosity from the surface to the CMB of magnitude 10^{21} Pa s was assumed. The Laplace transform variable is non-dimensionalized with a timescale of 1000 years. (b)**.** Same as for Figures 3.1a but for the "k" Love number in which is plotted the product of the spherical harmonic degree and the "k" Love number of the same degree. These results are for the same earth model as was employed for Figure 3.1a and comparison of these results with those in the previous figure will show that nk~h for all n.

Figure 3.2. The depth dependent viscosity models VM1, VM2 and VM3 were determined in a series of analyses that began by assuming the starting model VM1, which is similar to that preferred by Haskell (1935). Model VM2 was produced in a formal Bayesian inversion in which VM1 was employed as a first guess and the data sets employed to drive the inversion consisted of the Fennoscandian relaxation spectrum of McConnell (1968), the large number of site specific

relaxation times recorded in Peltier (1998b) and the observed nontidal acceleration of planetary rotation. Each of these observables has a specific Fréchet derivative (sensitivity kernel) associated with it such that the collectivity of the data provide resolution of the viscosity profile from the surface to the core mantle boundary. Model VM3 was determined by employing the same methodology but by assuming that the rotational observable was contaminated by a certain degree of modern, global warming induced forcing.

Figure 3.3. Relaxation spectra are show for models VM1, VM2 and VM3 for which the radial viscosity profiles are shown in Figure 3.2. Each relaxation diagram plots inverse relaxation time for each spherical harmonic degree for the sequence of viscous gravitational modes of relaxation that govern the response to surface mass loading at the horizontal scale represented by that spherical harmonic degree.. Evident is the fact that the individual modes define branches each of which is supported by effectively discontinuous variations of density in the radial structure of the model. Although these discontinuities are the same for all models the branch of inverse relaxation times associated with each depends upon the radial viscosity structure.. The fundamental mode which is referred to in the literature as M0 is that characterized by a non-monotonic variation of inverse relaxation time as a function of degree which is caused by the influence of the surface elastic lithosphere.

Figure 3.4. This shows the fits of models VM1, VM2 and VM3 to the famous Fennoscandian relaxation of McConnell (1958), demonstrating that the small horizontal scale of the Fennoscandian ice sheet provides, through the observed response to deglaciation, information on viscosity depth dependence that is restricted to upper mantle and transition zone depths.. The fact that the high lower mantle viscosity of VM3 has no effect upon the fit of VM2 to the Fennoscandian relaxation spectrum demonstrates explicitly that Fennoscandian rebound is

insensitive to lower mantle viscosity. Comparison of the fits of VM2 and VN1 shows that the upper mantle and transition zone viscosity of VN1 is too high.

Figure 3.5. (a) The analytical forms of the Fréchet derivatives for the individual spherical harmonic degrees in the McConnell (1968) spectrum for Fennoscandian rebound based upon the well founded assumption that the small horizontal scale of the ice sheet was such that only the fundamental M0 mode of the global model was excited by the deglaciation process. These analytical forms are from Peltier (1976). (b) Fréchet derivatives for example sites specific relaxation times for a site where the rebound was under the control of the Laurentide ice sheet (Bathurst Inlet) and a site under the control of Fennoscandian rebound (Angerman River). (c) Fréchet derivatives for polar wander speed and the nontidal acceleration of planetary rotation, the latter demonstrating that the earth rotation data provide information on mantle viscosity from the region extending from the core mantle boundary into the mid-mantle.

Figure 4.1 (a). Viscous part of the Heaviside form of the gravitational potential perturbation Green function for an Earth model in which the viscosity is assumed to be constant from the Earth surface to the core mantle boundary as a function of spherical harmonic degree from the site of application of the point mass load on the surface Time in thousands of years following the time the point mass load is applied to the surface. The 1/r singularity has been scaled out and the t=0 curve is the elastic Green function. This is the Green function provided to W. E. Farrell for his use in the companion paper to Peltier and Andrews (1976) from which this and Figure 4.1b are taken. Farrell and Clark (1976) used this result and 4.1b to provide an initial sketch as to how one may calculate relative sea level history. (b) Same as in (a) but for radial displacement. This figure is redrawn from Peltier and Andrews (1976). The Heaviside forms of the Green functions are determined by convolution of the impulse response forms with a Heaviside step function and

represent the response to the application of the surface mass load when this is left on the surface for all time. The difference (a)-(b) is simply the Heaviside form of the Green function for relative sea level that was provided to Farrell and Clark (1976) so that an initial discussion could be provided of the method for the prediction of relative sea level history.

Figure 4.2. Polar wander data from the International Latitude Service (ILS) for the period from 1900 to 1976 when the service was disbanded to be replaced by space based measurements that offered higher accuracy than the array of photo zenith tubes that provided the original ILS measurements. The figure plots the time dependent position of the north pole of planetary rotation in x and y co-ordinates relative to the (then) conventional international origin (CIO). Notable is that the 7 year "beat" between the annual cycle and the 14 month Chandler wobble is superimposed upon a secular drift at a speed of approximately 1 degree per million years in a direction close to what was the centroid of the ancient Laurentide ice sheet that once covered all of the Canadian land mass. This secular drift is a component of Earth's response to the GIA process.

Figure 4.3. Timings of eclipses of the Sun and Moon based upon naked eye astronomical measurements from both China and Persia over the past two millennia, from Morrison and Stevenson (1970). On the basis of these data it has been possible to infer the action of a nontidal acceleration of planetary rotation that acts in opposition to the influence of tidal friction. The strength of tidal friction may be inferred on the basis of the rate of recession of the Moon and is now accurately measured by Lunar Laser Ranging (LLR). If the modern strength of tidal friction is assumed to have remained constant in the past, then, as shown on the figure and the modern inset, one makes an increasingly large error in eclipse timings the further back in time for which the prediction is made. This has made it possible to measure the strength of the "nontidal

acceleration of the rate of planetary rotation" as discussed in the text, an effect due to glacial isostatic adjustment., namely the nontidal acceleration.

Figure 4.4. For Earth models with fixed PREM elastic structure and a series of two layer viscosity structures in which the upper mantle and transition zone viscosity is fixed to 0.4 x 10^{21} Pa s while the lower mantle viscosity is varied from low to high values. (a) the predicted values of the nontidal acceleration of planetary rotation as a function of lower mantle viscosity with the hatched region representing the range allowed by the observations. (b) the same but for polar wander velocity with the hatched region once more denoting the range of values allowed by the observations. Notable is that both rotational observables are fit by the same low contrast viscosity model. This is important because these data provide entirely independent constraints upon the radial viscosity structure of the Earth as they are dependent upon distinctly different elements of the planet' moment of inertia tensor. The loading history employed in these calculations is that of the ICE-5G (VM2) model of Peltier (2004).

Figure 4.5a. Polar wander time series from the Space 2008 data set of Ratcliff and Gross (2010). (a,b) Raw (dark grey) components of polar wander (dark grey) and after processing with a 6 year low pass Butterworth filter (red) and (c,d) the two linear fits 1976-1992 (rate 1.7 mas/yr) and 1992-2009 (rate 0.9 mas/yr) to the low pass filtered data. Figure from Roy and Peltier (2011).

Figure 4.5b. Changes in the J2 Stokes coefficient for the period 1976-2009 from the orbital parameters of 7 geodetic satellites (Cheng and Tapley, 2004) (a) Raw variations of J2 (dark grey) and after processing with a 20 year Butterworth low pass filter (green) (b) two linear fits for the periods 1976-1992 (rate and 1992- 2009 (rate -0.37+- 0.01) x 10^{-10})) yr^{-1} and 1992-2009 (rate -0.09 (+- 0.02) x 10^{-10}) yr^{-1}. This figure is from Roy and Peltier (2011).

Figure 4.5c. The total root-mean-square error for the Stokes coefficient fit (dark green) and the polar wander fit (red) as a function of the position of the pivot time with a common minimum observed to be near 1992.Subsequent to this time it is clear that mass redistribution effects due to global warming have begun to exert a dominant control over the influence of GIA.. This figure is from Roy and Peltier (2011).

Figure 4.6. (a), (b) respectively illustrate the ice covered regions of the planet under modern and Last Glacial Maximum conditions. (c) the coral-based and tectonically corrected Barbados record of relative sea level history of Peltier and Fairbanks (2006). (d) the records of relative sea level history from sites near what was once the region of thickest ice cover over Canada and Fennoscandia demonstrating that the rebound of the Earth's crust in such regions has a characteristically exponential form.

Figure 4.7. (a), (b) show the contributions to ice equivalent eustatic sea level from different geographical regions in the ICE-5G (VM2) and ICE-6G (VM5a) models of the glacial isostatic adjustment process respectively as well as the ice equivalent globally averaged eustatic rise. Note that LGM in these models is at 26,000 years before present rather than at 21,000 years ago as has often been assumed.

Figure 4.8. (a) the predictor present day rate of relative sea level rise over the surface of the Earth based upon a GIA model that includes the full influence of rotational feedback and coastline migration for a model with VM2 radial viscoelastic structure. (b) same as (a) but with the influence of rotational feedback eliminated. (c) the difference (a)-(b) demonstrating the fact that rotational feedback is dominated by the degree 2 and order 1 spherical harmonic that is controlled by the influence of the polar wander component of Earth's rotational response to the glacial isostatic adjustment process. (d) the sum of (a) and the predicted rate of radial

displacement of the crust, a sum that represents the time rate of change of geoid height (absolute sea level) with respect to the centre of mass of the planet which is strongly dominated by the degree 2 and order 1 influence of polar wander.

Figure 4.9. Similar to Figure 4.8 (d) but for the North American continent, showing the sum of the predicted present day rate of radial displacement of the crust, dRad, and the present day rate of relative sea level rise, dRSL over the continent. It should be noted that sea level is defined even over the land as the gravitational equipotential which defines sea level over the oceans continues to be defined over the continent. dGeoid is the time rate of changes of geoid height over the continent. Even though dRad and dRSL are precisely out of phase it is critical that when they are added there is a non-zero result for the time dependence of geoid height because, as explained in Peltier et al. (2018) it would otherwise be impossible to infer, on the basis of dGeoid alone, the present day rate of vertical motion of the crust.

Figure 5.1. Centre shows the present day prediction of the rate of relative sea level rise upon which are plotted the positions of 6 geographical locations for which relative sea level predictions are shown and compared to observations on the left and right margins of the central figure. Notable is the fact that, in spite of the significantly different variations of relative sea level history at these six different locations the predictions of the Toronto model of ice-Earth-ocean interactions correctly captures these distinctly different signatures of RSL history.

Figure 5.2. Various components of the most recent analysis of the Barbados coral-based data set of relative sea level history from Peltier et al. (2015). (a) geography of the island and locations of the three sites from which estimates of the rate of tectonic uplift of the island are available, the average of these three rates being 0.34 mm/yr as first inferred by Fairbanks (1989) on the basis of data from a single site. (b) these three distinct measurements of the uplift rate. (c) the raw

Barbados record of RSL history with the inset showing that the amount of uplift that has occurred since 21,000 years ago to have been approximately 7 m, as shown on the inset.

Figure 5.3. Shows the tectonically corrected relative sea level record from tie island of Barbados from the time of Last Glacial Maximum (LGM) (assumed to have occurred 26,000 years ago rather than 21,000 years ago as has conventionally been assumed). Notable is the fact that the ICE-6G (VM55a) model has been tuned so that the RSL prediction for this site passes through the shallowest water tips of the Montastraea annularis samples which have an error bar of 15 m length. This assumption has been made on the basis of the observation that during the Younger Dryas cold reversal it is the shallowest water tips of the Montastraea annularis samples that agree with the depth of the Acropora palmate samples that provide the most accurate control on sea level position.

Figure 5.4. A comparison between the fit of GIA model ICE-6G (VM5a) and those of the recently suggested models of Gowan et al. (2021) which are based upon an attempt to demonstrate that it might be possible to fit the Barbados constraints on RSL and eustatic sea level history, with a model of viscosity depth dependence characterized by a sharp increase across the 660 km depth if one were simply to dramatically reduce the global ice load and its time dependence from that employed in the ICE-6G_C (VM5a) model. The Gowan models not only dramatically misfit the eustatic sea level record of Waelbroecke et al. (2002) shown with notional error bars in the upper part of the figure, but at least as important the coral constraints at Barbados as well. The misfits to the coral constraints at Barbados are respective 38.1 m at LGM and 25.8 m at 30 ka. Although Gowan et al. realize that their models violate the deep sea core oxygen isotopic constraint they appear not to realize that they also grossly violate the actual sea level depth constraints provided by the coral samples.

Figure 5.5. (a) The satellite observed long wavelength free air gravity anomaly over the northern part of the North American continent and predictions of this anomaly using the SF1K seismic tomography model of Dziewonski and others. In parts (b), (c) and (d) the S-wave-based model of mantle tomography is mapped into a free air gravity anomaly by assuming either a negative (b) or a zero (c) or a positive (d) S-wave heterogeneity to density conversion factor. When the latter is assumed the internal loading theory of the mantle convection process fits the free air anomaly observation essentially perfectly. This argues that this anomaly is not associated with uncompensated GIA but rather to the mantle convection process.

Figure 5.6. Locations of data from the RSL collection of Vacchi et al. (2018) from the regions surrounding Hudson Bay. Especially important for the purpose of this paper are location 4 and 5, respectively from the east coast of James Bay and from the Richmond Gulf of the SE coast of Hudson Bay itself, as discussed in he text.

Figure 5.7. The collection of RSL data points from sites 4 and 5 in the Vacchi et al. (2018) collection. Also shown on this figure is the approximate elevation and age of the Marine Limit in this region, representing the highest level in the landscape ever reached by the sea as the crust has rebounded since the region was deglaciated. Notable is the fact that although these data are from regions well separated, they define the same simple exponential history of the rebound in this once ice covered region.

Figure 5.8. (a) fits of the predictions of the ICE-6G_C (VM5a) and ICE-7G_NA (VM7) models to the Vacchi et al. (2018) data set from SE Hudson Bay. The thin solid line is the exponential fit to the data determined by the nonlinear optimization process described in the text. (b) the depth dependent viscosity models VM5a and VM7, the primary difference between them being that the

radial profile in VM7 us such that viscosity continues to increase with depth below the 660 km seismic discontinuity.

Figure 5.9. (a) A parallel presentation to that in Figure 5.8 but for two different GIA models that differ only in their viscosity structures with the loading history fixed to that of ICE-7G_NA. Notable is that even though the viscosity structures of these models are radically different , as shown in part (b) of the figure, they misfit the SE Hudson Bay data in exactly the same way, in that their predictions of the present day rates of sea level fall are far to rapid to fit the observations (b) the viscosity models of Lambeck et al. (2017) denoted 2-layer, and that of Mitrovica and Forte, denoted MSE FA.

Figure 5.10. Predictions of the SE Hudson Bay data by the preferred model of Lambeck et al. (2017) which includes a modification of the ICE-6G_C loading history, with separate predictions show for both the east coast of James Bay and Richmond Gulf. Notable is that the nature of the misfit to the data is the same as shown on Figure 5.9, i.e. the predicted rates of sea level fall at present are far too fast to fit the observations.

Figure 5.11. A range of depth dependent viscosity profiles proposed by different authors including the VM5a and VM7 models of the Toronto group. The latter models are unique in that they are truly global, being comprised of a single model of the depth dependence of viscosity and a global model of the variation of grounded ice thickness on the continents as a function of space and time. The methodology employed by the Toronto group for the inference of the viscosity profile exploits the fact that different GIA observables are characterized by different sensitivities to viscosity depth dependence. Also illustrated on this figure which is from Argus et al. (2021), is the fact that rebound data induced by the removal of ice loads of different horizontal scale are

sensitive to viscosity over different ranges of depth, such that the greater the horizontal scale of the load the deeper into the mantle the sensitivity to mantle viscosity extends.

Figure 5.12. Location map of the collection of GPS receiver installations from which data are available to constrain the present day vertical and horizontal motions of the crust associated with the glacial isostatic adjustment process. These positions are shown against a background that is a color coded map of the vertical motion rate predicted by the ICE-6G_C (VM5a) model of the GIA process.

Figure 5.13. Same as Figure 5.12 but showing a series of specific traverses of the vertical motion field along which comparisons are shown on Figures 5.14 comparing the predictions of several models to the GPS observations of vertical motion of the crust. This figure is from Peltier et al. (2015).

Figure 5.14. (a), (b), (c) show comparisons between ICE-6G_C (VM5a) predictions of vertical motion along each of the traverses shown on Figure 5.13. Also shown on each of these traverses are predictions of two additional models, respectively for model ICE-5G (VM2) of Peltier (2004) and the copy of it produced by Geruo A et al. (2012) who were provided all of the inputs to the Peltier (2004) model and were able to quite precisely reproduce the results of this model using a somewhat different computational procedure. The ICE-6G_C (VM5a) model is clearly superior to its predecessor.

Figure 5.15. (a) map of the predicted present day vertical motion of the crust by the ICE-6G_D (VM5a) model, to be compared with the predictions of the same field by the model of Lambeck et al. (2017) in (b). Model ICE-6G_D (VM5a) differs from model ICE-6G_C (VM5a) only in the loading history of the Ross Sea and Weddell Sea embayments of Antarctica. (c) shows the difference (b)-(a) demonstrating that the model of Lambeck et al. (2017) drastically over predicts

the rate of vertical motion of the crust at all previously ice covered locations. Model ICE-6G_D (VM5a) was published in Peltier et al (2018) and is currently in heavy use by GRACE analysis centres to remove ancient ice age influence from time dependent gravity measurements. (d) shows a series of additional traverses along which vertical motion predictions are shown and discussed in Argus et al. (2021).

Figure 5.16. (a) present day GRACE observed equivalent water change in mm/yr based upon the JPL mascon solution. (b) predicted present day rate of equivalent water change by the ICE-6G_D (VM5a) model, (c) the difference between (a) and (b) demonstrating that the Toronto model extremely well fits the GRACE observations of time dependent gravity

Figure 6.1. Background density structure of the spherical Earth which is made up of *N-1* layers of uniform shells overlying a homogeneous core of radius r_1 and density $\overline{\rho}_1$. Here, $\overline{\rho}_k$ is the density of the shell, which is bounded by $r_{k-1}$and r_k. (After Wong and Wu, 2019).

Figure 6.2. Typical FE grid on the surface of the spherical Earth model has 0.5^ox0.5^o resolution, but the lines of such a grid is too close to be seen clearly, so a coarse 2^ox2^o FE grid is shown in (a). In (b) and (c), we compare the resolution of the 2^ox2^o grid versus the 0.5^ox0.5^o grid over the Great Lakes area. The finer grid significantly improves the representation of the lakes and land.

Figure 6.3. A This cartoon illustrates how spatial resolution of $\Delta\theta$ x $\Delta\theta$ at layer k in a FE grid can be changed to $2\Delta\theta$ x $2\Delta\theta$ resolution at the deeper layer k+1.

Figure 6.4. Mean shear velocity anomalies of the Mean Seismic Tomography model (S362ANI+M, SEMum, SGLOBE-rani and TX2019slab in (a) UM1 (100-400 km depth), (b) UM2 (400-670 km depth), (c) LM1 (670-1271 km depth) and (d) LM2 (1271-2891 km depth).

Figure 6.5. Logarithmic lateral viscosity perturbation ($\log_{10}[\Delta\eta(r,\theta,\phi)]$) in the 4 layers UM1, UM2, LM1 & LM2 deduced from the Mean Seismic Tomography Model (see Fig. 6.4) with $\beta=1$. Depth ranges of the four layers are given in Fig. 6.4.

Figure 6.6. Thermal structure beneath Fennoscandia at 3 representative depths deduced from geotherms and borehole heat flow data (80 km) and shear wave tomography model (150 & 220 km), (After van der Wal et al., 2013). Below each map is the log scale for the lateral viscosity variation converted from the lateral temperature variations if dry diffusion creep with grain size of 1 mm is assumed.

Figure 6.7. For an axisymmetric Earth model with composite rheology (A^* = 3.3x10^{-35} Pa^{-3}s^{-1} and $\eta=3x10^{21}Pas$), the evolution of σ'_E during a glacial cycle changes the regions of the mantle where linear rheology (light grey) or nonlinear rheology (dark grey) dominates. The ice load has uniform thickness and radius of 15^o (indicated by the solid line that extends from the center). Ice thickness changes linearly with time, but the load radius does not change during the glacial cycle. The epochs shown are 17 ka BP (glacial maximum), 11 ka BP (end of deglaciation), and 8 ka BP. (From van der Wal et al., 2010).

Figure 7.1. The normalized shear energy profile for an incompressible uniform half-space, loaded by a harmonic load with wave-number k. The vertical axis is the depth normalized by 1/k. The shear energy peaks at *k*z = -1, and the half-peak-values occur at *k*z = -0.3806 and -2.078.

Figure. 7.2. The earth parameters $\overline{m}$and the predictions $\overline{p}$ of the forward problem: $\overline{p}=I(\overline{m})$

Figure. 7.3. Two ways to display the sensitivity kernel for uplift rate on a laterally homogeneous Earth: (a) as a function of radius/depth and (b) as a function of the observer location. The Earth model has 5 spherical uniform shells above the CMB: (i) 100 km thick elastic lithosphere, (ii) shallow upper mantle (UM1) which extends from sub-lithosphere to 420

km depth, (iii) transition zone (UM2) which extends from 420 to 670 km depth, (iv) shallow upper mantle (LM1) which extends from 670 to 1330 km depth and (v) deep lower mantle (LM2) which extends from 1330 to the CMB. The ice load has a parabolic shape with angular radius of 15 degrees and a maximum height of 3663 m at 16 ka BP. It grows linearly from 106 kaBP to 16 ka BP, then decays linearly to 6 ka BP when it vanishes completely. (After Wu, 2006.)

Figure. 7.4. Sensitivity kernels for uplift rate (left) and tangential velocity (right) if the anomalous viscosity region is at a given depth (one of UM1, UM2, LM1 or LM2) and at a given angular distance from the load center (one of regions A, B, C, D or E). (After Wu 2006.)

Fig. 7.5. Sensitivity of gravity-rate-of-change (a) & (c) and uplift rate (b) & (d) to realistic ice model and lateral heterogeneity in the upper mantle (UM; see top row) and lower mantle (LM; see bottom row). The minimum and maximum values are also given above each map. (From Li et al., 2018).

Figure. 7.6. Sensitivity of RSL to lateral heterogeneity in the upper mantle (UM, see left column) and lower mantle (LM, see right column) at 4 times (ka before present): 16 (a &b), 12 (c &d), 8 (e & f) and 4 (g & h). Note that (a), (c) and (e) share the same color bar, (b) and (d) the same color bar, and (f) and (h) the same color bar. (From Supplementary Material in Li et al., 2018).

Figure 7.7. (a) RSL sensitivity at 10 ka with 1 m error, (b) is GRACE g-dot sensitivity in Laurentia and (c) GRACE g-dot sensitivity in Fennoscandia (After Steffen et al., 2012, 2014).

Figure 7.8 (a) Heaviside loading of a laterally heterogeneous axisymmetric Earth due to a degree 2 harmonic load. (b) The spatial variation of the normalized surface radial displacement Ur at 15 ka after loading is compared between the laterally heterogenous case (red solid line) and the

laterally heterogenous case (black dashed line) where a 2 order of magnitude jump in viscosity occurs at colatitude $\psi = 45^{o}$. **(c)** The normalized spectral amplitude of Ur of the two cases are shown. Mode coupling is shown for the laterally homogenous case, but not for the laterally homogeneous case. (After Wu, 2002a).

Figure 7.9. Effects of lateral heterogeneity under Antarctica on present-day velocities (mm/yr) for ICE-3G. Predictions in the top panel are for a laterally homogeneous Earth, while those in the bottom panel are for earth model with lateral viscosity variations in the mantle. (a) and (c) are for uplift rate while (b) and (d) are for tangential velocity. The scale for the tangential velocities is given below (d). (See Kaufmann et al., 2005).

Figure 7.10. Effects of lateral heterogeneity of different layers: (a) lithosphere; (b) upper mantle UM1; (c) transition zone UM2; and (d) lower mantle LM1+LM2) under Laurentia on present-day uplift rate (mm/yr). Solid and dashed contours represent uplift rates with positive and negative values respectively. (After Wu, 2005).

Figure 7.11. Effects of lateral heterogeneity under Fennoscandia on present-day velocities (mm/yr). (After Steffen et al., 2006).

Figure 7.12. Predicted present-day tangential velocity (mm/yr) for a laterally heterogeneous earth model induced by 4 single ice sheets or complexes in: (a) North American; (b) Greenland; (c) North Eurasia and (d) Antarctica. (After Wang and Wu, 2006a).

Figure 7.13. Predicted present-day uplift rate (a,c) and tangential velocity (b,d) for laterally homogeneous earth model RF and laterally heterogeneous earth model L20 with ICE-4G. Contours are in mm/yr. The scale of the tangential velocity vectors can be found on the right side of the title. (After Wang and Wu, 2006a).

Figure 7.14. Predicted tangential velocity for laterally homogeneous earth models RFA & RFB and laterally heterogeneous earth model 20A & 20B with ICE-4G. Contours are in mm/yr. The scale of the vector is indicated below figure (c). The viscosity contrast at 670 km depth for models RFA and RFB are 2.6 and 47 times respectively. The background viscosity profiles of 20A & 20B are RFA and RFB respectively. In addition, the viscosity perturbations in 20A and 20B are from seismic tomography model S20A with the assumption that seismic anomalies have thermal origin ($\beta=1$) and the effect of anelasticity is neglected in the scaling relationship. (After Wang and Wu, 2006c).

Figure 7.15. Contour plots of χ when (a) all 127 global RSL sites with long time record length and (b) only RSL sites near the center of GIA in Laurentia are used. Superimposed are the best solution (black diamond) and the confidence regions with $\Psi \le 0.5$ (dark grey) and $\Psi \le 1.0$ (light grey). Beta* means that the scaling law includes both the effects of anharmonicity and anelasticity. (After Wu et al., 2013).

Figure 7.16. Similar to Fig.7.15 except the left panel is for uplift rate data (from GPS) and the right panel is for the gravity-rate-of-change data (from GRACE) in Eastern Canada (top row) and Fennoscandia (bottom row). (After Wu et al., 2013)

Figure 7.17. Uncertainties (2 σ) of the shear velocity anomalies of the Mean Seismic Tomography model of Fig. 6.4 in: (a) UM1 (100-400 km depth), (b) UM2 (400-670 km depth), (c) LM1 (670-1271 km depth) and (d) LM2 (1271-2891 km depth).

Figure 7.18. Uncertainties (2σ) of $\log_{10}[\Delta\eta(r,\theta,\phi)]$ (in Fig. 6.5) in the 4 layers UM1, UM2, LM1 & LM2 from the Mean Seismic Tomography model (Fig. 6.4) with $\beta=1$.

Figure 7.19. Uncertainty grid for the best GIA Model. Contour interval is 0.05 mm/a. (After Vestøl et al., 2019).

Figure 7.20. Cartoon for elastic lithosphere with lateral thickness variation on top of a sub-lithosphere with uniform thickness in (a), and over an asthenosphere with lateral thickness variation in (b). Note that "min" and 'max" indicate the minimum and maximum thickness of the elastic lithosphere. (After Li and Wu, 2019.)

Figure 7.21. The mean Relative Sea Level (left panel) and 2s uncertainties (right panel) of RSL in North America at 3 different time steps 15, 9 and 6 ka BP. (From Li et al., 2020)

Figure 7.22. RSL curves at 6 sites in North America. Sites 1, 4 & 5 are in Hudson Bay, Site 6 is along the east coast of USA, just south of the ice margin at LGM, Site 20 is in the Florida keys, Site 24 is on the southern part of the US west coast. SLIPs are plotted as boxes with 2σ vertical and calibrated age errors. The marine limiting provides a lower constraint and the terrestrial limiting provides an upper constraint on RSL. The purple solid line represents the mean RSL, the green solid line represents the best-fitting 3D model in North America. The dark grey, grey and light grey shaded areas indicate the 1σ, 2σ and 3σ uncertainties from the mean, respectively. (From Li et al., 2020.)

Figure 7.23. The mean present-day uplift rate (a) and g-dot (c) and their corresponding 2σ uncertainties in (b) and (d) respectively. The purple dots and red dots in (a) represent GNSS stations from Peltier et al. (2015). The former indicates the mean present-day uplift rate with 2σ uncertainties fit the observed GNSS data at that site while the latter fits within two times the error bars. (From Li et al., 2020.)

Figure 7.24 Spatial distribution of the normalized viscous heating for the Composite Rheology model M5 at 13 ka BP and at 140 km depth. The location of vertical cross-sections in Laurentia and Fennoscandia shown in Fig. 7.25 are indicated by thick black dashed lines.

Figure 7.25. The time evolution of normalized viscous heating for 2 Earth rheology models (VM5a and M5) at the global site with maximum viscous heating (since the peak value at different time might be different). Note that viscous heating for both models peak around 13 ka BP, the time when the local ice above the global site with maximum viscous heating become ice free.

Figure 7.26. Cross-sectional view of the normalized viscous heating along the two thick black dash lines in Fig. 7.24 at 15, 13 & 10 ka BP for composite rheology model M5. Left column contains the vertical profiles in Laurentia, while the right column contains the vertical profiles below Fennoscandia. Note that viscous heating is concentrated within the top 200 km depth of the Earth model and at any time, the peak value under Laurentia is larger than the peak value under Fennoscandia.

Figure 7.27. Mohr diagram is a plot of the normal stress σ_n against the shear stress τ for the Mohr circle and the line of failure $\tau = \tau_o + \mu \sigma_n$.

Figure 7.28. Evolution of the state of stress below the center of the ice load and how they affect the Mohr circle in a thrust-faulting stress regime. (After Steffen et al. 2021).

Figure 7.29. Evolution of dFSM at Lac Témiscouata predicted by 5 different Earth models. Positive values of dFSM implies fault stability, while negative values implies fault instability is promoted. The observed timing of the earthquake from Shilts et al. (1992) is indicated by the horizontal red bar at the bottom. (After Wu and Mazzotti, 2007).

Figure 7.30. Osning Thrust in north central Europe experienced a paleo-earthquake with fault slip estimated to be around 1 meter. This is followed by a historic seismic event in 1612. The red curve is the predicted evolution of dFSM that can fit all these observations simultaneously. The

dotted curves indicate how the magnitude of the fault slip affects subsequent evolution of dFSM. (After Brandes et al., 2018).

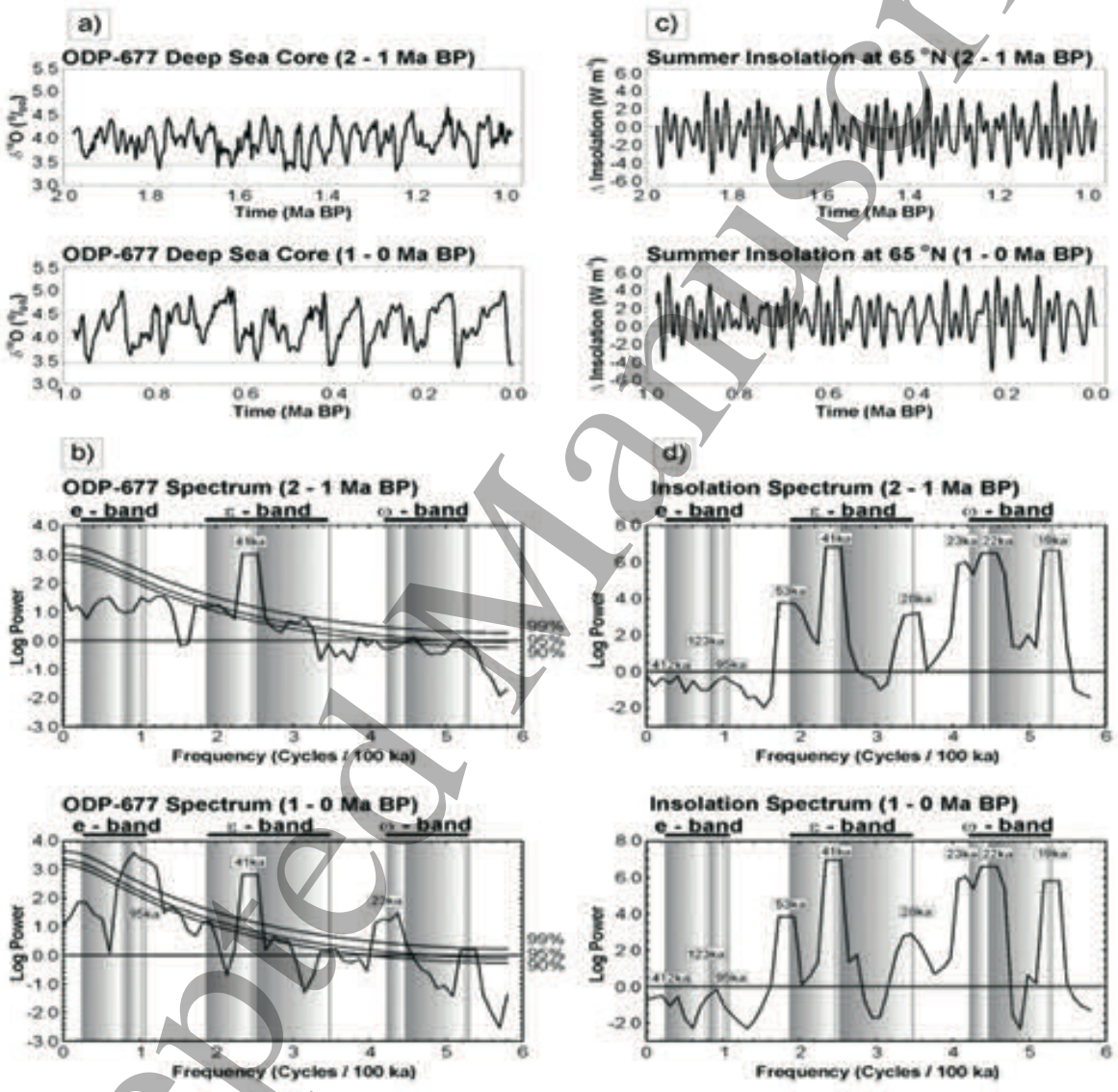

Fig1.1

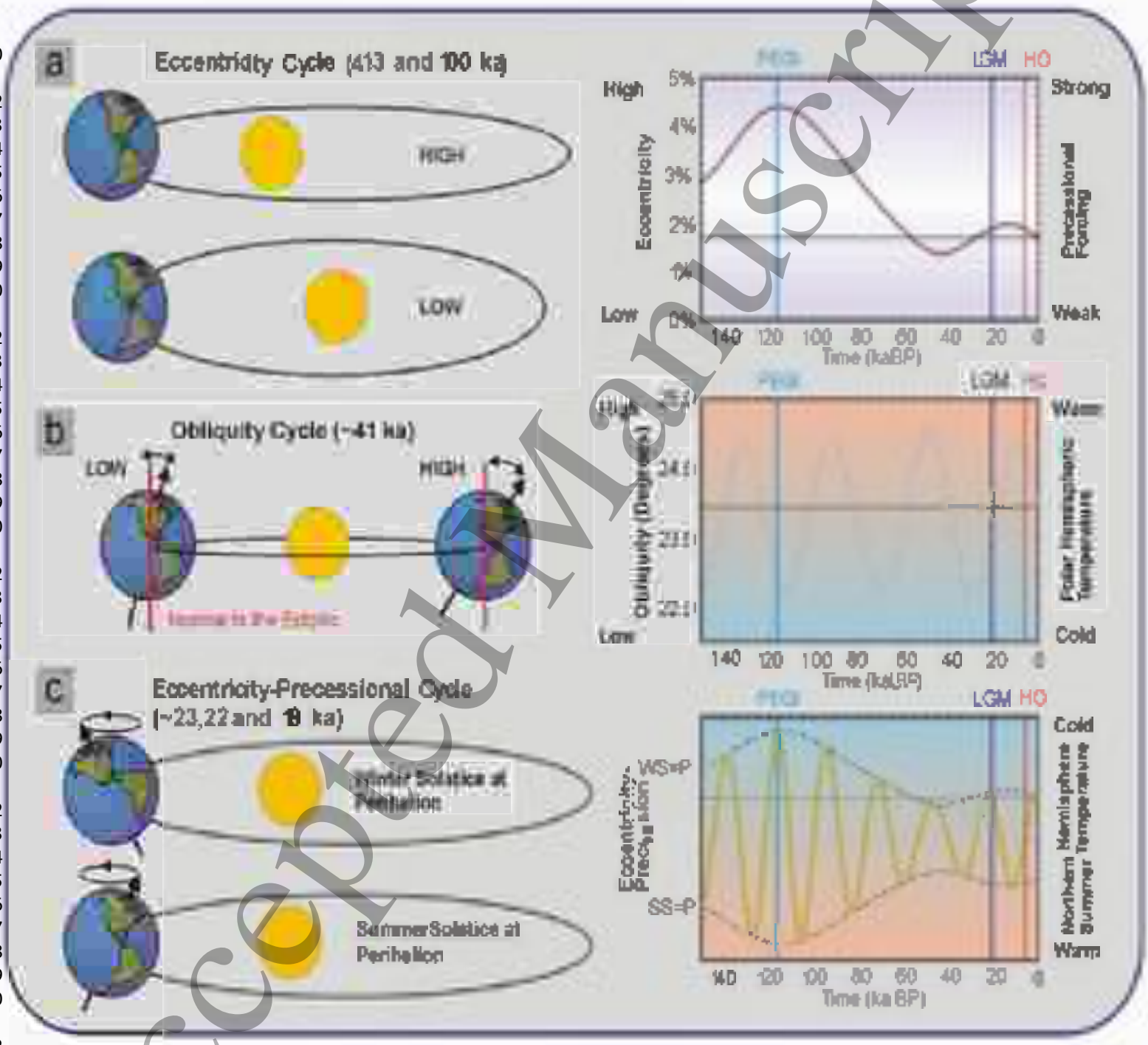

Fig 1.2

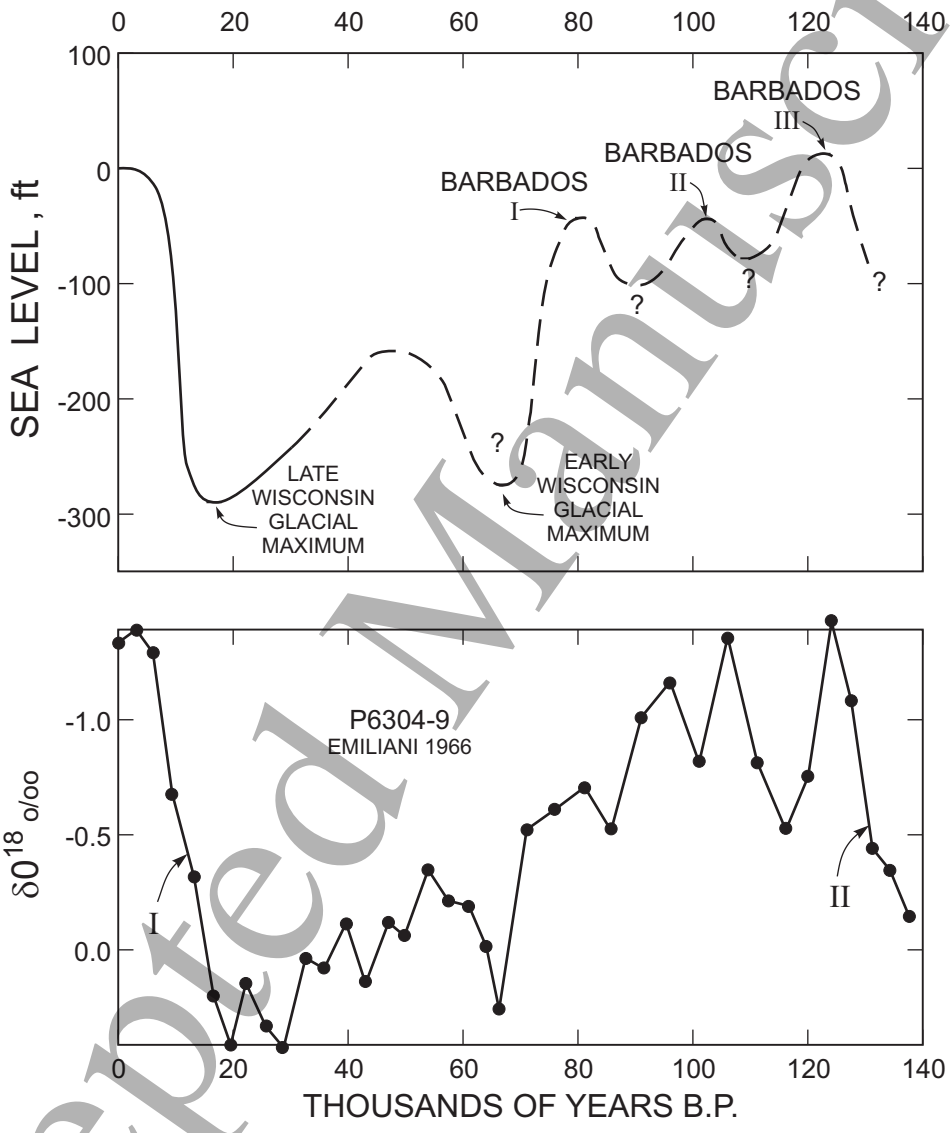

Fig 1.3 a-b

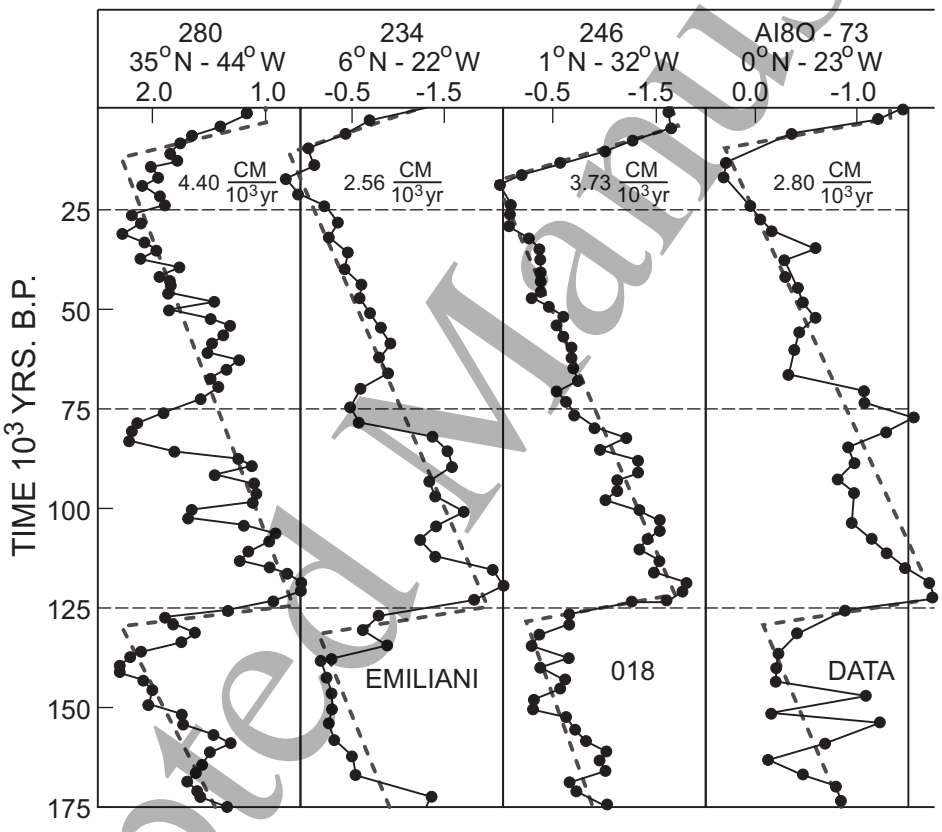

Fig 1.3c

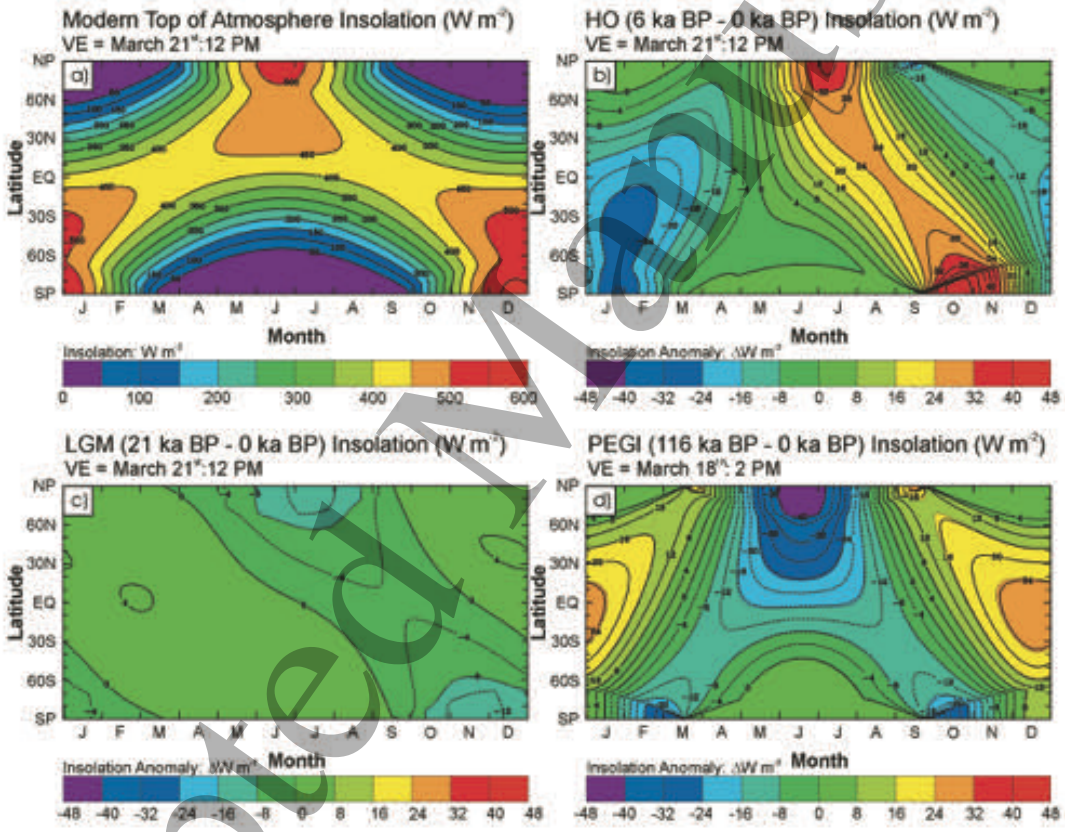

Fig 1.4

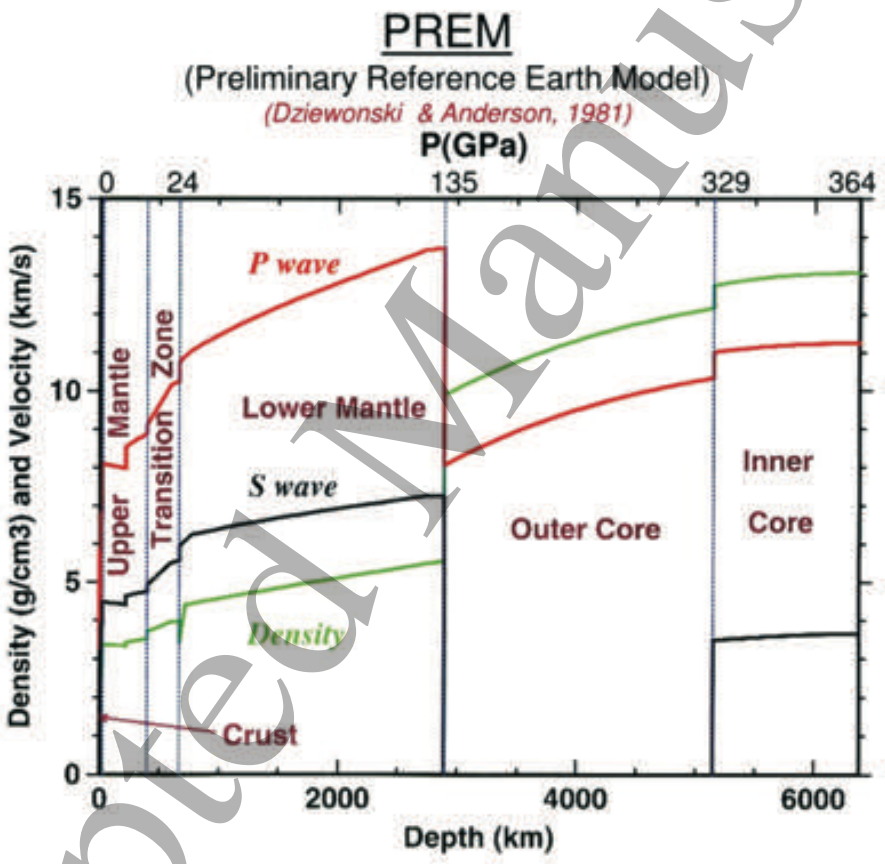

Fig 2.1

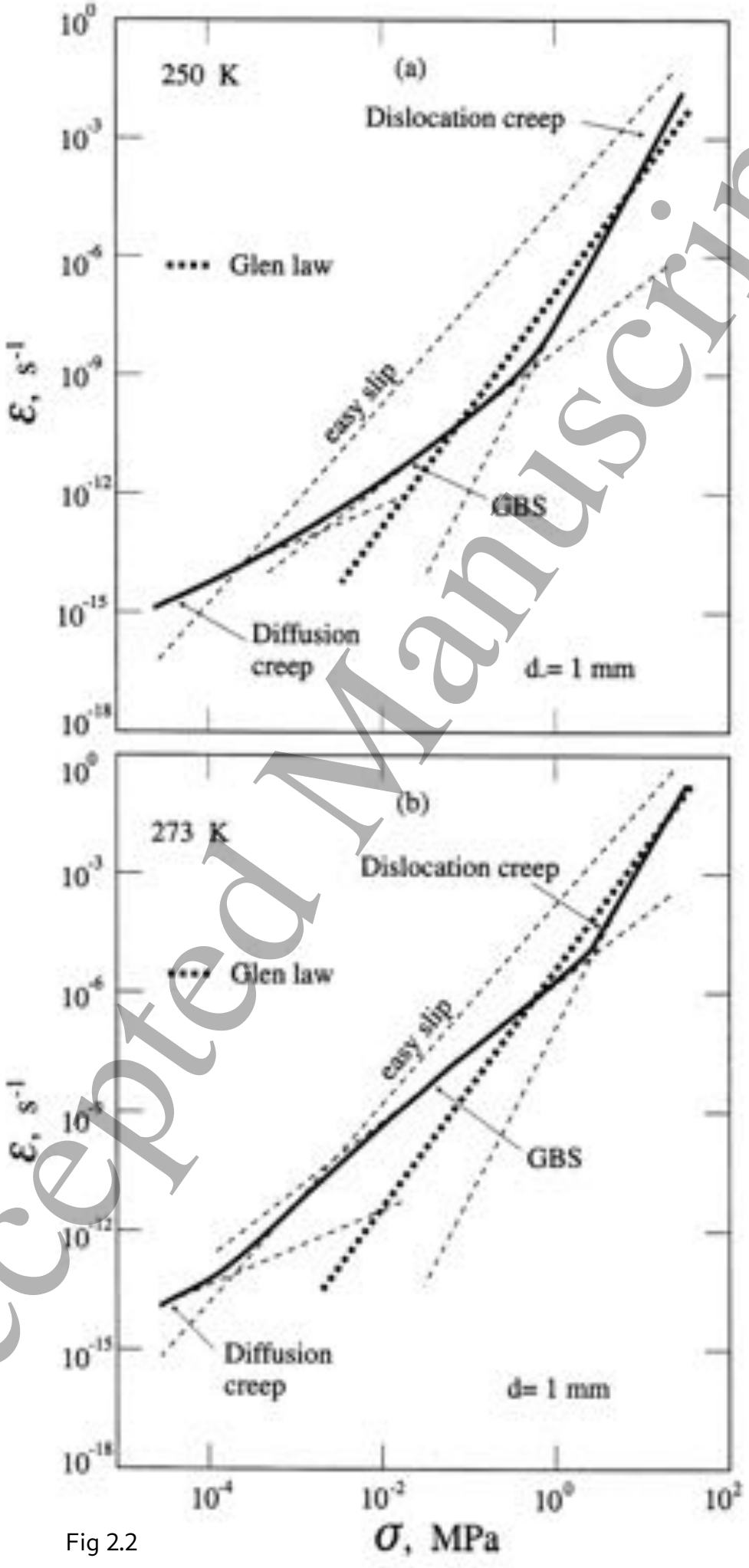

Fig 2.2

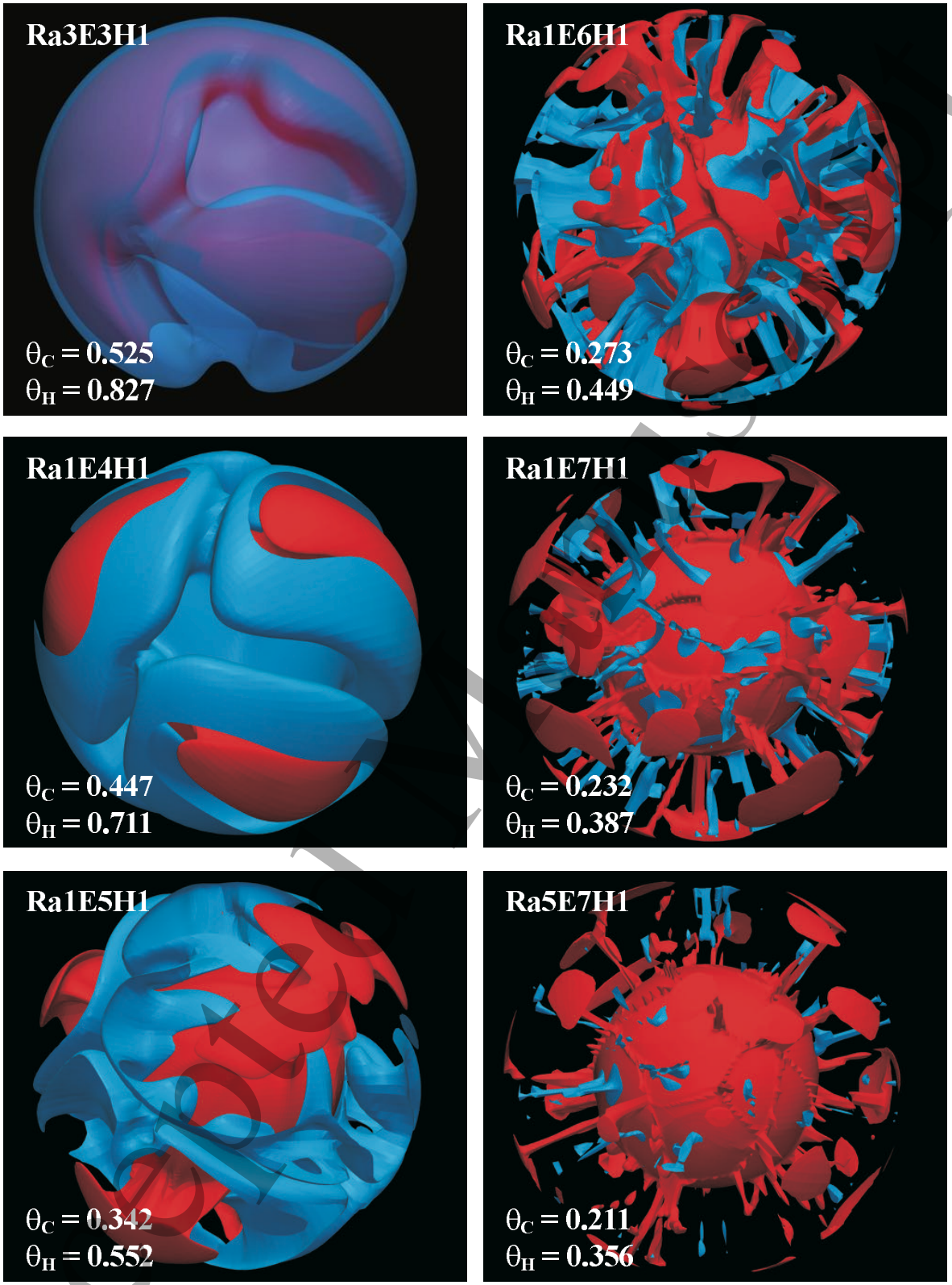

Fig 2.3

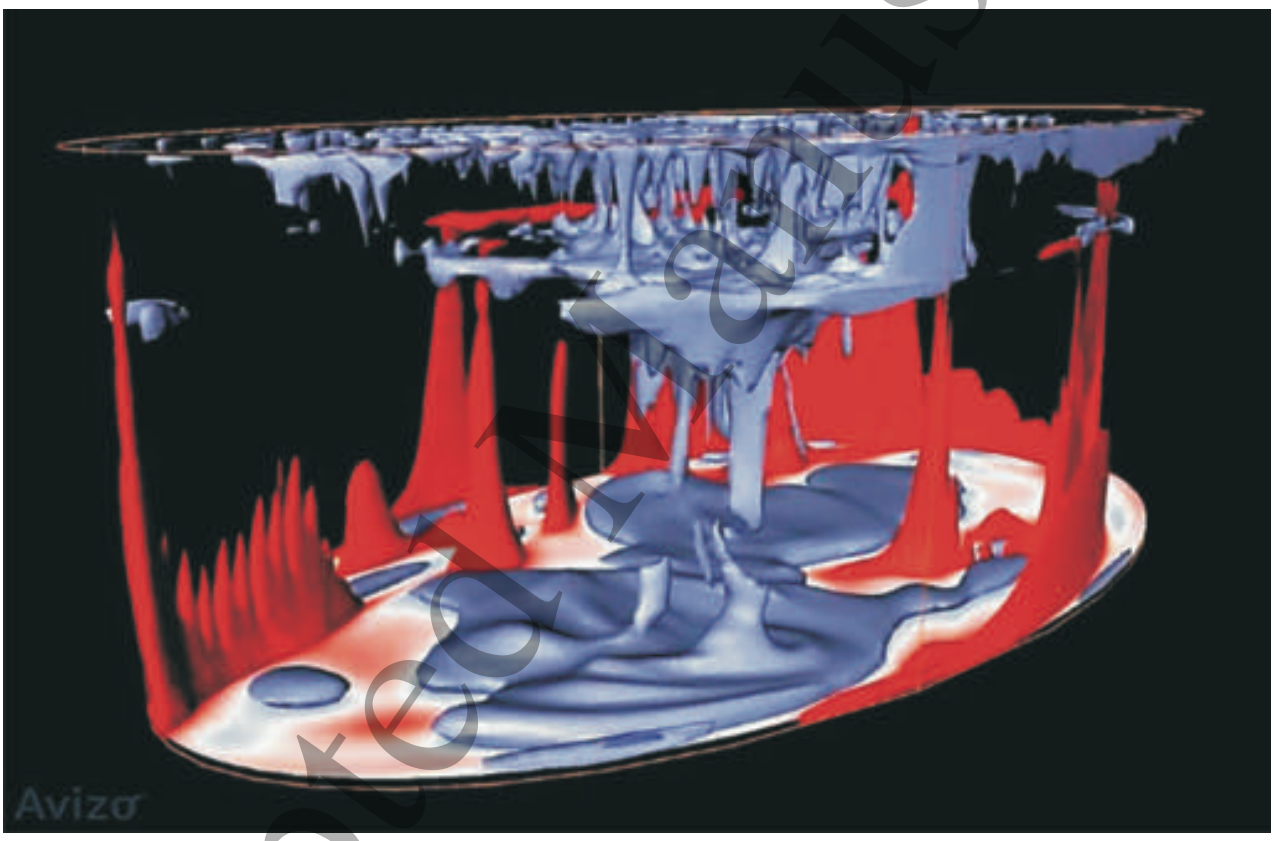

Fig 2.4

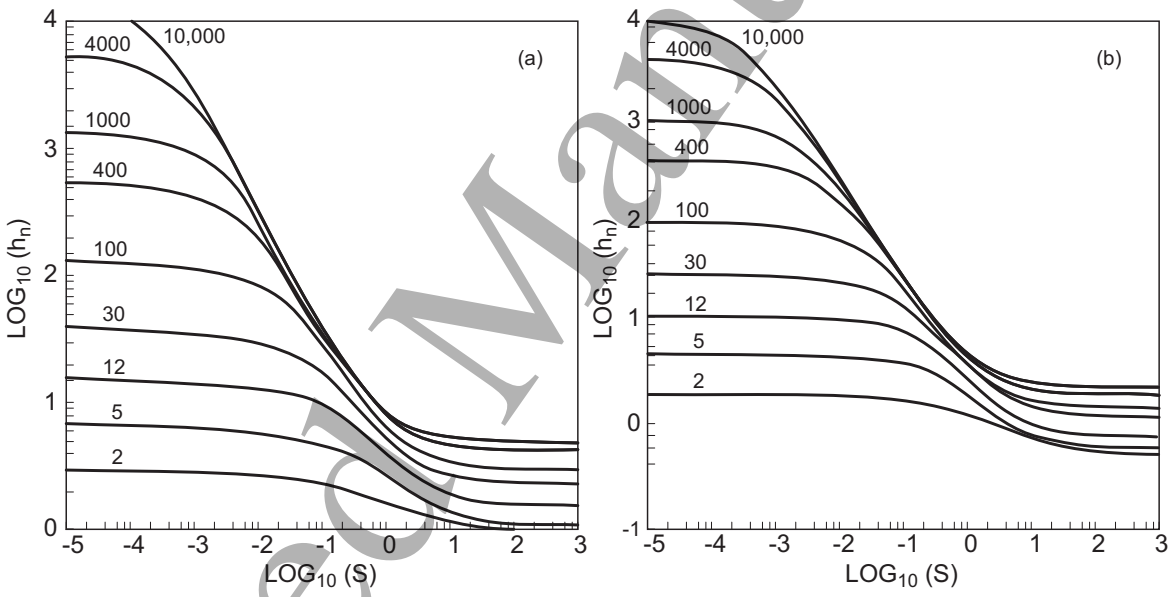

Fig 3.1 a-b

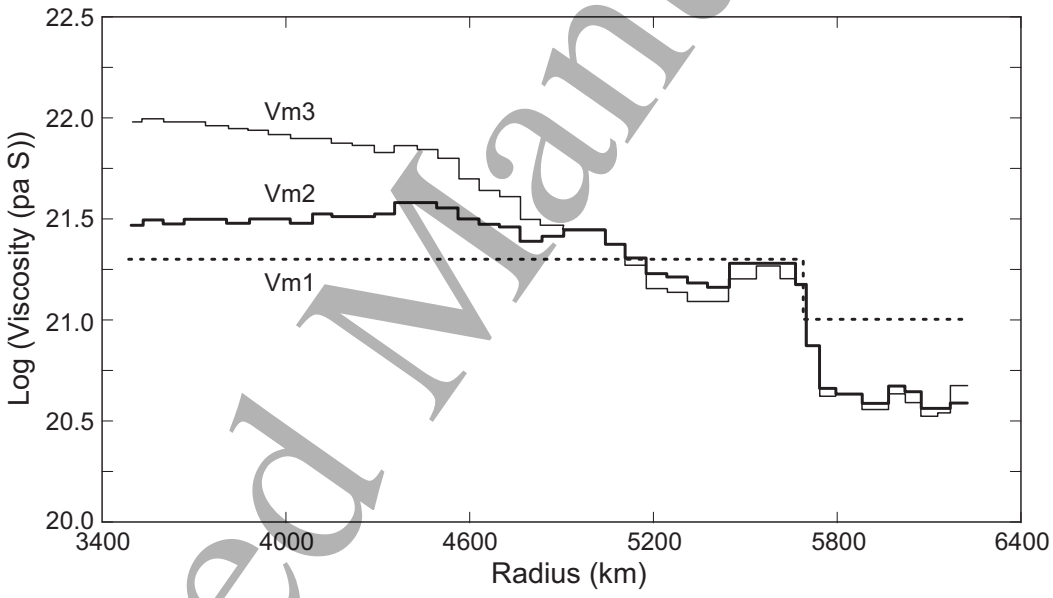

Fig 3.2

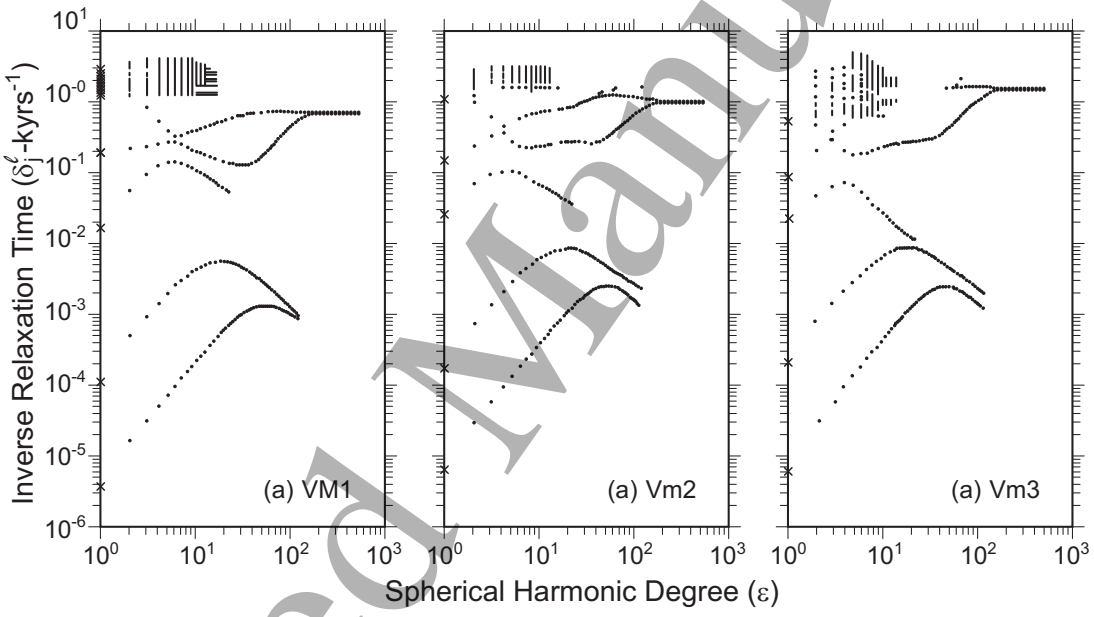

Fig 3.3

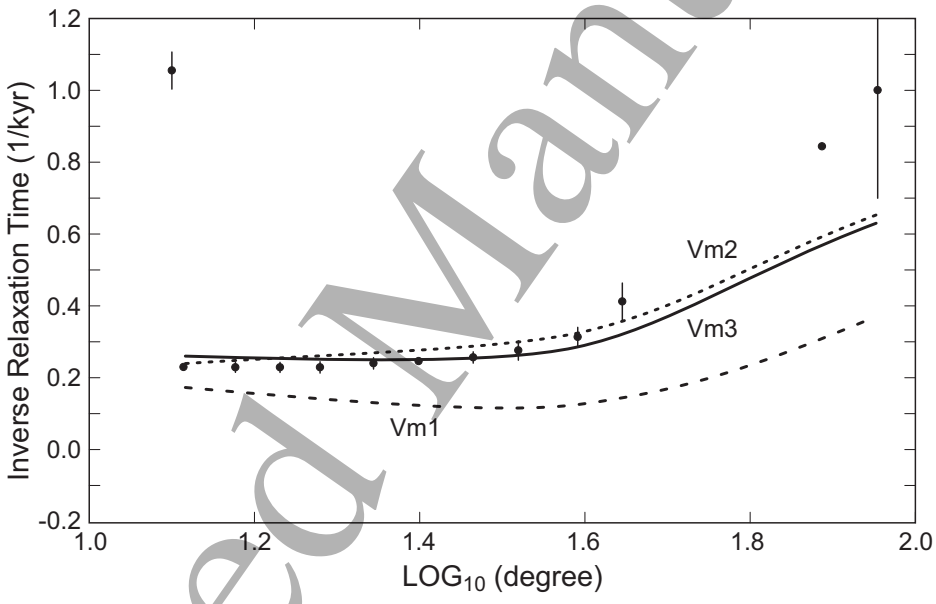

Fig 3.4

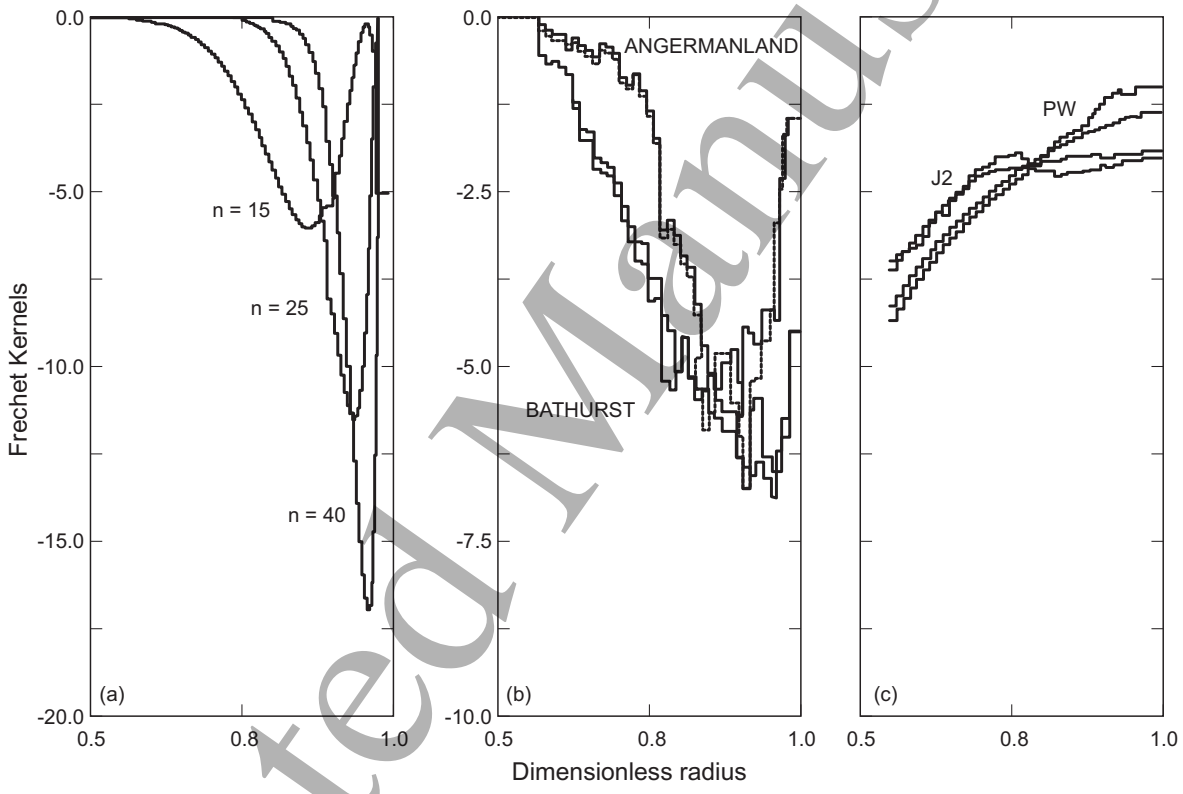

Fig 3.5

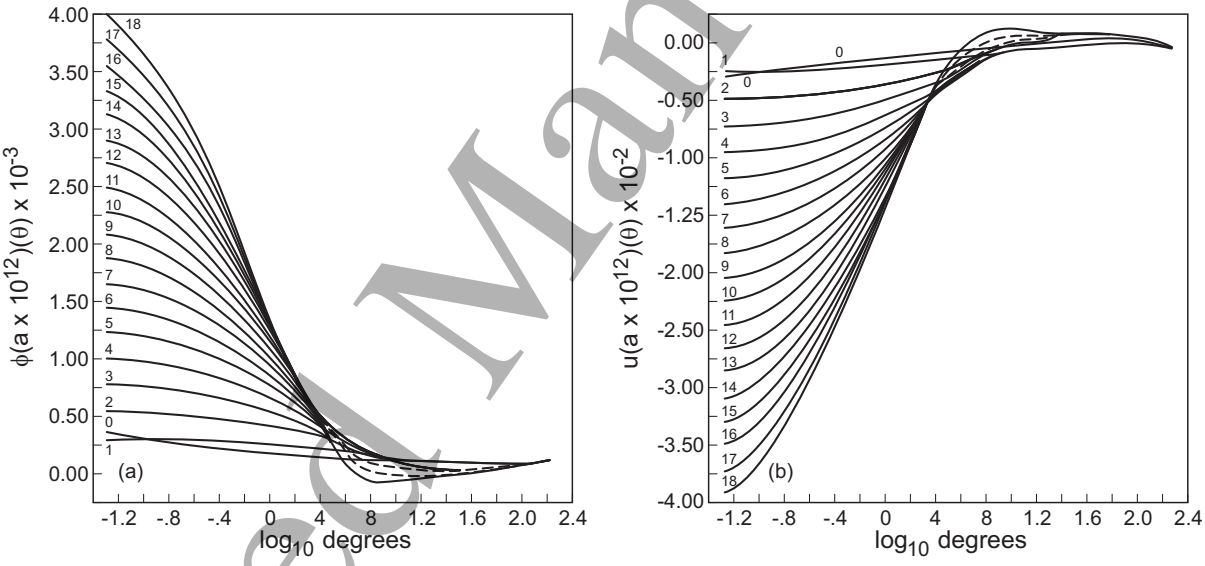

Fig 4.1

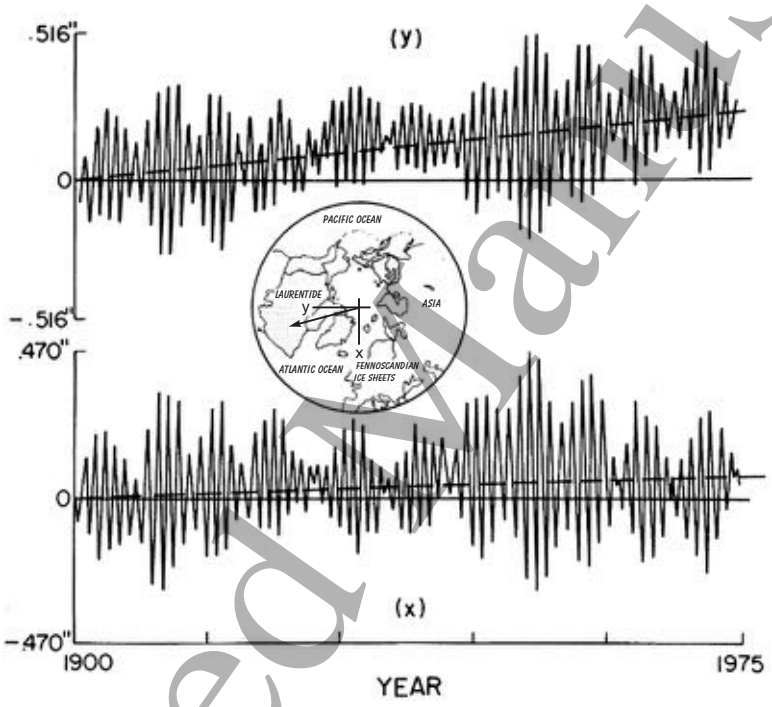

Fig 4.2

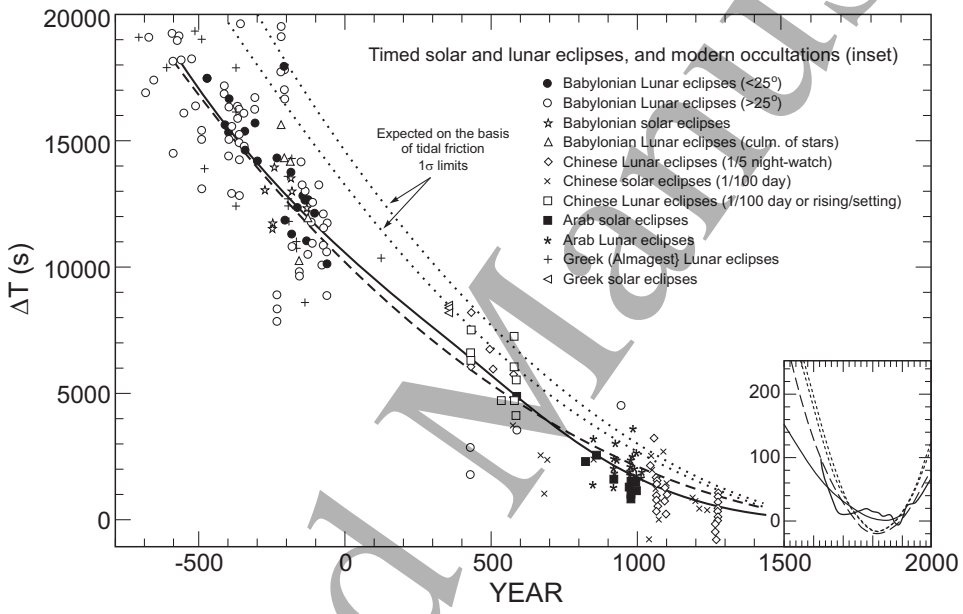

Fig 4.3

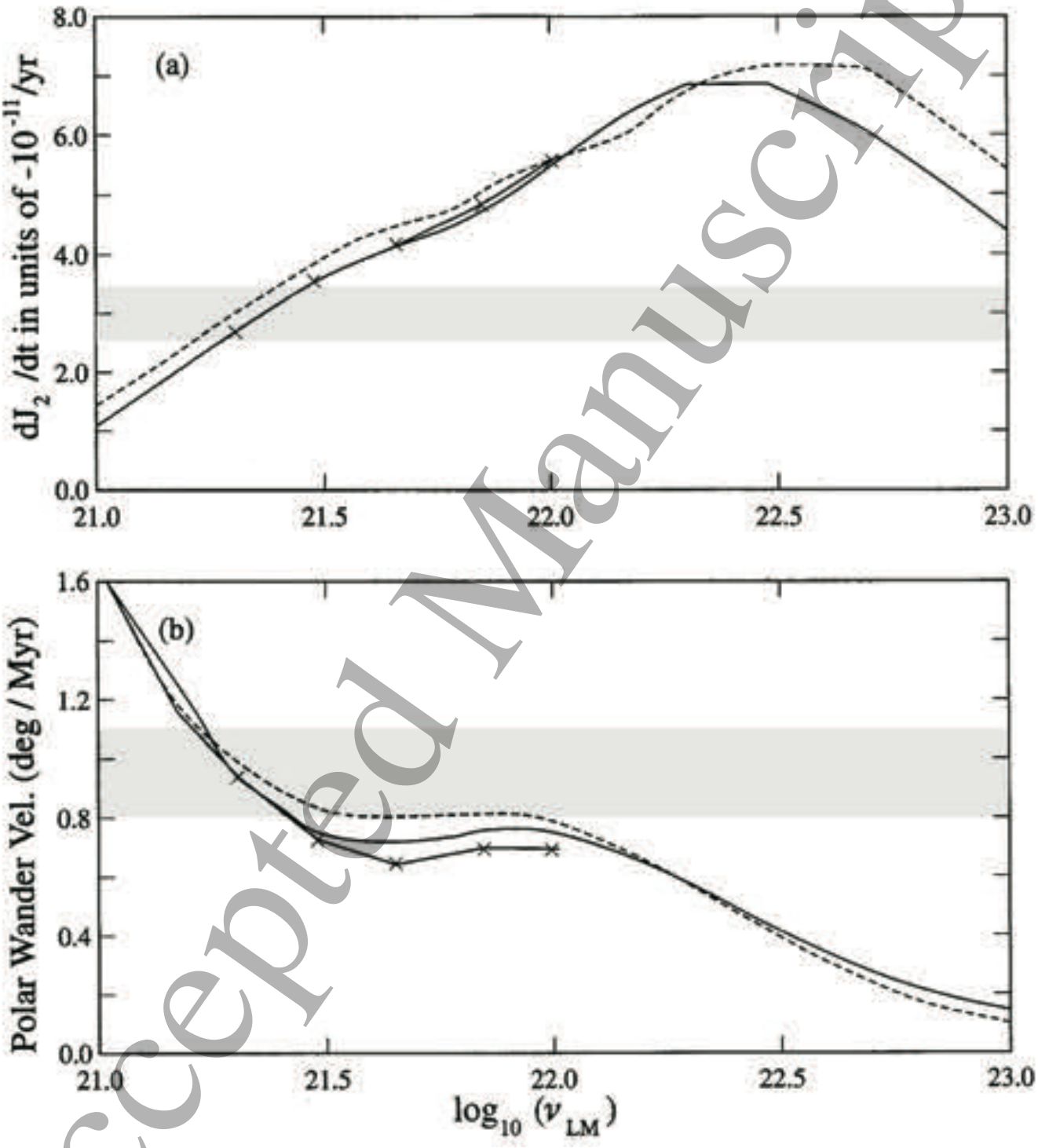

Fig 4.4

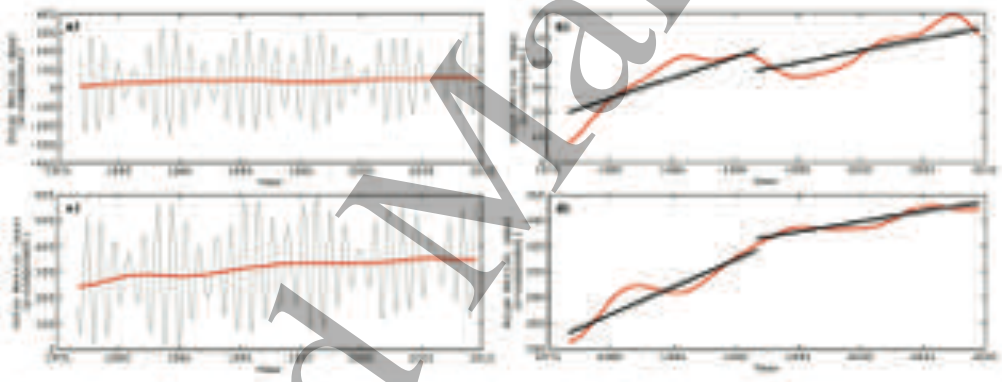

Fig 4.5 a

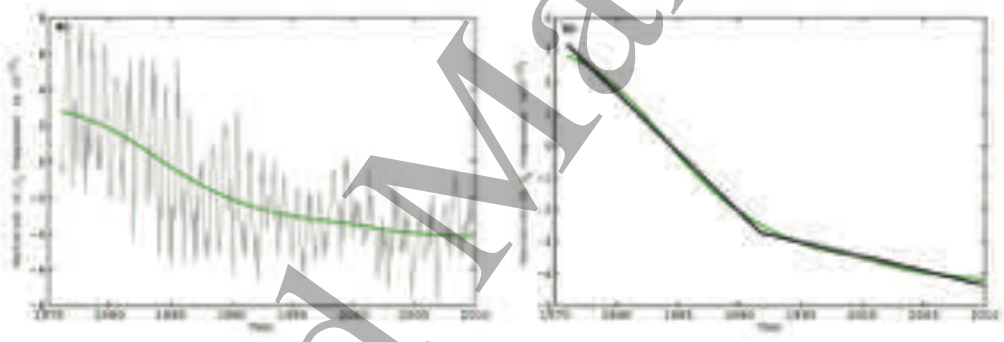

Fig 4.5b

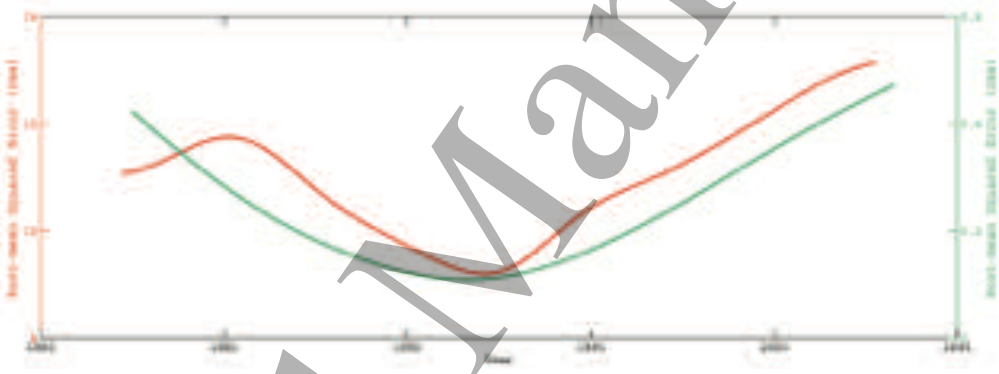

Fig 4.5c

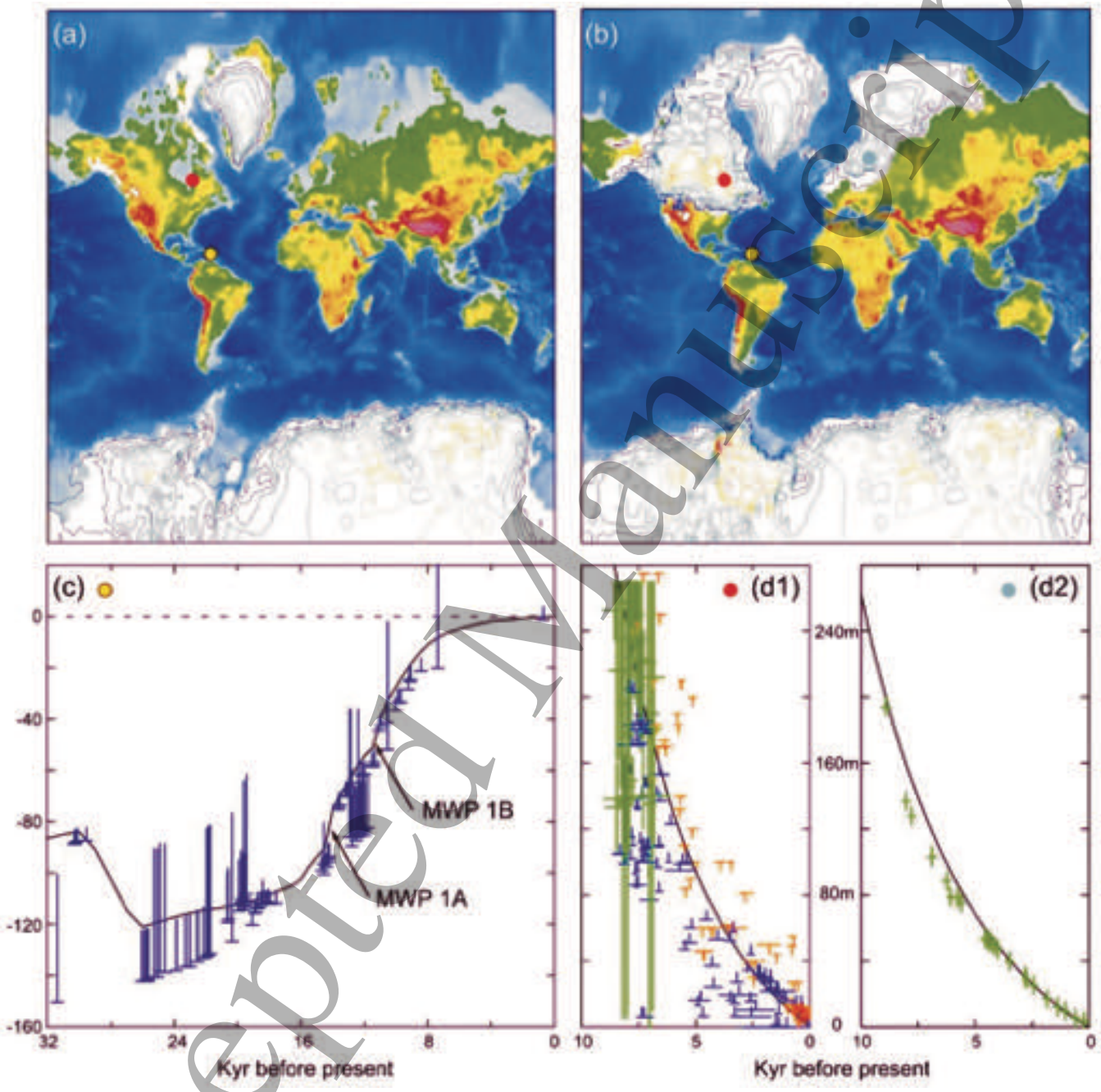

Fig 4.6

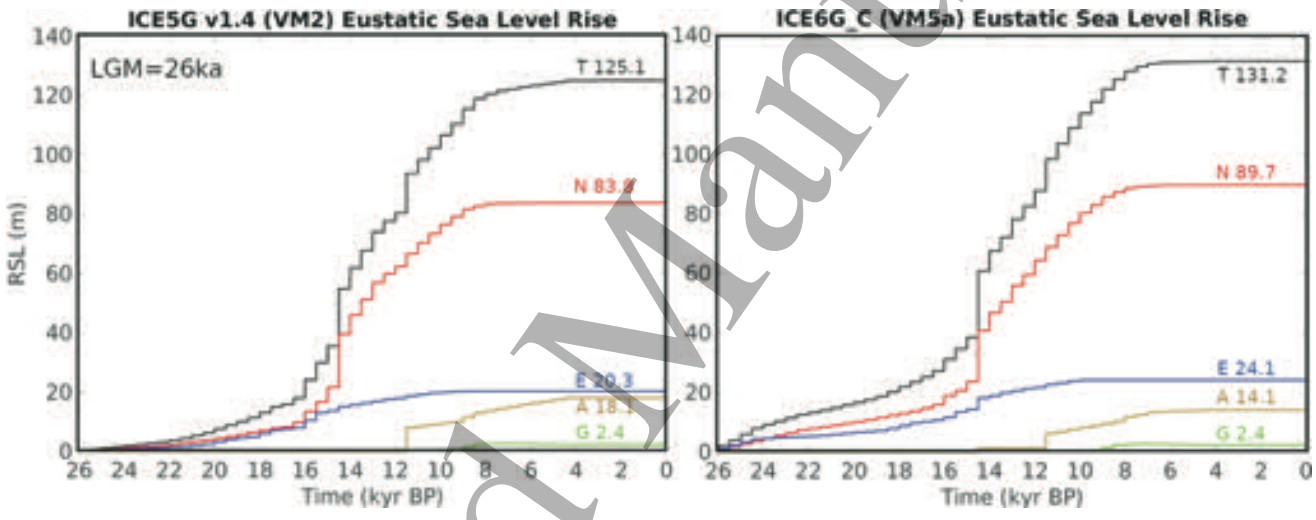

Fig 4.7

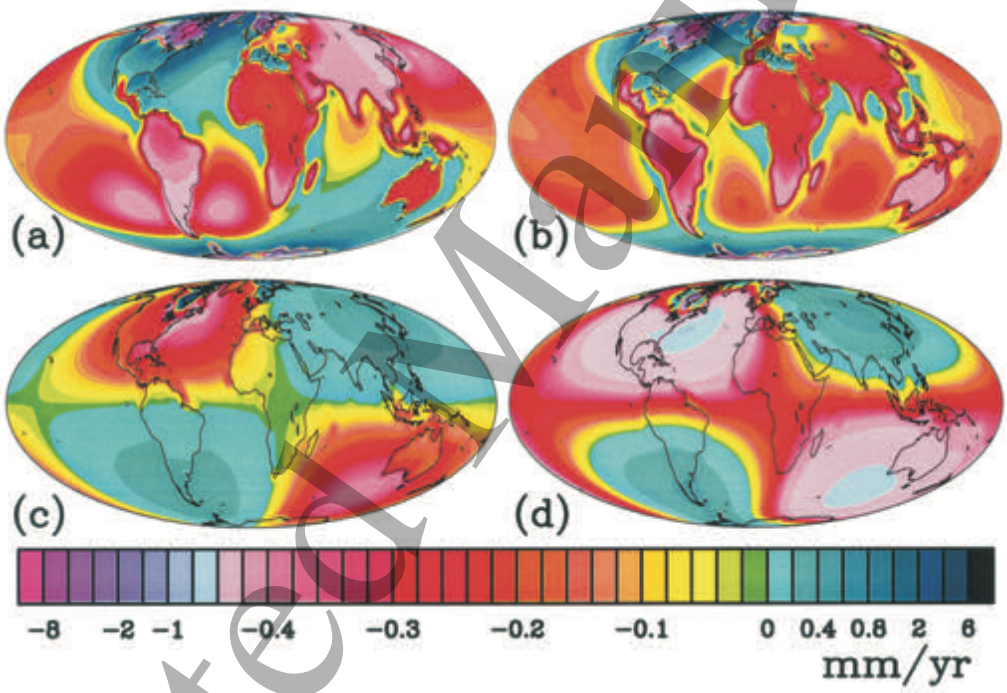

Fig 4.8

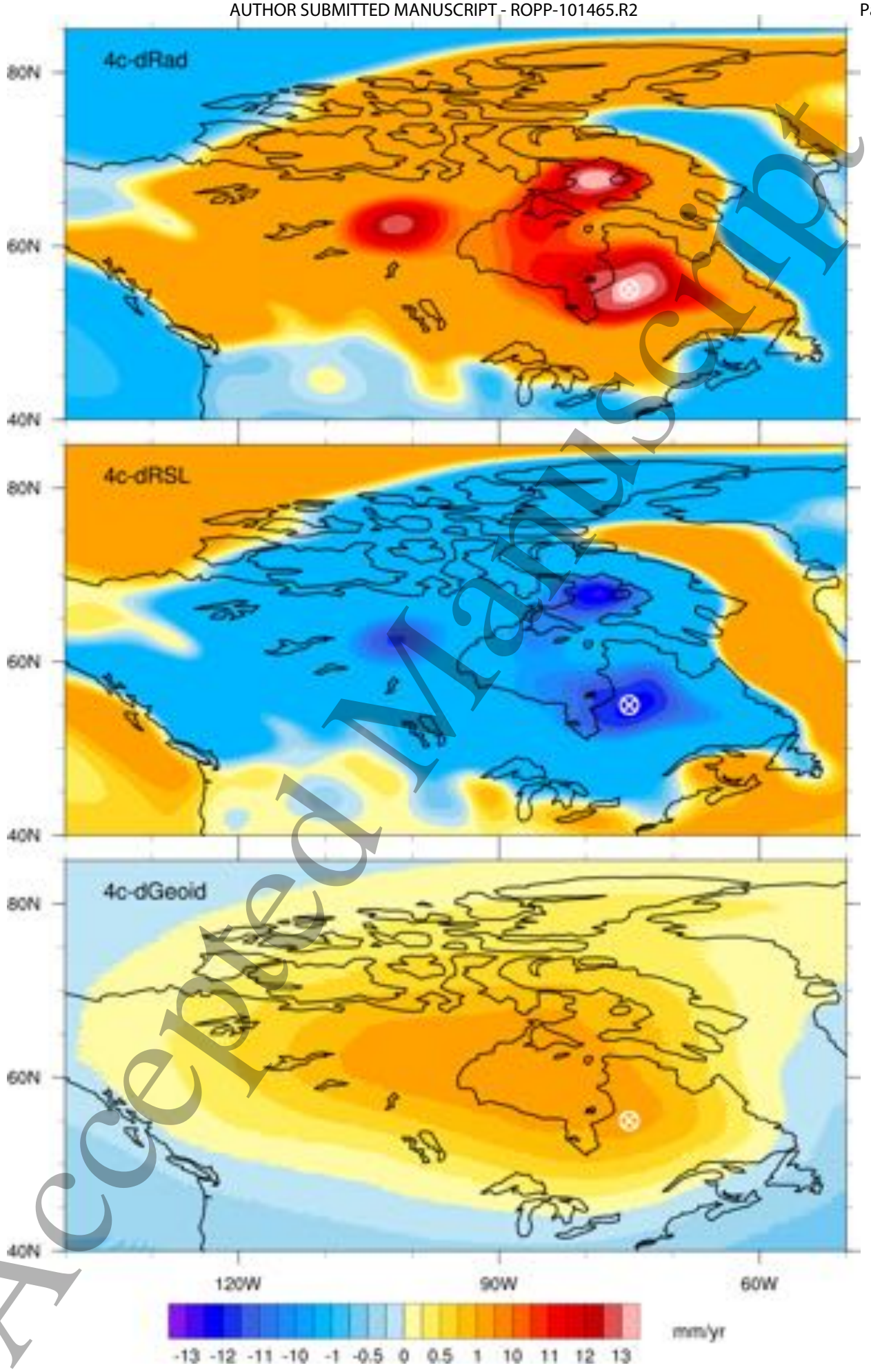

Fig 4.9

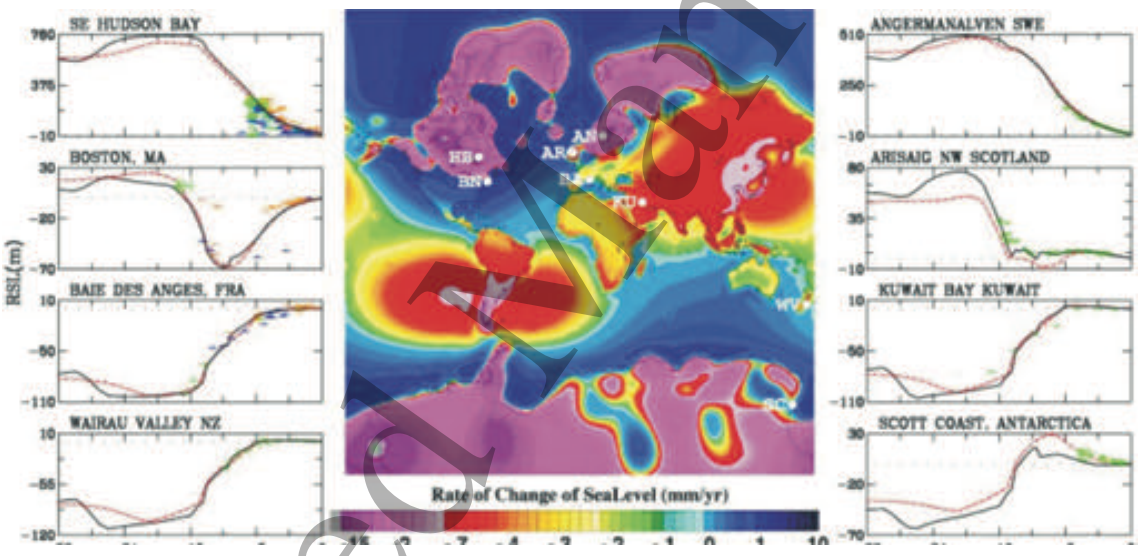

Fig 5.1

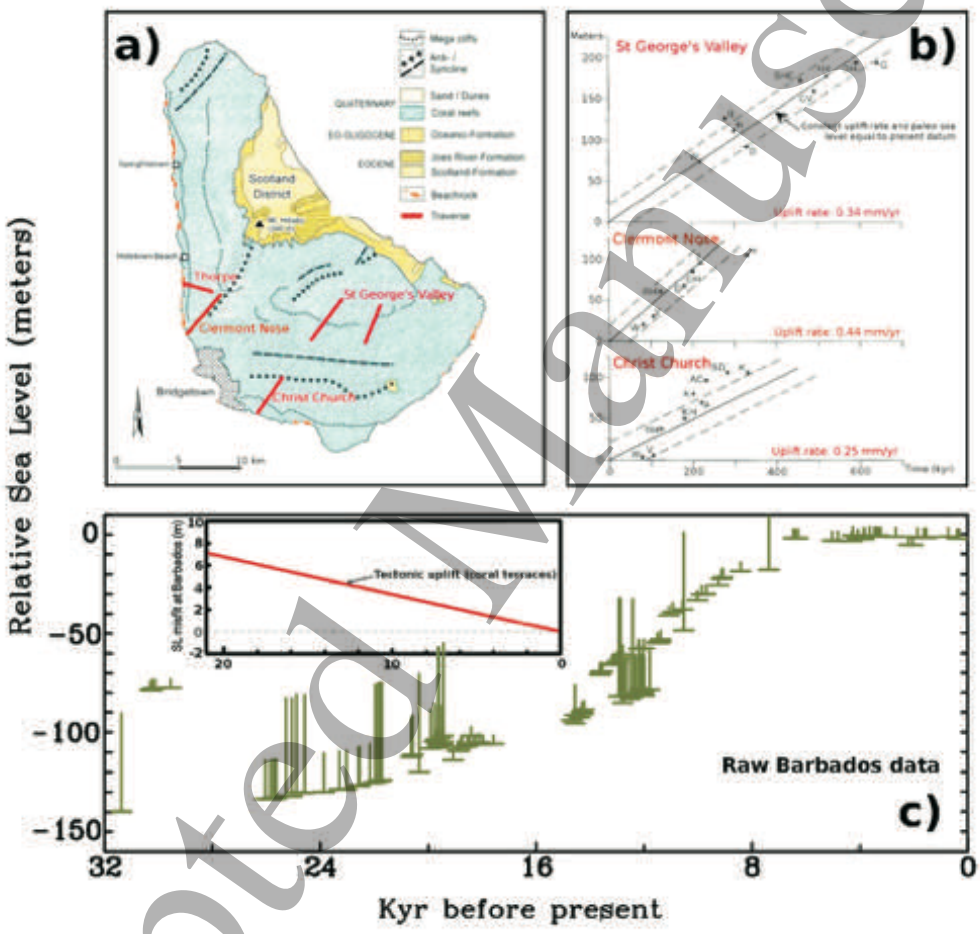

Fig 5.2

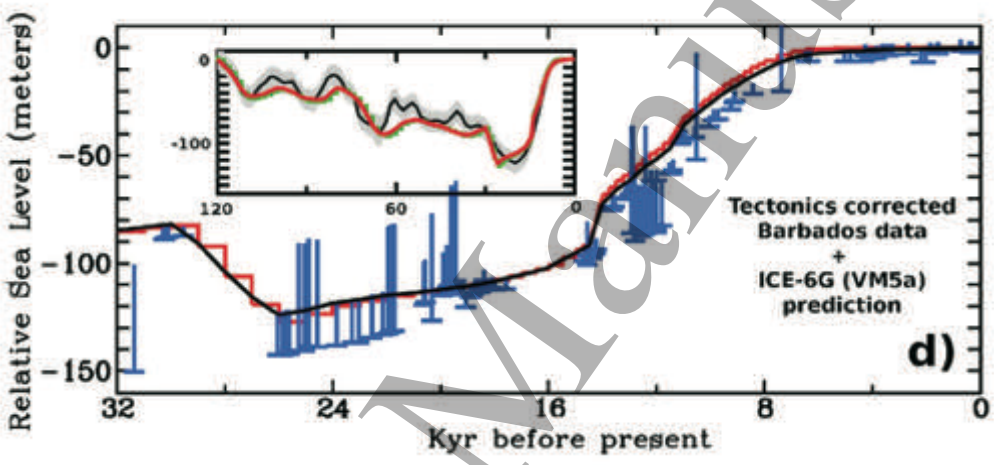

Fig 5.3

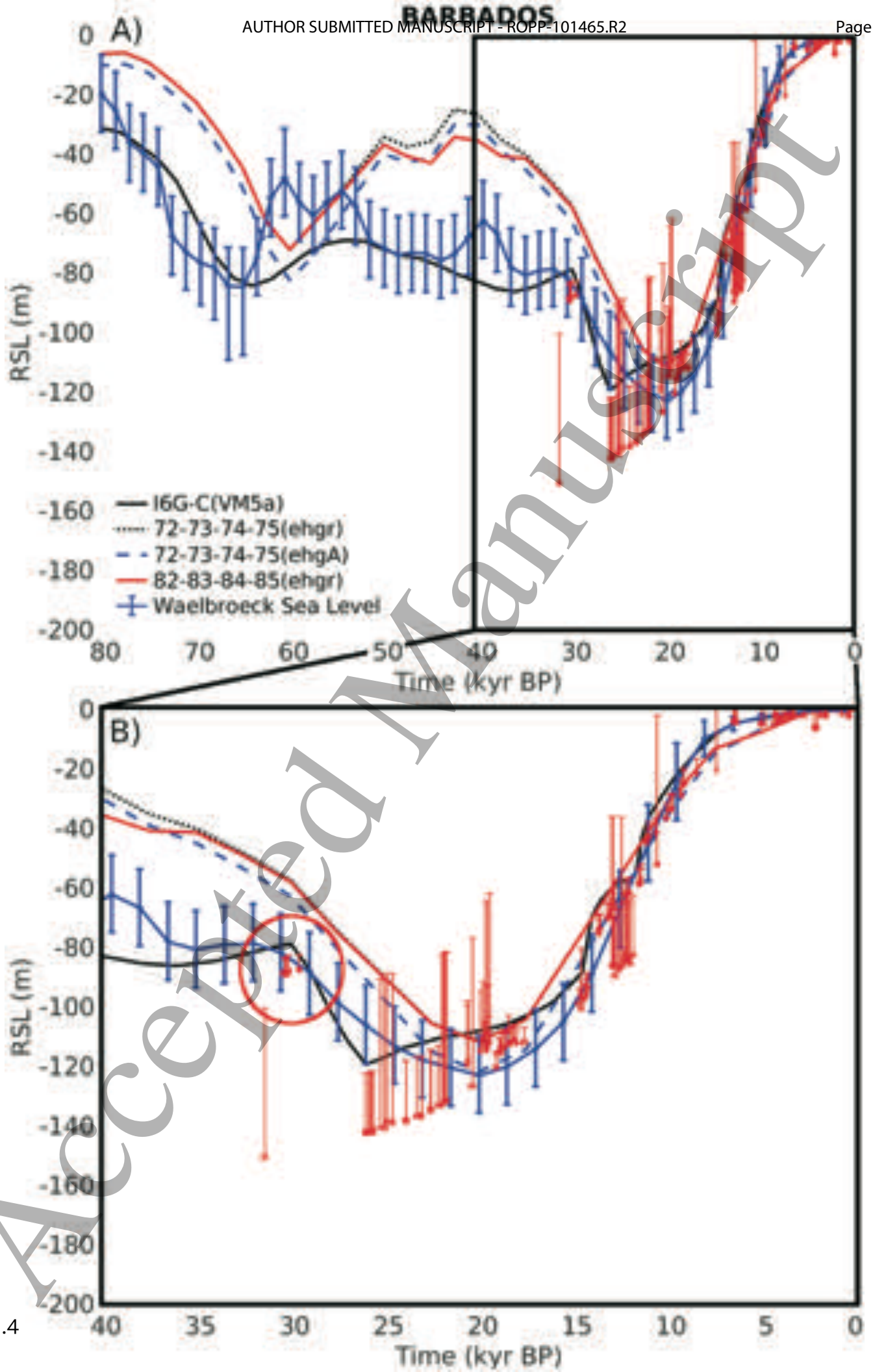

Fig 5.4

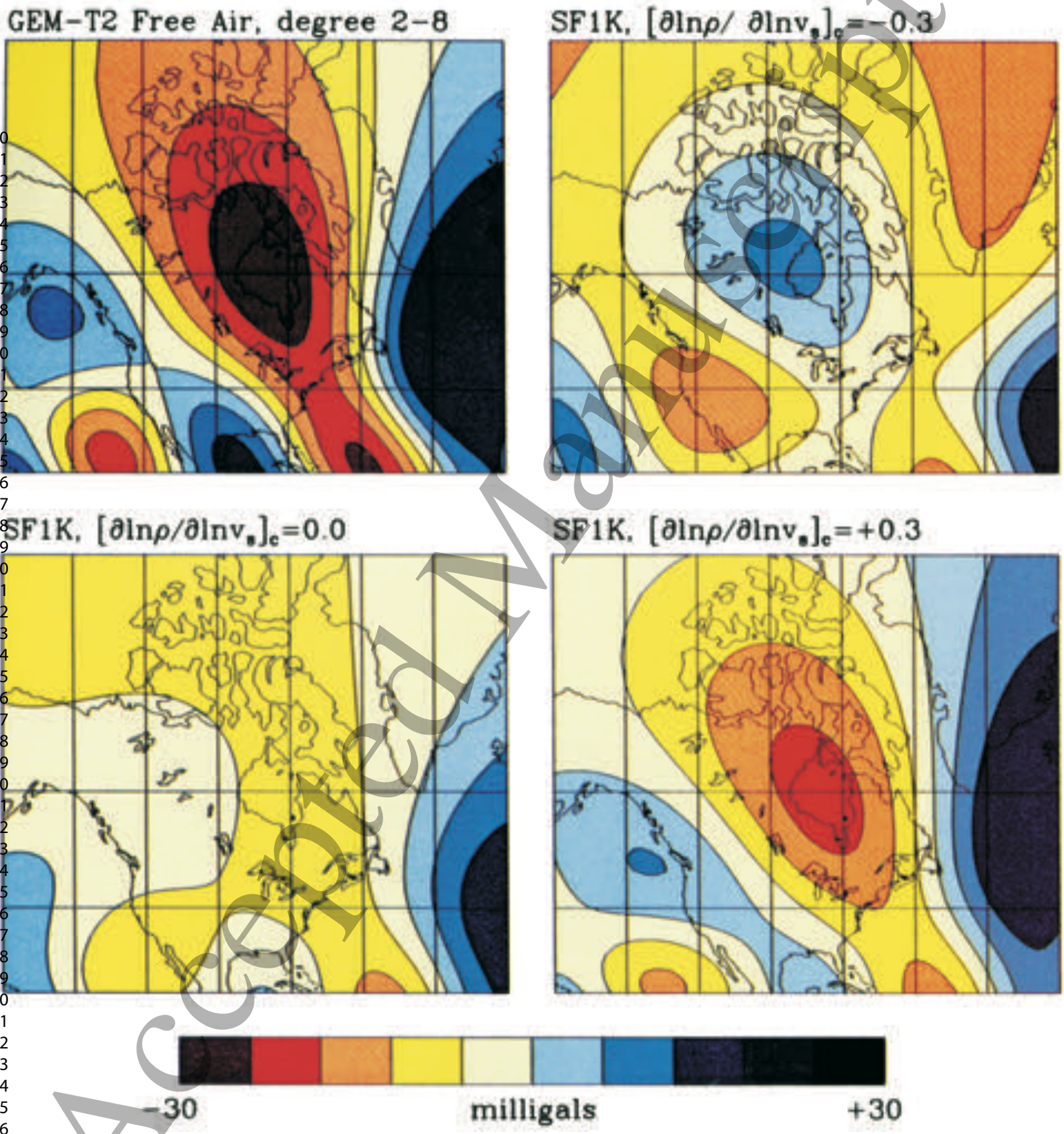

Fig 5.5

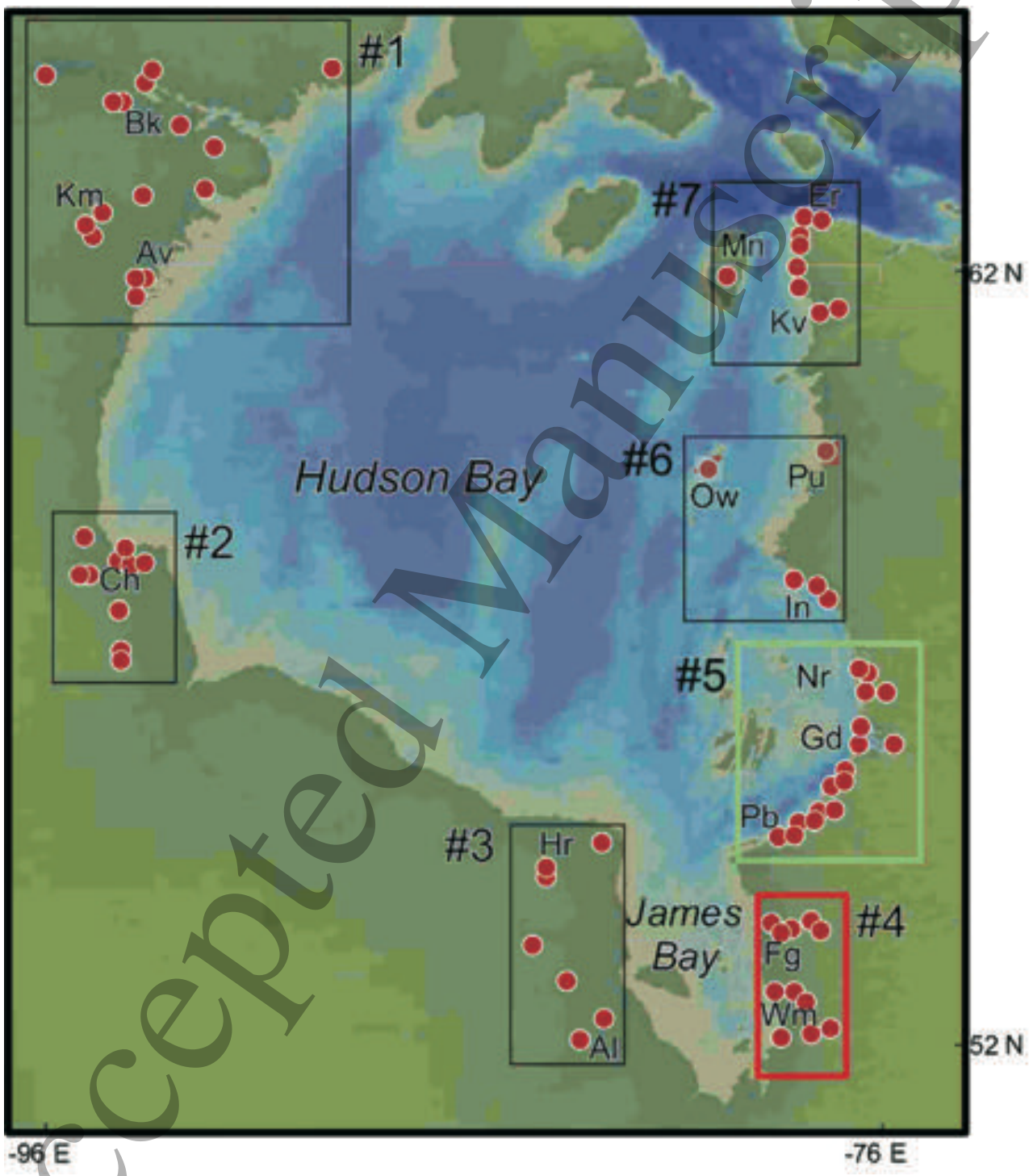

Fig 5.6

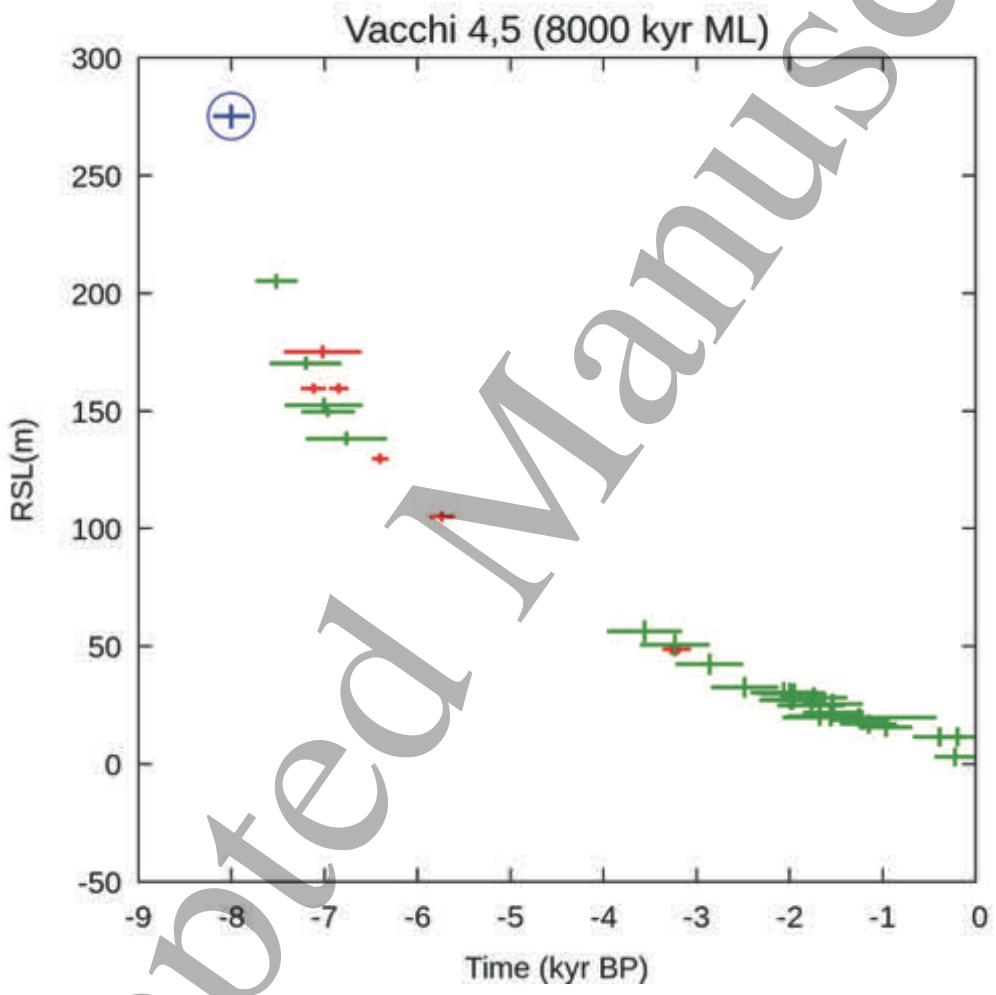

Fig 5.7

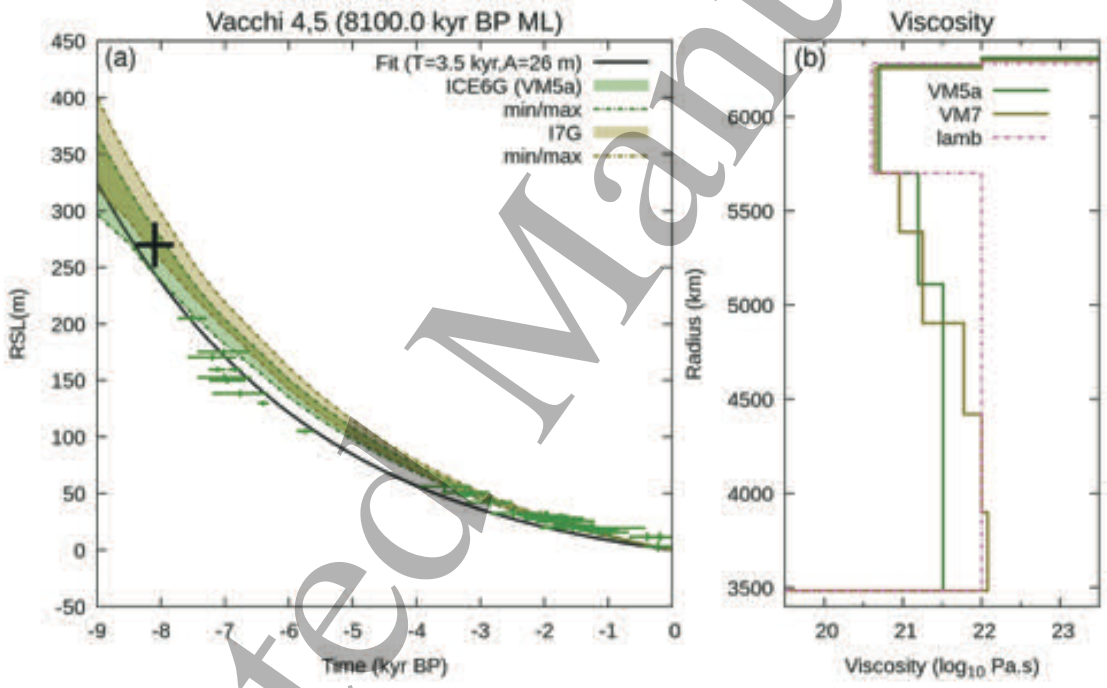

Fig 5.8

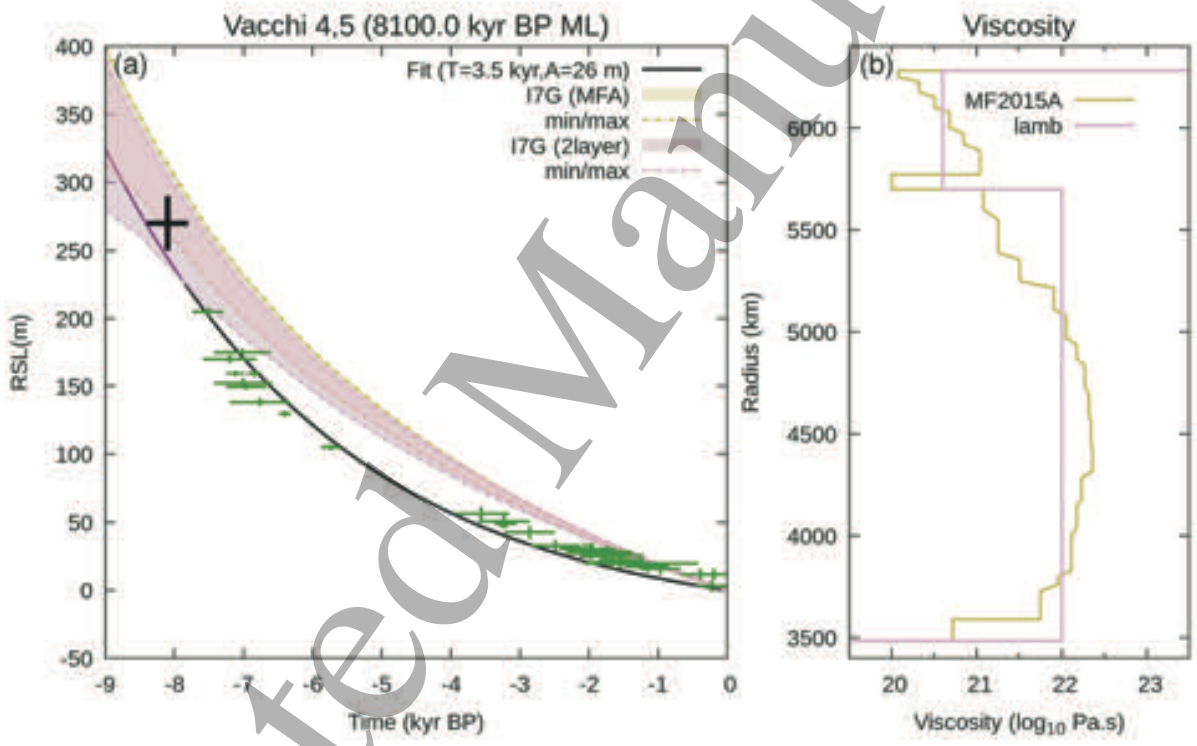

Fig 5.9

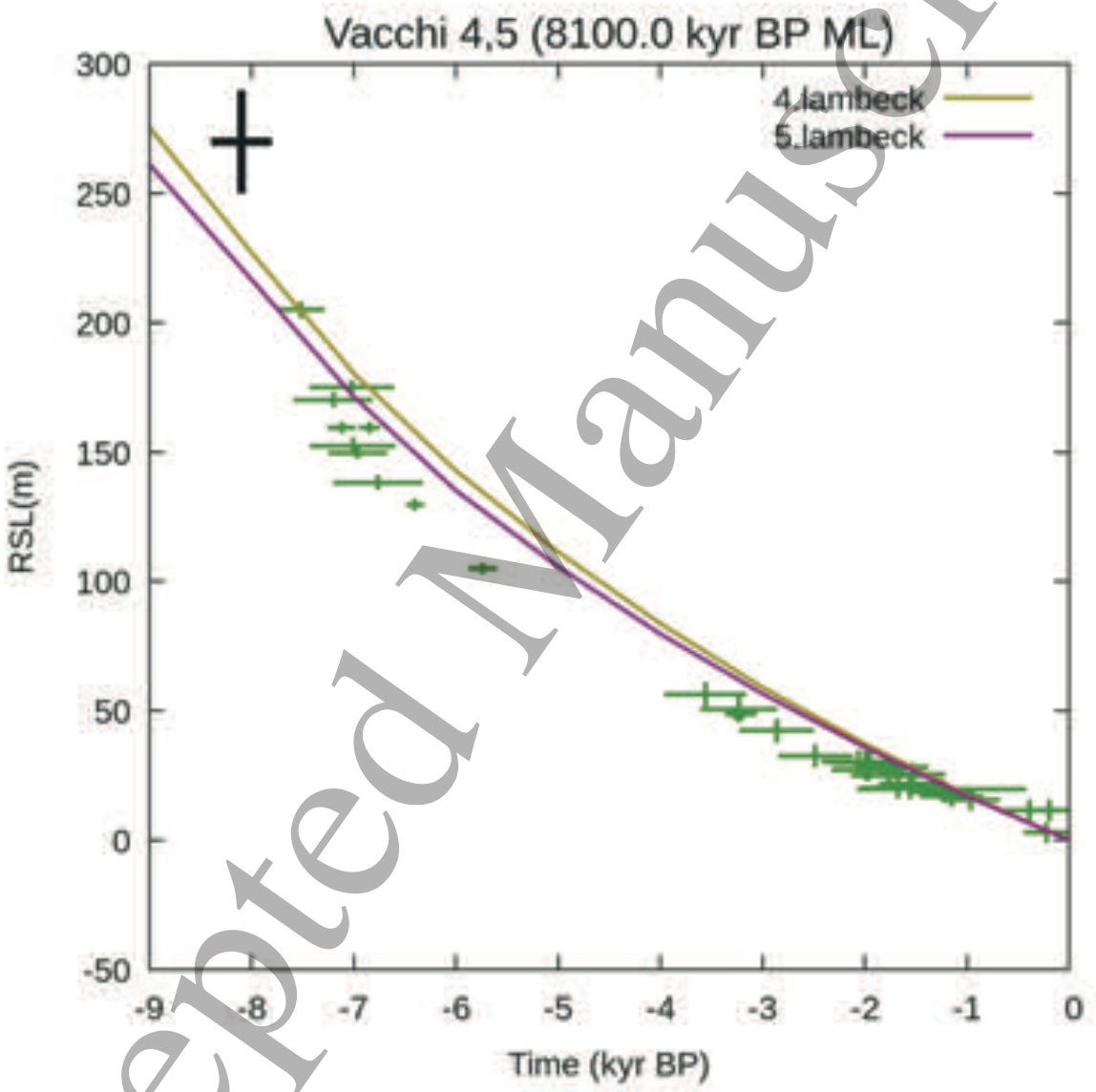

Fig 5.10

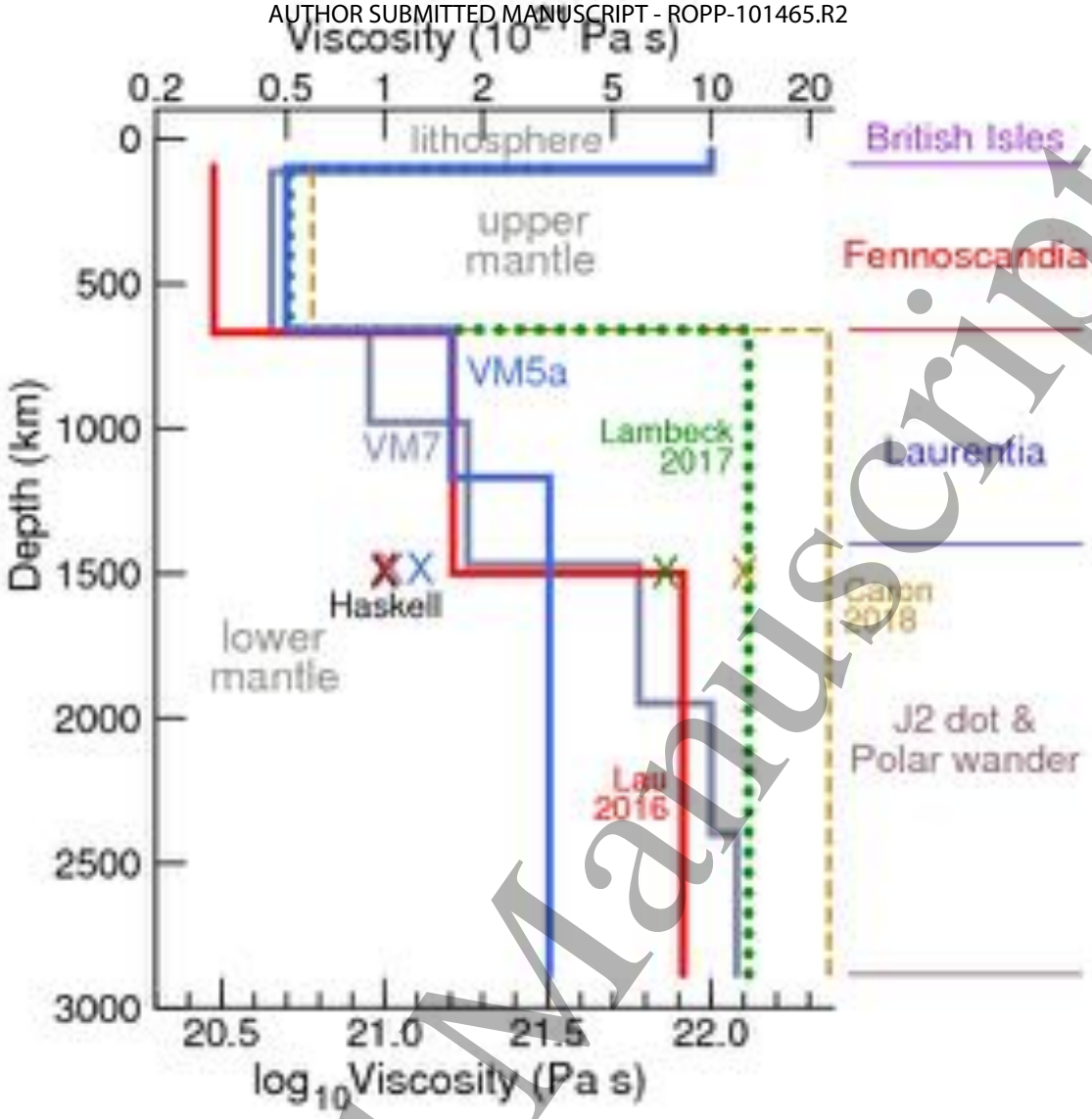

Fig 5.11

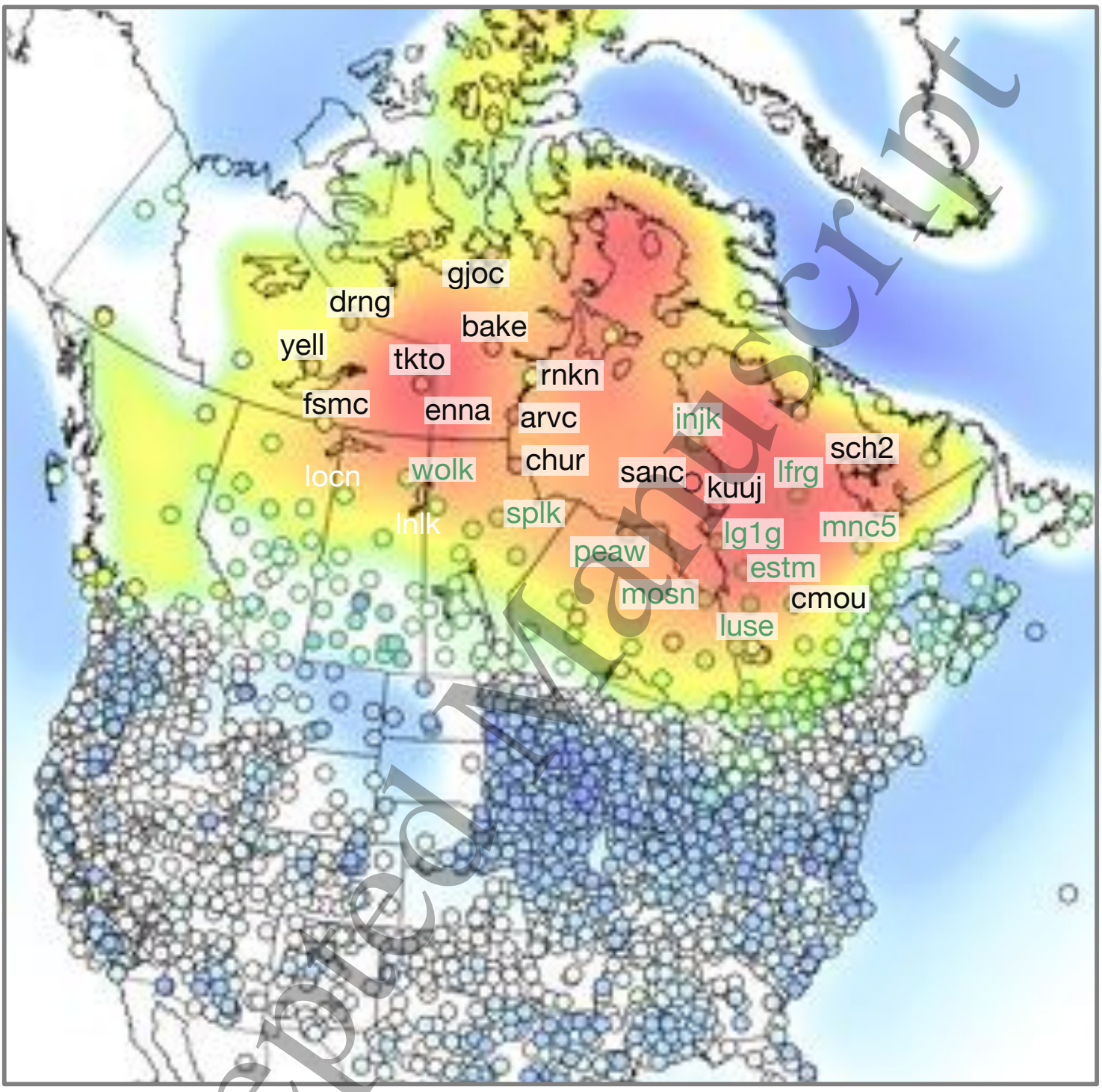

Fig 5.12

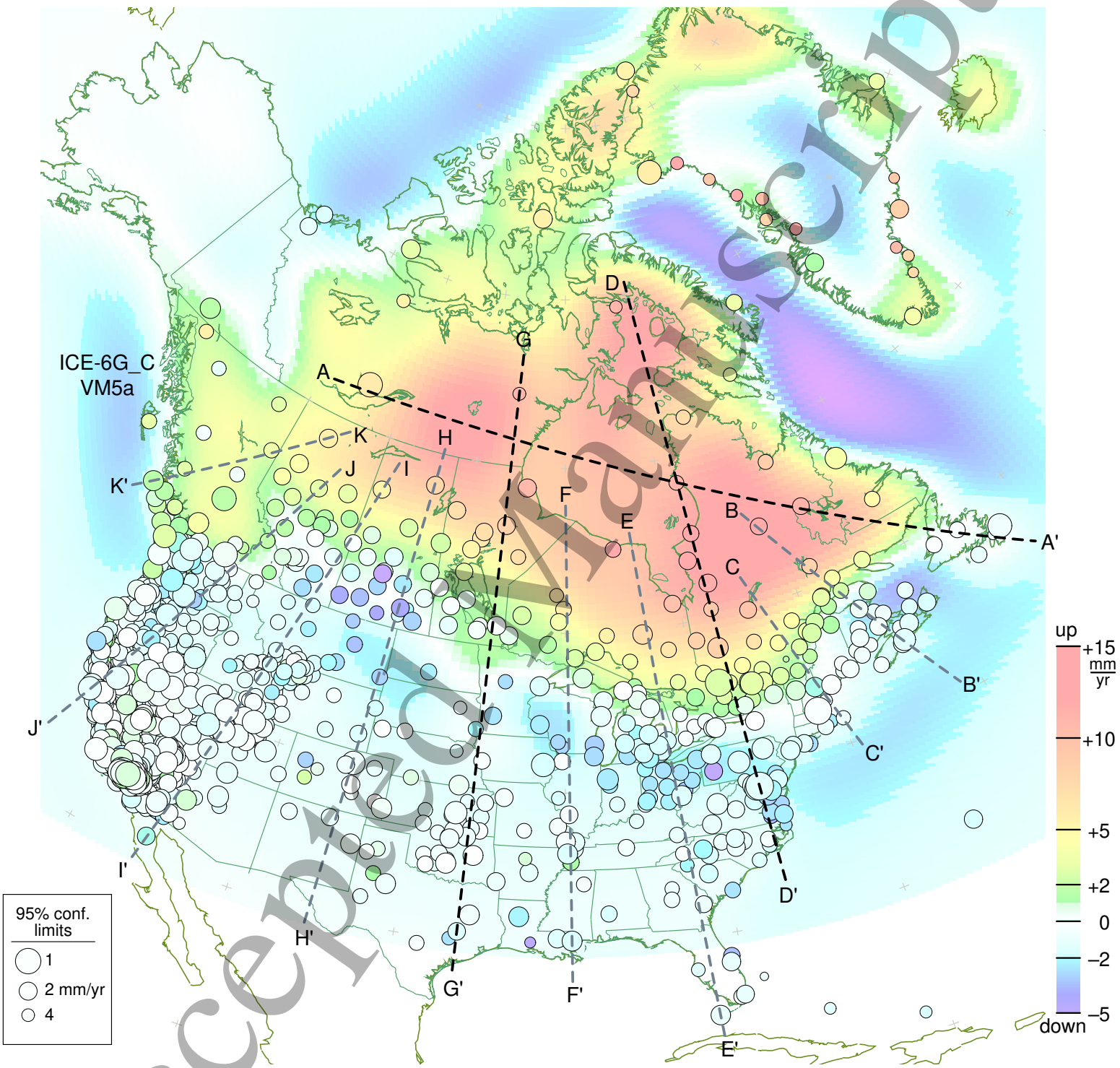

Fig 5.13

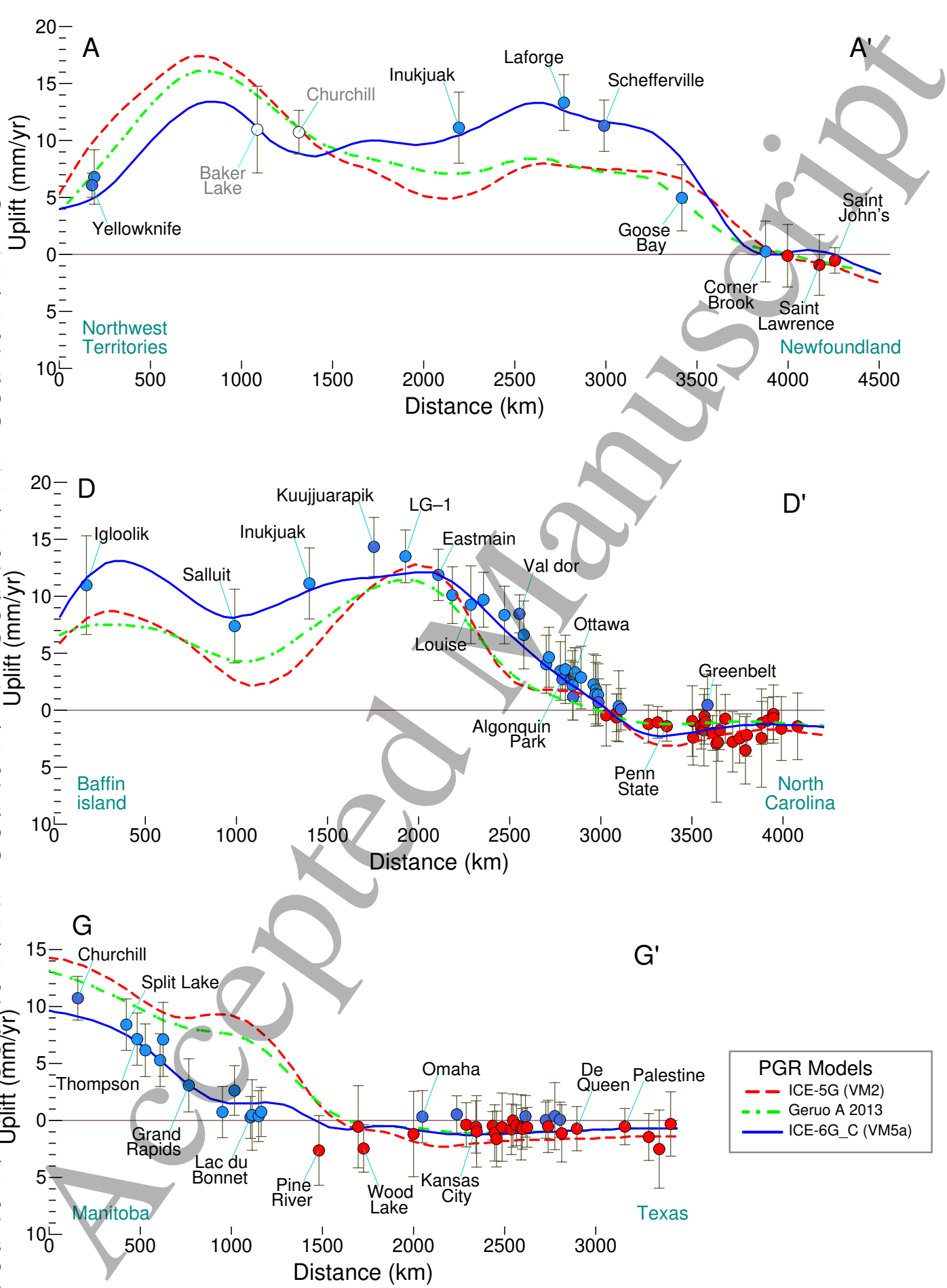

Fig 5.14a

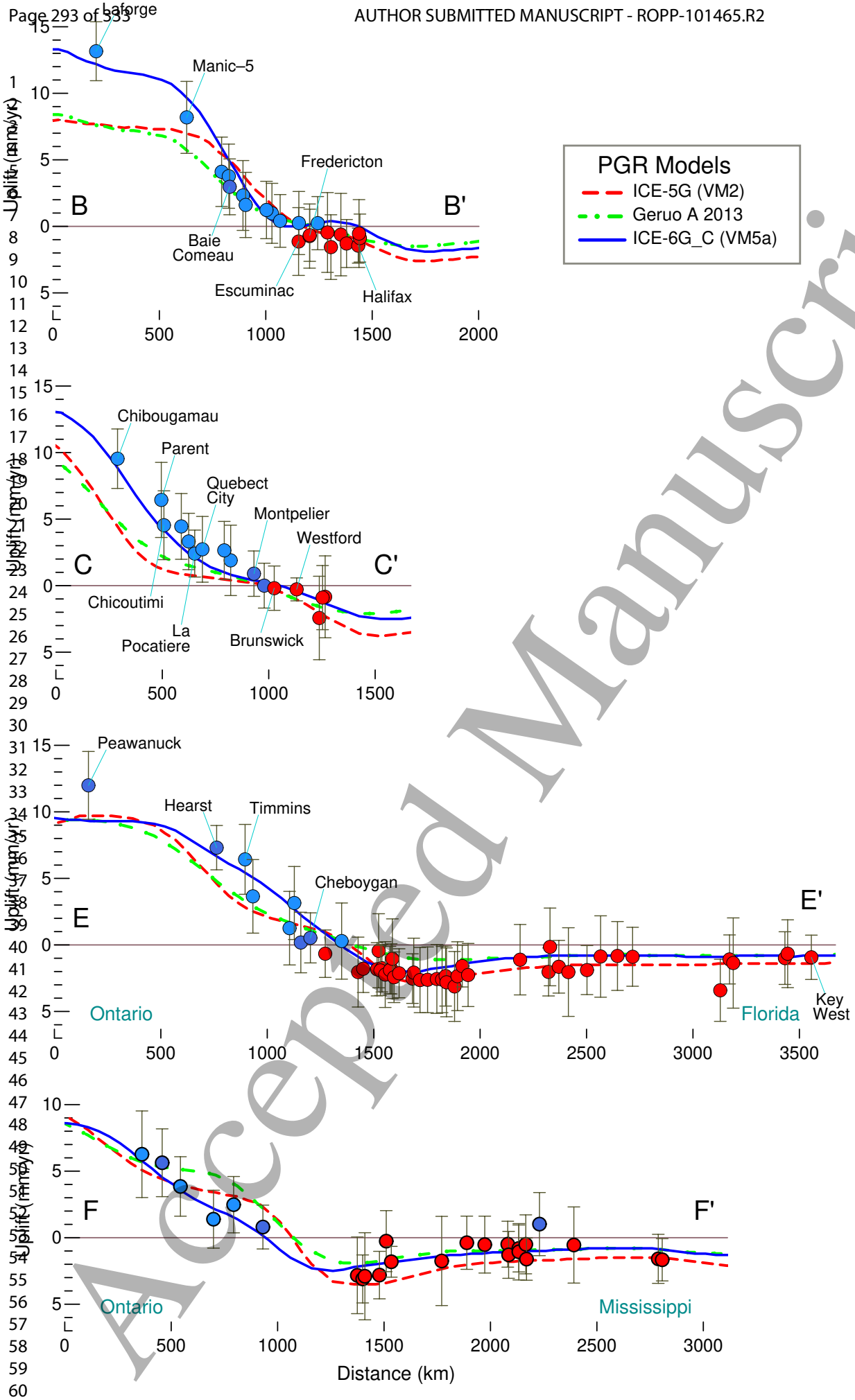

Fig 5.14b

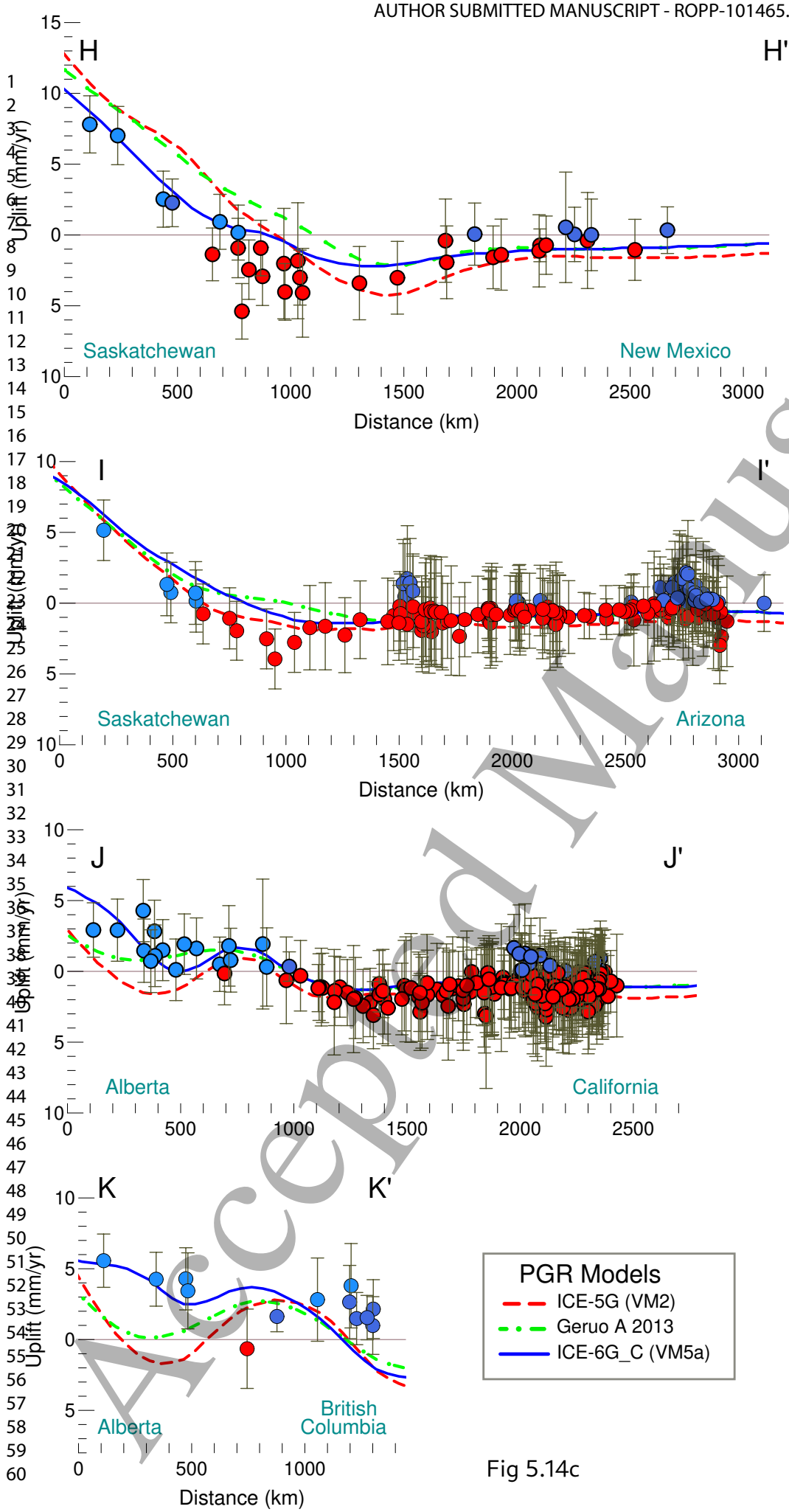

Fig 5.14c

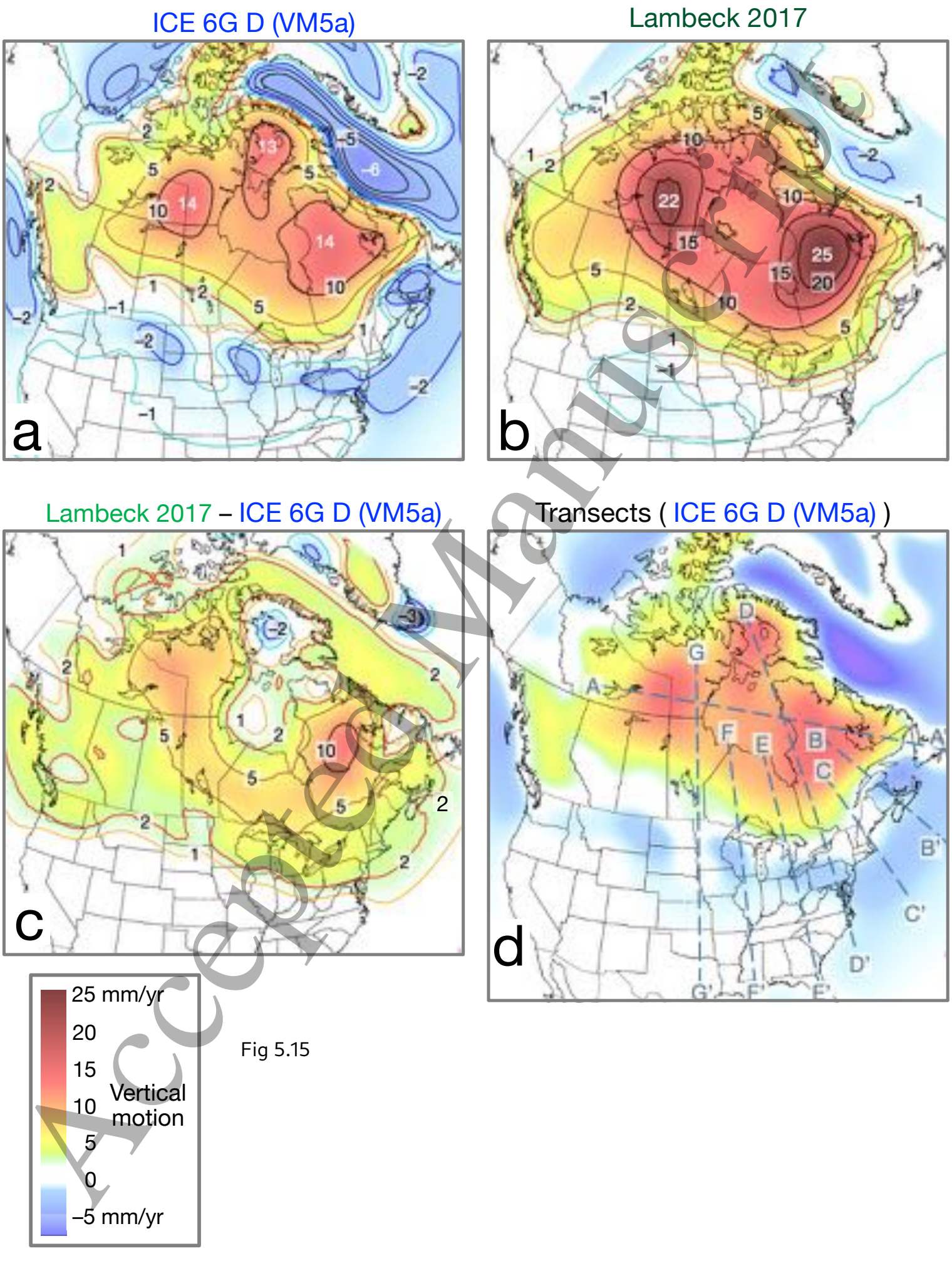

Fig 5.15

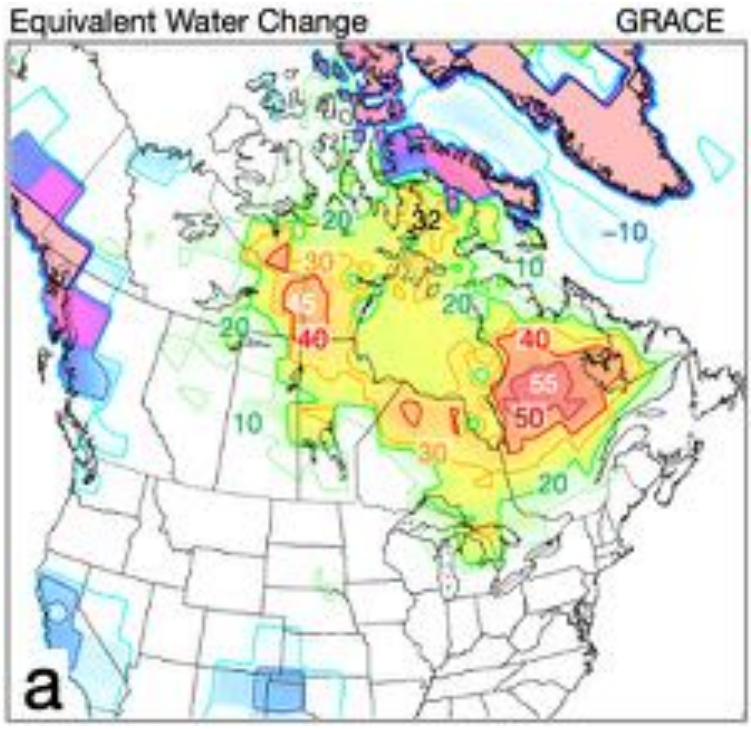

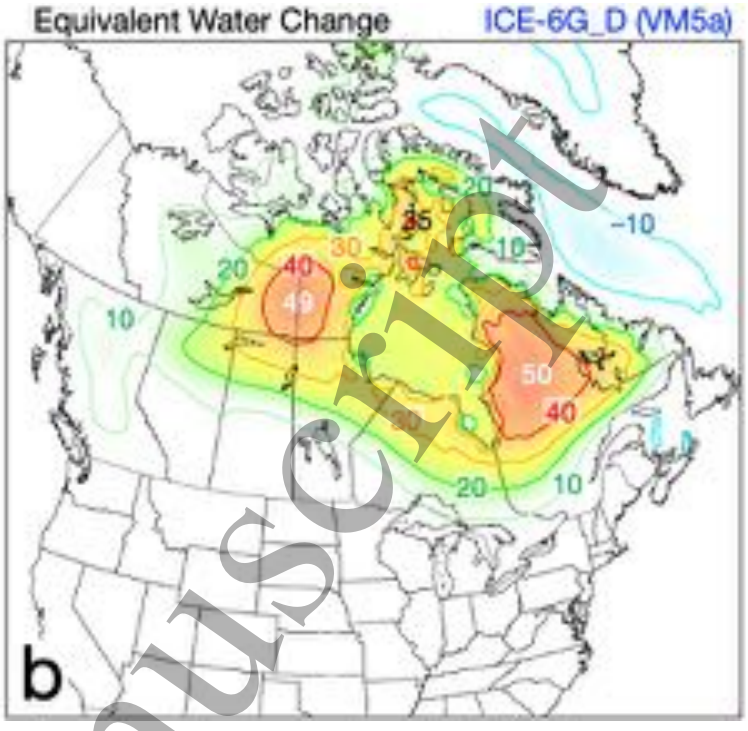

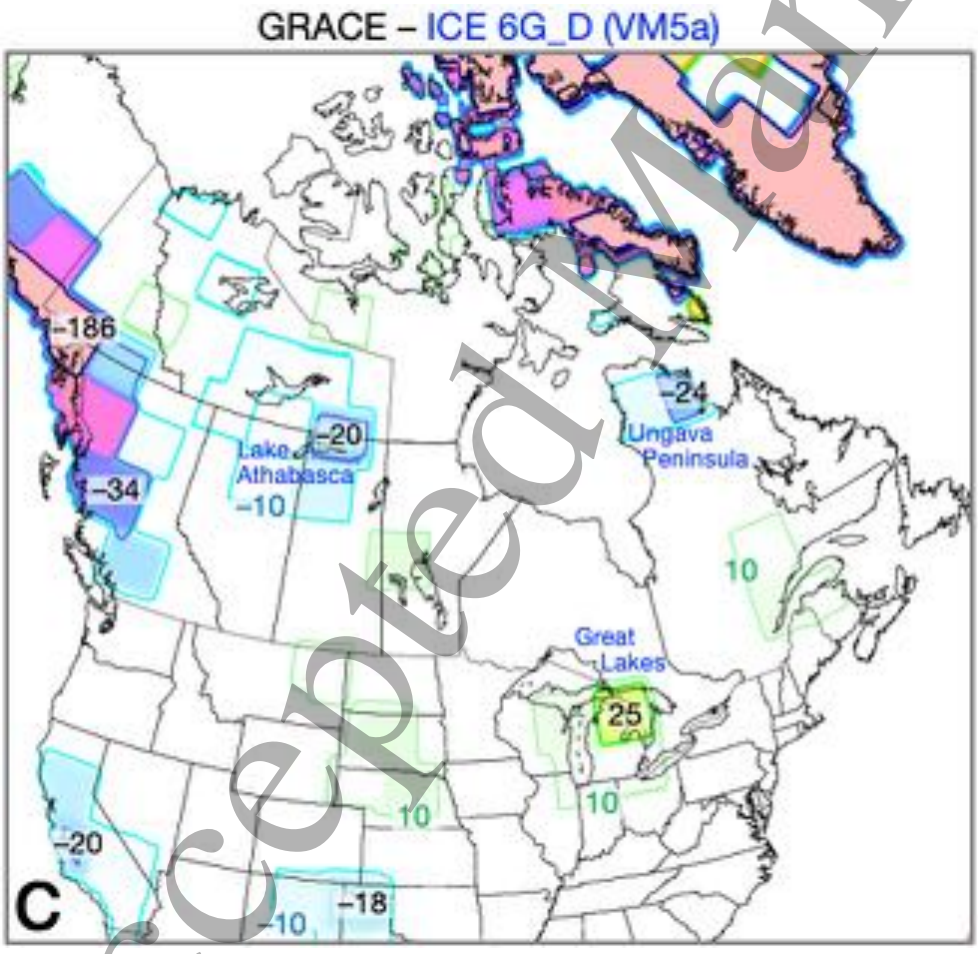

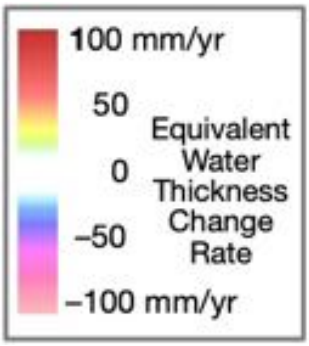

Fig 5.16

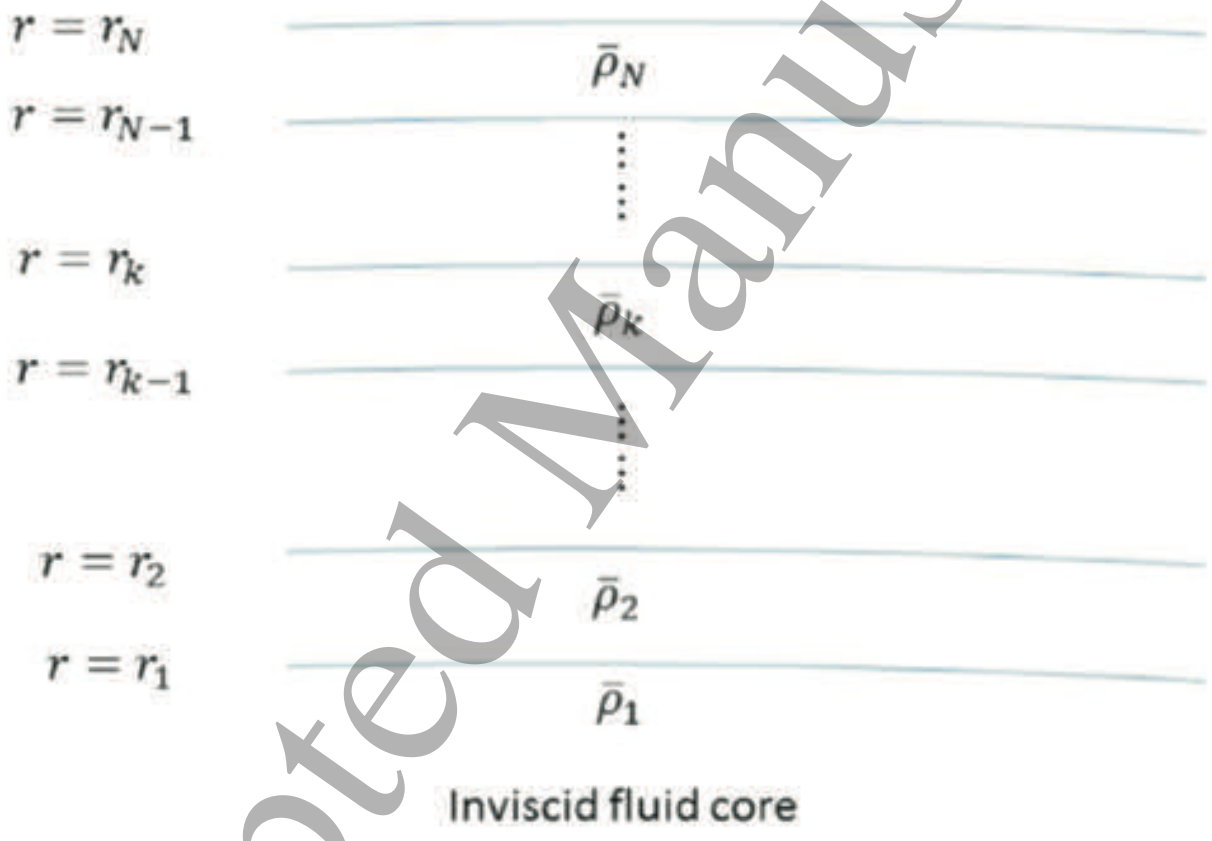

Fig 6.1

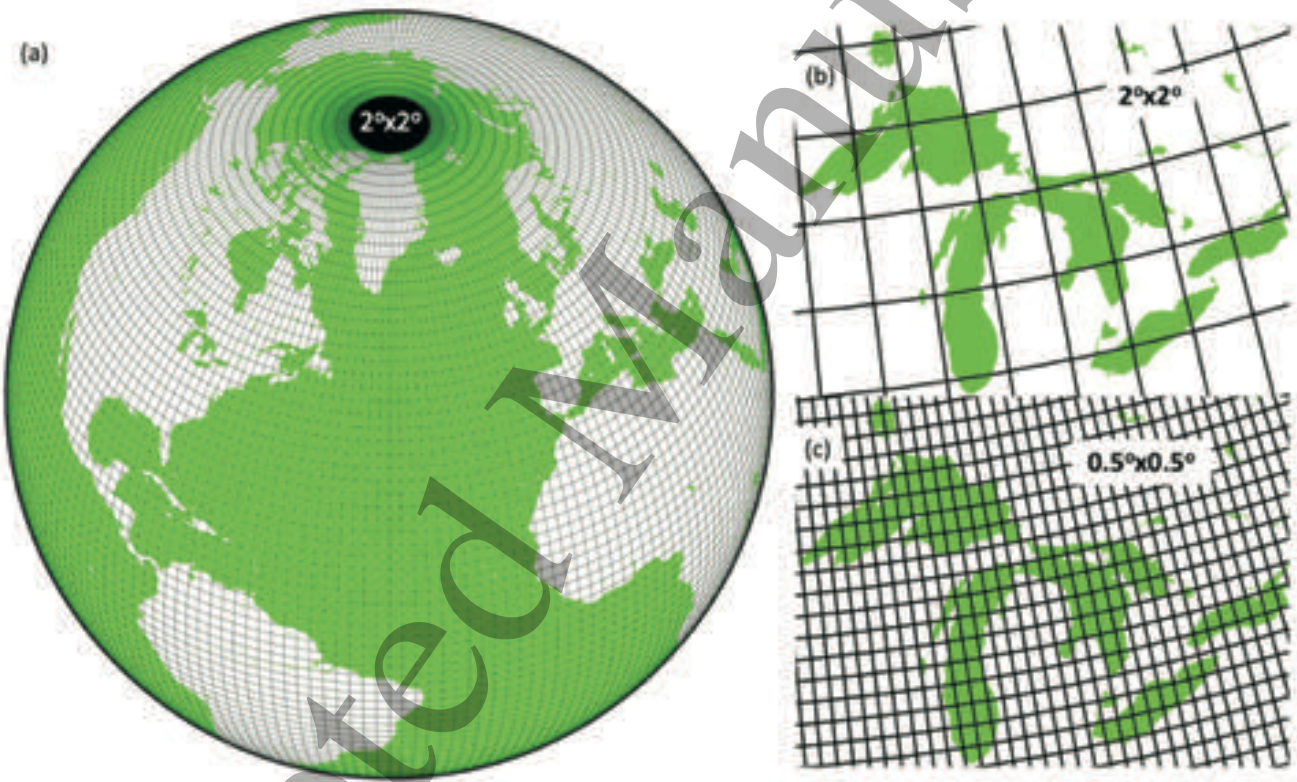

Fig 6.2

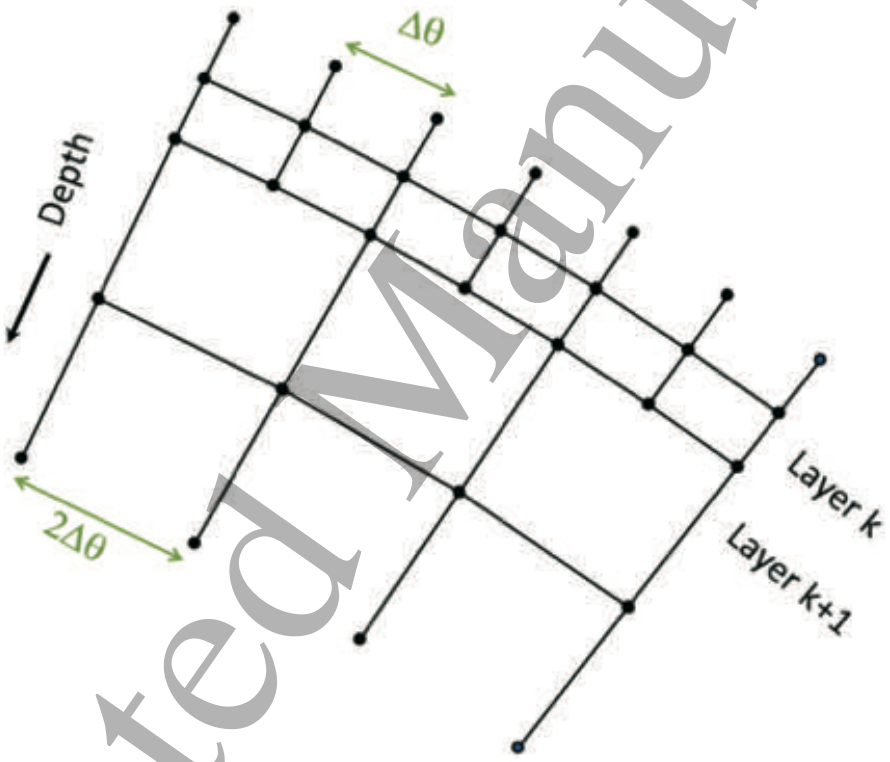

Fig 6.3

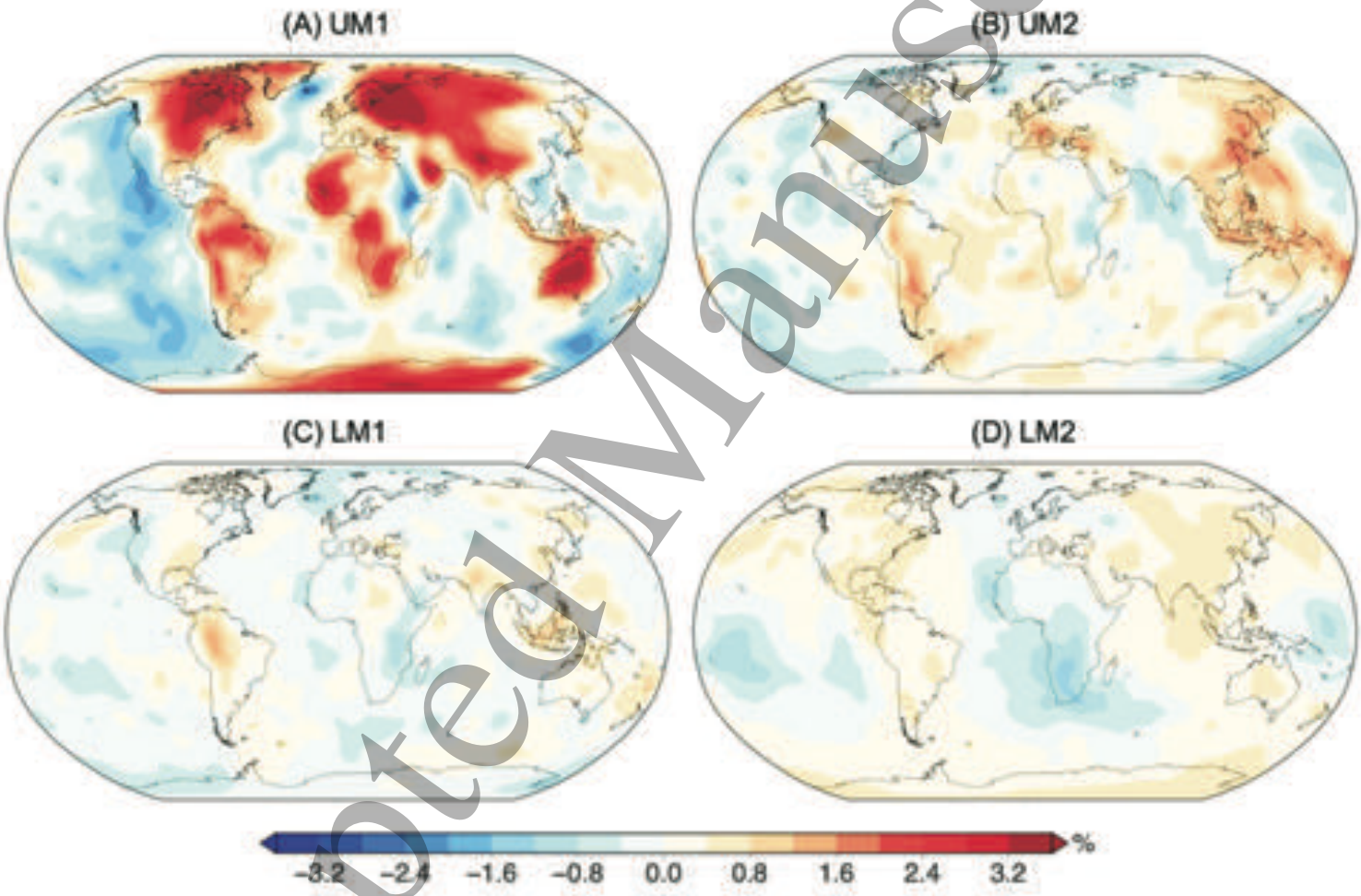

Fig 6.4

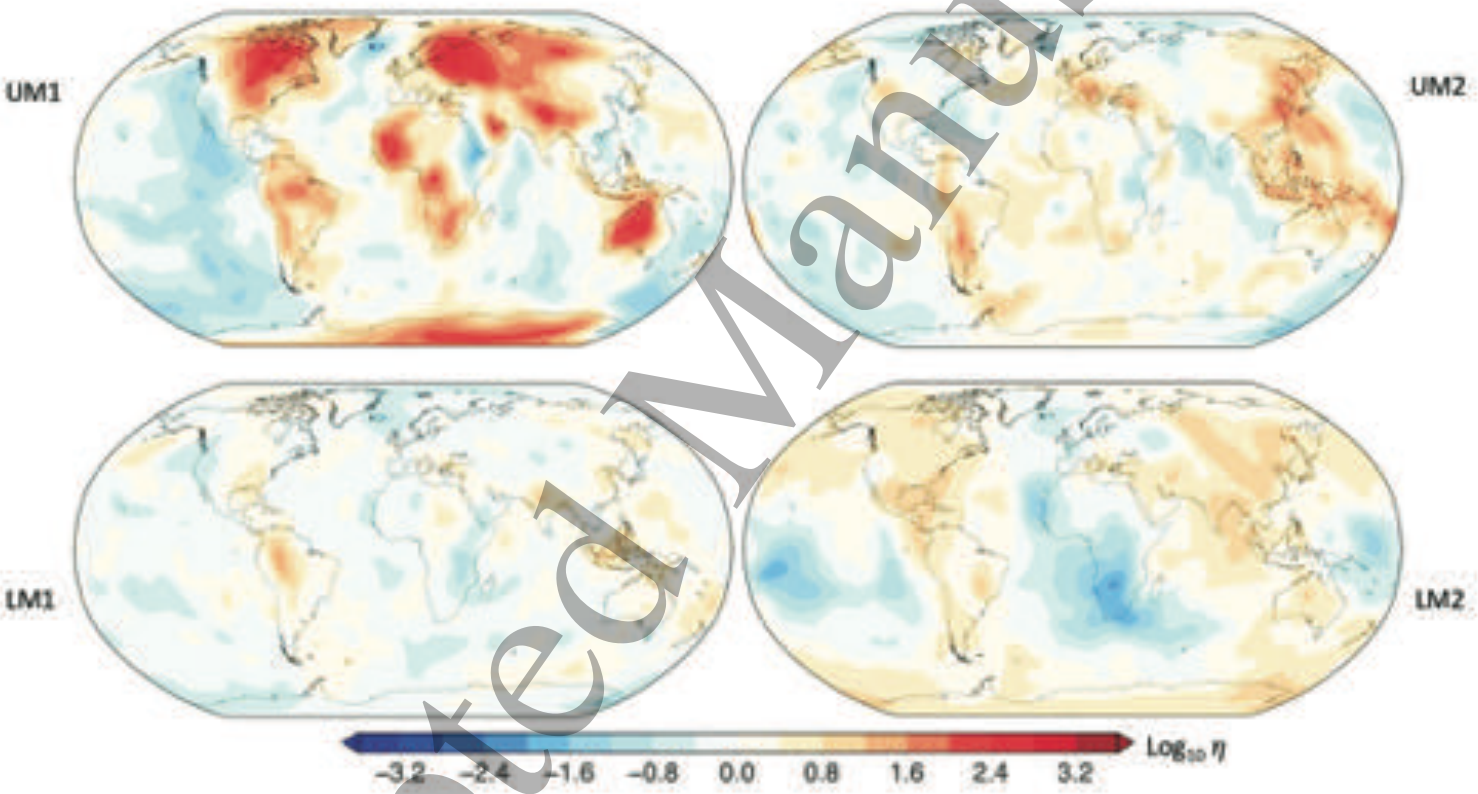

Fig 6.5

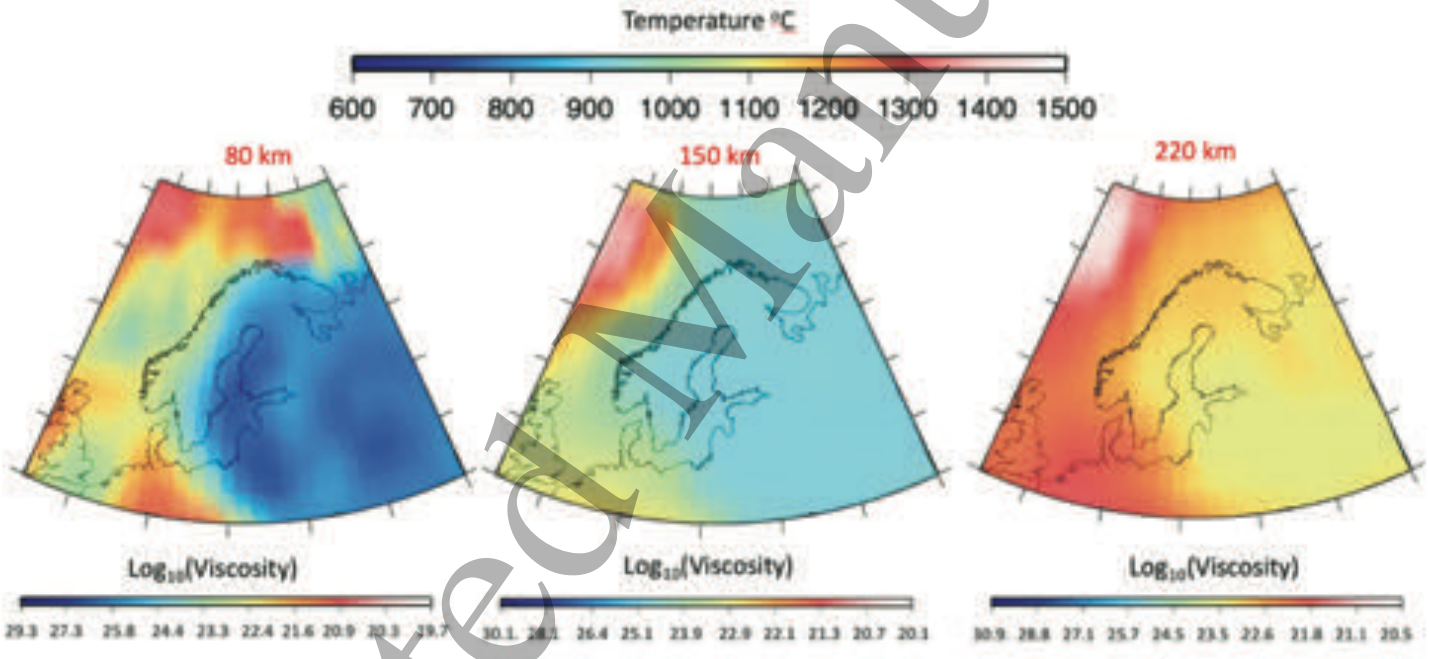

Fig 6.6

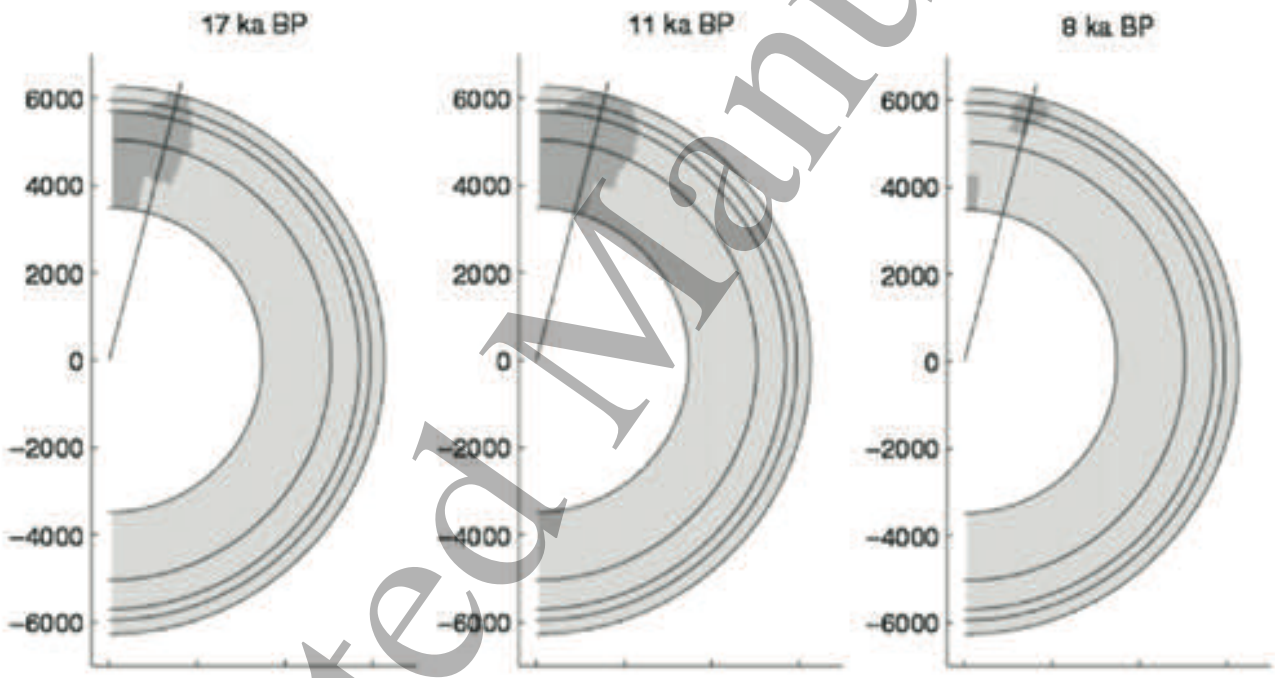

Fig 6.7

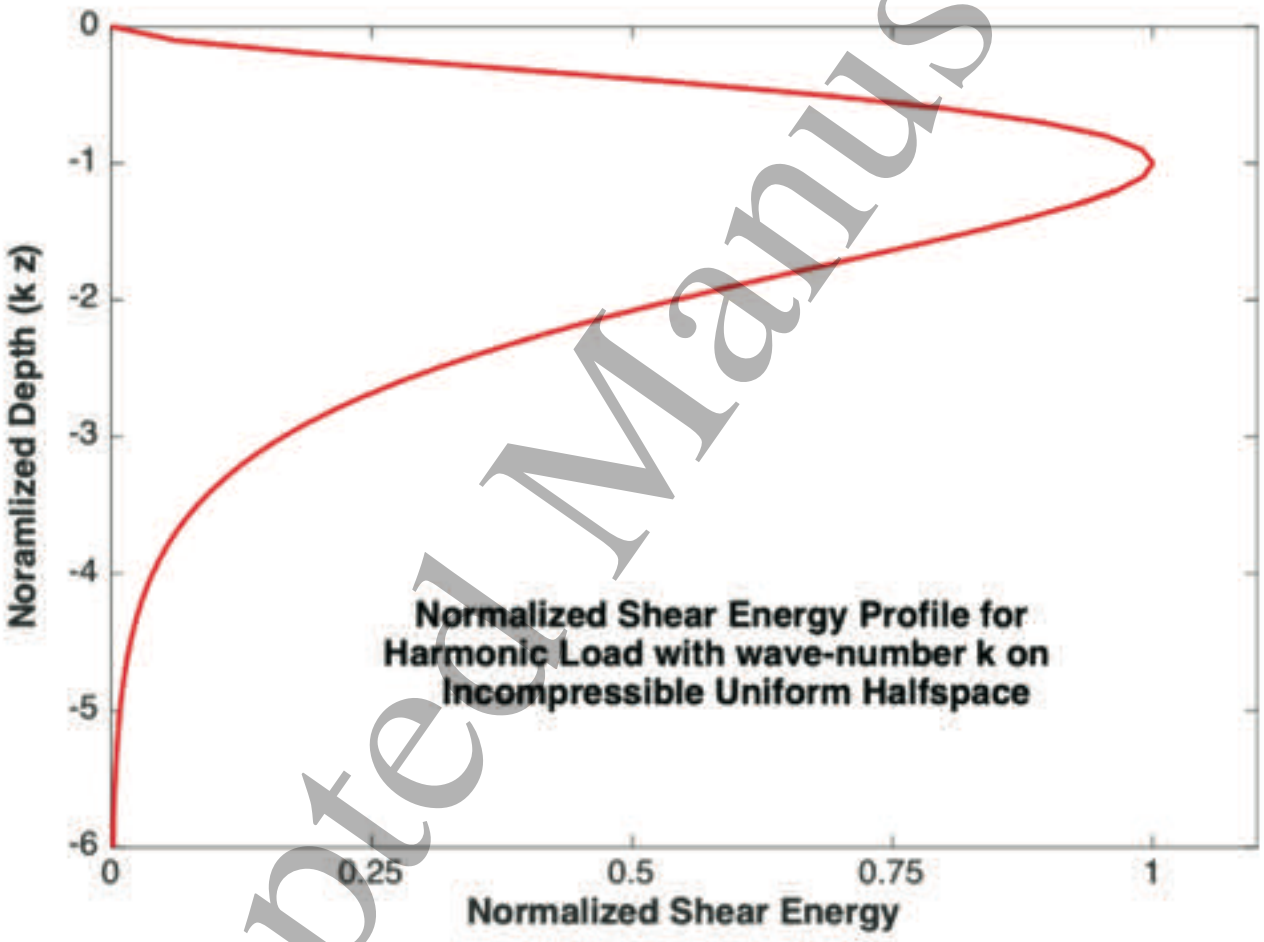

Fig 7.1

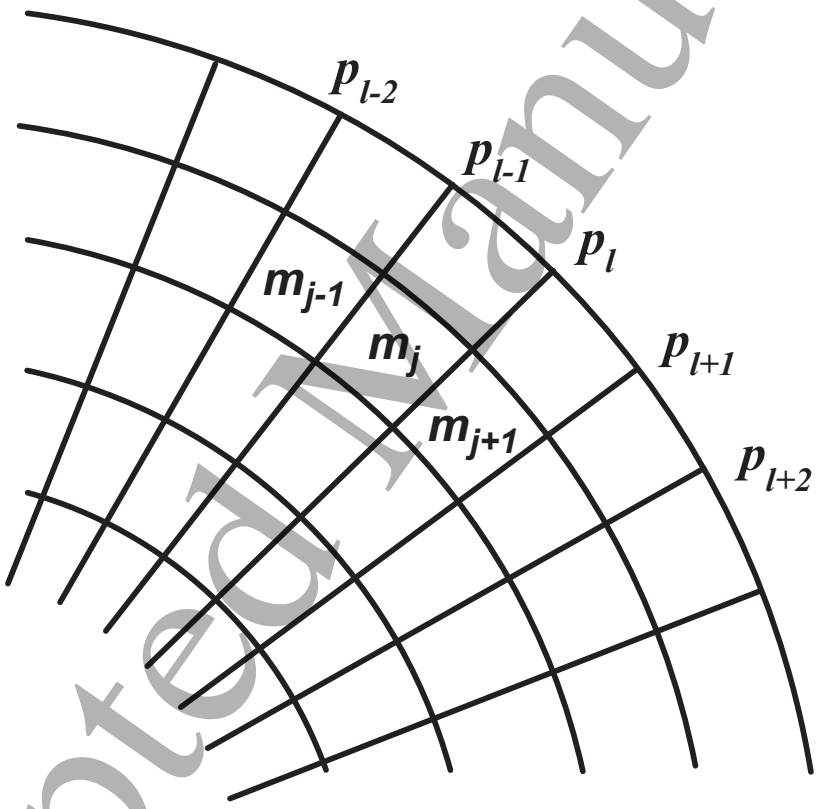

Fig 7.2

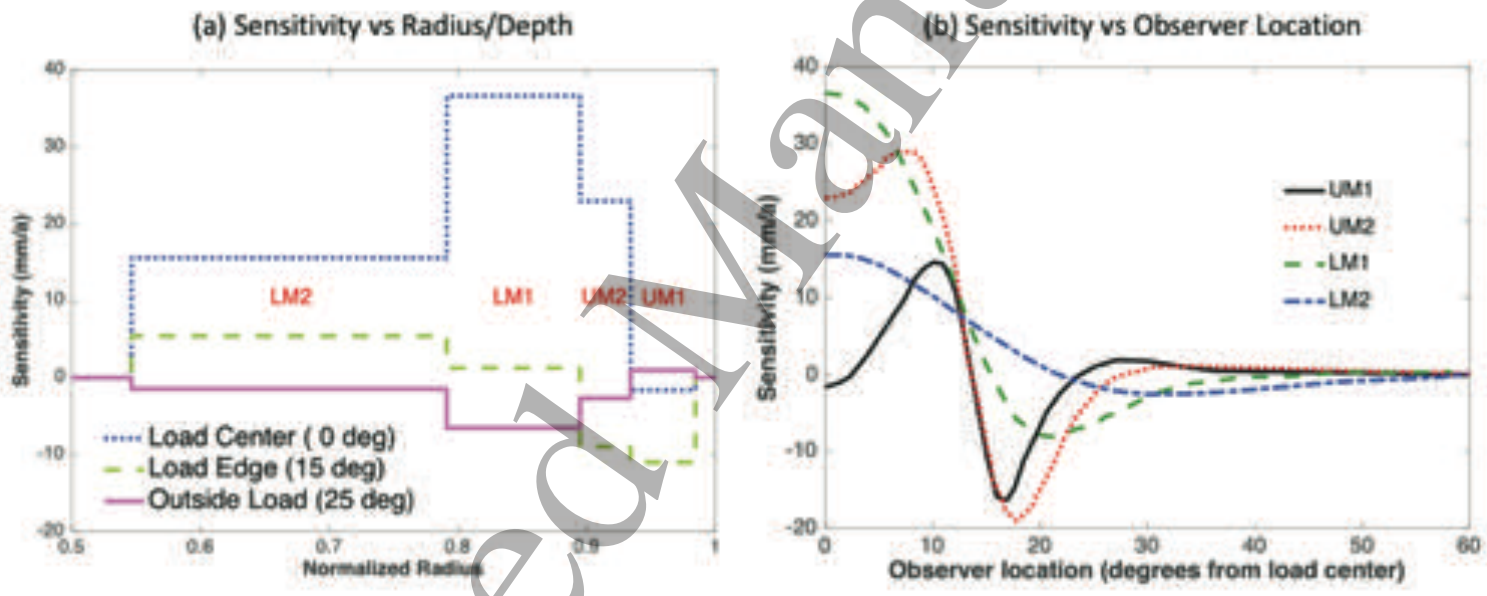

Fig 7.3

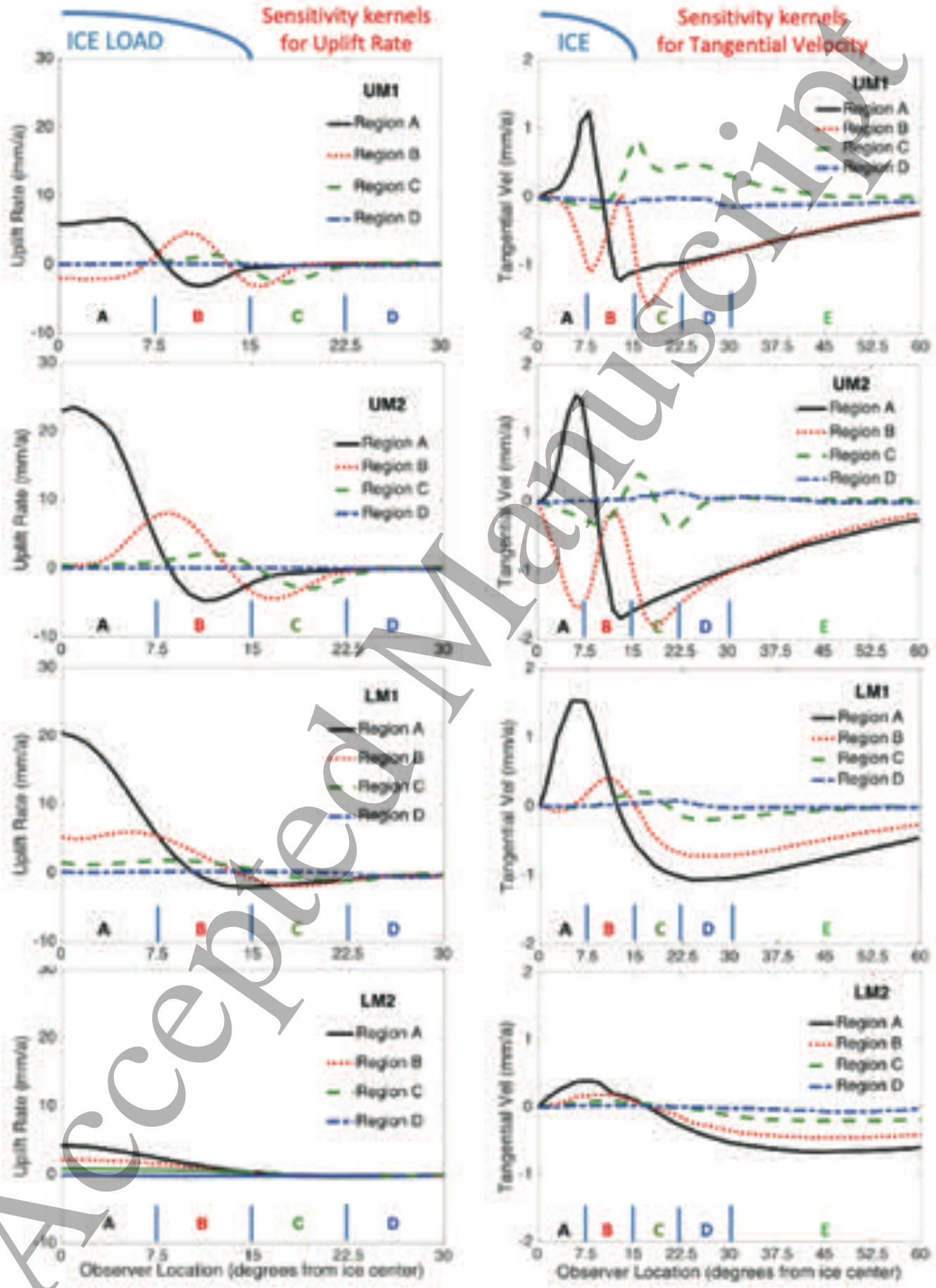

Fig 7.4

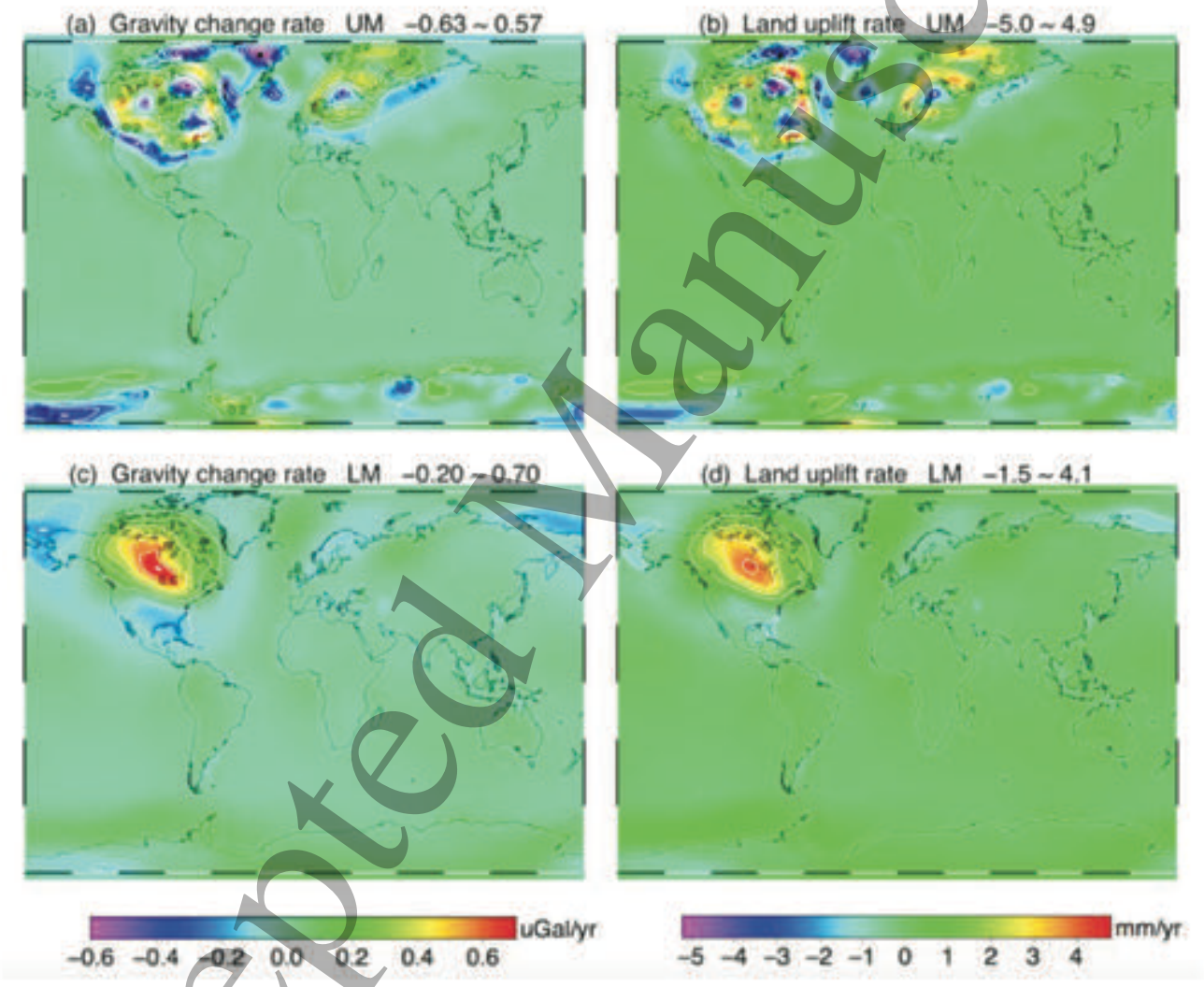

Fig 7.5

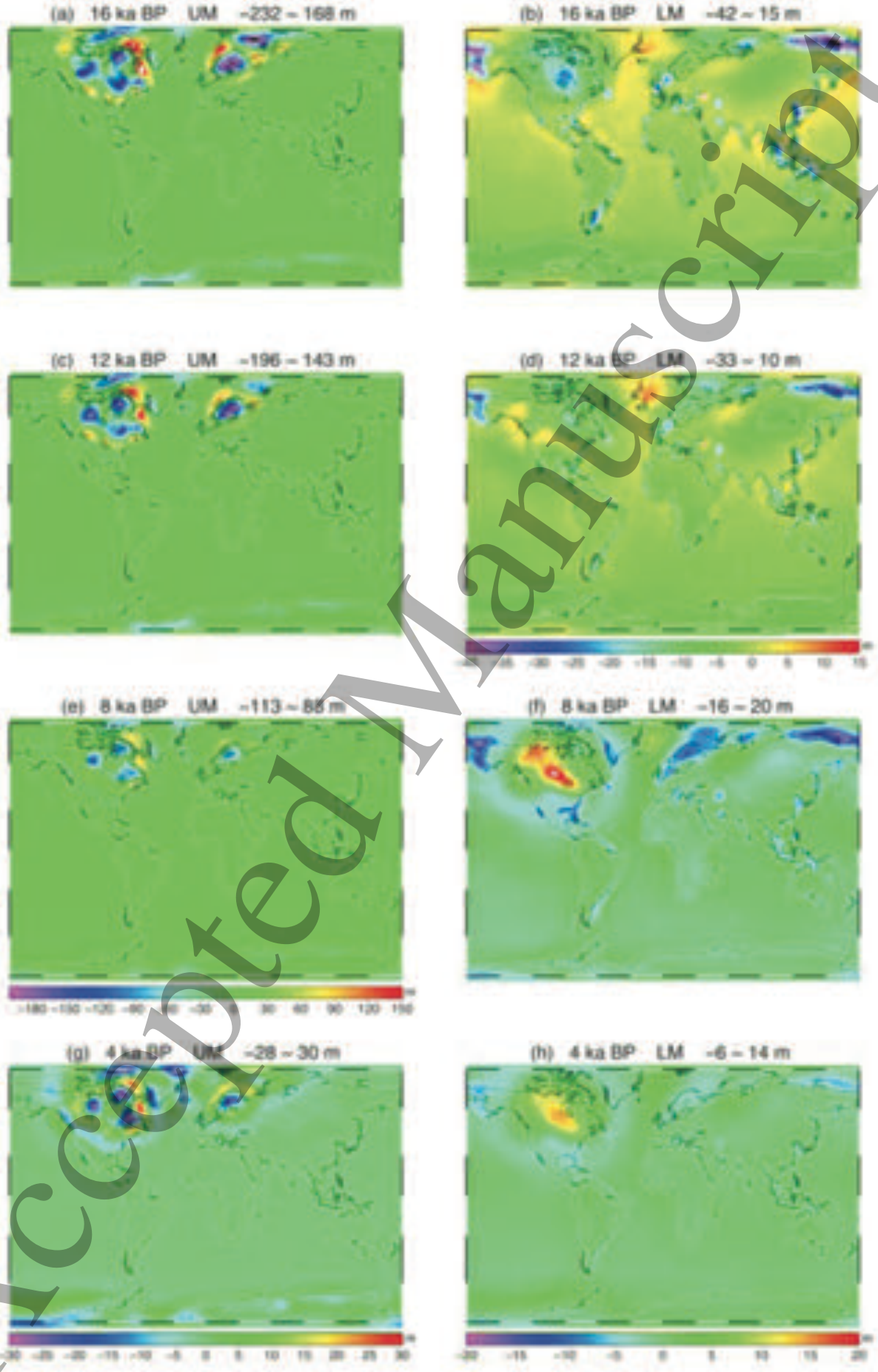

Fig 7.6

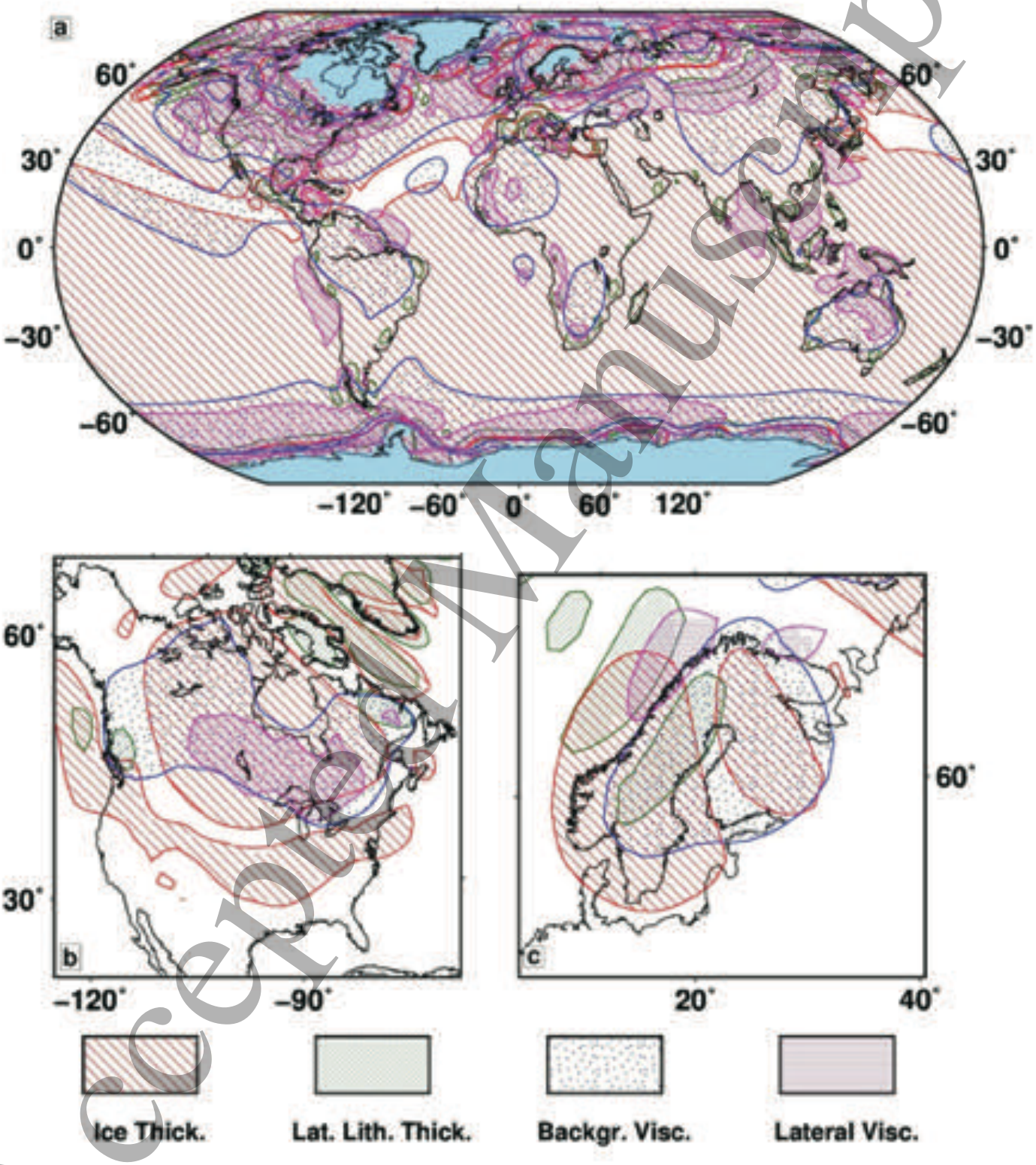

Fig 7.7

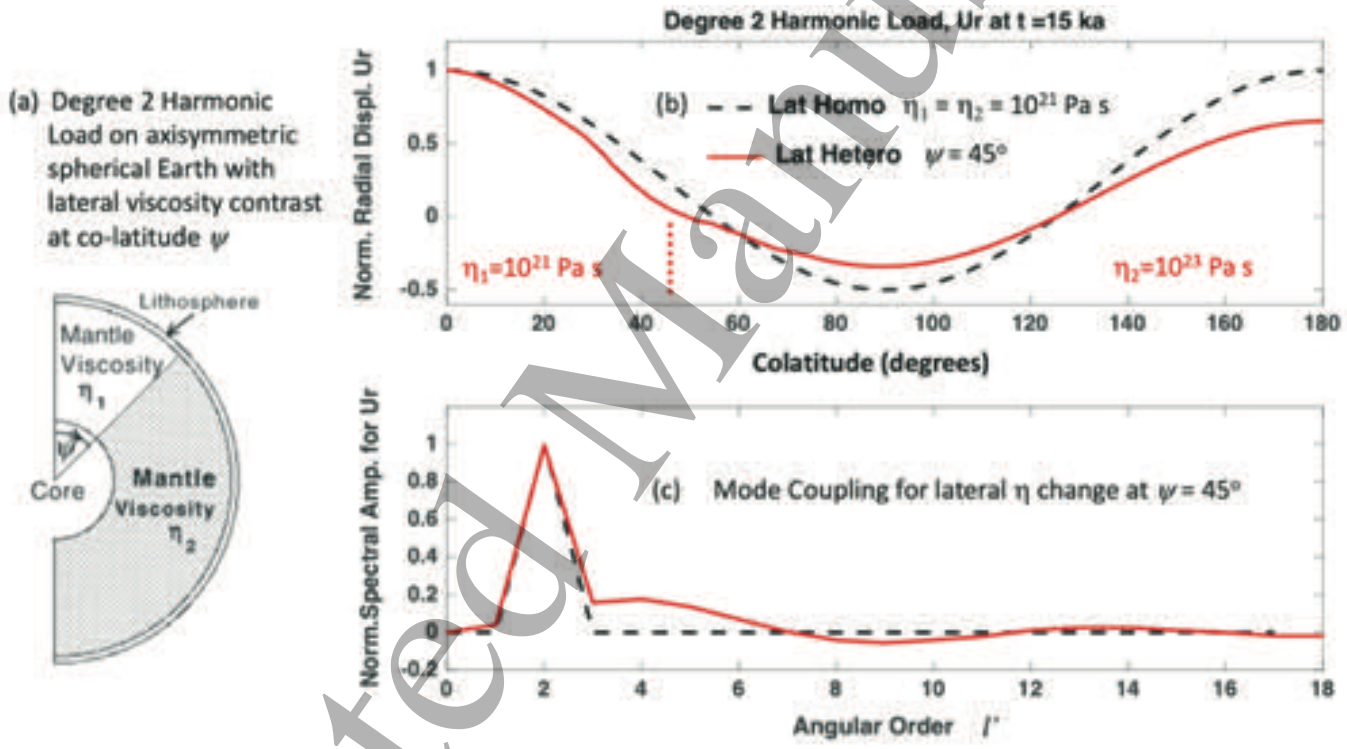

Fig 7.8

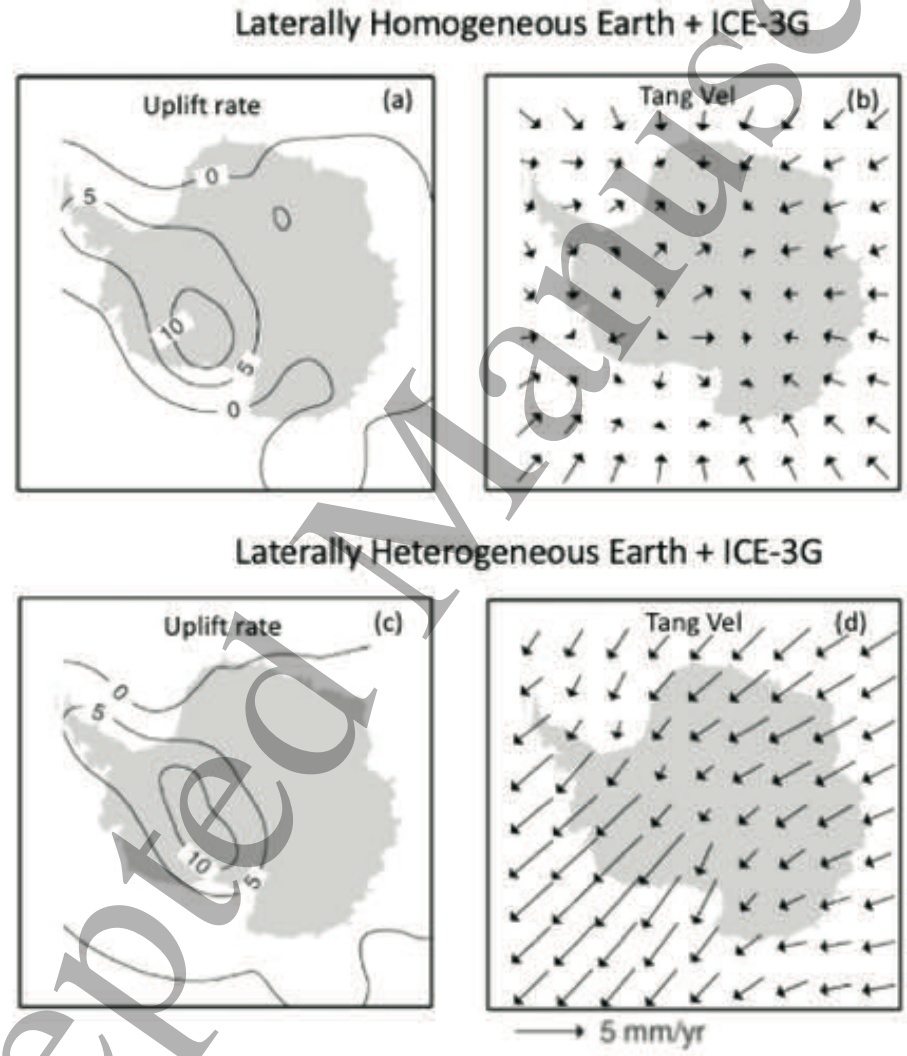

Fig 7.9

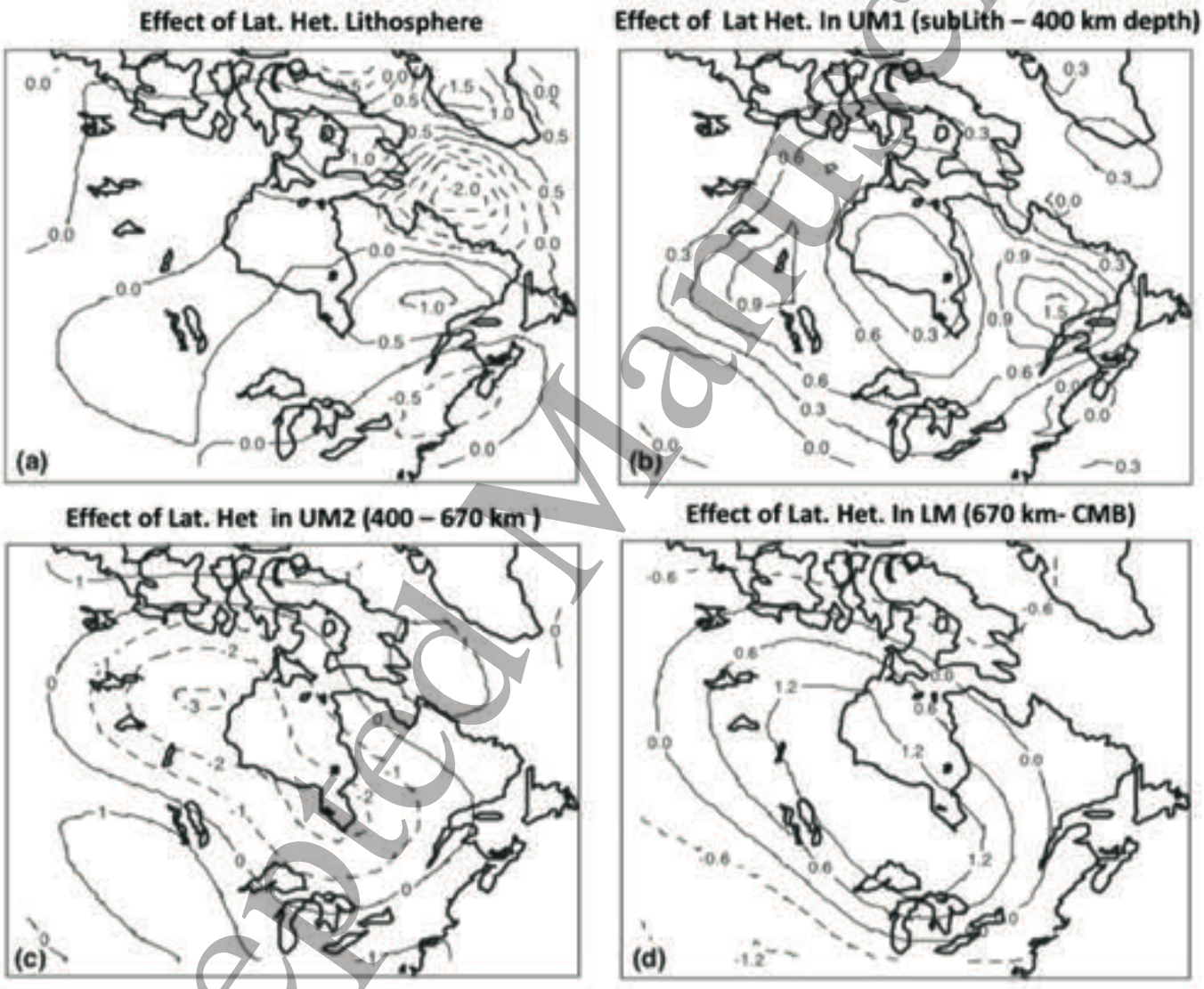

Fig 7.10

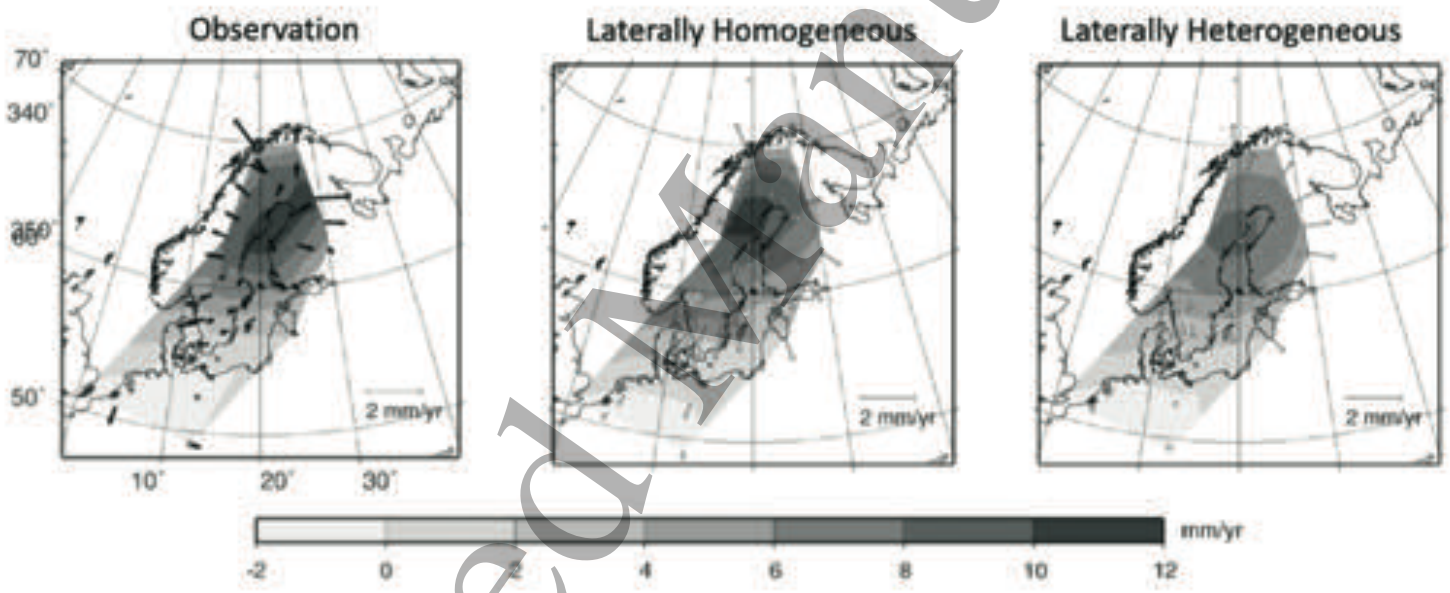

Fig 7.11

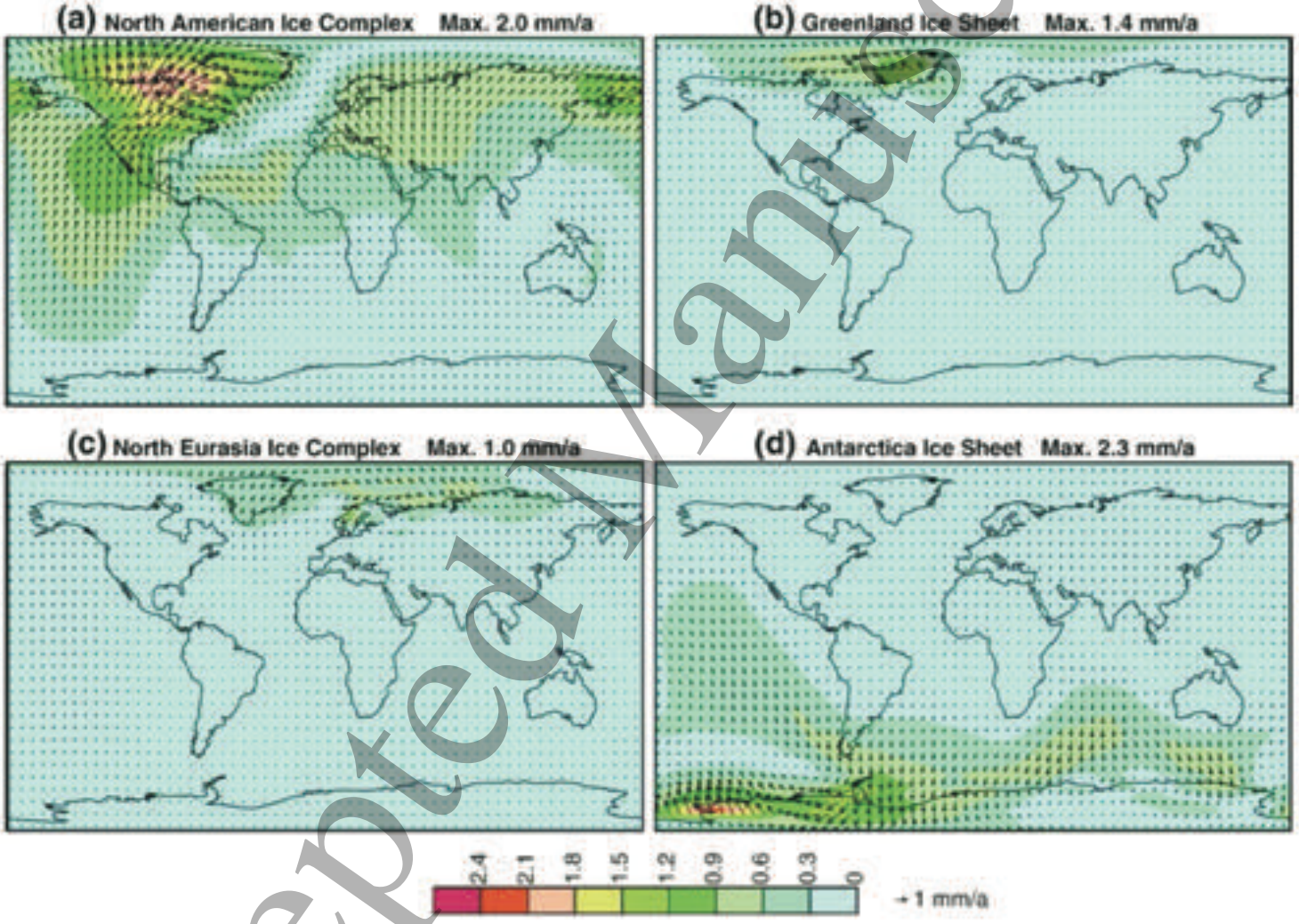

Fig 7.12

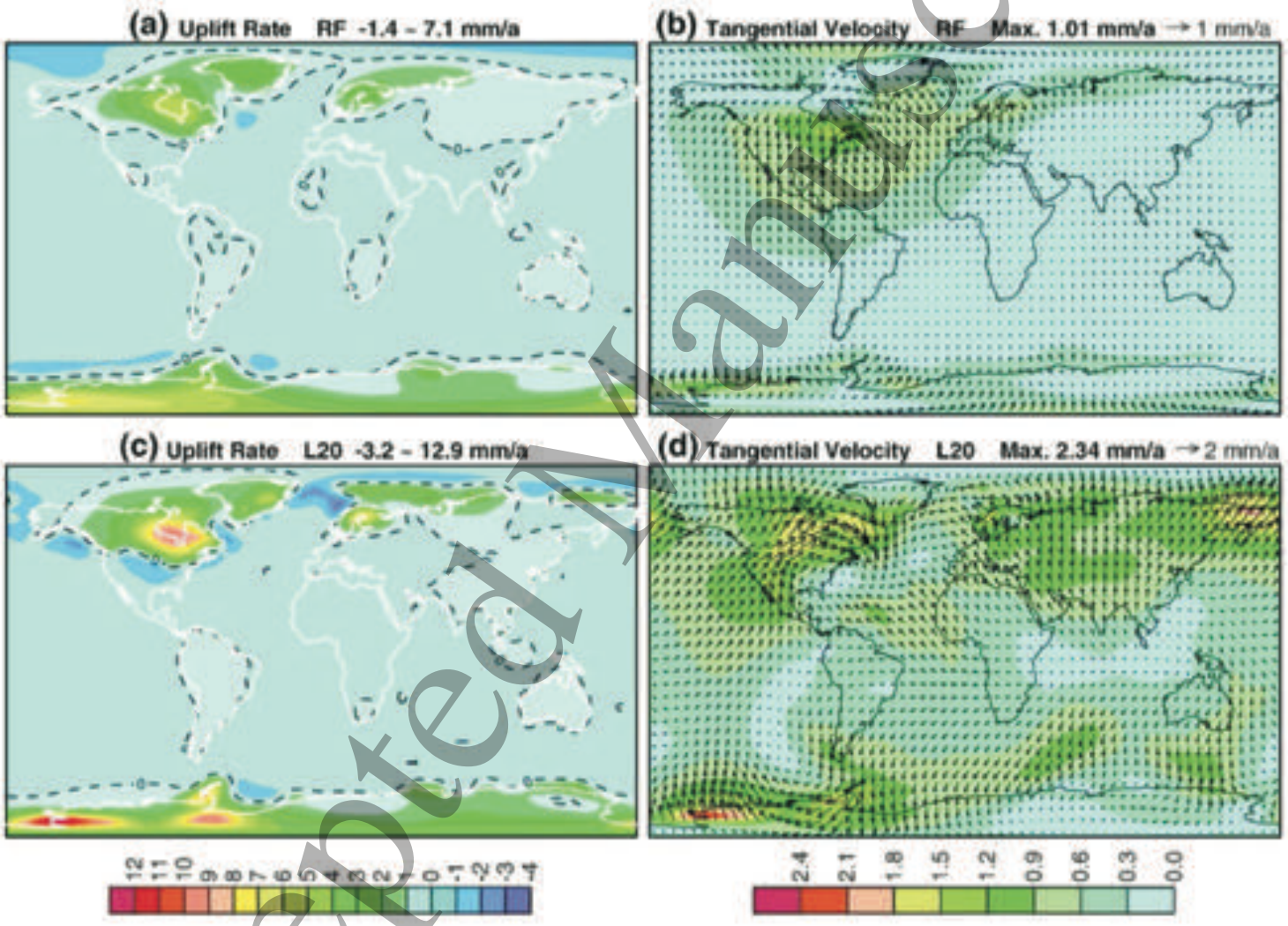

Fig 7.13

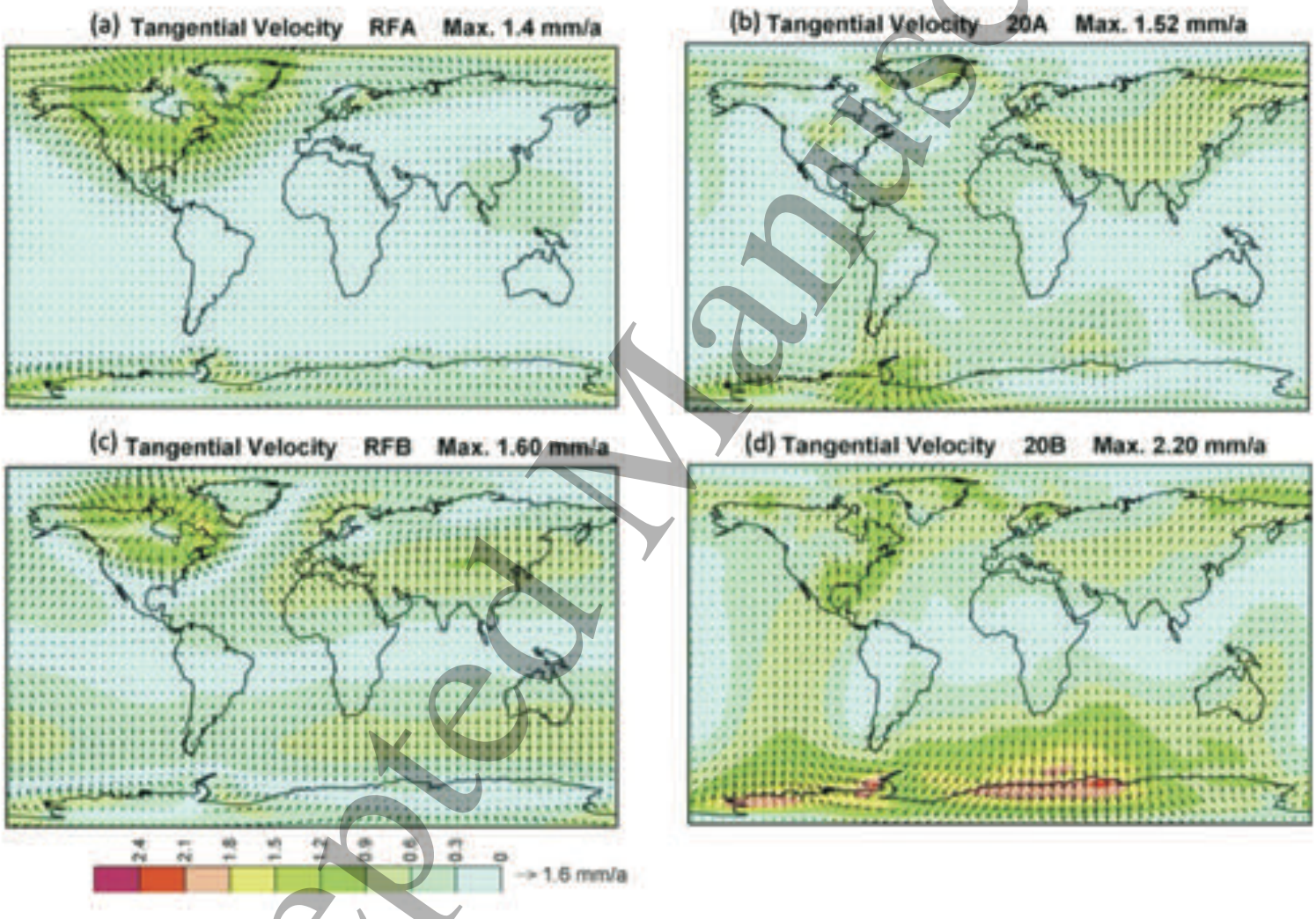

Fig 7.14

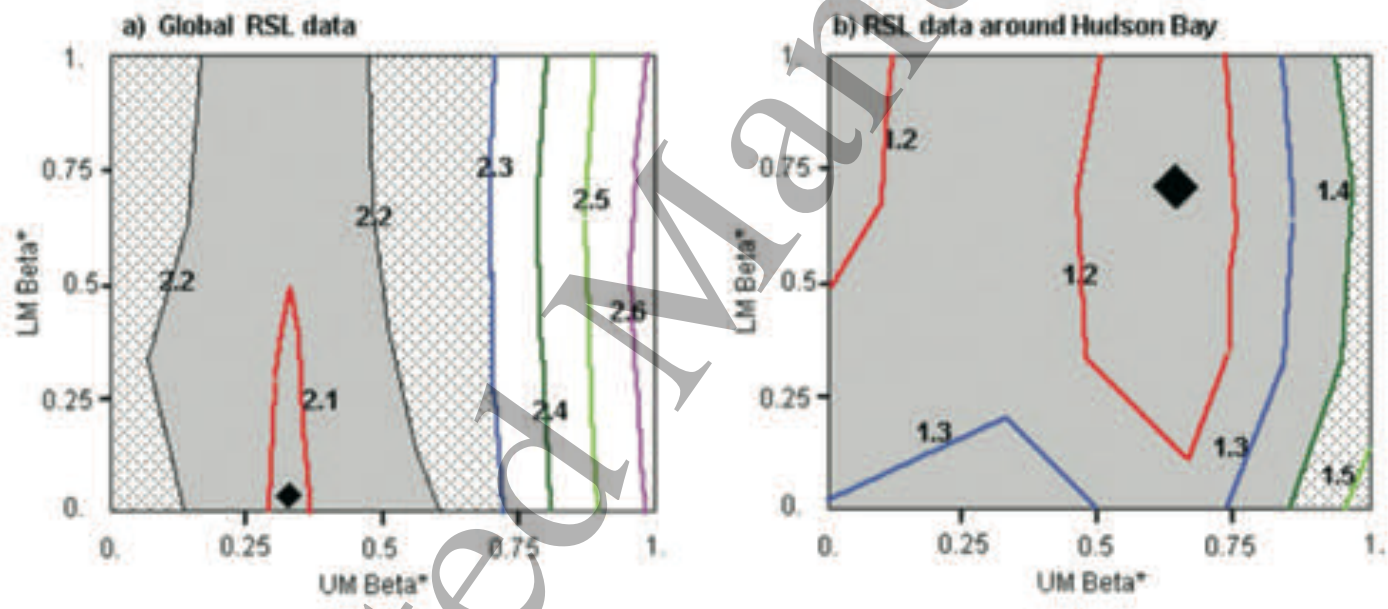

Fig 7.15

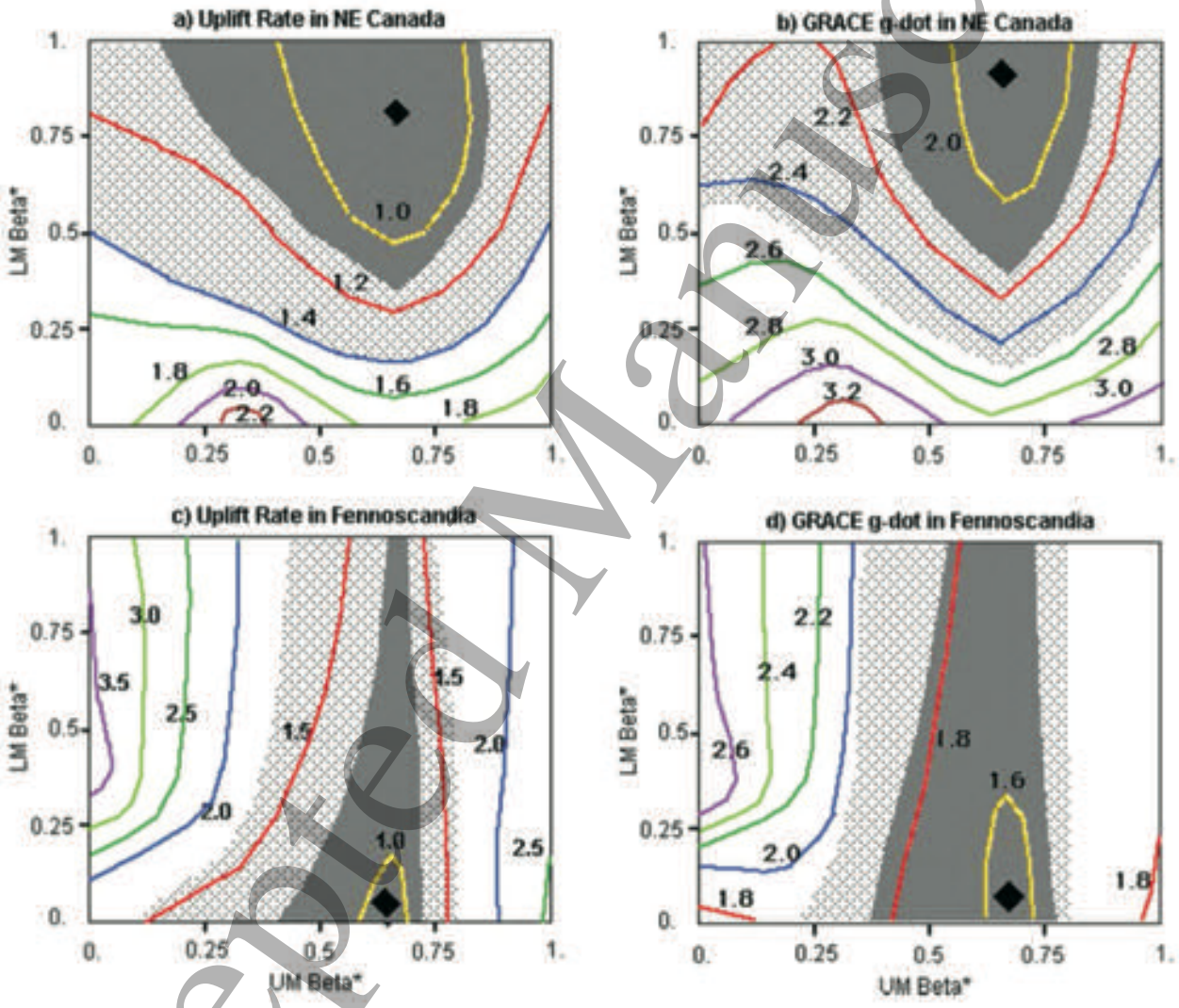

Fig 7.16

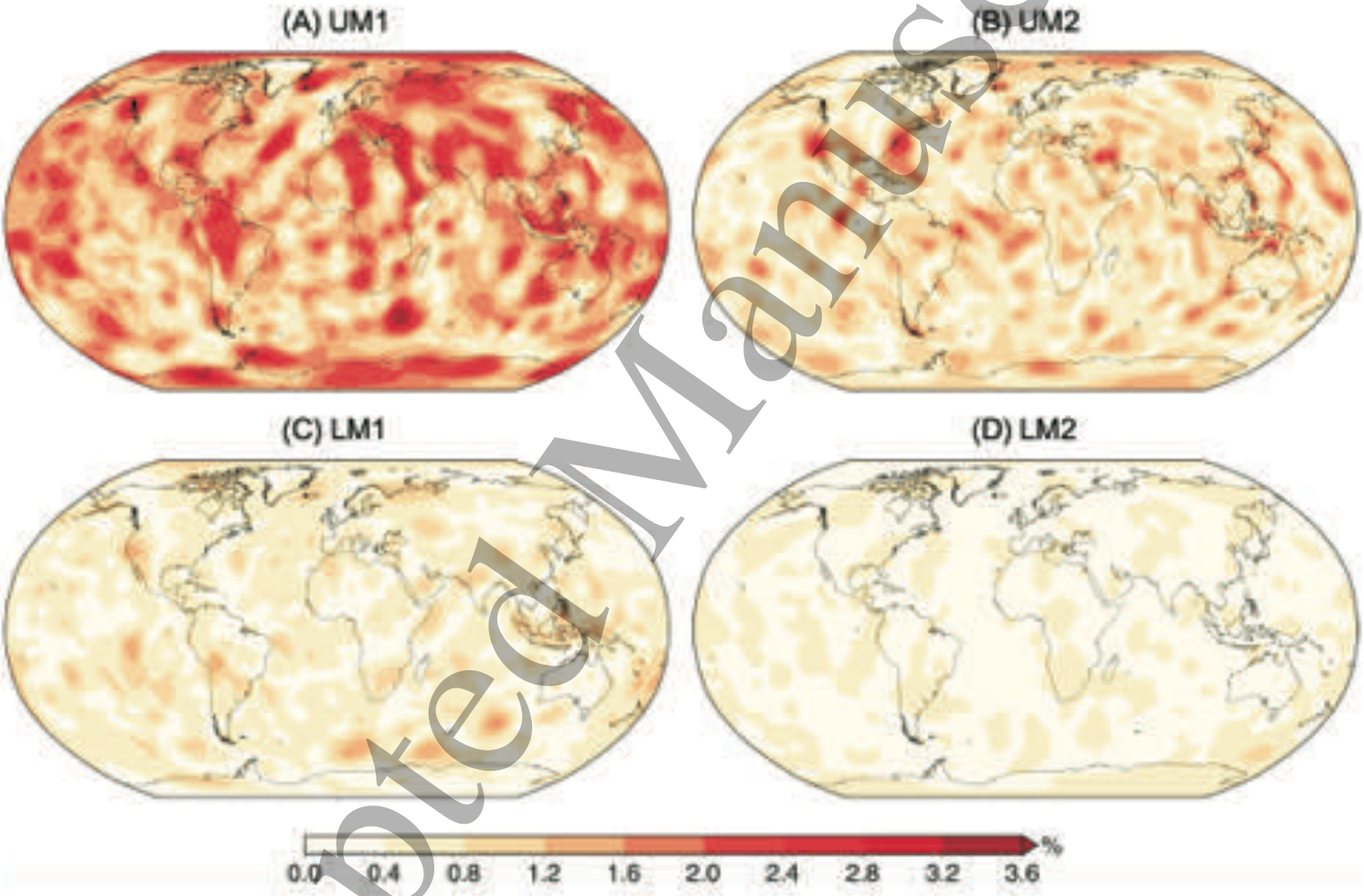

Fig 7.17

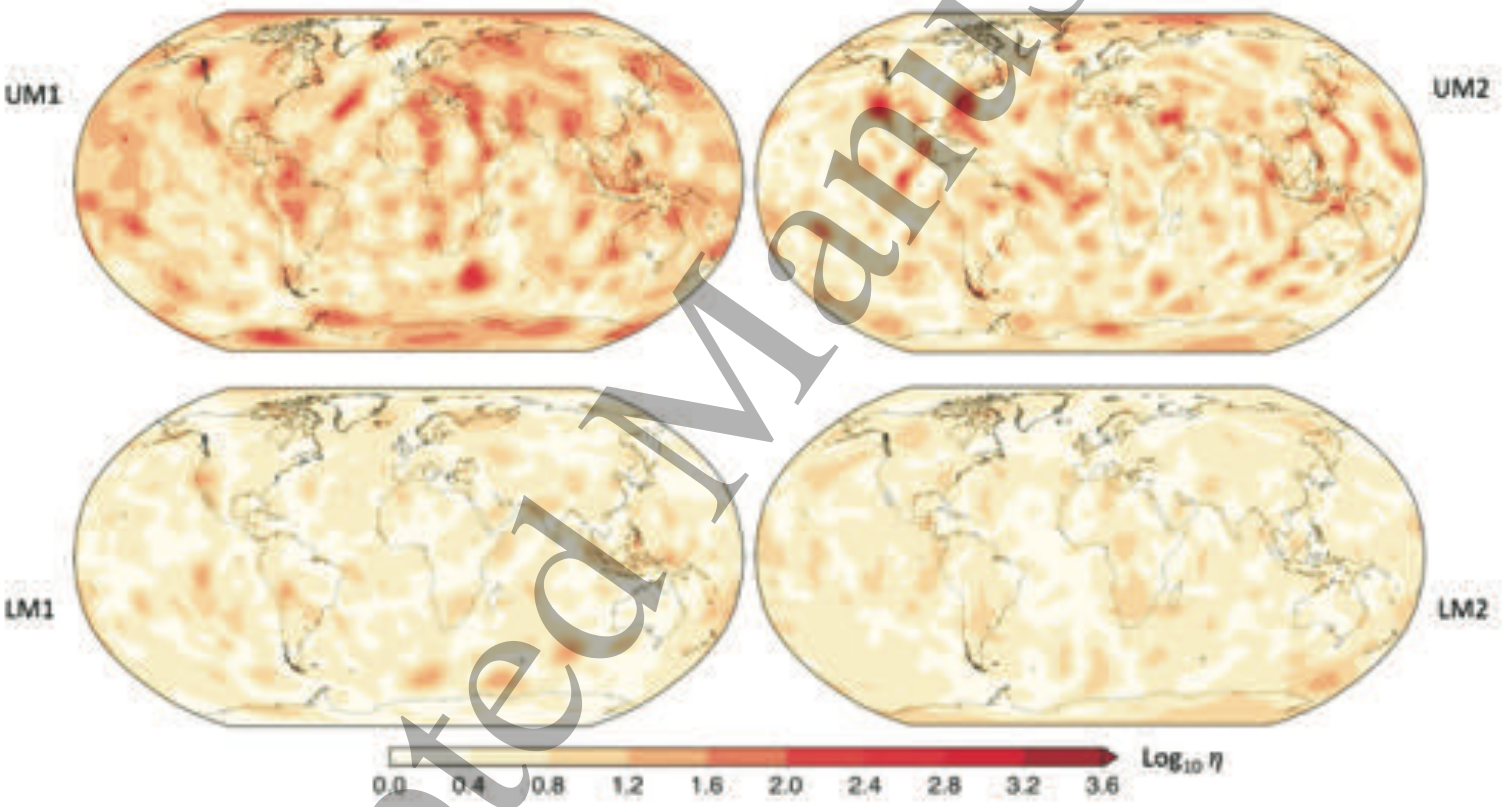

Fig 7.18

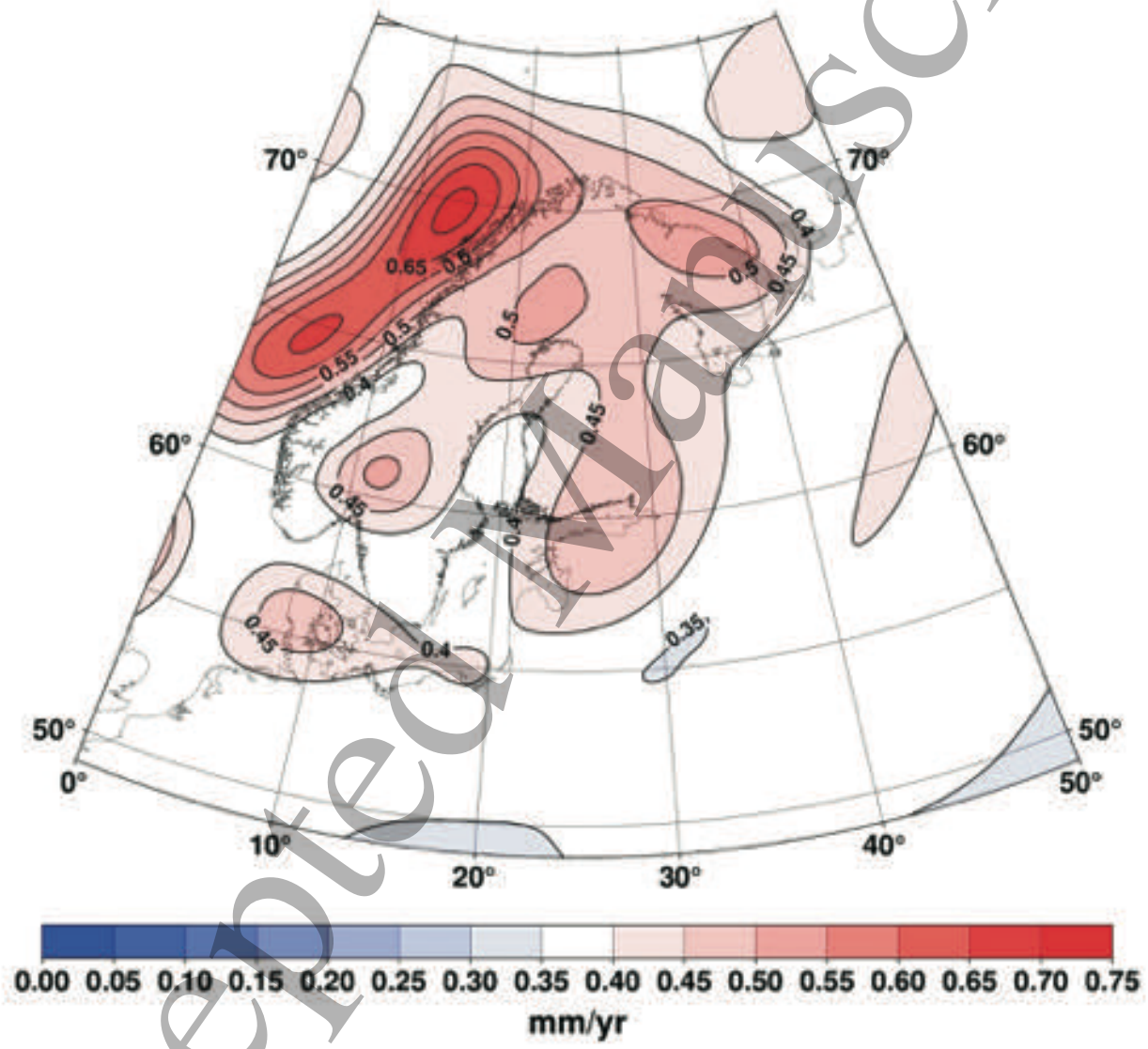

Fig 7.19

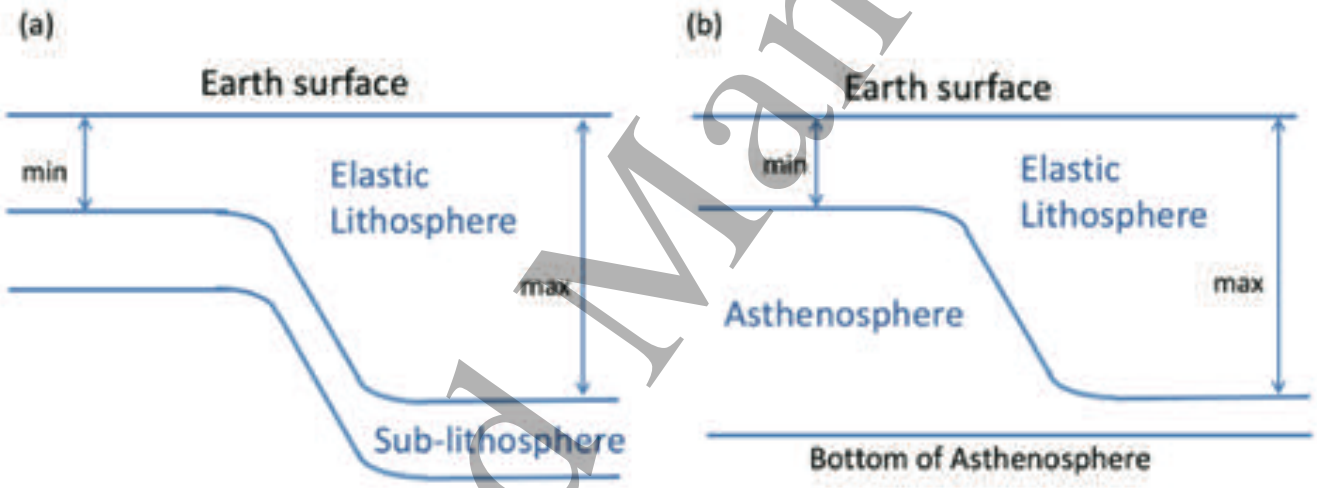

Fig 7.20

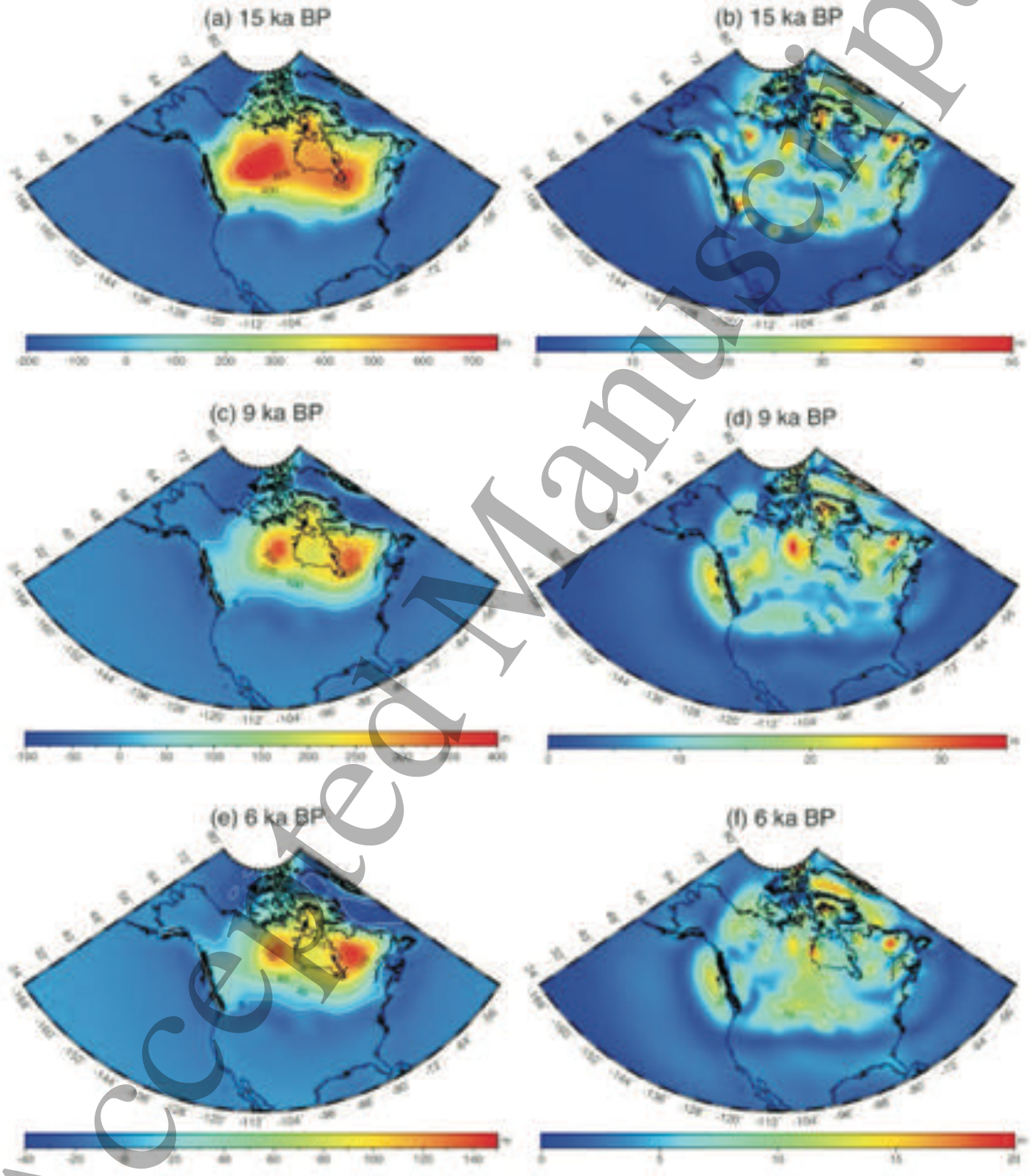

Fig 7.21

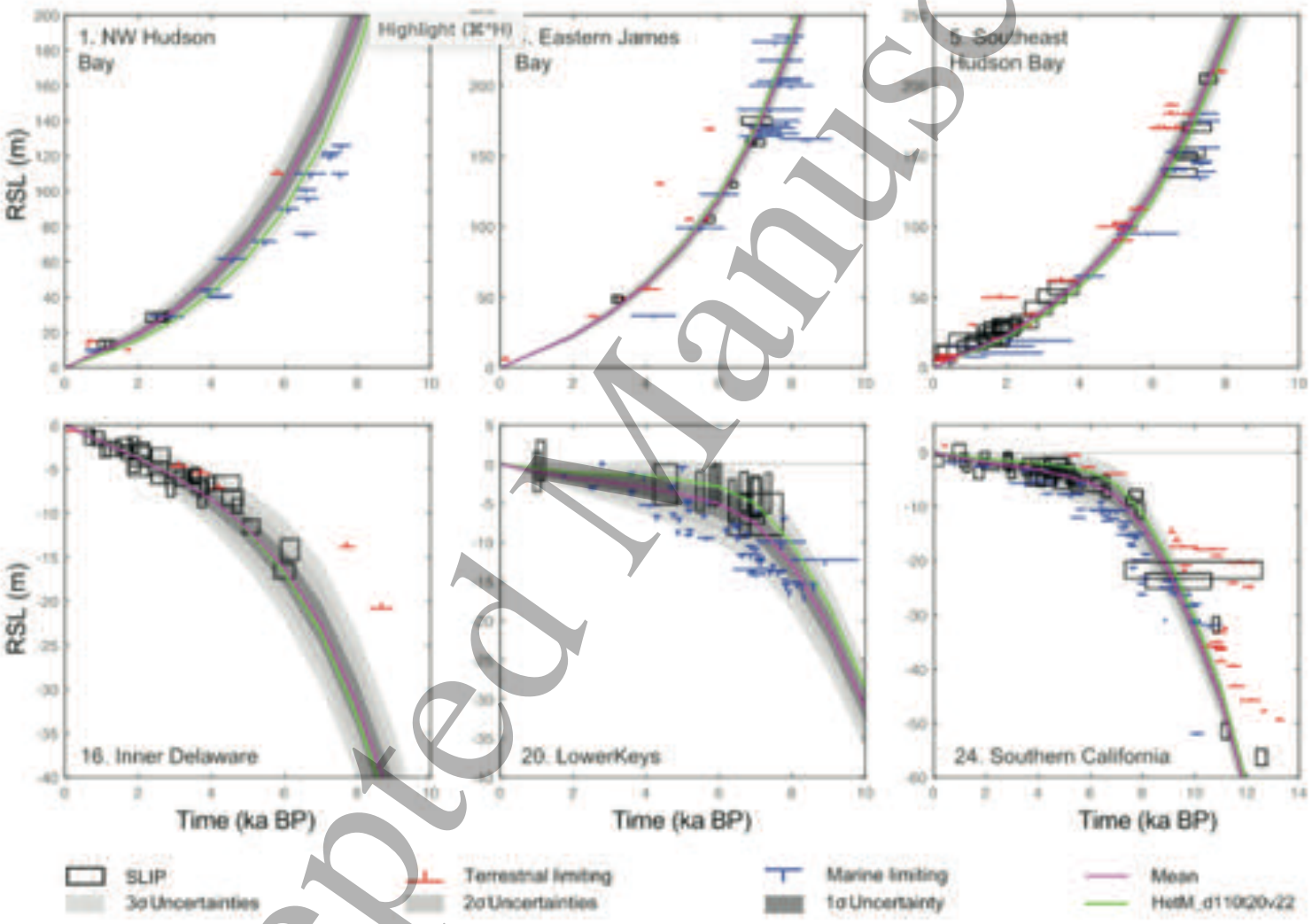

Fig 7.22

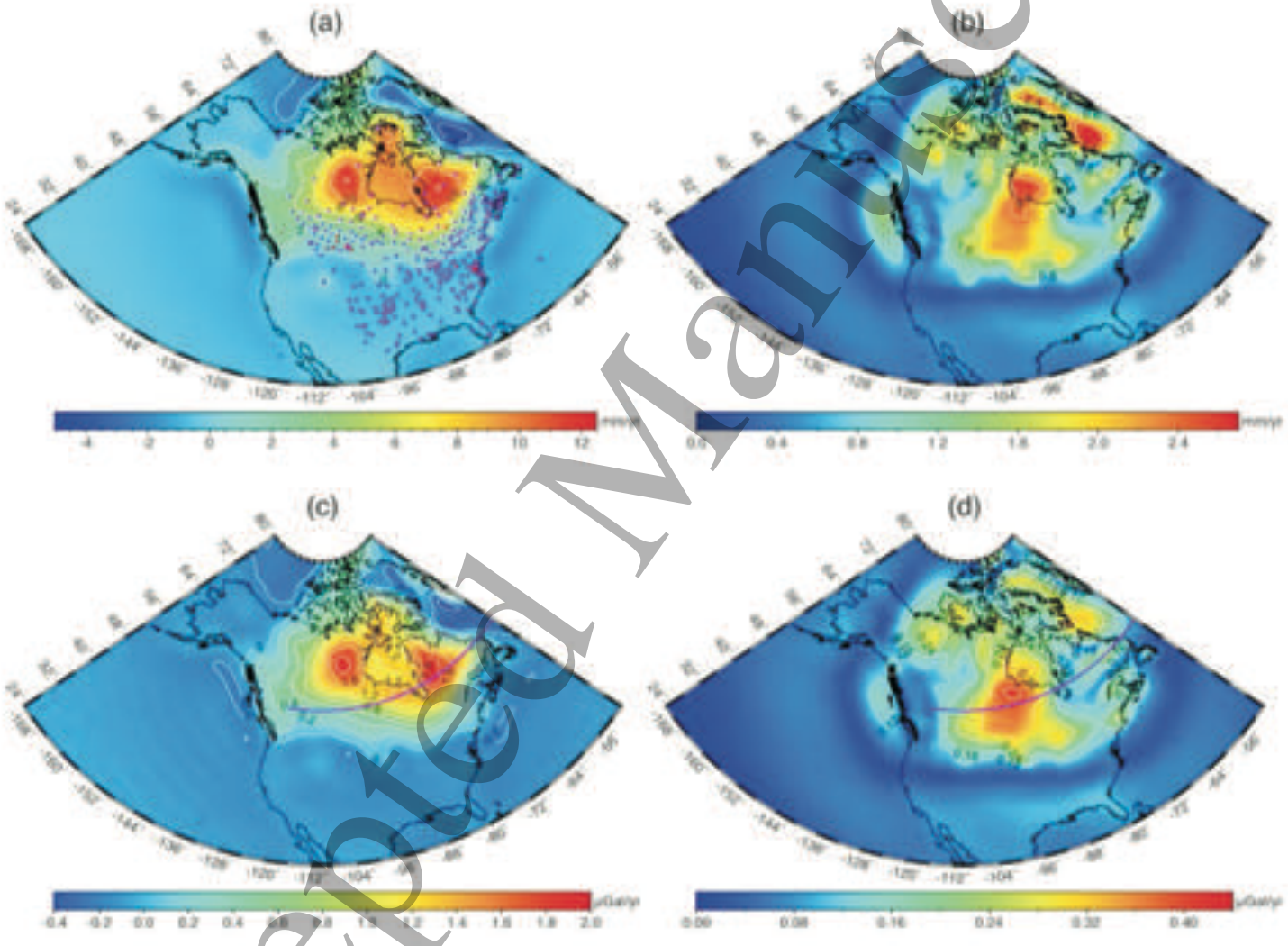

Fig 7.23

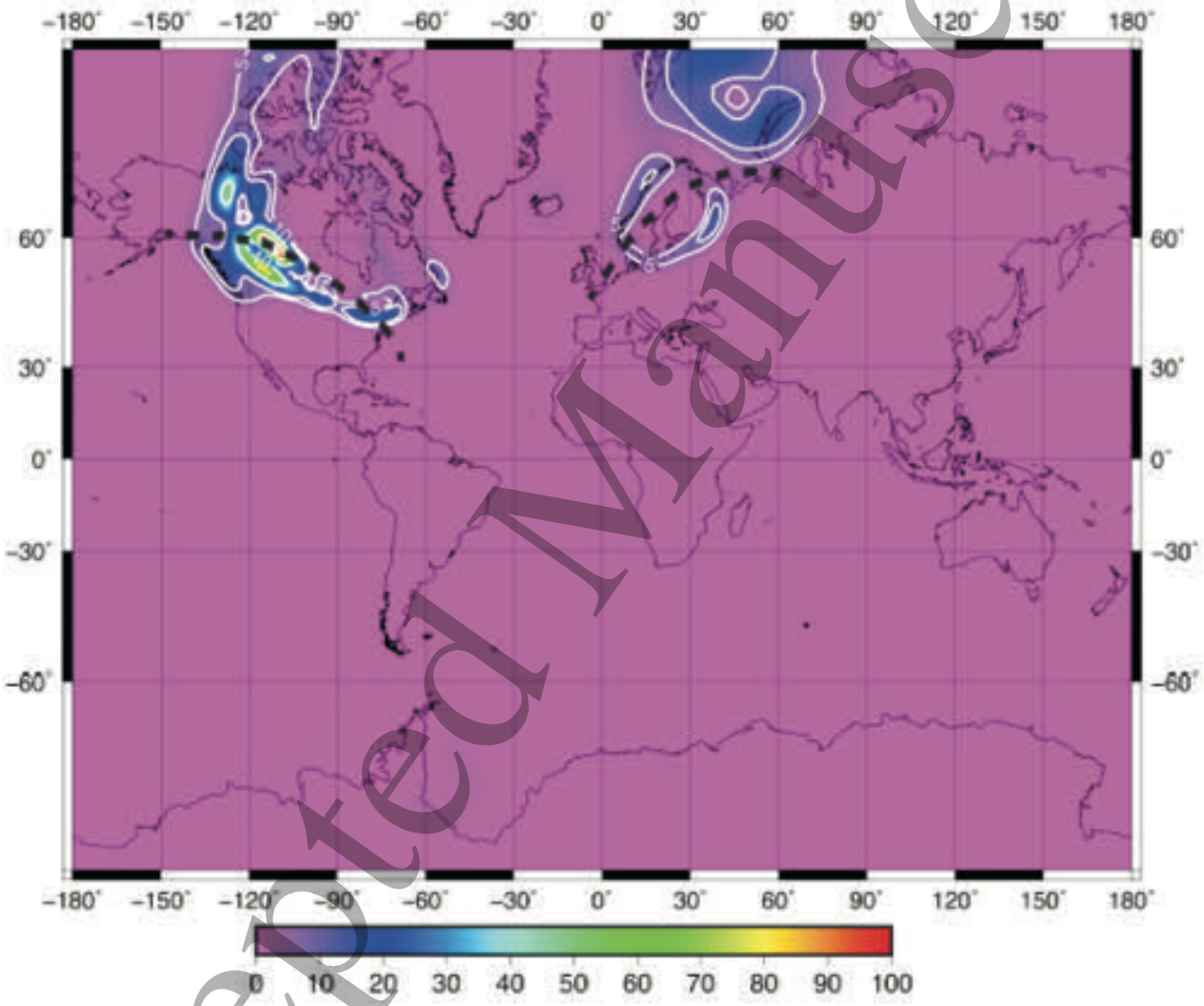

Fig 7.24

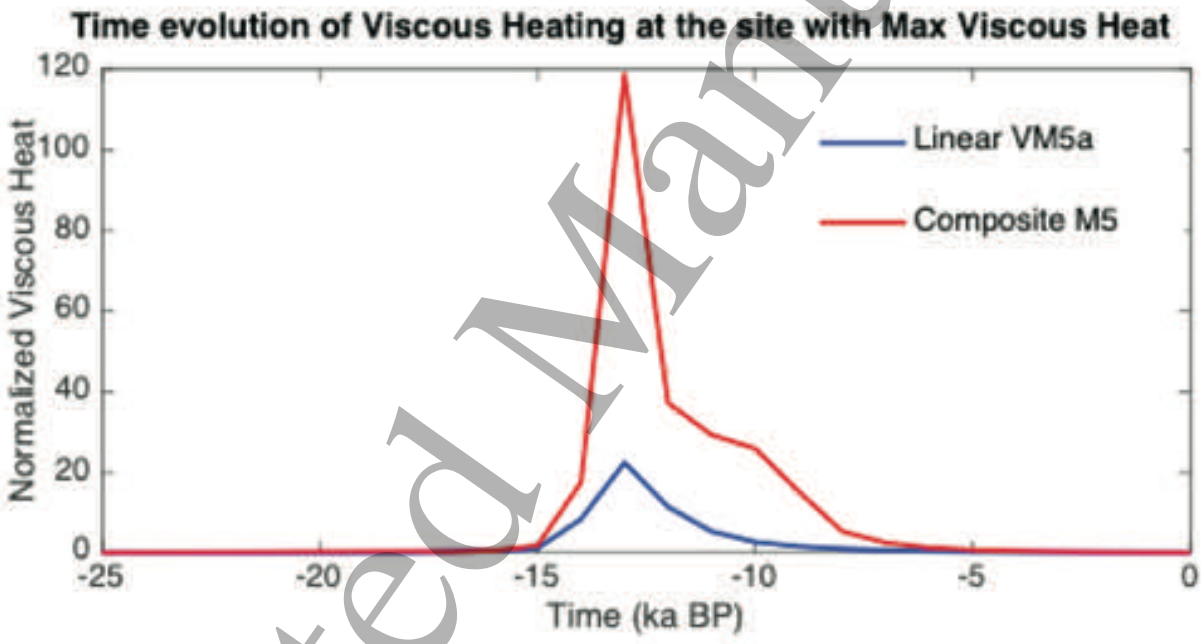

Fig 7.25

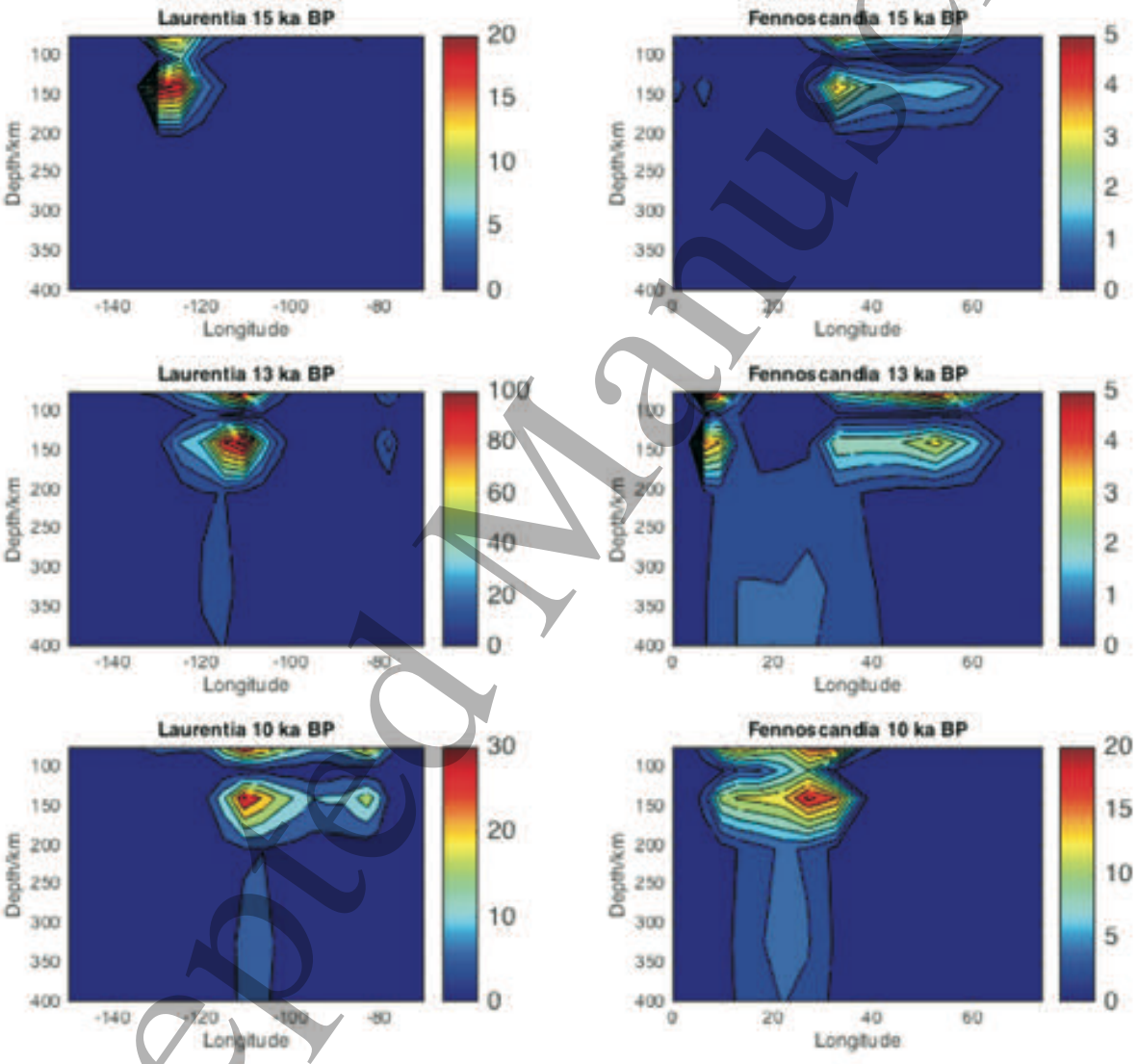

Fig 7.26

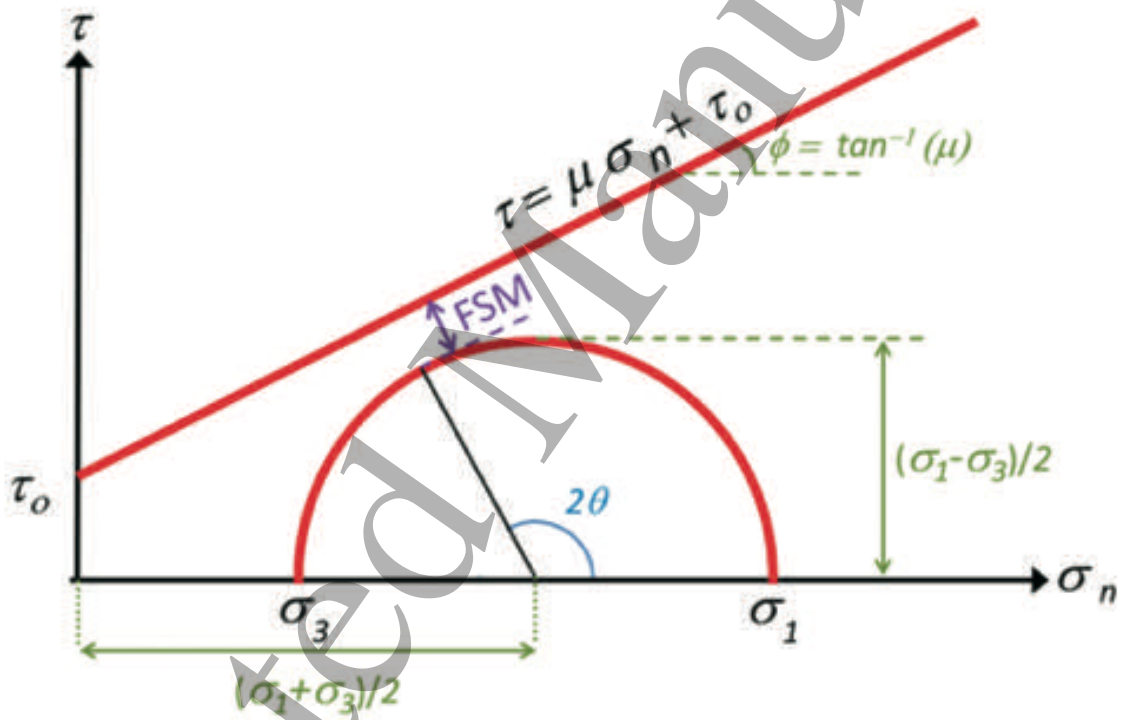

Fig 7.27

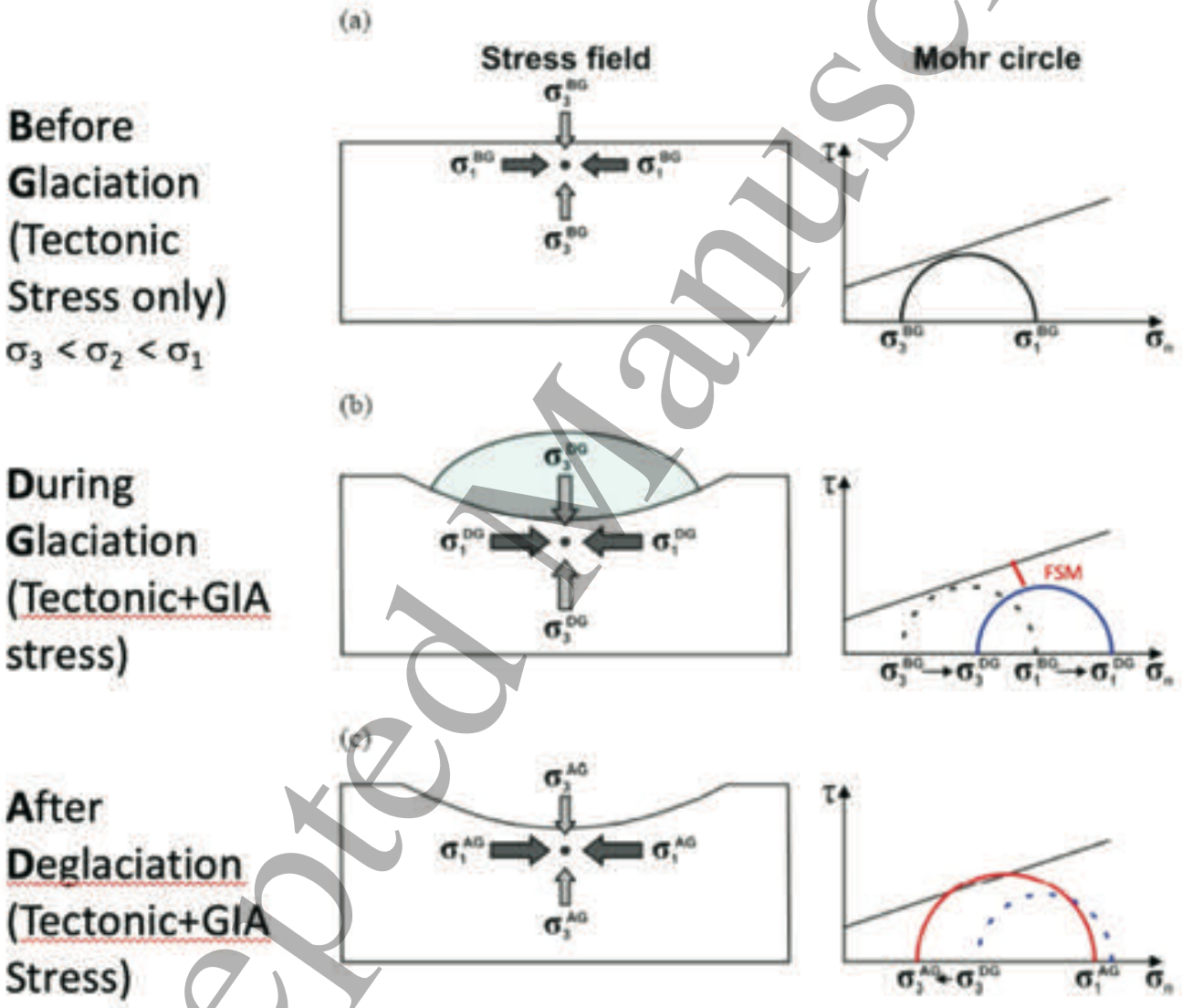

Fig 7.28

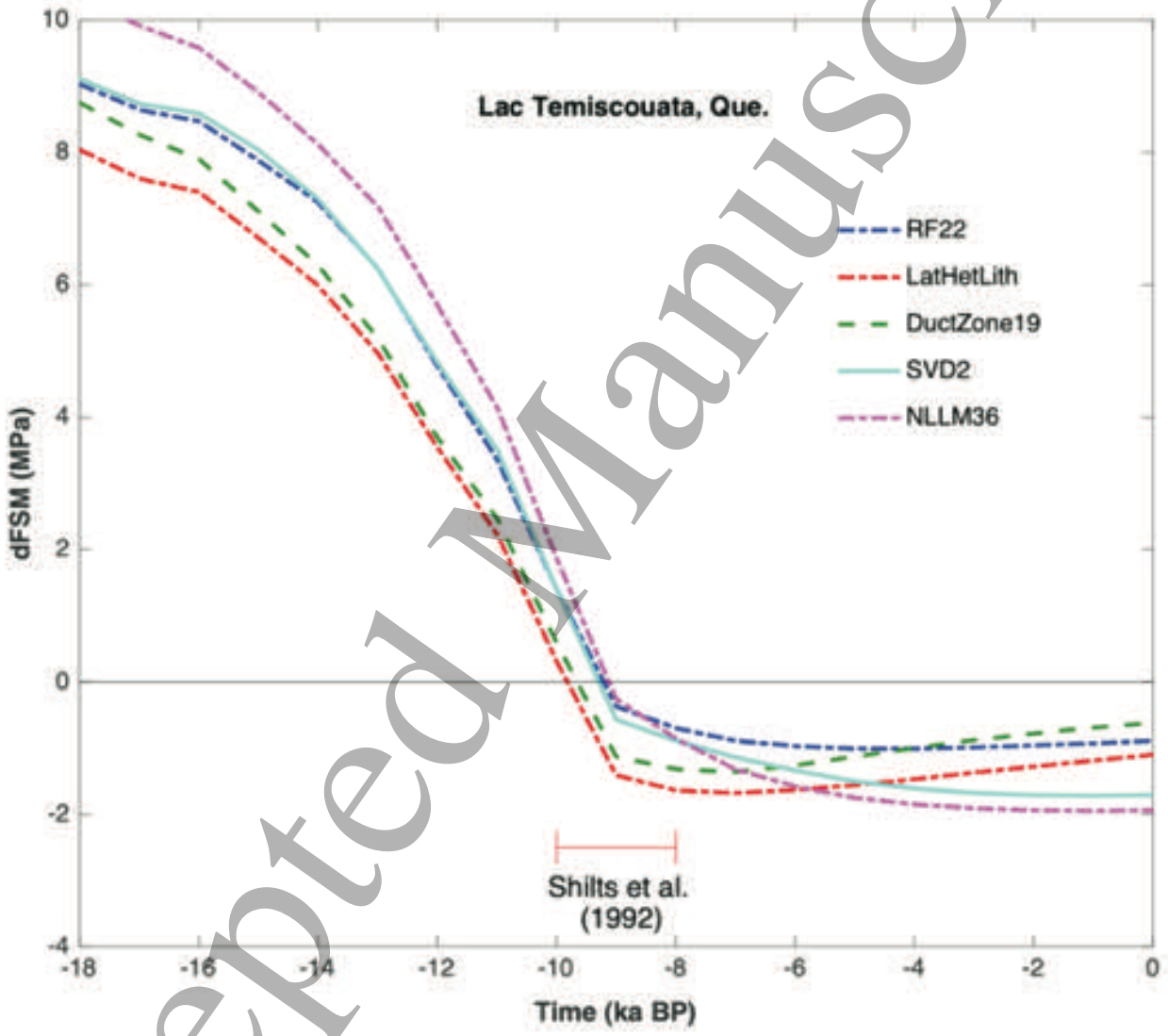

Fig 7.29

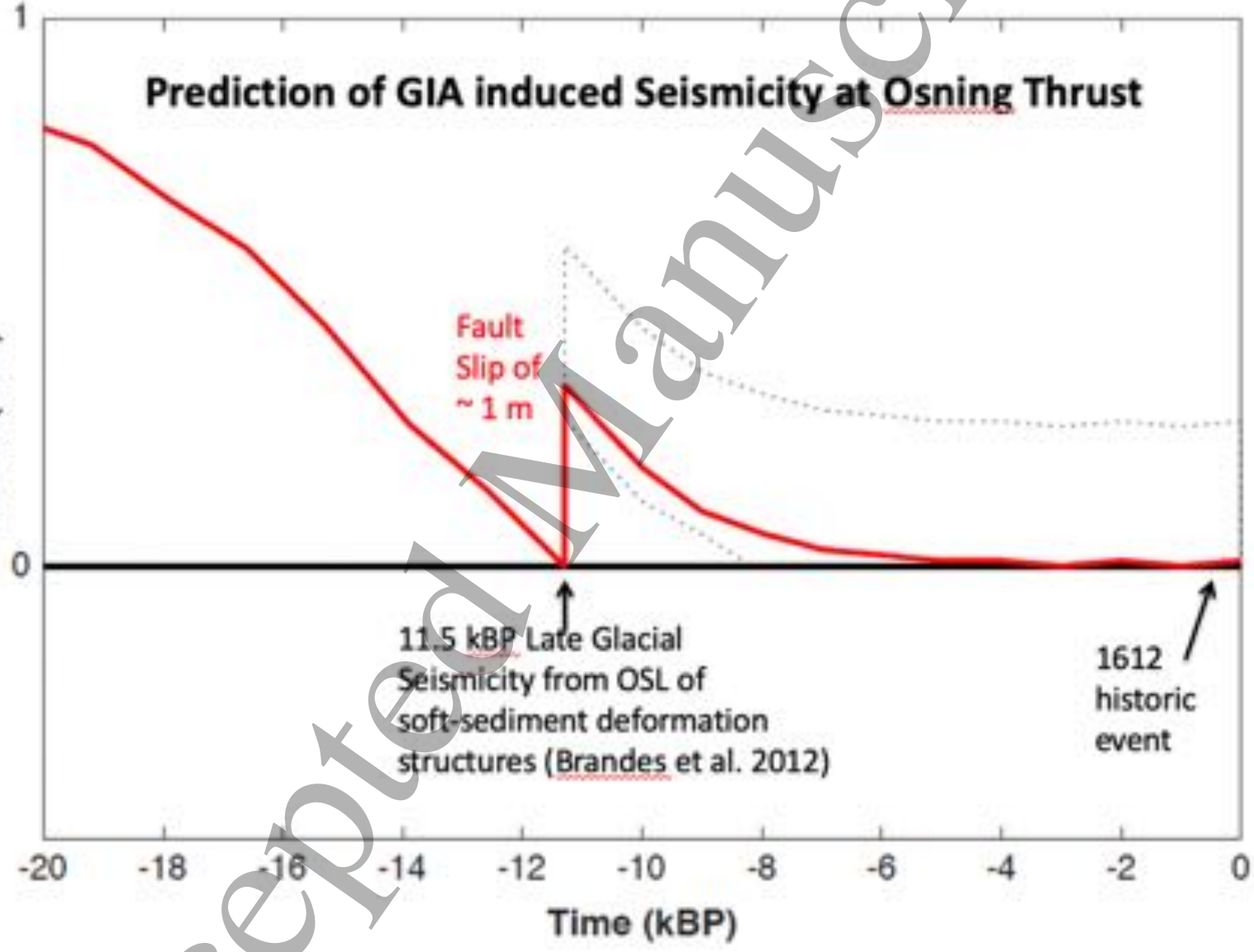

Fig 7.30